RESPONSE OF BLUE GLACIER TO A PERTURBATION IN ICE THICKNESS: THEORY AND OBSERVATION

Thesis by

Keith Alan Echelmeyer

In Partial Fulfillment of the Requirements

for the Degree of

Doctor of Philosophy

California Institute of Technology

Pasadena, California

1983

(Submitted April 7, 1983)

To my parents,

who first introduced me to the mountains

and the ways of nature

ACKNOWLEDGEMENTS

I am especially grateful to Barclay Kamb for many helpful discussions and suggestions concerning this thesis project. His keen physical insight and careful questioning provided much stimulation and help.

Without careful field work and data interpretation of Mark Meier, Barclay Kamb, Clarence Allen, and Robert P. Sharp at a time when I was but a wee lad, this project could not have been undertaken. Mark Meier graciously provided the much needed surveying data from their study. Hermann Englehardt and Brad Hager gave many helpful suggestions during the course of this study.

Parts of four years were spent on Blue Glacier. I owe a great THANKS to the many field assistants who helped in the rain and the snow and who even helped on the sunny days, instead of heeding the call of the mountains. This thanks is extended to Julie Brown (I am sorry you never saw the sun), John Brugman, Ian Dickerson, Bill Power, Carlos Quintana, Paul Schweitzer, and Nina Yanai. Special thanks go to Jim Mitchell for those days in the winter; Rich and Cindy Marriot, for their hospitality and ice cream; Howard Yanish of the Hoh Ranger Station, Olympic National Park, for his friendly help and hospitality, and to the rest of the rangerettes.

Olympic National Park graciously gave permission to work on the glacier.

Arthur Raefsky provided much help on the computational aspects of this work, as well as part of the computer code. Edith Huang and Kiku Matsumoto answered my unending questions on making the computer work. Jan Mayne, Kathi Kronenfeld, and Laszlo Lenches prepared many of the many figures. Barbara Niles and Jean Grinols helped with the business affairs.

To Marta Nyiri, I owe a special thanks (and apologies) for typing this thing.

Besides her many, many hours of help in preparing figures, Mindy Brugman provided unending encouragement during the preparation of this manuscript, and a much needed smile.

And last, but not least, I'd like to thank Mount Olympus and the surrounding peaks for all the enjoyment they provided.

This work was supported by National Science Foundation Grants EAR78-01715 and EAR80-08319.

ABSTRACT

A unique natural experiment has occurred on Mt. Olympus, Washington, in which the lower part of Blue Glacier has undergone a marked increase in ice thickness and a general decrease in surface slope. In response to this, the glacier flow velocities have increased considerably. The detailed study of the surface configuration and flow of the glacier during the period 1957-59, before the thickening (Meier,et al., 1974) provides a complete baseline against which the recent changes in geometry and surface velocity field are measured.

A detailed evaluation of the flow response to the changes in thickness and slope is made, testing for the existence of a quantitative observational relation among u, H, and α. A linear relation between the percentage ice thickness change and the percentage velocity increase is found. The slope of this response line is related to the exponent n in the flow law of ice, and the negative intercept represents an overall decrease in surface slope.

Detailed quantitative interpretations of the field measurements on the flow of Blue Glacier and its response to the change in surface configuration are made, using analytical and finite-element techniques.

A theoretical discussion of the effects of longitudinal stress gradients on the flow of an ice mass is given. This discussion leads to the development of an exponential Green's function which determines the effect of surface slope and ice thickness variations on the flow. This Green's function provides a weighting factor for longitudinal averaging of slope and thickness. The characteristic length scale up- and downglacier is dependent on the longitudinal strain-rate, the amount of basal sliding, and the flow-law parameters, being approximately three times the mean ice thickness. Application of this longitudinal averaging to

the observed slope and thickness changes results in a marked decrease in deviations of the response data from a linear regression on the velocity changes, showing that longitudinal stress gradients are important.

A finite-element computer code for the calculation of flow of ice in channel cross sections of arbitrary shape, including transverse flow components, is developed. The model is applied to flow in channels of idealized parabolic cross-sectional shape to reveal the basic effects of channel shape and flow-law parameters on stress and velocity distribution. The stresses are found to be dependent on the flow-law parameters. Components of transverse flow within the cross section that develop in response to transverse convexity of the glacier surface were calculated. Comparison with observations shows that much of the splaying of the velocity vectors within an ablation zone can be attributed to flow driven by this convex surface.

Analytical models of the flow of a glacier in which the flow law parameters vary with position are developed. These models show that there is a non-uniqueness in flow-law parameters obtained from borehole deformation studies. Studies of the response of a glacier to a change in surface configuration can partially eliminate some of this ambiguity.

The theory and finite element calculations are extended to channels that follow a curving course in map view, which is necessary for application to Blue Glacier, since in the reach studied the glacier flows around a gently curving bend of 90°. Longitudinal channel curvature causes asymmetry in the stress and velocity distribution within a symmetric channel. The stress centerline is shifted toward the inside of the bend, while the position of the maximum velocity is usually shifted outward of the center for $n \geq 3$. The effects of curvature are readily observable in the flow and crevassing of Blue Glacier.

The relation between perturbations in ice thickness and surface slope and the change in velocity is developed for arbitrary channels. Analytical and numerical results indicate that there is a linear relation between the changes in slope α, thickness H, and surface velocity u:

$$\log\left[\frac{u_1}{u_o}\right] = \Psi\,(n+1)\log\left[\frac{H_1}{H_o}\right] + n\log\left[\frac{\alpha_1}{\alpha_o}\right]$$

where Ψ is termed the response factor. For realistic channel geometries, Ψ is in the range 1/2 to 1. This factor represents the change in cross-sectional shape of an ice mass which accompanies a change in ice thickness within a given channel. The value of the stress exponent inferred from the observed flow response is significantly affected by this geometric factor, which is approximately equal to 0.82 for Blue Glacier. The slope of the response line implies that n=4 for the flow of Blue Glacier when this response factor is taken into account.

Finite element models of flow and the flow response within the different cross sections of Blue Glacier (as determined by radio echo sounding) compare well with the observed velocity patterns and response to change in thickness if channel curvature is included. These results again imply a stress exponent of n=4. The results also agree with the various field measurements which indicate that basal sliding contributes at most 10% to the overall motion of the glacier.

The results presented in this thesis represent the most detailed evaluation of the response of a glacier to perturbations in ice thickness and surface slope. They show that non-linear flow theory with n=4 is applicable to a good approximation. The relationship between the flow velocity, slope, and thickness found in this work has direct application to the study of effects of climatic change on an ice mass.

TABLE OF CONTENTS

CHAPTER I

INTRODUCTION

1.1 Introductory Remarks

In the analysis of glacier flow, one of the fundamental relationships is the dependence of the flow velocity on local ice thickness and longitudinal surface slope within a given bed configuration. Following the generally accepted form of glacier-flow theory (Nye,1957), it can be shown that this dependence plays an important role in determining how a glacier responds to a change in accumulation and ablation over its surface, that is, to a changing climate (Nye, 1963a,b). The dependence of the flow on thickness and slope enters into the perturbation analysis of glacier response via the partial derivatives, $\frac{\partial u}{\partial H}$ and $\frac{\partial u}{\partial \alpha}$, of the (cross-sectionally averaged) flow velocity u with the respect to local ice thickness H and surface slope α. These derivatives are closely related to the theoretical kinematic wave speed and diffusivity (Nye, 1960 ; Hutter, 1981). In the development of a dynamical response theory for glaciers, values of the parameters $\frac{\partial u}{\partial H}$ and $\frac{\partial u}{\partial \alpha}$ have not, up to now, been evaluated by direct observation.

The generally accepted form of glacier-flow theory has been called into question recently by Lliboutry and Reynaud (1981), who discount the concept of local control of u by H and α on the grounds that transmission of longitudinal stresses can cause u to be determined not locally but by conditions in "controlling zones" at a distance. Without a resolution of this contradictory claim, progress of glacier-flow theory and its application to realistic situations is severely hampered.

This thesis describes work carried out to test the basis of glacier-flow theory by seeking to evaluate observationally the dependence of ice flow on thickness

and slope in a specific glacier. A unique natural experiment has occurred on Mt. Olympus, Washington, in which the lower part of Blue Glacier has undergone a marked increase in ice thickness, amounting to some 10 to 20 m (up to 20%), and a general decrease in surface slope. In response to this, the glacier has noticeably advanced, and flow velocities have considerably increased (by up to 50%). A detailed and accurate study of the surface configuration and flow of the glacier during the period 1957-59, before the thickening (Meier, Kamb, Allen, and Sharp, 1974)[1] , provides a complete baseline against which the recent changes in geometry and surface velocity field are measured. The measurements allow a detailed evaluation of the response of the flow to changes in thickness and slope, testing for the existence of a quantitative observational relation among u, H, and α.

In order to confront the predictions of glacier-flow theory with the observational results, it is necessary to develop analytical and numerical models for calculating the flow in realistic channel configurations, taking into account important effects such as the averaging of longitudinal stress gradients, flow curvature in plan view, and possible depth variation of flow law parameters. These models show that the observed flow pattern and the observed flow response to the change in surface configuration can in fact be accounted for *in detail* by a form of standard glacier-flow theory based on a power-law-type constitutive relation for ice, in which a relation between u and longitudinally averaged H and α is implied. As such, the observed data set then provides perhaps the most accurate and unambiguous method to date for determining the numerical parameters in the flow law of ice for a glacier whose motion is largely determined by internal deformation.

1. [Denoted as M1 throughout this work.]

The observational data were obtained by standard triangulation techniques over a period of several years (1977-80), supplemented by the location of buried magnetic markers. A thorough and complete radio echo sounding survey was undertaken to complement the existing information on the configuration of the channel of Blue Glacier (M1; Corbató, 1965). Theoretical analysis of the stresses and flow in simple and realistic valley forms was undertaken by analytical and finite element techniques, extending the work of Nye (1965) to more - nearly three dimensional flow and different values of the flow law parameters. Important questions about the stress and velocity fields of a glacier flowing down a channel are addressed, such as the coupling with the flow law, effects of a depth variation of flow law parameters, effects of longitudinal curvature, and the stresses and flow induced by a convex upper surface. In addition, a theoretical discussion of the longitudinal averaging of stress gradients within an ice mass is given, providing a quantitative means of averaging ice thickness and surface slope from field data. With these results as a basis, the response of the flow of Blue Glacier to changes in surface geometry is evaluated by further analysis, enabling the observed flow response to be interpreted in terms of the various factors governing glacier flow.

1.2 Physical Setting of Blue Glacier

Blue Glacier (47° 49' N , 123° 42' W) is a relatively small valley glacier draining the north-eastern slopes of the Mount Olympus massif in Olympic National Park in northwestern Washington, USA. The glacier is 4.3 km long from its head at 2,375 m to the terminus at 1,255 m. With a mean width of 1 km, the glacier covers 4.3 km^2. The equilibrium line has a mean elevation of approximately 1650 m, giving an ablation area of about 2.5 km in length. The lower glacier is separated from the main accumulation basins by a major icefall of 300 m in height located about 0.5 km upglacier from the equilibrium line. The portion of the glacier

studied herein lies from the base of the icefall to the terminus and is shown in Plate 1. Within this region the glacier makes a gentle curve to the west through an arc of roughly 100° with a radius of curvature of about 1 km.

The mean surface slope of the glacier in this lower section is approximately 6°. Locally, the surface slope approaches 9° in some regions, such as over a 400 m region about 1.2 km above the terminus. For the last 350 m the glacier steepens to nearly 40° as it moves over a major bedrock step and thins into a characteristic wedge-shaped terminal lobe. (See Section 3.5 and Figure 4.1).

Average ice thickness of the lower region is about 150 m, with a maximum depth along the centerline of nearly 280 m . The channel shape is roughly parabolic with an aspect ratio of 1.6 (half -width to depth), as shown in Figure 3.7.

Ice flows in a northerly direction down the lower channel with a mean speed of 45 m/yr and a maximum speed in this lower region of ~ 65 m/yr (see Plate 1). A splaying crevasse pattern is found in the lower part of the section under study and a series of large transverse crevasses exist in the middle region of increased surface slope (see Allen, et al. 1960, for a complete description of the surface features).

The glacier is a temperate glacier (Harrison, 1972). There exists a large winter accumulation (10 m of snow) and summer ablation (5 m) in the strongly maritime climate of the Olympic Peninsula (LaChapelle, 1959, 1965). The copious quantities of winter and summer precipitation conform to the reputation of the Olympic Penninsula, and can lead to a dampening of spirits. But when the clouds clear, the ice can be as blue as the sky and the spirits can't wait to fly.

Fluctuations in the thickness and terminus position of Blue Glacier have occurred in the past. Heuser (1957), Hubley (1956), and Spicer (unpub.) discuss these fluctuations and their relation to climatic variations. The most recent

thickening and advance began in about 1958 with an initial increase in glacier volume of 0.4% per year as determined by LaChapelle (1965). If a steady rate of increase of this amount is assumed for the following 15-20 year period then the observed thickness change of up to 20 m can easily be accounted for. The glacier has seen a slight decrease in depth and little terminus advance during the last few years (1981-82).

CHAPTER II

FIELD METHODS FOR DETERMINATION OF VELOCITY AND SURFACE ELEVATION

The surface velocity field and the surface elevation of Blue Glacier were determined by the location of a large number of material points on the surface of the glacier at various times during the course of this study. Standard surveying techniques were used for the majority of the position determinations, being supplemented by magnetometer surveys and taping. A description of the field methods and data reduction are given in this chapter with attention to the accuracy and efficiency of the methods. The assessment of errors in the data plays an important role in determining the validity of the interpretations to be given in later chapters. Where standard methods are used the discussion is brief, while a more extensive discussion is given for other, less common methods.

The measurement of triangulation angles is described first, followed by a description of the network of triangulation points used in the surveys. The third section deals with the location of surface markers by theodolite triangulation, while in the fourth section the accuracy of the resulting coordinates is discussed. Location of buried markers by magnetometer surveys is discussed in the last section.

2.1 Angular Measurement

A Wild T2 theodolite was used for precise determination of horizontal and vertical angles from given reference points to markers located on the glacier surface. Standard techniques to eliminate leveling, collimation, and instrumental drift errors were employed. The resulting accuracy of the horizontal angles was approximately 2 seconds of arc, and of the vertical angles 4 seconds. A complete discussion of the distribution of these errors is deferred until a later

section, where their influence on the location of the markers is described.

2.2 The Triangulation Net

A network of triangulation points (TP) along the margins of the glacier was established for use as instrument sites. All of the TP sites except one were located at the approximate position of the corresponding point in the 1957 network, which had been carefully set up with regard to accessibility, visibility, and stability by Meier and others. A survey site beneath the cliffs of Apollo (TP3) was set up in a reasonably safe position, as the 1957 point had been destroyed by a rock avalanche. A short brass rod with a centering indentation was affixed with concrete to the bedrock or cairn at many of the TP sites. A one meter marker pole and flag could be fit over this fixed rod and secured with guy cables when the survey site was not occupied. In a few sites small holes were drilled into the bedrock as the reference point.

Early in the 1977 field program the internal angles in the net were surveyed with 3-6 repetitions of the angles involved to provide for a high-order precision in the network. TP sites 1 and 5 were selected as a baseline for the net, based on their stability and visibility. The horizontal coordinates of these two points were taken the same as in the 1957 network. The horizontal angles of the net were adjusted using the method of condition equations with unit weight (Allan, Hollwey, and Maynes, 1977). These equations include: 1) station conditions, such that $\sum \alpha = 360°$ about the site; 2) angle conditions a) $\sum \alpha = 180°$ for a given triangle, and b) the sum of two angles must equal the total angle included. These condition equations lead to a set of normal equations(Shchigolev,1965)which are solved to yield the optimal corrections to the surveyed angles. Using these corrected angles and the TP5 to TP1 baseline, the horizontal coordinates of the network were determined using the relations of the next section. The vertical

coordinates of the stations were determined as a weighted mean of the independent measurements from different sites, where the elevation of TP5 was taken as known from the 1957 network.

Based on the internal consistency of the network, the standard error of the triangulation site coordinates are $\sigma_x = \sigma_y = \sigma_z = 1$cm. Since the triangulation net survey involved many repetitions of a given angle the resulting coordinate errors are reduced from those stated below for the surface markers. (These estimates of accuracy hold for all sites except TP11 and TP12.These two sites could not be included in the network analysis because of a lack of inter-visibility with the other sites. These triangulation points have absolute position errors of 5 m. and relative location errors between them of 15 cm. A comparison of the horizontal coordinates with those of the 1957 sites shows little change. The vertical coordinates are significantly different due to the change of the reference point at most sites. The internal accuracy of these coordinates will not greatly affect the velocity determination as the velocities involve relative differences in position. If the velocity markers are observed from the same TP stations from survey to survey, then the TP coordinate errors will tend to cancel out and, in any event, their effect on the measured velocities will be small compared with that of direct errors in the marker locations. Following this reasoning the TP station coordinates are assumed to be exact in the error analysis that follows. The coordinates of triangulation points are given in Table 2.1. The location of TP sites are shown on the various maps used throughout this work. The brass rods or small holes in the bedrock were left in place so that future workers may have a fixed network of triangulation sites.

2.3 Survey of Surface Markers

During the course of this study the motion of a large number of marker poles

Table 2.1

Coordinates of Triangulation Points

TP	X(m)	Y(m)	Z(m)
1	451.99	2279.58	1468.41
2	1122.66	1837.29	1544.57
3	1274.54	570.51	1679.42
4	94.62	1616.26	1509.08
5	405.94	1276.64	1634.61
6	371.48	972.18	1614.48
7	201.31	712.76	1690.69
8 (Jelly Bar)	99.11	655.86	1721.03
9 (SB)	-0.01	999.97	1778.79
11	-205.50	2165.00	1290.00
12	-282.28	2324.19	1172.67

$\sigma_{x,y,z}$ = 0.01 m ,except for TP11 and TP12

implanted in the glacier surface was determined by triangulation from the instrument sites described above. The positions of as many as 123 markers were measured at intervals of two weeks to one year, giving a detailed picture of the surface velocity field of lower Blue Glacier through time. A majority of the markers were distributed along 14 transverse lines, labeled A through Q. These transverse lines spanned the lower glacier, from the crevassed terminal region up to the base of the central icefalls and including the ice stream decending from Blizzard Pass. Other markers include intermediate points along the longi-

tudinal centerline and scattered borehole casings remaining from previous years. In addition, five markers on the western lobe of the terminus were surveyed intermittently, as were six markers in the central icefall.

In this section a description of the surface markers, their positioning, and the method for determination of their location is given.

Surface markers which are to remain in the ice or firn for long periods of time must meet certain criteria in terms of durability, visibility, weight, influence on ablation, and cost. The markers used in this study were to remain implanted in the surface throughout the harsh winters experienced on Blue Glacier, exposed to storms with severe winds and heavy rime, before being covered in a deep, dense snow pack. Therefore it was desirable to have durable stakes which would remain as straight as possible. During the summer months, poles placed in holes drilled into the ice would, after a time, becomeimmersed in the liquid water filling the holes. In order for accurate vertical coordinates to be determined, the stakes must not float. The large number of markers and the limited access to the glacier required fairly light poles. For these reasons high strength aluminum (6061) poles were chosen for a majority of the markers. The dimensions of these poles were 3.7 cm OD x 0.16 cm wall and 3.7 m long. Some of the markers used above the firn line were 2 x 2 cm wood stakes 3.3 meters long. The wood minimized the conduction of heat into the snow and, thus, stake tilts were often smaller at the locations where wood markers were used than where aluminum poles were used. However, several of the wood markers were broken off by high winds during storms in the spring and fall. To keep the aluminum poles from melting down into the ice,corks or rubber stoppers in which holes had been bored were placed in the lower end of each hole, providing insulated contact with the ice.

The stakes were placed in the ice by one of four methods:

1. using a steam drill developed by Steve Hodge (Hodge, 1977), on loan from C. Raymond, University of Washington;
2. using a SIPRE hand auger on loan from CRREL;
3. in the firn, by means of a core tube;
4. using an experimental open flame (oxy-acetylene) drill developed by the author (which did not prove to be highly successful).

Stakes were periodically reset during the course of the ablation season. Methods for reducing the tilting of each stake due to differential melting, such as a sliding ring which was to move downward into the ablation cone surrounding each stake, and a thick piece of styrofoam insulation to deter the development of the large ablation cone, proved ineffective. As described below, the height of each pole above the ice surface and the tilt of each pole were measured close to the time of survey.

In addition to these markers, eight borehole locations were surveyed. Six of these boreholes were drilled and cased in 1957-61 by Shreve and Sharp (1970) and are designated S1, S2, M1, M2, L, B. The other two boreholes were drilled during 1977 by Englehardt and Kamb (1979) on the F and H profiles. These two holes were marked by aluminum poles.

For the purpose of this study (comparison of the surface elevation and velocity field in 1977-78 with that in 1957-59), data are required at given spatial locations in an Eulerian sense, that is, at points fixed in the initial configuration space, not moving with the medium. Because there are gradients in elevation and flow velocity over the glacier surface, erroneous apparent changes from 1957-59 to 1977-80 in surface elevation or velocity

could result if the markers were at positions considerably different from those of 1957-59. Correction for descrepancies in marker position could be made by interpolation within the surface elevation and velocity fields, but this could lead to a considerable loss in the accuracy of determination of the changes in elevation and flow veloctity if the positions of the markers were significantly different in the 1957-59 and 1977-80 surveys. Optimal placement of the surface markers was sought at initial horizontal positions such that the midpoint of each motion interval would be the same as that of the corresponding 1957-59 interval. A rough estimate of the velocity increase in 1977 was based on preliminary observations in 1976 by Kamb and the author. It was determined that the velocities could be as much as 30-40% greater than those observed in 1957-58. Therefore, the initial locations of the surface markers in 1977 were calculated by projecting the 1957 coordinates up glacier an amount corresponding to the velocity increase (and an additional amount for the earlier time of initial placement during the summer of 1977).

In order to place the poles accurately at positions with these optimal initial coordinates, the following system was developed. Plane table maps with TP sites and initial stake locations at the anticipated time of implacement were constructed. Such a map was properly oriented at each of two triangulation sites selected for a particular line of stakes. An observer at each TP site would align a telescopic alidade on the plane table along the line from the TP site to a desired marker location. Using hand held radios, a party on the glacier surface was guided to the intersection of these two alidade lines, at which point the stake was placed. With practice, this method allowed for rapid and accurate (to within 3-8 meters) stake placement at specified locations.

The 1957-59 survey was carried out for about 50 markers located along nine transverse profiles,designated by letters a to i. Due to the loss of the lower line (a) in 1958, results for only eight of these profiles were reported by M1, the profiles *b* to *h* being renamed *a* to *g*. Results were also reported for an additional profile with closely spaced markers inserted between the original *h* and *i* profiles, and designated *h* in the revised lettering scheme of M1. This additional line of markers was not reproduced in the present survey. Throughout the present study the original 9-line labeling scheme is followed (using capital letters), hence lines *a* to *g* as reported by Meier et al.(1974) correspond to lines B to H as reported here. For example, data for the stake *a*3 in M1 will correspond to B3 in this study, while *i*3 orI3 designates the same stake position in both reports.

During August of 1977, using the method described above, approximately fifty stakes were placed in positions corresponding to the 1957 positions along profiles A through I. Three to four additional markers were placed along each profile so as to extend the transverse lines outward toward the glacier margins. Additionally, above the I profile five additional transverse lines of markers were implaced in the glacier surface: J,K,L,N,Q. These lines extended the areal coverage to the base of the central icefalls and to points within the ice stream decending from Blizzard Pass. The map in Plate 1 shows the location of the 123 stakes monitored at various times in this study. The extended areal coverage is helpful in accurately describing the flow field near the margins for comparison with the modeling calculations of later chapters and in obtaining a more complete description of the longitudinal variation in velocity.

From two triangulation points chosen for efficiency and for accuracy of marker positioning in a given profile, the coordinates of each stake were

determined at different times during the study period. The time interval between surveys was approximately two weeks during the spring, summer, and fall of 1977 - 1978. Additional surveys were made during the winter of 1979 and at various times during the summers of 1979 and 1980. Approximately 20,000 angles were measured. A survey of the stake network took from one to four days and was carried out under a variety of weather conditions.

A computer code was developed to reduce the surveying data to stake coordinates and velocities. Preliminary coordinates of the top of each stake were reduced to coordinates for a parcel of ice originally at the base of the stake at the time of the first survey. This original parcel is termed the reference point; it is this reference point for each marker stake whose motion is reported and discussed in this study.

The preliminary coordinates were computed using the angles obtained from the theodolite survey. Standard formulae (Allan, Hollwey, and Maynes, 1977) with a small correction for atmospheric refraction and curvature were used. Figure 2.1 gives definitions of the angles and distances used. The coordinates of the unknown point G,determined from TP's E and F, are given by

$$X_G = \frac{X_E \cot\beta + X_F \cot\alpha - Y_E + Y_F}{\cot\alpha + \cot\beta} \tag{2.1}$$

$$Y_G = \frac{Y_E \cot\beta + Y_F \cot\alpha + X_E - X_F}{\cot\alpha + \cot\beta} \tag{2.2}$$

$$Z_G = \frac{Z_G^E + Z_G^F}{2} \tag{2.3}$$

where

$$Z_G^E = Z_E + A\cot V_E \quad \text{and} \quad Z_G^F = Z_F + B\cot V_F \ . \tag{2.4}$$

Here V_E and V_F are the angles from the vertical at E and F to the top of the

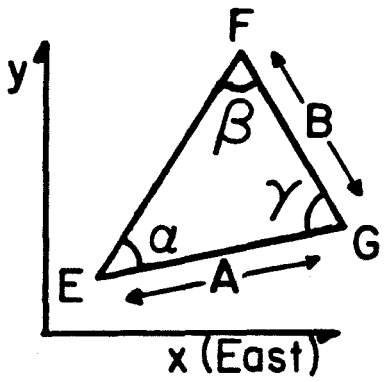

Figure 2.1 Notation for angles and distances used in triangulation.

marker pole at G, and Z_E, Z_F are the vertical coordinates of E and F corrected for the instrument height.

The coordinate system used was oriented such that the Y axis was directed toward true north and the x axis eastward, with z positive upward as elevation above mean sea level. The origin of this system was chosen such that the triangulation site South Base (designated SB) has coordinates which correspond approximately with those given by Meier, et al. (1974) (i.e. (0,1000,1780)).

Reset corrections were applied by adding an accumulated reset for each stake as the marker was periodically reset. At the time of a reset the following parameters were measured: distance, D, and azimuth, φ, from the old to the new position, H_o and H_n, the old and new stakes heights, respectively, and Δice, the change in the ice surface over the distance D between the old and new positions, being positive if the new surface height was higher than the old. Then, for this individual reset, the correction to be applied to the coordinates is given by

$$R_x = -D\sin\varphi \tag{2.5a}$$

$$R_y = -D\cos\varphi \tag{2.5b}$$

$$R_z = -(H_n - H_o + \Delta\,\text{ice})\,. \tag{2.5c}$$

These reset corrections were cumulative so that the calculated coordinates refer to the original parcel of ice (the reference point):

$$R_x(t) = \sum_i R_x(t_i)\,, \quad t_i \leq t \tag{2.6}$$

Usually, within a day of the survey of a given stake a measurement of the tilt of the stake was made. The large number of stakes and the frequent bad weather required a rapid and efficient means of measuring tilts reproducibly. For large tilts (greater than 15°) the angle of tilt and its azimuth could be measured accurately with a Brunton clinometer and compass. Smaller tilts required a better method of measurement, because the azimuth and maximum tilt were difficult to measure directly. Instead, a direction, designated E, was determined as the mean direction along the transverse profile within which the stake was located. At right angles to this and oriented down glacier was another direction designated D. The tilt of each stake was determined by measuring with a Brunton clinometer the angle of the pole with the vertical in each of these directions. Within the data reduction code a value of the row parameter was prescribed for each marker, R, being the azimuth of the direction D, counterclockwise from true north. If no overriding direction was prescribed as input, this row parameter was used in the computations of the tilt corrections. Given the tilt angles T_E and T_D, and the row parameter, the following relations for the tilt correction hold.

$$TX = -L\,[\,\sin T_E \cos R - \sin T_D \sin R\,] \tag{2.7a}$$

$$TY = -L\,[\,\sin T_E \sin R + \sin T_D \cos R\,] \qquad (2.7b)$$

$$TZ = +L\,[\,1 - \cos(\,\sin^{-1}[\,\sin^2 T_D + \sin^2 T_E\,]^{1/2})\,]\,, \qquad (2.7c)$$

where L equals the total length of the pole. These results hold for small angles T_E , T_D, while an equivalent expression is easily obtained for larger tilts using the maximum tilt and its azimuth. (The relations (2.7) assume that the base of the pole does not move relative to the ice, which is a good approximation for all but the largest tilts.)

These tilt corrections relate the top of the stake to the base, which, upon correction for the cumulative resets, allow coordinates of the reference point to be given at the time of each survey. These coordinates are then used in the velocity determination.

Early in the spring of 1978, many of the poles left in place in September, 1977 were not visible, being buried under several meters of snow. Wood stakes (2 x 2 cm x 3 m) were placed at positions estimated from previous velocity measurements and the September coordinates using the method of two alidades described above. These stakes were then used as temporary markers until the original markers became visible or until the buried magnets fastened to the original stakes could be located as described below. At the close of the 1978 field season (late September) a large number of stakes were removed, leaving those along the centerline. Of the stakes remaining, about half were reset a large, predetermined distance up glacier so as to allow an additional determination of annual velocities at fixed Eulerian points. Other markers were left in their September, 1978 positions to allow a direct comparison with the second annual velocities of M1 measured from 8/58 to 8/59. These correspond approximately to a Lagrangian type velocity determination, with points fixed in the moving medium.

During February and March of 1979, measurements of wintertime velocities were made along the centerline using wood stakes, periodically reset upward to account for the very large amount of accumulation during this period. These stakes were left in place, and those that survived, together with those left in place at the close of 1978, were resurveyed in June, July and early August of 1979. These measurements allow winter and spring velocities to be determined. During September, 1979, several more stakes were removed, and of those remaining, several were reset a given distance upglacier while others were left in place, corresponding to the two types of velocity measurements previously described.

Finally, in 1980, over a period of two weeks during July, surveys were made of the 20 poles left in place in September 1979.

The velocities determined from these measurements are described in Chapter IV.

2.4 Accuracy of the Marker Locations

Although the T2 theodolite has a precision of one second, the accuracy of any angle measurement will depend on the leveling and stability of the instrument, time dependent atmospheric conditions, the care taken and techniques used by the observer, and other factors. These will lead to a distribution of random errors about an estimate of the true angle, as well as the possibility of a systematic and/or gross error. The accuracy of an angle measurement is found to be two to three seconds of arc (as shown below), even though the theodolite can be read to one second.

Throughout this study we are concerned with the best estimate of the standard error, σ_x, in the measurement of a given parameter x. This is defined as

$$\sigma_x = [\ \frac{1}{N} \sum_{i=1}^{N} (x_i - \bar{x})\ ]^{1/2} \qquad (2.8)$$

where x_i are the N measured values of x with a mean of $\bar{x}$. The mean, $\bar{x}$, is an estimate of the true value of x.

Gross errors, such as mistakes in the recording of data or misreading of the minutes scale of the theodolite, are not necessarily random. The best method to eliminate these large systematic errors is to filter the data. Filtering of the coordinate data was accomplished by examining the difference between the forward and reverse angles to each marker from a given triangulation site during each survey, in both the horizontal and the vertical (denoted $\Delta\alpha_H$ and $\Delta\alpha_V$, respectively). In addition, the difference between the two elevations Z_G^E and Z_G^F (as defined in (2.4)) calculated from the two TP sites used in the triangulation were examined. Anomalous measurements were either corrected by some means or the data were eliminated.

The accuracy of the coordinates derived by triangulation of a surface marker and then reduced to the original reference point are given as a combination of the errors in the theodolite measurements, tilt measurements, and any resetting data.

The accuracy of the preliminary coordinates is related to the accuracy of the angle measurements, σ_α. Two ways of estimating the error σ_α are available:

The first is to repeat a large number of measurements of a given angle and examine the distribution of the measured values. It would be impracticable to undertake this process for all angles measured. The applicability of this method to surveys carried out under varying conditions by different observers may also be questioned. It would probably underestimate σ_α if performed for only a few surveys under better-than-average conditions.

The second method is based on the scatter of the angular measurement differences $\Delta\alpha_H$ and $\Delta\alpha_V$ about their mean values within a given survey set. $\Delta\alpha_H$ (or $\Delta\alpha_V$) may have a large value for each forward/reverse (F/R) data pair within a given set. If this value is constant within the set it merely reflects instrumental or leveling factors which may be eliminated by averaging the forward and reverse angles,with the mean representing a good estimate of the true angles involved. In practice $\Delta\alpha_H$ and $\Delta\alpha_V$ are not generally a constant within a given set. Scatter in these parameters within a given set is introduced by random errors in the angular measurements. The standard deviations of $\Delta\alpha_H$ and $\Delta\alpha_V$ about the mean *within a set* will give a reliable estimate of the standard error, σ_α, associated with each measured angle within that set. Thus for a given set, I, of angles surveyed,

$$\sigma^I_{\alpha_{H,V}} = \left[\frac{1}{N-1} \sum_{k=1}^{N} (\Delta\, \alpha^k_{H,V} - \bar{\Delta}\, \bar{\alpha}^I_{H,V})^2 \right]^{1/2} \qquad (2.9)$$

where N is the number of F/R pairs within the set and $\bar{\Delta}\, \bar{\alpha}^I_{H,V}$ is the mean of the $\Delta\, \alpha_{HorV}$ for set I. The majority of survey sets in this study contain a relatively large number (6-12) of F/R pairs and thus the statistical basis of using (2.9) is justified. This method accounts for the large variations in observational conditions experienced throughout the study by evaluating the errors within each particular set. Hence, this method of error estimation (2.9) is utilized for all survey calculations.

The distribution of standard errors in the horizontal and vertical angles obtained in this manner is shown in Figure 2.2 for all measurement sets. The mean standard errors in the horizontal and vertical angles, taken as an average over all sets (and therefore all angles), were

$$\sigma_{\alpha_H} = 3.0'' \quad \text{and} \quad \sigma_{\alpha_V} = 5.0'' \ .$$

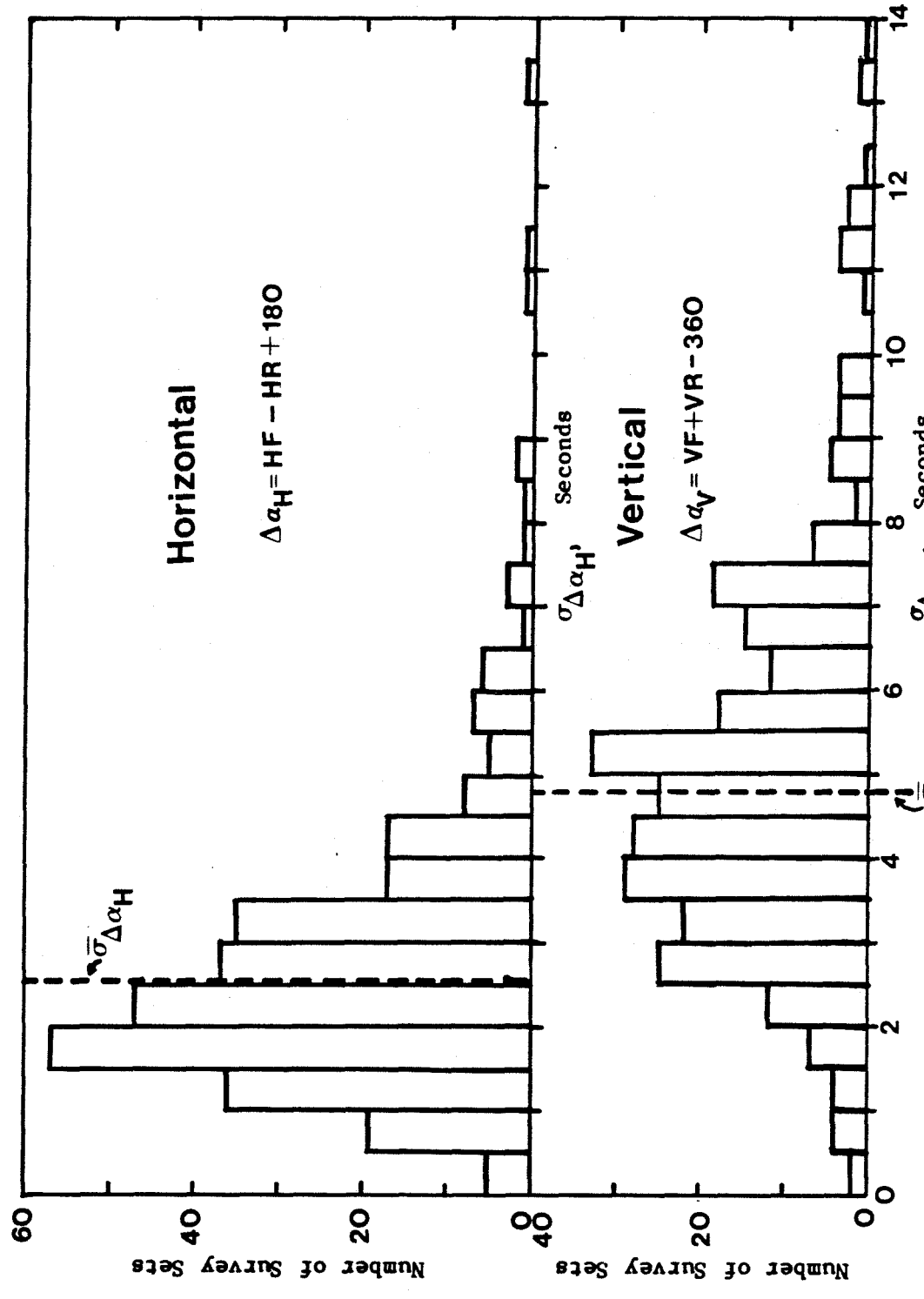

Figure 2.2 Distribution of standard deviation in difference between forward and reverse angles among survey sets.

These estimates of the mean error in the angular measurements probably give an overestimate of the true errors. This is because instrumental drift during a set of readings contributes to $\Delta\alpha_{H,V}$, but this drift is, to some extent, eliminated by averaging the forward and reverse angles. In addition, misalignment of the trunion axis with the rotation axis in the instrument can cause an increase in the scatter of $\Delta\alpha_H$ within a particular set if the vertical angles to the markers span a wide range within the set. This increase in scatter is not due to inaccuracies in the data set. The averaging of the forward and reverse angles to a marker eliminates this effect but the method of error determination used here does not take this psuedo-increase in the scatter of $\Delta\alpha_H$ into account, thus leading to a larger apparent error for the set. As several of the sets routinely surveyed unfortunately had a significant range in inclination of the telescope, the mean errors stated above will be slight overestimates of the true values.

Many of the large angular measurement errors ($\sigma_\alpha \geq 10''$) shown in Figure 2.2 are associated with the measurements made in February/March 1979. The use of an inadequate theodolite for some of the measurements and the extreme conditions encountered during this winter period lead to a large error in the angles. Other large errors occur in the earlier data sets where adequate shading of the instruments was not provided.

The mean standard error obtained by the methods used in this study agree well with those of Hodge (1972), $\sigma_{\alpha_H} = 3.1''$, $\sigma_{\alpha_V} = 5.3''$, Meier (1960), $\sigma_{\alpha_H} = 3''$, $\sigma_{\alpha_V} = 6''$, and Raymond (1969), $\sigma_{\alpha_H} = 3.0''$, which were determined by the first method mentioned above.

In order to assess the accuracy of the coordinates of the surface markers, a means of incorporating the errors in the measured parameters into an estimate of the errors in the coordinates must be established. This is given here, following

Shchigolev(1965). Let $f(x^1,x^2,...,x^I)$ be a function of the variables x^i, i=1...I. Then the standard error is related to the standard errors of the x^i by the relation

$$\sigma_f = [\sum_i (\frac{\partial f}{\partial x^i})^2 \sigma_{x^i}^2]^{1/2}, \tag{2.10}$$

provided the variables x^i are independent.

The error in the preliminary coordinates is derived from (2.1)-(2.4) using equation (2.10). Expressions for the resulting errors are given as

$$\sigma_{X_G} = \left\{ [(X_F - X_G)\frac{\sigma_\alpha}{\sin^2\alpha}]^2 + [(X_E - X_G)\frac{\sigma_\beta}{\sin^2\beta}]^2 \right\}^{1/2} / [\cot\alpha + \cot\beta] \tag{2.11}$$

$$\sigma_{Y_G} = \left\{ (Y_F - Y_G)^2 \frac{\sigma_\alpha^2}{\sin^2\alpha} + (Y_E - Y_G)^2 \frac{\sigma_\beta^2}{\sin^4\beta} \right\}^{1/2} / [\cot\alpha + \cot\beta] \tag{2.12}$$

$$\sigma_{Z_G} = \frac{1}{2}[\sigma_{Z_G}^{2_E} + \sigma_{Z_G}^{2_F}]^{1/2} \tag{2.13}$$

where

$$\sigma_{Z_G}^E = [\frac{\sigma_A^2}{\tan^2 V_E} + \frac{A^2}{\sin^4 V_E}\sigma_{V_E}^2]^{1/2} \tag{2.14}$$

and

$$\sigma_A^2 = \frac{D}{\sin\gamma}[\cos^2\alpha\ \sigma_\alpha^2 + \frac{\sin\alpha}{\tan^2\gamma}\sigma_\gamma^2]^{1/2} \tag{2.15}$$

$$\sigma_\gamma^2 = \sigma_\alpha^2 + \sigma_\beta^2 \tag{2.16}$$

$$\gamma = 180 - \alpha - \beta \tag{2.17}$$

and D is the distance between E and F. (A similar relation holds for $\sigma_{Z_G^F}$.)

From these equations standard errors were calculated along with the coordinates for each measurement set, using the values of σ_α obtained internally for each set as described above. The results are shown in Figure 2.3. The mean standard errors for a total of approximately 1,200 marker locations were

$\bar{\sigma}_X$ = 1.5 cm $\quad\quad$ $\bar{\sigma}_{HZ}$ = 2.3 cm

$\bar{\sigma}_Y$ = 1.8 cm $\quad\quad$ $\bar{\sigma}_Z$ = 1.3 cm

where the σ_{HZ} refers to the mean error in the horizontal position. (The above mean errors are obtained when all survey sets except those with extremely large errors are considered. If all sets are included in the averaging then the mean coordinate errors are slightly larger.) These errors are comparable to those found in previous studies.

Perhaps the largest source of error for the final coordinate determination of a given stake are those errors arising due to the inaccuracy of tilt measurements. If the tilts are measured at a time separated by a few days from the time of the survey (due to bad weather, etc) the tilt could be in error by up to 5 degrees depending on the severity of the intervening weather and the length of the time interval. For a pole of length 3.7 meters this could amount to ca. 32 cm of error in the resulting coordinates at the base of the stake. A loss of accuracy of this magnitude could easily cause a significant (~ 2 cm/day) error in the velocity determined from measurements over a period of two weeks. Indeed, it is felt that the inherent errors in tilt measurements may be the primary cause of the short-term variations in the measured velocities. With this in mind an attempt was made both in the field and in the data reduction scheme to give as accurate as possible an estimate of the tilt *at the time of the survey*. An estimate of the standard error in the tilt corrections is obtained from equations (2.)7 using (2.10):

$$\sigma_{TX} = L[\cos^2 T_E \cos^2 R \sigma^2_{T_E} + \sin^2 R \cos^2 T_D \sigma^2_{T_D} + (\sin T_E \sin R + \sin T_D \cos R)^2 \sigma^2_R\ ]^{1/2} \quad (2.18a)$$

$$\sigma_{TY} = L[\cos^2 T_E \sin^2 R \sigma^2_{T_E} + \cos^2 R \cos^2 T_D \sigma^2_{T_D} + (\sin T_E \cos R - \sin T_D \sin R)^2 \sigma^2_R\ ]^{1/2} \quad (2.18b)$$

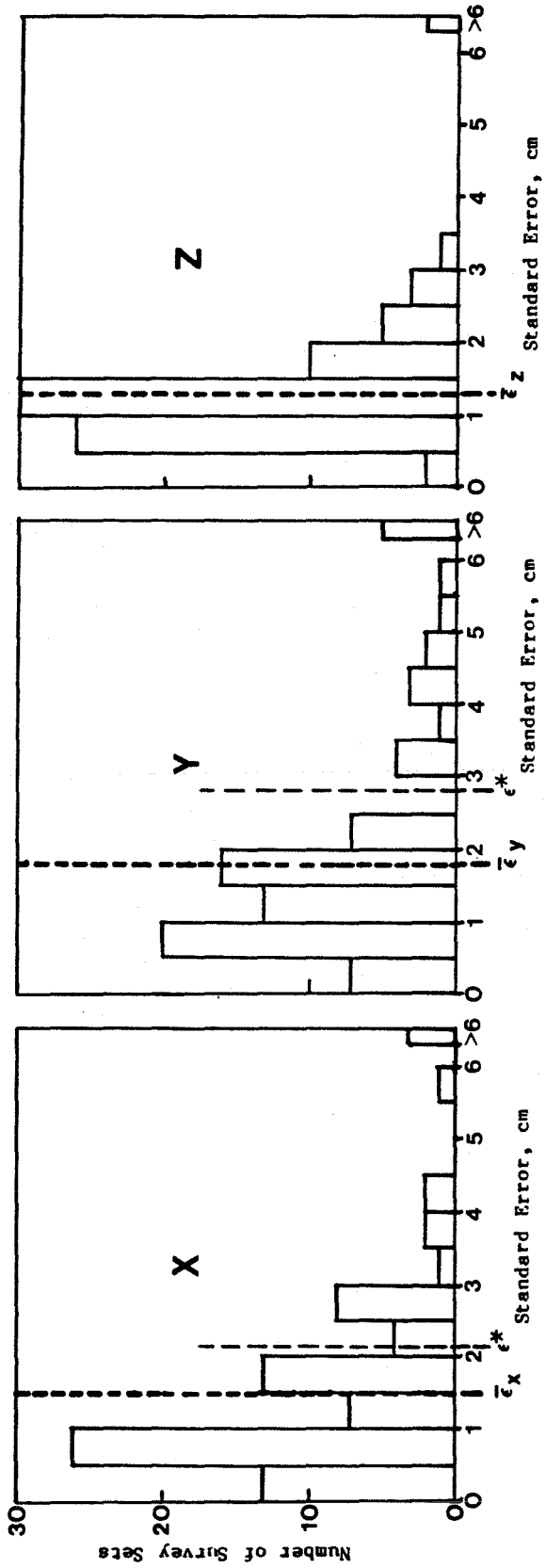

Figure 2.3 Distribution of standard error in surveyed coordinates of markers among survey sets. $\bar{\epsilon}$ is the mean standard error in all survey sets except those with extremely large values, ϵ^* is the mean error over all sets.

$$\sigma_{TZ} = \frac{L}{2} \frac{1}{\sqrt{1-\gamma^2}} \left[\sin^2 2T_D + \sin^2 2T_E \right]^{1/2} \sigma_{T_D} \qquad (2.18c)$$

where

$$\gamma^2 = \sin^2 T_D + \sin^2 T_E$$

and R, T_D,T_E,L are defined above.

Table 2.2 shows the variation in the accuracy of the tilt correction given various errors in the tilt angles and in the direction of tilt, for a 3.7m marker pole. It is clearly seen that neither the absolute magnitude of the tilt nor the direction of tilt play an important role in determining the tilt correction errors as long as $|T_E|$, $|T_D|$ are relatively small ($\leq 15°$)). The key factor in determining σ_{T_x} and σ_{T_y} is the actual error in the tilt measurement $\sigma_{T_E}(=\sigma_{T_D})$. Increasing the error in the tilt angles from 1° to 2° doubles the error in the tilt correction. Tilt angles were measured to $\frac{1}{2}°$ and therefore it is probable that a good estimate of the accuracy of the tilt angles is 1°. (This may vary depending on the care taken by the observer during measurement of the tilt.) Larger tilts ($\geq$ 15°) may well have an error of 2°, because poles with these large tilts were generally exposed for much of their length and, thus, quite flexible. Therefore, for tilts of less than 15° a standard error of $\sigma_{T_x} = \sigma_{T_y} = 7$ cm (for 3.7 meter stakes) has been included in the error of the final coordinates for the velocity calculations. For stakes with larger tilts $\sigma_{T_x} = 12$ cm has been used. These errors resulting from the tilt measurements are in general greater by a factor of 3 or more than those obtained from triangulation. The corresponding errors in the vertical tilt correction are assumed to be 0.8 cm and 1.5 cm, respectively.

Table 2.2
Errors in Tilt Corrections

(Angles in degrees)

$\sigma_{T_d}=\sigma_{T_E}$	σ_R	T_D	T_E	R	σ_{T_x} cm	σ_{T_y} cm	σ_{T_z} cm
1	3	0	0		6.4	6.4	0.0
		5	0	0	6.4	6.6	0.5
				90	6.6	6.4	0.5
		5	5	0	6.6	6.6	0.8
		5	10	0	7.2	6.5	1.2
				45	7.2	6.4	1.2
1	5	5	5	0	6.9	6.9	0.8
2	3	0	2	0	12.8	12.8	0.4
2	3	5	5	0	12.8	12.8	1.5
2	5	5	10	45	18.5	12.8	2.4
2	10	5	5	45	15.0	12.7	1.5

The errors in the particular reset corrections are given by a similar analysis, using (2.5). With values determined from field measurements ($\sigma_\varphi = 1°$, $\sigma_D = 1\,cm$, $\sigma_H = 1cm$, $\sigma_{\Delta ice} = 2cm$ for all but the largest resets) the corresponding errors in the reset corrections are $\sigma_{R_x} = 0.9\,cm$, $\sigma_{R_y} = 1.0\,cm$, $\sigma_{R_z} = 2.0\,cm$, for a representative reset of $R_x = 20$ cm, $R_y = 50$ cm, $D = 54$ cm, $\varphi = 22°$. As the resets are cumulative, the errors sum quadratically, i.e.

$$\sigma_{R_x} = [\sum_i \sigma^2_{R_x(i)}]^{1/2} \quad . \tag{2.19}$$

As a majority of resets were less than one meter horizontally, values of $\sigma_{R_x} = \sigma_{R_y} = 1\,cm$, $\sigma_{R_z} = 2\,cm$ were assumed for each reset. Thus, if a total of N resets apply to any particular point the standard error of the reset correction given in cm is $\sigma_{R_x} = \sigma_{R_y} = N^{1/2}$ and $\sigma_{R_z} = 2N^{1/2}$. These reset corrections are used when calculating glacier motion. N is the number of stake resets in the time interval over which the motion is calculated, rather than the total number of resets that the stake has undergone.

Combining the values of the errors cited above an estimate of the mean error in the coordinates of the base of a marker at a given time are

$\bar{\sigma}_x = 7.1$, $\bar{\sigma}_y = 7.2$ and $\bar{\sigma}_z = 2.5$ The relatively large horizontal errors are due mainly to the errors in the tilt. Few observational analyses of glacier flow have incorporated these large errors due to tilting of the markers, but seldom do poles remain within 1–2° of vertical. These errors can be extremely important in any study of short - term velocity flucuations. Neglecting them can lead to deceptively small errors in a motion survey.

2.5 Use of Magnets as a Surface Velocity Marker

Extension of the annual velocity measurements to points above the equilibrium line requires some means of establishing a marker which will either be locatable under the winter's accumulation, or will protrude from the snow cover so as to be observable in the following field season. The latter case would require a marker to withstand the extreme winter storm conditions, including a heavy coat of rime, while, at the same time, the markers must be quite long so as to avoid being buried by the winter snows, which can be of the order of eight to ten meters deep in the upper regions of Blue Glacier. Markers which satisfy these requirements would be impractical for this study. Therefore, buried markers which could be located from the surface were used.

Buried markers have been used in several studies in the past. Mathews (1977) has described the use of tuned loops which are located horizontally by electromagnetic methods, but these require a separate means of depth determination and prove to be fairly expensive. Lliboutry (1961) has discussed the use of magnets in studies related to the deformation of firn. Continuing on these lines, Harrison et al. (1978) have discussed the use of magnets for determining velocity and accumulation on Variegated Glacier, Alaska, which is situated in a region of high winter accumulation. Magnets were located at depths of up to 10.5 meters and thus provided a useful method for annual velocity measurements

well above the firn line. Harrison et al. (1978) have given a thorough discussion of the method and its accuracy. Their numerical results indicate that magnets at depths of up to ten meters may be located to an accuracy of a few centimeters.

During the first two years of the present study, magnets were placed on stakes from the G profile up glacier to the base of the icefall to ensure the determination of the velocity field in this region. Although the equilibrium line generally lies above the location of the G profile, the firn edge does not usually withdraw above this profile until sometime well into the summer. It was hoped that markers set out in the previous fall could be located in May or June rather than later in the summer, providing some information as to the temporal variation of velocity even at locations where the stakes would not melt out until later in the year. In addition, it was thought that during a strongly positive balance year, some or all of the markers in profiles I, J, K and L might remain buried throughout the summer. However, it turned out that 1978 was a negative balance year (Marriot, personal communication) and the equilibrium line advanced up glacier well into the region of the L profile. Thus, many of the buried markers were recovered later in the ablation season. Measurements made of the actual location of these magnets relative to the location obtained from the magnetometer search allows a quantitative test of the method described by Harrison et al.(1978, denoted as HMF in the following discussion). This section is devoted to a discussion of the magnets as buried velocity markers and an analysis of the practical accuracy of the method based on the recovered magnets. Much of the discussion follows that given in HMF.

Forty-nine magnets were taped in vertical orientation to stakes set in the ice or firn in late September, 1977, at known, recently surveyed positions. The magnets were Alinco 5A9 grade V alloy with dimensions 20.3 cm in length by 1.9 cm

in diameter. The magnetic dipole moment as measured in June, 1977, averaged about 5,000 γm^3 (one γ equals 10^{-5} gauss). The magnets had been stored together until their use in September, 1977, and therefore any determination of the moment should have been made just prior to implacement, but at that time it was not known to the author that such storage would effect the moment strength. (An idea of the error in the dipole moment of the magnets was given by measurements on the magnets recovered in 1978; their moments were significantly ($\approx$ 11%) less than the values observed in 1977, before storage and rough handling.)

During May and June of 1978, a Geometrics 826A nuclear magnetic resonance magnetometer (capable of reading to one γ) was used for the location of the buried magnets. Temporary stakes had been placed at positions determined by the two-alidade method described above (section 2.3),using projected coordinates from the 1977 locations. About these stakes an initial coarse search was made at points in a square grid about 3 to 4 m apart (depending upon the observer). A large anomaly in the magnetic field was identified and a rough location of its peak (to $\sim$ 1 m) was found. Forty-six magnets were located in this manner, in time periods ranging from one minute to 1 1/2 hours (in the latter case a poor temporary stake placement had been made). The remaining three magnets were searched for but not found; they were in highly crevassed or avalanche - prone areas, and had apparently been lost into the depths of the glacier.

From the full width of the magnetic anomaly at half amplitude, an approximate estimate of the depth of the magnet can be made (see HMF). A more accurate estimate of the depth may be obtained using the following relation for the peak amplitude of the anomaly in terms of the depth of the magnet, Z, its magnetic dipole moment M, and the inclination (or dip) of the earth's magnetic field

φ (HMF,eqn. 6):

$$| B^e - B^{peak} | \approx \frac{2M\cos\varphi}{Z^3}\left(1 + \frac{3}{16}\tan^2\varphi \right). \qquad (2.20)$$

In this expression B^e is equal to the strength of the earth's field ($B^e \approx 56020\ \gamma$) and ψ at Blue Glacier is 20.5°. The peak amplitude of the anomaly is approximately 9 γ at a 10 m burial depth and 75 γ at 5 m. A comparison of the depths obtained from equation 2.20 and from the width at half - amplitude at several stakes is shown in the following table.

Table 2.3
Magnet Depth Estimates by Two Methods

- Z (2.20)	- Z (1/2 ampl.)
6.3 m	6.1 m
5.7	5.7
6.5	6.8
6.4	8.0
6.3	6.2
6.3	6.1
6.5	7.0
6.8	7.0

It is seen that the simple half - amplitude method provides an estimate of the depth of the magnet which is close to that estimated from (2.20). This method may be easily employed in the field while the measurements are being taken. The depths ranged from 4 to 8 m below the sensor, which was 1.1 m above the snow surface in the coarse survey, with a mean of 5.6 m for the lower four profiles (G-J) and with the depth increasing upglacier (Z_G = 4.3 m, Z_J = 6.4 m).

Following the coarse search and depth determination, a fine-scale study of the anomaly was made over an array centered approximately over the peak. The magnetic field was measured at the positions of nine 1.5 m. - long aluminum poles placed in a 3x3 square grid at a spacing d chosen so as to optimize the horizontal coordinate determination. HMF give the optimum value for the grid

spacing as $d \approx 1/3|Z|$, where $|Z|$ is the depth of the magnet. At this spacing, errors in the calculated horizontal coordinates of the magnet as deduced from field measurements within the square array are minimized. (For the minimization of the error in the depth determination a spacing, $d \approx (1/6)|Z|$, should be used. If M is not known then optimum results are obtained with $d \approx 1/2|Z| - 5/8|Z|$.) One side of the array was oriented to magnetic north and a horizontal reference plane through the grid poles was established using a small level suspended on a string.

The background field was measured at 2-4 points distant 20-30 m from this fine array before and after field measurements within the array were made. The person handling the magnetometer could not wear a metal belt, boots with metal shanks, watch, etc. because all these metal objects were observed to introduce error in the B-field measurements. The sensor was placed as far as possible from the observer and control box. The entire operation took approximately 20-30 minutes to set up and make the required measurements at the nine grid points.

The resulting data provide an overdetermined data set for the calculation of the three (or, if desired, four) unknowns $\hat{x}, \hat{y}, \hat{z}, (\hat{M})$, which describe the magnet's location relative to the center of the array and its magnetic moment moment. A linearized least squares minimization is then used to determine these unknowns. A four-dimensional extension of the procedure developed by HMF was used in this study to include an unknown magnetic moment. Appendix A describes the development of this least squares procedure, following that of HMF, with the inclusion of this fourth unknown.

Both this four-dimensional least-squares system and a similar three-dimensional system, where M was assumed known, were used in this study. The

value of the dipole moment M measured after recovery was used in the 3-d formulation. Generally, the two methods yield very similar results. The mean differences between the 3- and 4-d solutions is 4.5% in (x^2+y^2), 2.5 % in z, and 6% in M. The standard deviations of the residuals were, surprisingly, not significantly lower for the 4-d solution (ca. 1.0γ) than the 3-d solution (ca. 1.1γ). Thus, if the magnetic moment is not well known in advance, the 4-d least squares solution will yield values consistent with those for which the dipole moment is known.

The errors in the resulting coordinates resulting from errors in magnetic field measurements and magnet tilt are discussed in HMF. The error in the depth resulting from an error in the field measurement varies inversely with the moment and directly with the fourth power of the depth. The error in the moment varies inversely with moment and directly with depth. The horizontal coordinates are approximately three times as sensitive to these errors as the depth. Random and systematic errors in $B^{observed}$ combine quadratically, $\sigma_B^2 = \sigma_m^2 + \sigma_{BG}^2$, where σ_m is the standard error in the B - field measurements due to random fluctuations and σ_{BG} is a systematic error introduced by an error in the background field. If the magnet were actually tilted a small amount (10 %), then the error in the horizontal coordinates would be even larger. Large tilts (80–90°), such as those found for a few stakes hit by an avalanche in the winter of 1977-78, lead to large errors in all coordinates.

Using the results of HMF and an estimate of the standard errors in the field measurements, the resulting errors in the coordinates $\hat{x},\hat{y},\hat{z}$ for a representative magnet of dipole moment M = 5,000 γm^3, buried five meters at a magnetic latitude corresponding to Blue Glacier, are given in Table 2.4a. A majority of the magnets were tilted from 5–10° in a down glacier direction. The background field measurements were perhaps made too close to the magnet (HMF

recommend 40 meters), and thus may lead to an even larger systematic error. Given these errors, however, the magnets can be located to within approximately 10-20 centimeters horizontally, which, over a period of one year, introduces an error of only ≈ 1/6–1/3% in the annual velocity determination.

The eventual recovery of 37 magnets and the measurements relating their actual position to the origin of the magnetic search array provides an excellent means for determining the actual errors obtained in practice and a comparison with those estmated above. In addition to the distance and direction from the center point of the array, the dipole moments of the recovered magnets were determined in the field. A 3.3-meter vertical hole was cored in a snow field and the magnet lowered into this hole, taped to a wooden stake. The field directly over the magnet was compared with the background field at the same point when the magnet was removed. From (A.2), with (x,y) = (0,0) and z known (distance from the center of the sensor to the center of the magnet), the moment can be calculated. The accuracy of the moment determination was approximately 3% as determined by errors in the measured quantities. Comparison of these measured moments with those measured by a similar method at the beginning of the study (before storage) indicates an approximate mean change of 11%, indicating that measurement of the dipole moment just before implacement is important if accurate locations are required for deeply buried magnets.

The difference between the measured and calculated coordinates is shown in Table 2.4b for about 40 magnets that were recovered. (The mean depth of burial was 4.4 m. in June, 1978.) As shown in this table, horizontal coordinates agree to within 11-13 centimeters, while the depth agrees to within 16 cm. The moments resulting from the 4-d least squares minimization and measurements in the field differ by approximately 5-6%. The values in the first two columns represent the mean deviation between observed and calculated coordinates in those cases

for which the least squares procedure showed a good rate of convergence and low residuals, thus excluding several stakes that had been hit by an avalanche or broken by winter storms. Columns three and four of Table 2.4a show the mean differences in coordinates when all markers are included. The mean difference is seen to increase by about 5 cm., and the deviation from the mean also increases, as might be expected. The stakes that were hit by an avalanche (G_1,H_1,I_3) gave odd shaped B - field anomalies. The results of Lliboutry (1968) show that the peak of the anomaly of a horizontal magnet is located at a lateral distance $z/2$ from the point directly over the magnet. When used for estimating the locations of these highly tilted stakes this lateral displacement gives a good correspondence with the observations.

The measured location of the magnets relative to the grid origin (and the temporary marker) suffered from errors in the measurement of the distance, D, and azimuth of the horizontal offset and in the vertical offsets. The error in the vertical consists of error in the stake height above the surface, changes in the surface level over the distance D, and a summation of resetting errors (the temporary stake at the grid origin was periodically reset). Combining these errors, the accuracy of the actual magnet location relative to the temporary stake was determined, as listed in rows 7-9 of Table 2.4a. The mean of the differences between the observed and calculated coordinates (Table 2.4b) are similar to the probable errors shown in the final row of Table 2.4a. Given the errors in the measurements, the magnets can be expected to lie within 15 cm. or less from the coordinates obtained through the solution of least squares minimization (A.3).

From this discussion of the location of buried magnetic markers and the errors observed in practice, it is clearly seen that the method described by Harrison et al.(1978) provides an accurate means of providing surface velocity

and accumulation data in regions where the markers may become buried. The error analysis given in HMF provides an accurate description of the realistic errors involved. The magnetic markers used in the present study have provided shorter-term (September through May) velocity determinations than could have been obtained without them for those markers high up in the region of study, and annual velocities for some markers at which this information could not have been obtained at all without them.

Table 2.4a
Differences Between Calculated and Observed Coordinates of Buried Magnets

Mean Differences in Coordinates	Excluding Worst Values 3-D	4-D	All Located Magnets* 3-D	4-D
$\overline{\lvert\Delta X\rvert}$, cm	13.6 ± 10.2	13.6 ± 9.1	18.3 ± 18.0	17.2 ± 12.1
$\overline{\lvert\Delta Y\rvert}$, cm	12.1 ± 8.8	11.6 ± 9.4	16.9 ± 13.5	16.4 ± 13.7
$\overline{\Delta D}$, cm	11.4 ± 9.6	11.1 ± 8.3	15.4 ± 14.0	15.2 ± 13.9
$\overline{\lvert\Delta Z\rvert}$, cm	16.2 ± 9.6	18.5 ± 13.1	20.2 ± 15.4	22.8 ± 17.7
$\overline{\lvert\Delta M\rvert}/M$	---	6.1 ± 5.3 %	---	---

$\overline{\lvert\Delta X\rvert} = \lvert X^{Observed} - X^{Least\ Squares}\rvert$ (mean value), $D^2 = (x^2 + y^2)$, $\overline{Z} = 4.4$m
*-All located magnets, including those with extreme tilts and poor convergence.

Table 2.4b
Errors in Magnetometer Survey and Offset Measurements

	Source	Error	Error in Coordinates, cm X	Y	Z
1	Magnetic Field Measurement (Random)	± 2 γ	5.2	5.0	3.2
2	Background Field (Systematic)	- 2 γ	0	2.2	- 7.2
3	Moment Error (too low by ~ 5%)	- 250 γm^3	0	12.0	9.2
4	Tilt of Magnet (45°AZ)	5° (10°)	9.0 (17.5)	9.0 (17.5)	1.0 (2.0)
5	Inclination of B^e	± 1°	0	4.0	1.0
6	Total Error in Location from least squares anal.	5° tilt 10°tilt	10.4 (18.3)	14.0 (222)	12.0 (12.5)
	Positioning Errors				
7	Azimuth & Distance	5°–10° 3 cm	6 6	6 6	
8	Marker Height (including resets)	2 cm each	-	-	7
9	Total Combined Error (Magnet Calculations +	observed offset	12)	20	14

Calculated for magnet of moment M = 5000 γm^3 at ~ 5 m depth, following HMF, mean offset measured from origin to actual magnet = 55 cm.

CHAPTER III

THICKNESS , CHANNEL GEOMETRY, AND SURFACE SLOPE OF BLUE GLACIER

3.1 Ice Thickness and Channel Geometry

An accurate knowledge of the ice thickness and channel shape of lower Blue Glacier is required for interpreting the glacier's response to a change in surface configuration and for numerical modeling of the flow. C.R. Allen has determined the ice thickness of Blue Glacier at several points by seismic reflection (Meier et al.,1974,Fig.1). The areal coverage of these points is rather sparse, particularly toward the margins, above the firn line, near the terminus, and between profiles E and G. A gravimetric determination of the bedrock configuration was made by Corbató (1965). Although the accuracy of the ice-thickness values obtained in this way is more difficult to assess than for seismic measurements, the results of Corbató (1965) and others (Bull and Hardy,1956; Hodge,1972) indicate that an accuracy of ± 5 to 10% can be expected, comparable to that attained in the seismic work.

In the present work, radio echo sounding was used to obtain additional ice depths. The method has been used extensively in polar regions for ice depths up to several kilometers (Robin, et al. 1969; Gudmandson, 1971). Recent developments have allowed use of this method on temperate glaciers. The method gives depths accurate to 2 - 5% and is advantageous in the ease of data collection and reduction.

3.2 Instrumental Set-Up for Sounding of Temperate Glaciers

The presence of liquid water in temperate ice has, until recently, made the probing of such glaciers by electromagnetic waves relatively ineffective. Water filled voids produce a large amount of scattering in the EM radiation and thus

obscure any reflection from the bed, as shown by Smith and Evans, (1972) and Strangway, et al. (1974). The work of Watts and England (1976), involving a model in which spherical, water filled cavities are distributed in an ice matrix, showed that the scattering is proportional to the frequency of the radiation, and suggested that a reduction in frequency below that normally used in polar ice soundings (30-100 MHz) might lead to an adequately increased signal to noise ratio, whereas an increase in system performance would not. Watts and England determined a set of criteria for echo design based on their studies. The sounder should provide a short (1-2 cycle) pulse with center frequency of approximately 5 MHz at a sufficiently large radiative power.

The mono-pulse generator used in the present study was designed by R. Vickers of Stanford Research Institute with the above criteria in mind, and is described by Watts and Wright (1981). A 12 V source (1 kg Gel Cell) provides power to a high voltage generator. When the resulting high voltage (several hundred volts) exceeds the breakdown voltage of a set of transistors, the transistors flip to a conductive state and avalanche rapidly, giving rise to a sharp high voltage pulse of short duration (rise times are of the order of tens of nanoseconds and pulse length is approximately one cycle). The transistors return to their resistive state, and the process is repeated, at a repetition rate of approximately 1000 pulses/second. The pulse is radiated by a resistively damped antenna which will allow passage of the pulse outward from the feed point but will not support an inward traveling wave, thus effectively damping out any ringing of the signal. The antenna is described by Sverrison, et al. (1980). The internal impedance of the antenna, Z, varies with distance x outward from the feed point

$$Z(x) = \frac{\psi}{h - x} \tag{3.1}$$

where h is the half length of the antenna and ψ is a parameter dependent upon

h, the radius of the wire, the desired wavenumber of the signal, the impedance of the ice, and the desired bandwith of the antenna. ψ was taken to be 100 Ω. The continuous variation in impedance determined by equation (3.1) was approximated by using lumped elements spaced 1 m apart, and consisting of metal foil resistors sealed in heat shrink tubing. The half length of the antenna was set at 10 m, yielding a center frequency for the pulse of

$$f_{cen} \approx \frac{55}{h} = 5.5 \text{ MHz}.$$

The size and weight of the transmitter were of the order 20 x 15 x 15 cm and 2 kg, respectively, including the battery. Power usage was such that a standard Gel Cell would power the system for up to 60 point measurements.

The receiver consists of an antenna similar to that used for transmission, fed into a junction box containing a pair of Shotky-barrier diodes (which clip the signal to $\pm$ 1/2 volt), a 3 m length of coaxial cable, and a small, portable oscilloscope. No amplifier is needed since the reflected signal is of the order of a few millivolts for depths of up to 400 m. The oscilloscope used for most of the measurements in this study was a Non-Linear Systems MS-15 Miniscope, with a 15 MHz bandwidth at -6 db. The small size and weight of this scope (20 x 20 x 8 cm and 1 kg), its low power requirements (1 alkaline 6-V battery supplies power for approximately 40 point measurements), and its relatively low cost make it ideal for work which involves backpacking a long distance and measurements in highly crevassed areas. However, the small (4 x 3 cm) display screen requires extra care to insure that accurate arrival times are measured. The amplifiers of the scope used in the study were easily saturated by the incoming air wave (discussed below), and thus an additive correction factor was required for the measured arrival times to account for this saturation. The correction factor was determined to be 0.3 μsec by comparison with delay times indicated on a higher-

quality (but heavier and more power-consuming) oscilloscope.

The trace of the incoming signal was photographed using a 35 mm SLR camera fitted with a lens reversing ring (so as to provide a macro-lens image of the small screen) and with a light shield (to allow the photograph to be taken in the high radiation environment on the glacier). With this equipment, the total weight of the receiving system was of the order of 2.5 kg, including the 6-V battery.

The transmit and receive antennas were normally laid out in a broadside parallel arrangement, separated by a measured distance of 40-60 m. The air wave (discussed below) was used to trigger the oscilloscope. The time delay between peaks in the air wave and the bottom return was measured to the nearest 1/16th of a division (.06 - .03 μsec). The corresponding peaks should differ in phase by π radians due to the phase shift upon reflection from a higher permittivity medium. The total time required for a measurement, including the deployment and recovery of the antennas, timing, and photography, was of the order of 3-5 minutes (with some practice).

An electric dipole antenna placed at the interface between two dielectric media, such as air and ice, produces a complex field of radiated energy. In the work of Annan (1973) and Tsang et al. (1974) it is shown that four travelling waves are generated. Two of the waves are spherical waves, subject to geometrical spreading as the wave front moves through the medium. One such wave propagates in the air at a speed c (= 300 m/μsec), while the other is a spherical wave in the ice moving with a slower phase velocity v. As shown in Jackson (1975),

$$v = \left[\frac{\varepsilon'}{2c^2} \left(\sqrt{1 + \tan^2\delta} + 1 \right) \right]^{-\frac{1}{2}} \approx \frac{c}{\sqrt{\varepsilon'}} \qquad (3.2)$$

where

$$\varepsilon = \varepsilon_o \left(\varepsilon' - \frac{i\sigma}{\omega\varepsilon_o}\right) ,$$

$$\tan\delta = \frac{\sigma}{\omega\varepsilon'\varepsilon_o} ,$$

ε_o is the permittivity of free space, σ,ε the conductivity and complex permittivity of ice, respectively, tanδ the loss tangent, and ω the circular frequency. For glacier ice at 0°C, $\sqrt{\varepsilon'} \approx 1 + 0.85\rho$, where ρ is the density, and tan$\delta \approx 0.05$ (Gudmansen, 1971). For a typical density of glacier ice, $\varepsilon' = 3.2$, and thus the phase velocity of waves of radio frequency in temperate ice is 168 m/μsec. The spherical wave in the ice is reflected from the bedrock channel, and thus part of the transmitted energy returns to the surface after the reflection. In addition, there is an arrival of the unreflected spherical wave at the receiver which travels just below the air-ice (or firn) interface at the speed v_{ice} (or v_{firn}), causing interference with the air wave arrival. This direct surface wave is visible as a secondary signal if the antenna spacing is large enough to allow time resolution in the oscilloscope trace. The spherical waves are subject to minimal attenuative loss, as governed by the conductivity.

In addition to these two spherical waves, there is an evanescent wave which travels in the air upward from the interface. The presence of this wave is required to satisfy the boundary conditions at the interface imposed on the electric field when there is a spherical wave in the ice. Similarly, a head wave is generated within the ice by the spherical wave in the air. This head wave travels horizontally at the interface with a speed c and merges with the spherical wave in the ice at a point governed by the critical angle in the lower dielectric (for ice ($\approx 35°$). These various waves are shown in Figure 3.1a near the transmitter. The radiation pattern of a dipole antenna placed at the interface between the two

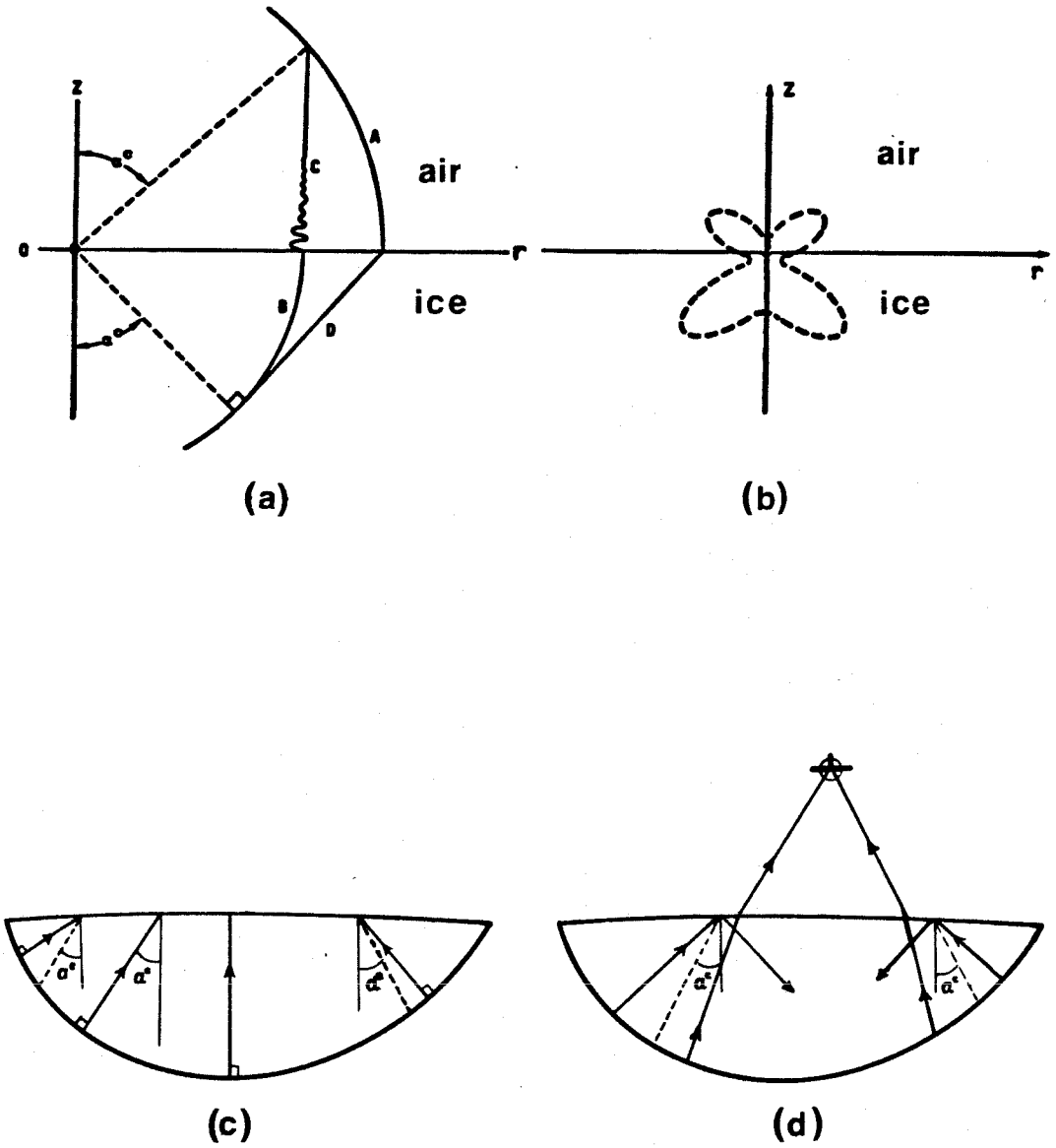

Figure 3.1 a) Wavefronts about a dipole source on the surface of a glacier. A and B are spherical waves in the air and ice, respectively, wave C is an evanescent wave in air decaying exponentially, and D is the head wave in ice. α^c denotes the critical angle in ice. b) Radiation pattern on an electric dipole at ice-air interface (adapted from Annan, 1973). c) Near field reflections received at surface antenna (T/R antenna spacing small relative to depth). d) Far field reflections received above surface at aircraft. Some bottom reflections are totally reflected at ice-air interface.

dielectric media air and ice is peaked at the critical angle, as shown in Figure 3.1b. The standard geometrical-optics limit for the radiation in the ice only applies in the far field, at approximately 5-10 λ_o, where λ_o is the free-space wavelength. For the system used in this study, this distance is roughly 275-550 m. On most glaciers, these near-field considerations of the radiation pattern apply to the energy reflected at the channel walls as well.

The above discussion is important in that it shows that, in the near field of a dipole antenna placed at the interface between two diectrics (and similarly, in the near field of the reflecting boundary), radiation may be received by specular reflection from a point outside the critical cone (which is defined to be a cone of half-angle equal to the critical angle (35°) about the vertical downward into the lower dielectric). Put more simply, if the nearest reflector is the steeply sloping side of the bedrock channel, which is well off to the side of the transmitter relative to vertical,energy may still be received at the receiving antenna by a specular reflection from this reflector. This is contrary to the discussion of Walford and Harper (1981) but is not in conflict with the work of Robin (1975), which applies to far field sounding from aircraft. Figure 3.1c,d shows the differences in near and far field reflections. This major difference between high-altitude, high frequency airborne sounding and ground-based, low frequency sounding must be taken into account if proper interpretations on the geometry of the reflecting boundaries are to be made.

3.3 Radio-Echo Sounding Results

During the field seasons of 1978 and 1979 radio echo sounding measurements were made at approximately 200 points over lower Blue Glacier. The area of coverage extended from the base of the central icefall and within the Blizzard Pass icestream down glacier to the terminus. A majority of the measurement sites

were located so that the centerpoint between the two antennas was at one of the surface velocity markers, whose positions were accurately known. Measurements were generally made by a party of two, one person handling the transmitter and one the receiver. Photographs were taken of the CRT trace in most cases, and the delay times for one or more reflections were measured and recorded.

The quality of the returns varied considerably, ranging from cases where there was no discernible bottom return (only a diffuse scattering return) to cases with a single, clean return of large amplitude. The strength of the return signal is dependent not only upon scattering from water inclusions, but also upon the roughness of the reflector. The reduction in power for a reflection from a rough surface is proportional to the smoothness of the surface relative to the reflected wave. Several returns were visible in some of the traces. The quality of the resulting photographs was generally only fair due to poor control and stability of the photographic set-up. Figure 3.2 shows a sampling of the photographed signals. Problems were encountered in regions of thin ice and large amounts of debris, as near the glacier margins and terminus. The use of a shorter antenna (and its accompanying higher frequency) might have alleviated some of the problems in these areas.

Given the delay times for bottom returns and the measured antenna separation, depth profiles along the labeled transverse lines B-Q were constructed. Since the reflections are produced under the assumptions of the near field theory described above, the locus of possible reflection points for a given delay time and antenna geometry define an ellipsoid. Under the assumption that the reflector is coplanar with the transverse profile along which the antennas were separated, the ellipsoid reduces to an ellipse in a plane normal to the bed.

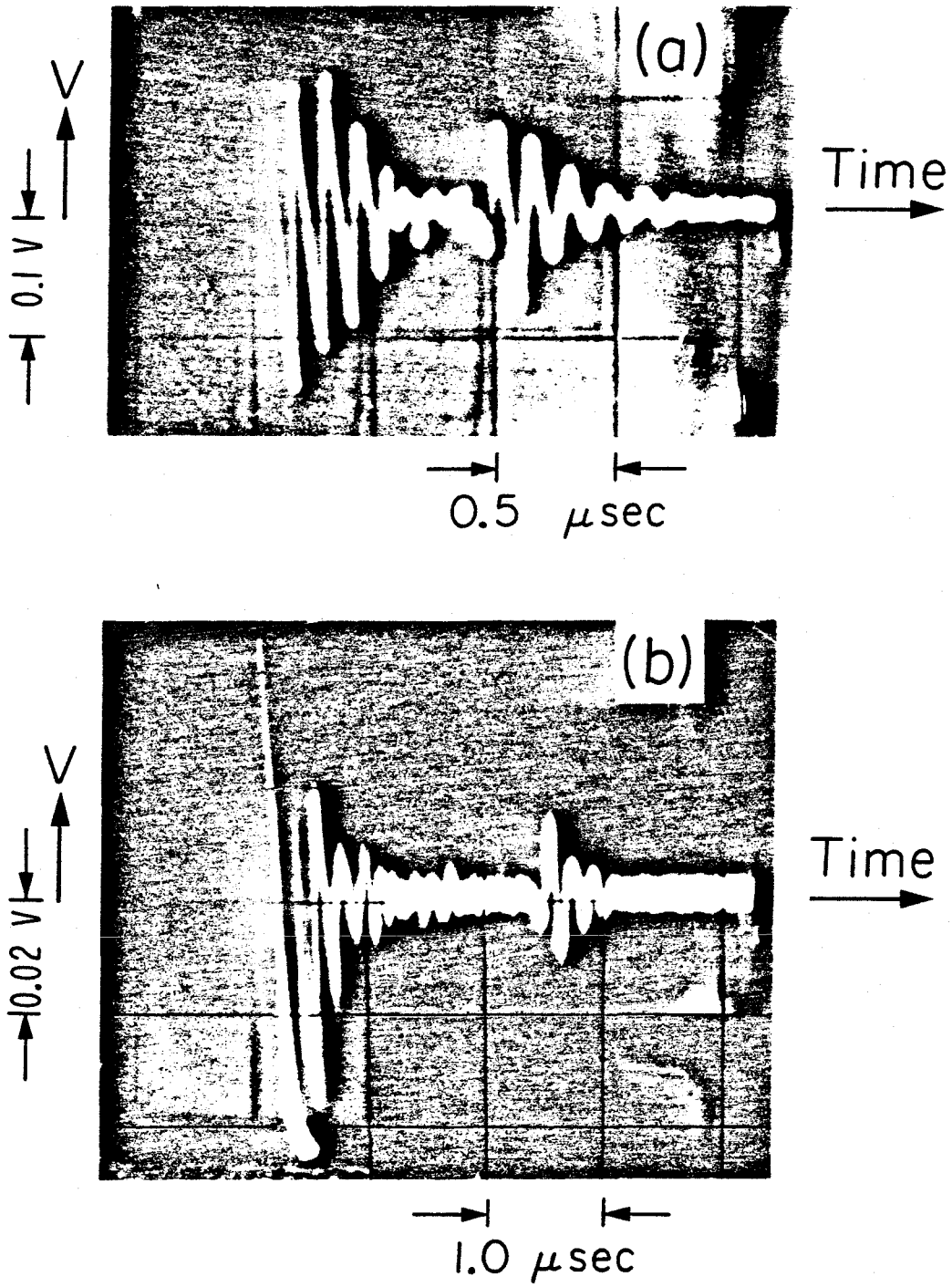

Figure 3.2 Photographs of oscilloscope traces showing large air wave and smaller bottom reflection (for good quality returns). One μs equals approximately 84 m in ice depth.

Let R be the antenna spacing, c the speed of light in vacuum, v the speed of the EM wave in ice given by (3.2), and t the delay time between triggering of the scope and the arrival of the bottom return (corrected for the oscilloscope, if needed). (The correction of the travel times for passage through a firn layer as described by Harrison (1970) is negligible for most of the firn depths encountered in this survey.) Then the equation of the resulting ellipse is

$$x = a\cos\varphi \quad , \qquad y = b\sin\varphi \quad , \qquad \varphi \in [-\pi\ ,\ 0\ ] \tag{3.3}$$

with semimajor axis, a, given by

$$a = \frac{v}{2}\left[\, t + \frac{R}{c} \right] \tag{3.4}$$

and the semiminor axis, b, given by

$$b = \left[\, a^2 - (\frac{R}{2})^2 \right]^{\frac{1}{2}} = \left[\, (\frac{v}{2})^2 \left[\, t + \frac{R}{c} \right]^2 - (\frac{R}{2})^2 \right]^{\frac{1}{2}} \quad . \tag{3.5}$$

The coordinates (x,y) are defined in a local coordinate system centered midway between the two antennas with x directed along the glacier surface toward the transmitter and y normal to the surface positive downward.

The ellipses for all data points along a transverse line were plotted with the local origin of each point located at a point corresponding to the actual coordinates of the surface marker about which the sounding measurement is centered. The vertical elevation relative to the western-most point of the profile must be taken into account, so as to allow for the effects of surface topography. In addition, the location of the glacier margins are indicated on the same plots. The smoothed envelope of these reflection ellipses, constrained to pass through the glacier margin points, is the best estimate of the glacier bed along the transverse profile. As expected, the greater the density of the sounding points along a profile, the better constrained the bed topography. Figure 3.3 shows an

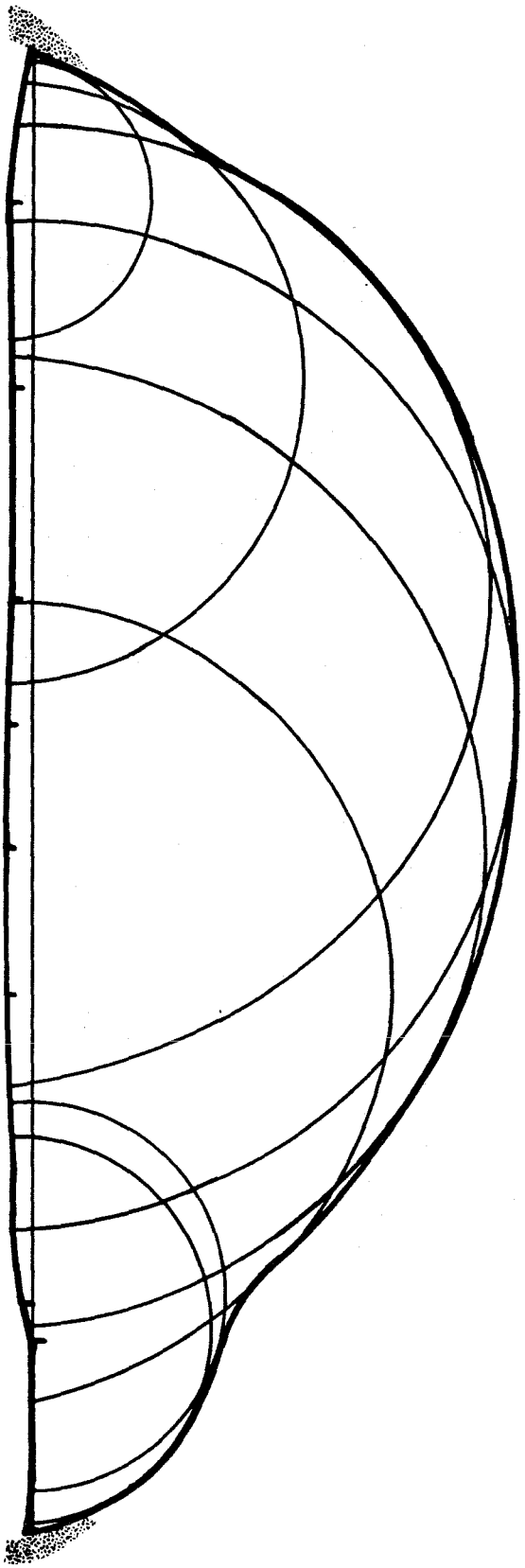

Figure 3.3 Construction of transverse cross-section from radio-echo sounding data. Ellipses are centered at midpoint of antenna arrays along surface (1 cm = 30.8 m).

example of this depth profile construction. Poor quality data will generally give rise to a reflection ellipse which lies entirely within the envelope of the remaining data or will cause a distortion of the envelope such that the glacier margin condition can no longer be met. Thus some filtering of the data is required.

3.4 Accuracy of the Ice-Thickness Determination

The accuracy of the calculated ice thickness is determined, in part, by the accuracy of the measurement of the time delays and of the antenna spacing. Additional errors may arise in the thicknesses calculated along the uppermost profiles due to neglecting the passage of the bottom return through a firn layer. If the firn layer is 20 m thick this may give rise to a 3-4 m error in the depth estimate. Other errors may arise due to the fact that the smooth envelope of the reflection ellipses is only a minimal profile in the sense that the loci of points on the ellipses are first arrivals, so that in the center of a profile the depth may actually be greater than that determined by an ellipse whose equation is governed by an arrival from a reflector toward the side, and thus not directly beneath the point of observation. One can easily imagine a geometry for which no density of observations will yield the correct depth near the centerline. Airborne sounding at a higher frequency would help minimize the errors in this case because of critical refraction in the far field, causing the illuminated footprint to be of reduced size. An estimate of errors of this type may be determined by a comparison with the bedrock topography as determined by gravity measurements (Cordató, 1965) and by direct reference to the depth of boreholes drilled to (or near) bedrock. The comparison is given below. Further errors may be introduced by assuming that all of the reflection points lie in the plane of the profile rather than an ellipsoid. These errors should be small because the channel is slowly varying in the longitudinal direction.

Using equation (2.10) and the relation for the semiminor axis of the reflection ellipse, (3.5), an estimate of the standard error σ_b in the ice thickness due to errors σ_t in the delay time, and σ_R in the antenna separation, is given by:

$$\sigma_b = \frac{1}{b}\left\{ (t + \frac{R}{c})^2 (\frac{v}{2})^4 \sigma_t^2 + \left[\frac{1}{2}(t + \frac{R}{c}) (\frac{v}{2})^2 - \frac{R}{2} \right]^2 \sigma_R^2 \right\}^{\frac{1}{2}} . \qquad (3.6)$$

For b = 200 m, t = 2.2 μsec, R = 50 m, and $\frac{1}{2}$v = 84 m/μsec, the standard error in the ice thickness is seen to be

σ_b = 8.5 m if σ_t = 0.1 μsec and σ_R = 2 m

σ_b = 4.3 m if σ_t = 0.05 μsec and σ_R = 2 m .

For a thickness of 100 m or 300 m these values change only slightly. Since the delay times were recorded to 1/16th of a division, it is appropriate to take $\sigma_t \approx 0.03 - 0.06$ μsec. A general value of σ_b may therefore be taken to be 5 m. The ice thickness is therefore determined to an accuracy of ± 2-5 % (= ± 5 m). The resulting error is seen to be somewhat smaller than that for seismic and gravity thickness determinations.

Several boreholes have been drilled into Blue Glacier in the past by various workers. Those that reached the bed (or the debris layer near the bed) provide an excellent means for checking the accuracy of the radio echo sounding depths. Table 3.1 lists the boreholes, their depths, and the corresponding ice thicknesses determined in the present study. The ice thickness as derived from the radio echos has been converted to vertical thicknesses from the direction of the surface normal. Boreholes J and Z were drilled in 1963 and 1970, respectively. The estimated bedrock elevations to which these holes penetrated and the corresponding radio echo bedrock elevations are listed rather than the depths, so as to avoid errors resulting from surface elevation differences. The agreement

is seen to be excellent, averaging 3-6 m between the radio echo and borehole depths. Comparison between the echo-sounding and the two holes C and A2 is improved because the they were drilled very close in time to the ice radar study. It should be noted that the accuracy of the radio depth estimates is dependent upon the construction of a bed profile and not upon single measurements, which may arise from oblique reflectors. A case in point is borehole C, at which the measured reflector distance, 119 m, represents reflection from a reflector close to the margin, while the vertical depth of 133 m given by the constructed bed profile is primarily influenced by echos obtained at other points in the profile.

Boreholes B, L, and H, listed in Table 3.1, are not known to have reached the bed. Hole H encountered debris at a level probably several meters short of the actual bed. Hole B is similar, but L appears to have reached the bed.

Table 3.1
Borehole Depths and Radio-Echo (R-E) Sounding Results

Site	Depth,m	Bed Elevation	R-E Depth,m	Bed Elevation,R-E	Reference
C	132.2	1573	133	1572	1
A2	262	1294	268	1288	2
J	--	1523	165	1525-1530	3
Z	--	(1575)	--	1560	1
B*	--	1362	260	1345	1
L*	--	1471	140	1468	1
H*	260	1328	269	1319	2

* - Boreholes not known to have reached bed

1. 1. Englehardt, Kamb,and Harrison (1978)
2. 2. Englehardt, pers. comm.
3. 3. Kamb, pers. comm.

Using the results of the present radio echo survey, contour maps of ice thickness (Figure 3.4) and bed elevation (Figure 3.5) were constructed. The photogrammetric base map produced by the United States Geological Survey in 1978

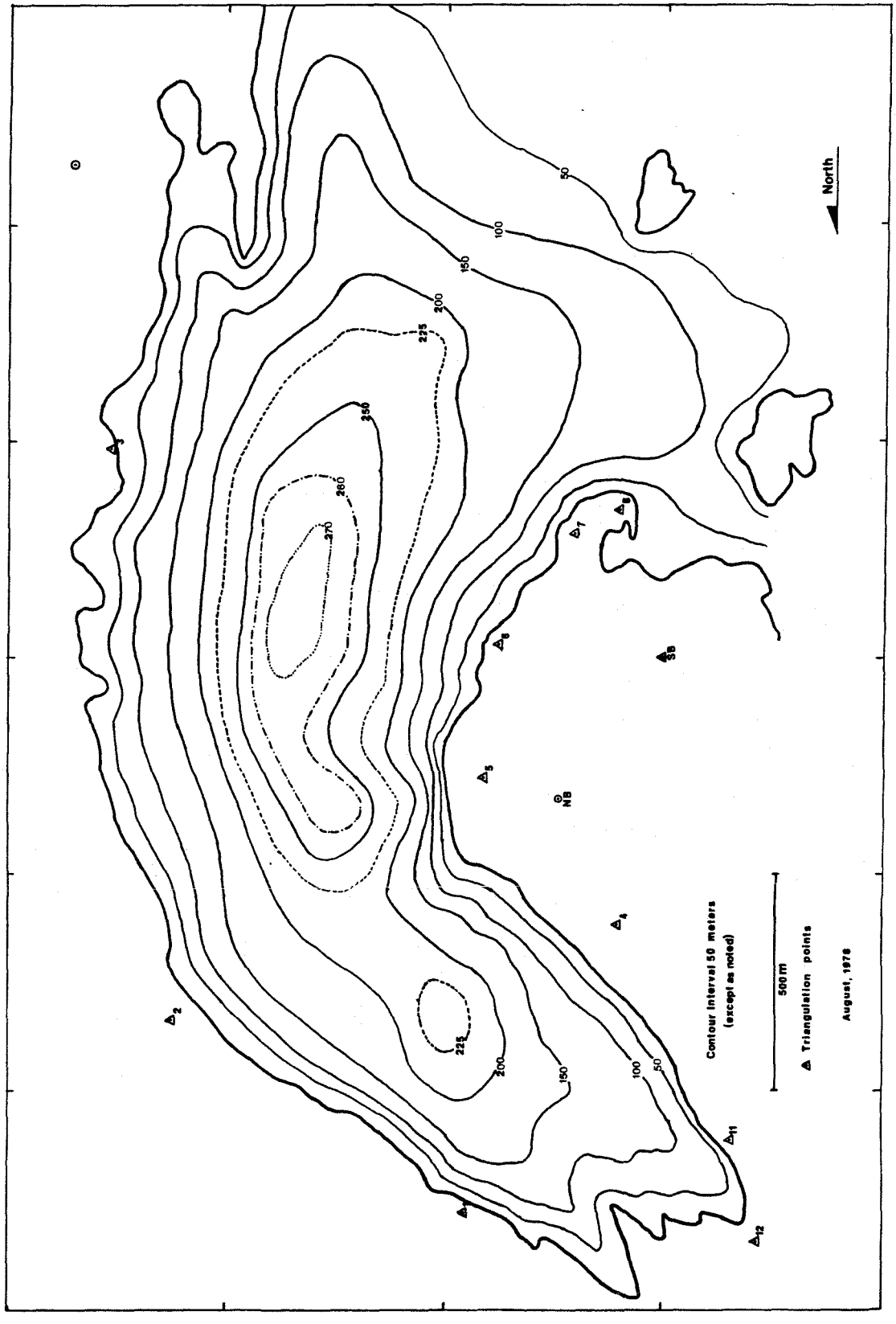
BLUE GLACIER ICE THICKNESS
North
Contour interval 50 meters
(except as noted)
500 m
Triangulation points
August, 1978
NB
SB
50
100
150
200
225
250
260
270

Figure 3.4

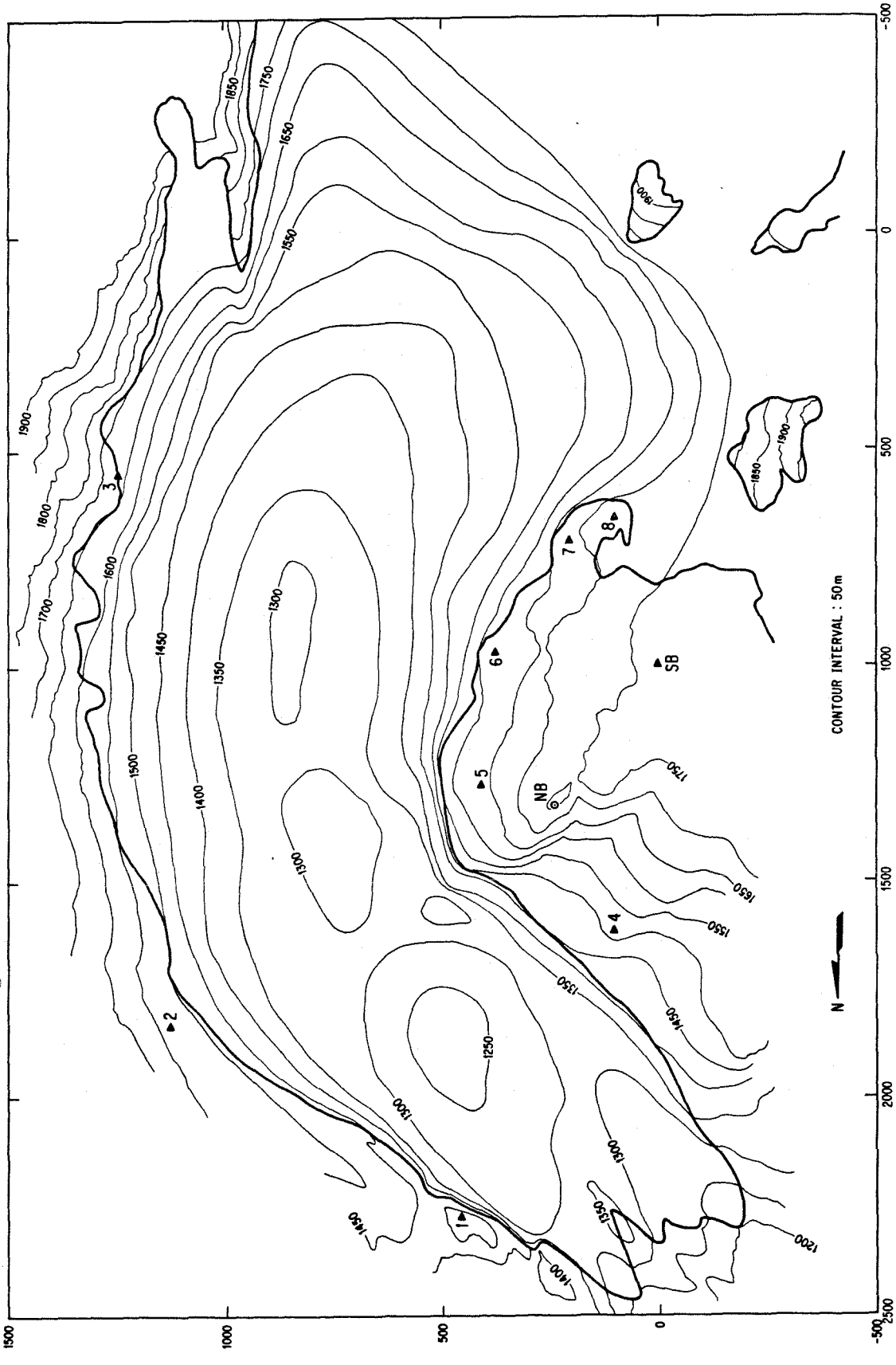
BED ELEVATION
CONTOUR INTERVAL : 50m
N
SB
NB
1
2
3
4
5
6
7
8
1900
1800
1700
1600
1500
1450
1400
1350
1300
1250
1200
1150
1100
1050
1000
950
900
850
800
750
700
650
600
550
500
450
400
350
300
250
200
150
100
50
0
-50
1500
1000
500
0
-500
-500
0
500
1000
1500
2000
2500

Figure 3.5

(Driedger, personal comm.) was used as the control for the surface elevation and glacier outline at unsurveyed locations. Features of these maps are similar to those shown in Corbató (1965). The actual ice thicknesses are greater than those observed by Corbató in 1960 and 61, as is expected. The greatest measured depth was 275 m in the region of H4. The bed elevations appear to be slightly lower in the central regions of the glacier than those obtained gravitimetrically. These discrepancies may, in part, be due to errors in the delay time correction factor for the oscilloscope, and, additionally, due to errors in the regional gravity field determination and the three dimensional data fitting procedure used in the gravity survey. Overall, however, the correlation is good, as is the correlation with results from seismic shots for which the quality of the reflection was fair or better (Allen,pers. comm.). Higher resolution of the channel shape near the margins was obtained from the radio-echo survey.

A longitudinal profile extending from the base of the central icefall to the terminus along a central streamline is shown in Figure 3.6. The 2x vertical exaggeration in this figure clearly shows the undulatory nature of the glacier bed. Closed basins are present in the channel form near the H and C profiles. The descent of the glacier from the F profile, where the bed is relatively flat, into the basin near C gives rise to the zone of extension at E and D, as evidenced by the numerous large transverse crevasses in this region. Similarly, the break in slope above the steep terminal region gives rise to extensional crevassing below a zone of generally splaying crevasses. The slope of the ice surface is significantly less than the local channel slope in the vicinity of K and J along the centerline. The mean thickness along the centerline from the base of the icefall to the terminal lobe is 180 m, while the mean thickness along the centerline from I to B (the region of study in 1957) is 234 m.

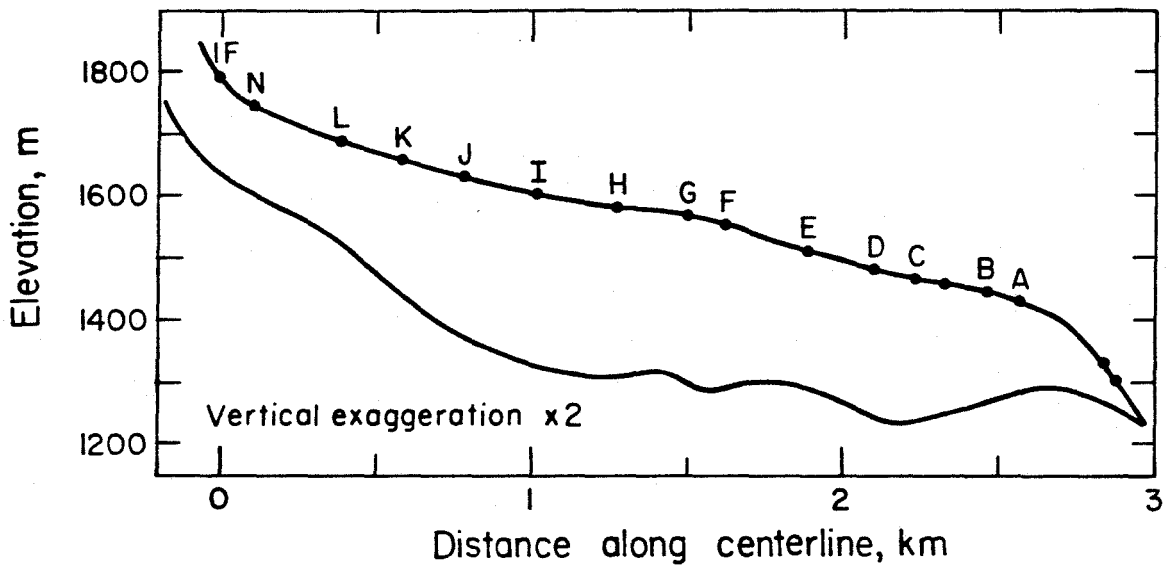

Figure 3.6

Longitudinal cross-section along centerline from base of icefall to terminus in 1978.

The cross-sectional depth profiles resulting from the transverse radio-echo lines are shown in Figure 3.7. Specific profiles will be discussed more fully in the treatment of flow modeling (Chapter X). Noteworthy in Figure 3.7 is the position of greatest depth in each cross section. In several profiles the depth maxima are located to the west of the geometric centerline of the channel, toward the inside of the bend about which the glacier flows. This is prominent where the curvature of the bend is large (profiles C-H), while profiles where the curvature is small show a more nearly centered depth maximum. The margins of the channels are generally sloping except where the ice abuts on a nearly vertical bedrock cliff (as in F and B). This geometry is important in discussing the distribution of shear stress within the ice.

The results of the radio echo study described in this section provide a complete description of the ice thickness and form of the bedrock channel for that portion of the Blue Glacier below the icefalls. The accuracy of these parameters is believed to be ± 5 m.

3.5 Surface Slope Measurements

The forces which drive glacier flow are determined, in part, by the inclination of the glacier surface, to first order (Nye,1952). Therefore, any discussion of the steady flow and the response of this flow to a change in surface configuration must include a specification of the surface slope (defined as the inclination to the horizontal, positive downward), and its variation in time.

The surface slope is commonly specified in a local sense (over a distance on the order of the ice thickness). However, this procedure has been shown to be inadequate in determining the flow on the Blue Glacier (M1) and elsewhere (Budd, 1968; Bindschadler others,1977). The latter authors have found that the flow appears to be governed by a slope which is averaged over a distance equal

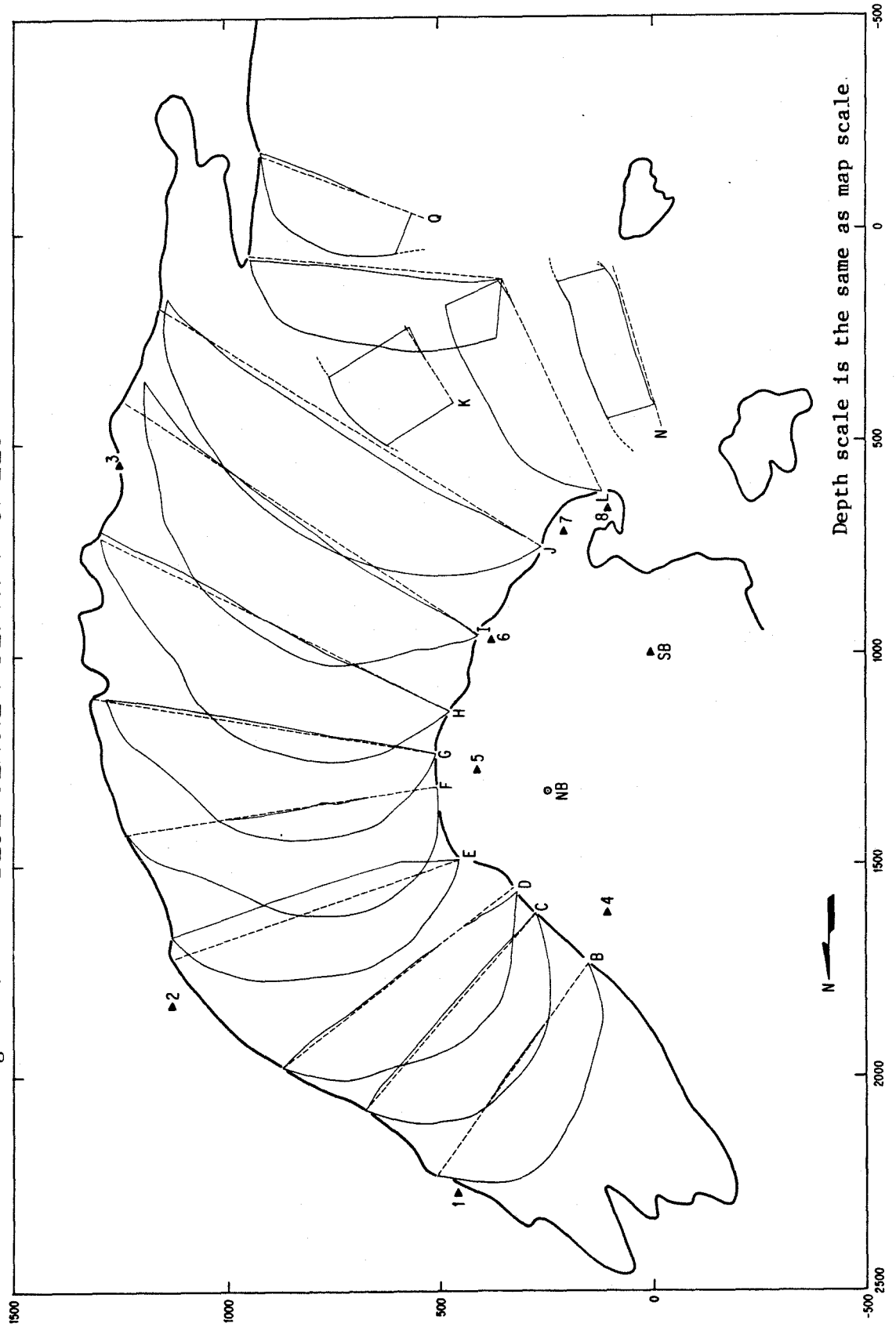
BLUE GLACIER DEPTH PROFILES
Depth scale is the same as map scale
1500
1000
500
0
-500
2500
2000
1500
1000
500
0
-500
N
NB
SB
A
B
C
D
E
F
G
H
I
J
K
L
N
Q
1
2
3
4
5
6
7
8

Figure 3.7

to many times the ice thickness, although the method of slope averaging used (a simple boxcar-type window) is somewhat unrealistic. (A theoretical explanation of slope averaging is given in Chapter VI.) In this section, surface slopes over different length scales are presented.These results will be used in discussing the flow response.

Using an Abney level or Brunton pocket transit the local slope was determined along the flow direction at each of the surface markers in 1978 by sighting from eyelevel to a mark of equal height at a measured distance of 100-200 m (about one ice thickness). In what follows this estimate of the slope will be denoted $< \alpha >_s$. Its value is listed in Table 3.2 . The accuracy is $\pm$ 1/2°. This local slope presumably corresponds to that listed by M1 in their Table 1, which was obtained from a topographic map. The slope measured at this small scale shows large spatial variation, appearing to be somewhat random in its fluctuations.

The coordinates of surface markers and their heights above the surface provide an accurate means of determining the surface slope at a medium length scale (300-550 m) (~ 2 ice depths). At each marker, the slope is determined from the difference in elevations of the two points along the same streamline in adjacent profiles up- and down- glacier, divided by the straight-line horizontal distance between these markers. For example, the slope at G3 is determined from the elevation difference between H3 and F3. (This method was modified at the end profiles.) It was thought that this would provide a more accurate estimate of the change in slope from 1957 to 1977 than would the use of a curvilinear metric. (The actual slope at this medium length scale is less than that shown in Table 3.2 because of the use of the straight-line distance between the points.) With proper account taken of the surface ablation in determining the height of a marker, the error is believed to be $\pm$ 0.03-.04°. Problems with this averaging scheme do arise because the length of the averaging window changes

with position, as the distance between profiles varies over the glacier. It was felt, however, that the inaccuracies involved in using a 5 m contour map of the surface and a more uniform averaging scale would be greater than those of the method used here.

This medium-scale average slope, denoted $<\alpha>_m$, is listed in Table 3.2, column 3, for 1977, and is displayed in Figure 3.8 along with results from the 1957 data set. As expected, there is much less high-frequency variation in $<\alpha>_m$ than in $<\alpha>_s$, both longitudinally and laterally. The difference between $<\alpha>_m$ and $<\alpha>_s$ is distributed normally about a mean of $-0.2°$ and there appears to be no correlation between $<\alpha>_m$ and $<\alpha>_s$. The mean centerline slope at this scale is $\overline{<\alpha>}_m = 6.14°$ in 1977 from I to B, while if all markers in the profiles I-B are included $\overline{<\alpha>}_m = 6.46°$. This is due to the steeper slopes along the western margin of the glacier, that is, toward the inside of the bend as seen in Plate 1.

In Figure 3.9 the longitudinal variation of $<\alpha>_m$ along the centerline is displayed. The two estimates at I correspond to limiting the data to the same region as studied in 1957 (the lower value) and to an incorporation of data from profile J, which was not available in 1957. The higher profiles (L, N) show a transition to the steep icefall above N, and lie in a region of marked longitudinal compression. The steepening at profiles D and E is accompanied by longitudinal extension (see Chapter IV) and a consequent increase in transverse crevassing.

Longer-scale averaging of the surface slope was performed by measuring the arc distance along a streamline and the accompanying drop in elevation. This enables an average to be taken over distances of up to 5-11 times the mean ice depth. Over the entire interval from N to B (2345 m) the slope was 7.24° in 1977. Over the interval I to B (1435 m or ~ 6 ice depths) the slope was 6.21° in 1977

Table 3.2
Short and Medium Scale Surface Slopes (Degrees)

$<\alpha>_s$ = slope measured over 100-200 m(~ 1H) along Streamline, 1977-78,± 0.4°
$<\alpha>_m$ = slope measured over 300-550 m(~ 2H) along Streamline,1977,± 0.02°

Location	$<\alpha>_s$	$<\alpha>_m$	Location	$<\alpha>_s$	$<\alpha>_m$
B1	7.3	5.90	H4	3.5	4.65
B2	(5.7)	5.34	H5	3.2	4.20
B3	4.7	4.48	H6	(4.0)	4.59
B4	4.8	4.81	H7	(6.2)	(5.10)
B5	4.5	5.90	I1	(7.91)*	8.57
C1	5.8	6.81	I2	(7.50)*	(7.56)
C2	6.5	6.32	I3	(5.93)*	7.41
C3	5.7	6.06	I4o	(5.05)*	7.01
C4	5.8	5.80	I5	(5.25)*	6.45
C5	6.3	6.35	I6	(5.58)*	6.30
C6	7.3	6.14	I7	(5.02)*	5.22
D1	(12.8)	12.05	I8	(5.76)*	5.06
D2	7.8	10.39	I9		4.88
D3	7.7	9.24	J2	6.8	9.52
D4	8.0	8.68	J3	8.8	9.87
D5	7.0	7.77	J4	9.0	9.32
D6	(5.0)	6.04	JJ5	7.8	7.92
E1		11.94	J6	7.2	6.29
E2		10.31	J7	5.8	5.11
E3		8.56	J8	4.2	5.58
E4		8.02	J10	11.0	
E5		7.66	K3		8.06
E6		6.62	L2	14.7	13.09
F1	9.5	9.68	L4	11.5	11.31
F2	8.6	7.75	L5	8.5	9.83
F3	7.5	6.82	L6	11.3	
F4	7.2	6.13	L9	12.7	
F5	6.0	5.99	L10	5.8	
F6	5.7	6.21	L11	7.2	
G1	8.3	7.20	L12	10.8	
G2	5.8	5.20	M1	10.8	
G3	5.5	5.13	N2	14.0^+	
G4	4.7	4.43	N3	14.2^+	
G5	4.7	4.21	N4	14.7^+	(15.82)
G6	4.3	4.59	N5	18.7^+	
G7	5.0	4.65	Base of Icefall	(23.8^+)	
H0	9.5		Q1	24.2	
H1	4.5	6.59	Q2	16.2	
H2	(3.3)	5.17	Q3	11.8	
H3	3.5	4.67	Q4	11.3	

( )* ≡ Slopes computed from I to H (~ 300 m), not from J to H;
( ) ≡ Approximate values

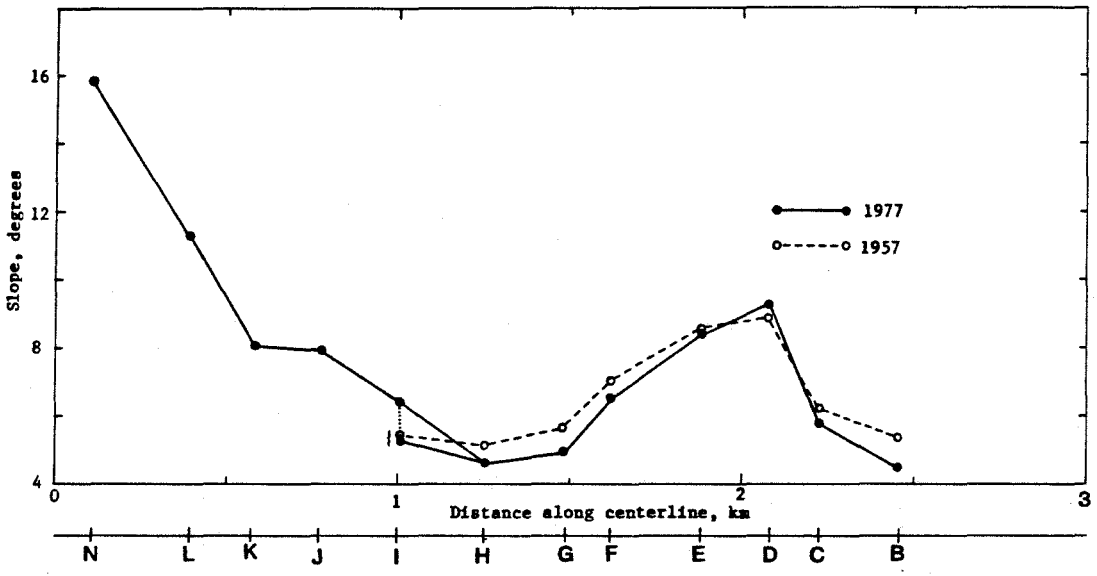

Figure 3.8

Longitudinal profile of surface slope at medium averaging scale (~2 x thickness). Slopes determined from surveyed position of markers. Accuracy is ±0.04°.

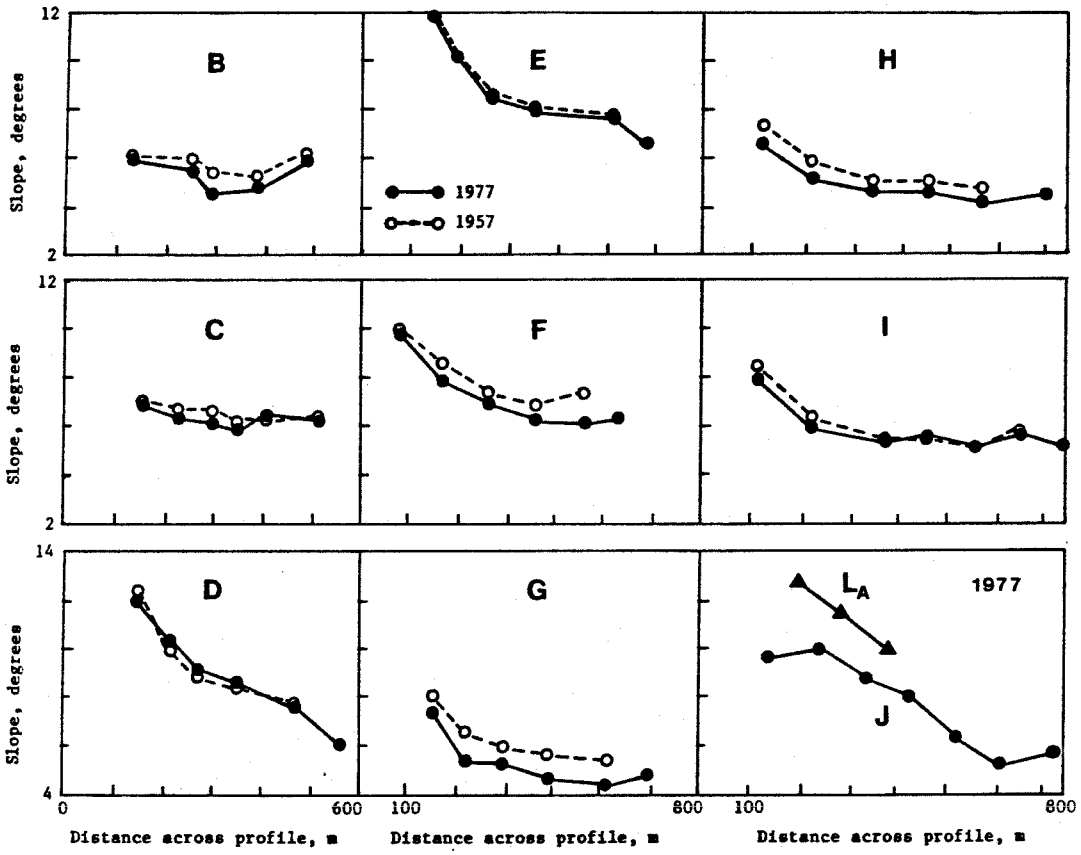

Figure 3.9 Surface slope across transverse profiles, medium averaging scale (~ 2 x thickness). Slope for profile I is taken from I to H and not from J to H, so it is lower than the true value.

and 6.51° in 1957. The accuracy of these estimates is ± 0.08°. They are denoted $<\alpha>_L$. This length of this averaging scale roughly corresponds to the 2-4 km averaging window that was used by Bindschadler and others (1977) on the deeper Variegated Glacier, which was found to correlate well with the flow velocity. However, $<\alpha>_L$ cannot be interpreted as the slope is determined over a length L centered over each profile, except at the center of the reach studied, since the averaging window does not shift position.

As will be noted, the corresponding surface slopes in 1957 are generally greater than those determined in 1977 by about 5%. The value of the mean slope $<\alpha>_L$ for 1957 is relatively close (≈ 0.7° difference) to the effective slope of M1, as derived by a method based on continuity of ice flux within a streamsheet.

Table 3.3
Longer Scale Surface Slope
(centerline only, all angles in degrees)

$\langle \alpha \rangle_L$ ($\pm$ 0.08°)

Window*	1957	1958	1959	1977	1978	1979
B-I	6.51	6.29	(6.20)	6.21	6.03	(5.91)
B-N	---	---	---	7.24	---	---

$\overline{\langle \alpha \rangle}_m$, 1957 and 1977

B-I, centerline	6.49	6.14
B-I, all markers	7.03	6.47
B-N, centerline	----	7.59

$\langle \alpha \rangle_L$ over 1400-2350 m (~ 6-11H)
$\overline{\langle \alpha \rangle}_m$ = mean over medium-scale values (~ 2H)

* - lower and upper profiles of averaging window used
( ) - approximate values

CHAPTER IV

VELOCITY FIELD OF BLUE GLACIER

The measurements described in Chapter II lead to a complete determination of the surface velocity field of Blue Glacier. The spatial variations over the entire reach below the icefalls have been investigated. The measurements were carried out over a five-year period, from 1977 to 1981, hence temporal variations in velocity on a variety of time scales can be revealed.

Since the general features of the velocity field have been described by Meier et al.(1974), a brief discussion, emphasizing the aspects augmented in the present work, is sufficient here. Particular consideration is given to those aspects which are relevant to the model calculations presented in later chapters.

Many features of the Blue Glacier velocity field are common to the flow of other glaciers, representing the interplay between the valley form, the shape of the glacier surface (and the mass balance defining it), and the nonlinearities in the flow law.

4.1 Calculation and Accuracy of Surface Velocity

Let a particle of ice be denoted by its initial position $\mathbf{X}$ in a reference configuration at some initial time ($t = 0$). The position of the particle at a later time (t) is denoted $\mathbf{x}$, and is a function of the initial location and time: $\mathbf{x} = \mathbf{F}(\mathbf{X},t)$. The time rate of change of $\mathbf{x}$ for a fixed particle is the instantaneous velocity at a given point and time

$$\mathbf{u} = \mathbf{u}(\mathbf{x},t) = \left[\frac{\partial \mathbf{F}}{\partial t}\right]_{\mathbf{x}} , \tag{4.1}$$

which, in terms of Cartesian components, $\mathbf{u} = (u^1,u^2,u^3) = (u,v,w)$, can be written

$$u^i(x,t) = \left[\frac{\partial F^i}{\partial t}\right]_{\mathbf{X}} \tag{4.2}$$

A finite difference approximation to 4.2 may be written as

$$u^i(\bar{\mathbf{x}},t) \approx \frac{x^i(\mathbf{X},t_1) - x^i(\mathbf{X},t_o)}{t_1 - t_o} \tag{4.3}$$

where

$$t \in [\, t_o\,,\, t_1\,] \quad \text{and} \quad \bar{x}^i \in [\, x^i(\mathbf{X},t_o)\,,\, x^i(\mathbf{X},t_1)\,]\,.$$

Equation 4.3 may be interpreted as the average velocity of the ice at a point $\bar{\mathbf{x}}$, such that $\bar{x}^i = \frac{(x^i(\mathbf{X},t_o) + x^i(\mathbf{X},t_1))}{2}$, over the time interval $t_1 - t_o$. Thus, the velocity determined at a given marker stake over the period of a year will, in general, refer to $\mathbf{u}$ at a different point in space than will velocities determined over shorter time periods. If the velocity gradients are small then this distinction between the midpoints of the motion intervals need not be made. This is the case for most of the velocities reported here. However, the motion of a marker which is not reset to its initial position over a period of more than one year (such as the borehole casings and a few of the markers along the longitudinal centerline) will be affected by this difference in $\bar{\mathbf{x}}$. At these longer time periods ($\geq$ 2 yr.), the motion of the marker will be comparable to the distance over which the velocity can be expected to vary significantly.

From the approximation 4.3, the velocity field of lower Blue Glacier was determined. All combinations of the position data for a given marker were utilized in defining the temporal variation of $\mathbf{u}$ at a (nearly) fixed location on the glacier surface. If a marker was surveyed n times over the period 1977-80, then a total of $\binom{n}{2}$ average velocities could be estimated over time intervals ranging from $\min_{i\neq j}|t_i - t_j|$ to $(t_n - t_1)$ (excluding any large resets).

In addition to the individual components of **u**, the horizontal velocity u_H, its azimuth relative to true North (φ, positive clockwise), the magnitude of **u**, $u_{tot}(\equiv (\mathbf{u}^T\mathbf{u})^{\frac{1}{2}})$, and the plunge relative to the horizontal (ϑ, positive downward) were determined. These various parameters are listed in Appendix B for the annual velocities from 1977 to 1980.

An estimate of the errors in the velocity components can be obtained from errors in the coordinates and reset corrections, using the relation (2.10). Specific probable errors in each annual velocity are listed in the last columns of the tables in Appendix B. Mean values of these estimates are σ_{u_H} = 0.15 m/yr, σ_w = 0.05 m/yr for average velocities over a one year interval, and σ_{u_H} = 2.2 m/yr, σ_w = 0.6 m/yr for a two week interval. The accuracy in the annual centerline velocities is thus about 0.3 % in the horizontal and 1.5 % in the vertical.

According to the above estimates, the accuracy of the annual u_H and w are somewhat better than those given in other studies. This is mainly due to the explicit measurement of the tilt of each marker, which reduces the uncertainty in the position of the reference point at the base of the marker. The larger relative errors in the short-term velocity results is brought about by the increased effect of errors in this tilt measurement at short times.

4.2 General Features of the Surface Velocity Field

The positions of the velocity markers are shown in Plate 1 for 1977 and 1978, with components given in the tables in Appendix B. Streamlines of flow are seen to trace gently arcing paths as the glacier descends from the base of the icefalls to the terminus. The contours of velocity in Plate 1 show a smooth variation over the glacier surface. The relatively high velocity ice streams emanating from the icefalls and Blizzard Pass (between Mts. Apollo and East Olympus) show a gradual merging and slowing near the L profile, becoming fully merged by J. The

velocity patterns found by the present work in the region spanned by profiles B to I are similar to those obtained in the 1957-9 surveys by Meier et al.(1974), except that the velocity high near profile E is more pronounced in the recent results. The additional markers near the margins allow a better delineation of the velocity field in the marginal shear zones. Below the B profile the velocity is seen to increase as the ice moves over the steeper terrain toward the terminus. Relatively high velocities (40 m/yr) persist to near the terminus. During the period of observation, these velocities more than compensated for the ablation at the terminus, and thus the terminus advanced. (This is especially noteworthy in view of the fact that the terminus of Blue Glacier lies at the lowest limit of glaciation in the conterminous United States.) The high terminal velocities are due, in part, to a basal sliding contribution that is abnormally large.

The longitudinal variation in flow velocity **u** along (or close to) the central streamline marked in Plate 1 is shown in Figure 4.1, together with the surface slope and the plunge of the velocity vector (both measured positive downward in the direction of flow). The plunge shows the expected relation to slope (Paterson, 1981,pp.59-60), indicating a flow downward relative to the surface above the equilibrium zone (L-I), nearly surface-parallel in this zone, and increasingly upward as the terminus is approached.

The magnitude of the velocity is fairly constant throughout a major section of the lower Blue Glacier, as is seen in Plate 1. The magnitude of **u** does show some correlation with the slope. The transition from the steep icefall to the ramp area at N-L causes a distinct longitudinal compression. The steeper region at D-E shows a velocity peak, and gives rise (through longitudinal extension) to the transverse crevassing found in this region. The very steep terminal region has a relatively high velocity even though the ice is thin there. Thus, although longitudinal gradients in the longitudinal strain rates are generally small, the local

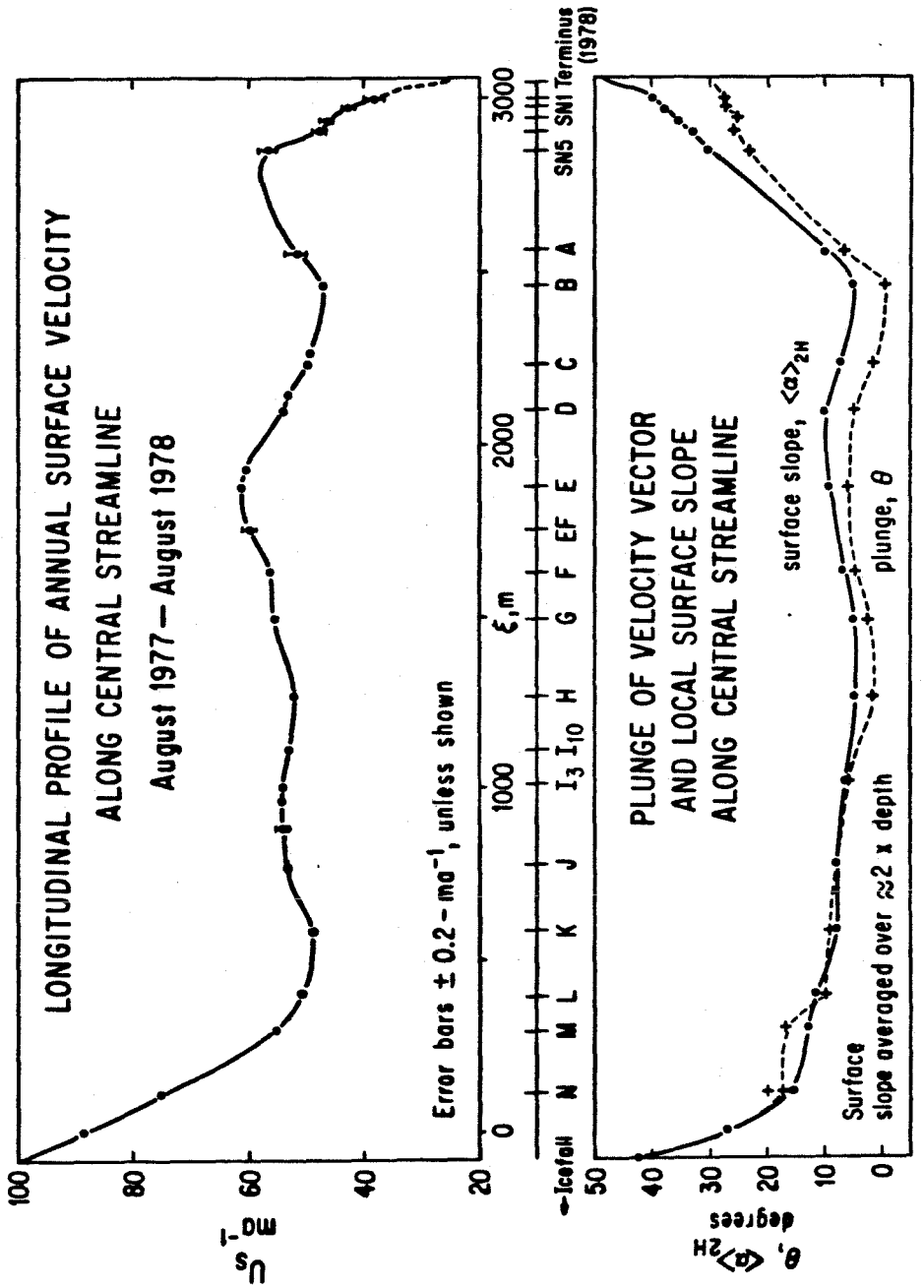

Figure 4.1 Longitudinal profile of annual surface velocity along central streamline. The lower figure shows plunge of velocity vector (dashed line), and medium-scale surface slope(solid line) downward from horizontal. SN1-SN5 designate markers near terminus.

surface slope (as averaged over a few ice thicknesses) does seem to influence the rate of flow.

At the terminus a vertical ablation rate of 6-7 cm day^{-1} was measured. If this rate were to persist for roughly six months then the total ice removed would amount to about 16-17 m retreat of the terminus horizontally. The 24 m a^{-1} velocity at the snout shown in Figure 4.1 would then account for a terminal advance of 7-10 m a^{-1}. Given that there also exists a small amount of ice "calving" at the terminus (large blocks periodically break off and are removed by the stream) this calculated rate of advance agrees reasonably with the observed advance of 5-9 m a^{-1} during this time.

Transverse profiles of velocity are shown in Figures 4.2a-c. The typical form is that of a higher-order parabola with relatively steep gradients near the margins. In general, the profiles B-I of surface velocity found in this study agree in form with those of M1, which is to be expected. The detailed shapes in the marginal regions differ, due to the better resolution of the present study and the small changes in channel width.

A few notes on the construction of these profiles are in order, for they will be compared in detail with the results of the modelling in later chapters. In many places the margins of the glacier are ill-defined due to the presence of stagnant ice or perennial snowfields, which may not be completely incorporated into the moving glacier. For example, profiles I and J could be extended to the east onto the lower slopes of Apollo, without crossing any clear demarkation between glacier and marginal snow slope. Creep of firn and ice down these slopes is reflected in a centerward component of motion in the flow vectors of the easternmost markers (I13, J10). This component of motion is particularly prominent along that part of the lower slopes where the small, steep glacier tongue that descends

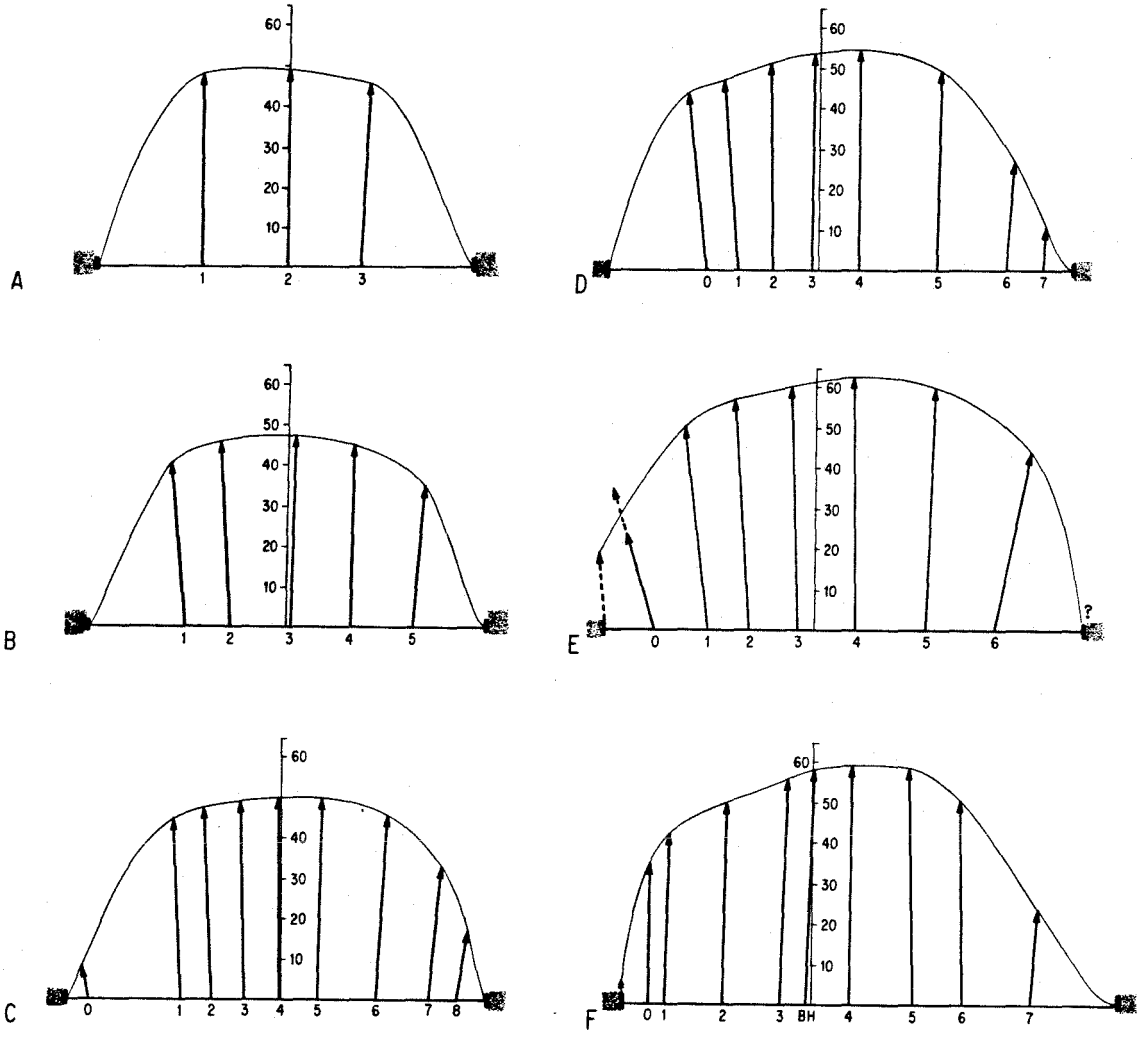

Figure 4.2 a

a-c Transverse profiles of annual velocity. Length of velocity vectors is shown at a scale enlarged 6.35 times the horizontal scale. This allows direct comparison with Meier, et al. (1974), Figure 4. Velocities shown are for 1977 to 1978. Vertical axes are at position of central streamline, except for L_B and Q. Markers L8 and L9 are near junction of profiles L_A and L_B, where flow direction is different than for rest of profile. Dashed vectors indicate approximate values. The two vectors at E0 show values obtained over the summers of 1977 and 1978, respectively, and are subject to large errors. Profile Q shows 1978 summer velocities.

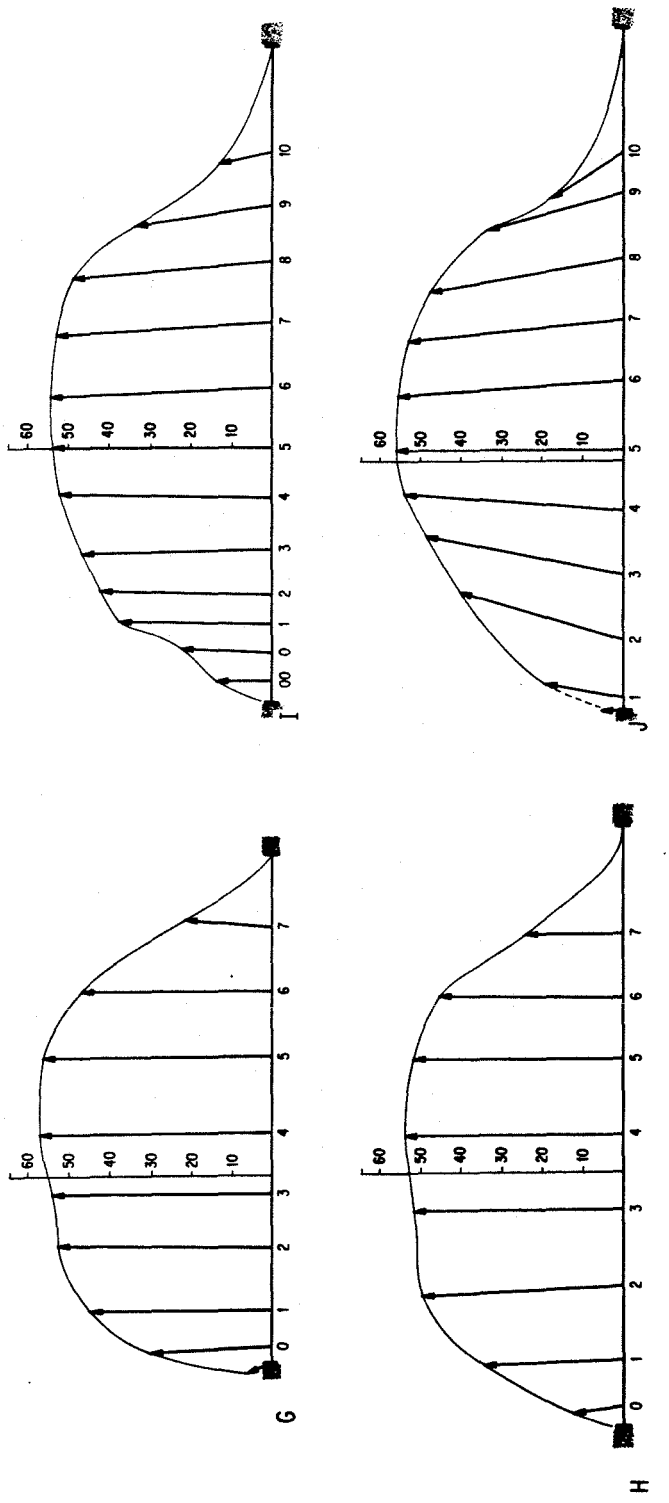

Figure 4.2b

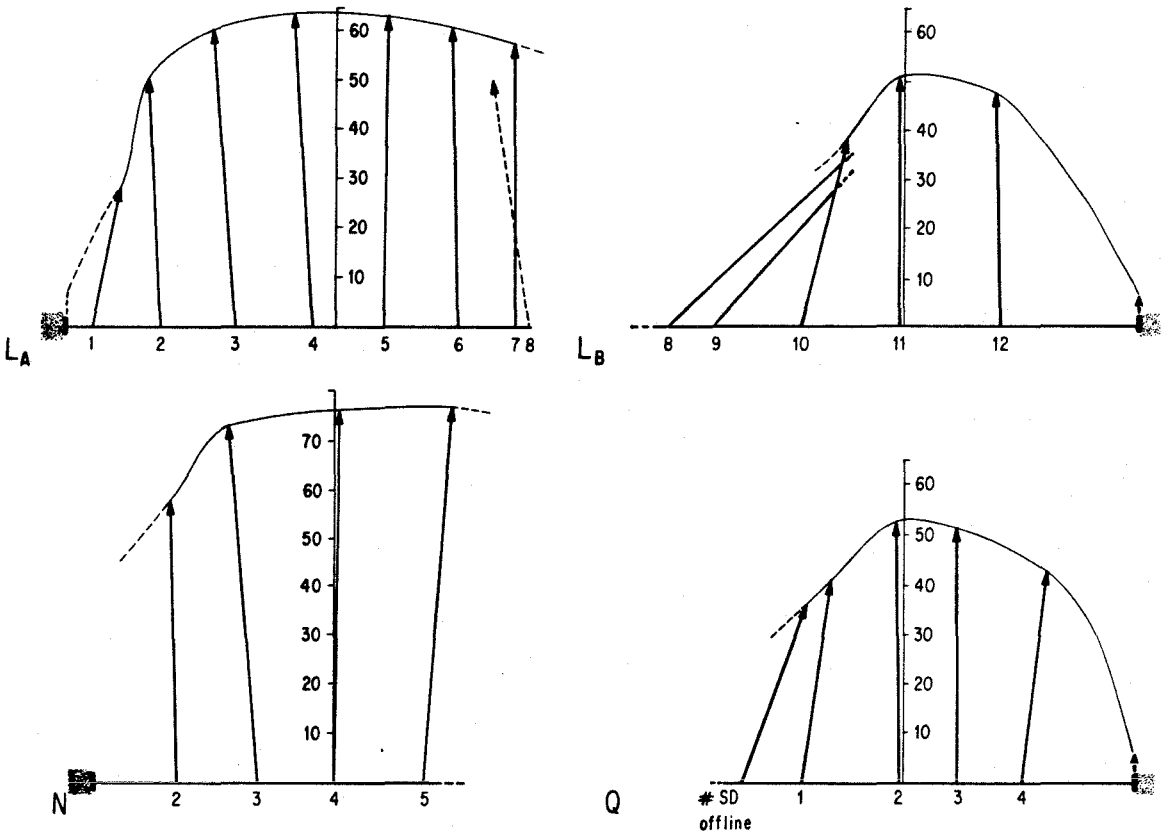
60
50
40
30
20
10
L_A
1 2 3 4 5 6 7 8
60
40
30
20
10
L_B
8 9 10 11 12
70
60
50
40
30
20
10
N
2 3 4 5
60
50
40
30
20
10
Q
SD
offline
1 2 3 4

Figure 4.2c

from near the summit of Apollo reaches and merges with Blue Glacier. Similarly, the westernmost ice of profiles B and C may be somewhat stagnant. There is therefore a problem in defining these margins and specifying the velocity there,unless it is actually measured. (Similar problems are encountered in the construction of thickness profiles.) The marginal points shown in the diagrams represent the author's best estimate,but they are subject to the problems and uncertainties indicated.

Marginal sliding has been indicated on the diagrams, both at places where it was measured in the present work (see section 4.5) and where observed by Meier et al. (1974). At steep valley walls where the marginal slip was not measured a marginal sliding of ~ 5 % of the centerline velocity has been assumed (dashed marginal vectors), based on the values observed elsewhere along the margin. This yields more reasonable profiles.

A few velocity values in the profiles are subject to unusually large errors because of extreme stake tilts, marker location off the line of the profile, etc. In particular, E 0 lies within a small, yet steep and active icefall along the inside of the bend, making the necessary stake maintenance often unfeasible. Similarly, the entire A profile, L1, and several of the markers in the terminus lobe were subject to crevasse-block rotation and slumping, and they could not always be reached late in the season for determining accurate tilts and for resetting.

The velocity profiles shown for L and N display 1977 summer velocities rather than annual velocities because better coverage was available during this field season than over the yearly interval. Similarly, Q displays 1978 summer velocities. These velocities are greater than the mean annual values (by about 10 %) due an increased basal sliding contribution during the summer period (see section 4.3). Profile L is divided into two parts, one (L_A) with an N-S trend below the

northern and central icefalls, and the other (L_B) striking E-W below the ice stream emanating from Blizzard Pass and the southern icefall. The markers L 8 and 9 lie within an intermediate icestream coming from the region near the central icefall septum (Allen et al., 1960), and thus do not have flow vectors which are sub-parallel with the rest of L_A or L_B, although they are plotted as members of these two sections of L. The displayed flow vectors of L8 and L9 do not imply a crossing of streamlines, but rather a convergence of the different icestreams.

There is a definite lack of symmetry about the center-line in most of the profiles, especially above profile D. The maximum flow rate occurs at a position generally to the east of the center, that is, toward the outside of the bend around which the glacier flows. This cannot be due to channel asymmetry, for, as seen in Figure 3.4, this would tend to cause the maximum to lie west of the center, where the channel is deeper. The observed location of u^{max} is a direct consequence of the horizontally curving channel, as originally pointed out by Kamb (M1,p.196) and developed here in detail (see Chapters VIII and X).

A transverse component of flow causes a convergence or divergence of the velocity vectors across a profile. In the region above the H profile the vectors converge as a direct consequence of the valley becoming narrower, causing the convergence of different ice streams, and of the concave upper surface and the influx of ice from the slopes of Apollo. Similarly, the divergence in the lower profiles reflects the convexity of the upper surface. This outward component of flow is particularly noteworthy at E0,E1,D0, and D1, where there is a large transverse surface inclination toward the margin where there is a local widening of the valley. (The flow driven by a non-level upper surface will be discussed in Chapter VIII.) It should be noted that the expected convergence above the equilibrium line and divergence below it (Nielsen, 1955) is not strictly realized on Blue Glacier because of the superposition of the effects of the changing channel

width. Also, the reasoning of Raymond (1969,pp.110-114) in analyzing the laterally diverging flow that is present at depth in Athabaska Glacier is not strictly applicable to the situation on Blue Glacier, because of the relatively small amount of basal sliding that occurs, as discussed in section 4.4.

4.3 Trends in Velocity over the Period 1977 to 1980

A brief discussion of short-term ($\leq$ 4 yr.) temporal variations in $\mathbf{u}(\mathbf{x},t)$ of interest to the present study is given in this and the following section. A complete description of longer term (1957-1980) changes is given in Chapter V.

Short-term flow velocity fluctuations (over days to months) are generally taken to indicate changes in the amount of sliding occurring at the base of a glacier (Iken, 1978, 1981; Hodge ,1972; Paterson, 1964). Longer-term changes (over months to years) can, additionally, indicate changes in surface geometry and internal deformation of the ice mass. Variations on both of these time scale ranges were observed on Blue Glacier during this study. They can be used to give information on the role of basal sliding in the motion of the glacier and to check the validity of the longer-term study that comprises the main subject of this work.

Figures 4.3 - 4.10 show temporal fluctuations at representative markers. As the position data were obtained over various time intervals through several years, a large number of mean velocities may be determined from combination of the data. The values thus represent average velocities over time periods ranging from a week to several years, and the various time scales are represented by the different symbols in these figures (as defined in Figure 4.3a). Changes in these mean $u_H(\mathbf{x},t)$ values are produced by motion within the spatially varying velocity field as well as by the temporal variations in the velocity field, which is of interest here. As described in Chapter II, an attempt has been made to

Figures 4.3 - 4.10

Horizontal surface velocity at selected markers during the period 1977 to 1980 are shown. Three symbols are shown in these figures, representing three different measurement periods. Averages over 1 month or less are represented as circular dots, averages over 1 month to 12 months are squares, and averages over periods greater than 12 months are triangles. Symbols are placed at the midpoint of each interval. Errors in the short period values average 0.25 cm/day, while errors for periods greater than three months to one year average 0.06 cm/day and are 0.03 cm/day for periods greater than 1 year. Solid lines represent trends in annual velocities, except for Figure 4.10, where they define the trend over summer, 1977. In Figures 4.6b, 4.7a, and 4.7b solid lines show the trend from 1977 to 1979 and 1978 to 1980 separately, while the broken line shows the mean trend from 1977 to 1980. In those figures representing markers which moved with the ice over the entire period 1977-80 (no large resets upglacier, e.g. Fig. 4.3a), a dashed line showing the local velocity gradient ($\dot{\varepsilon}_{\xi\xi}$) is shown. Positions of the markers are shown in Plate 1, including the borehole casings (designated BH).

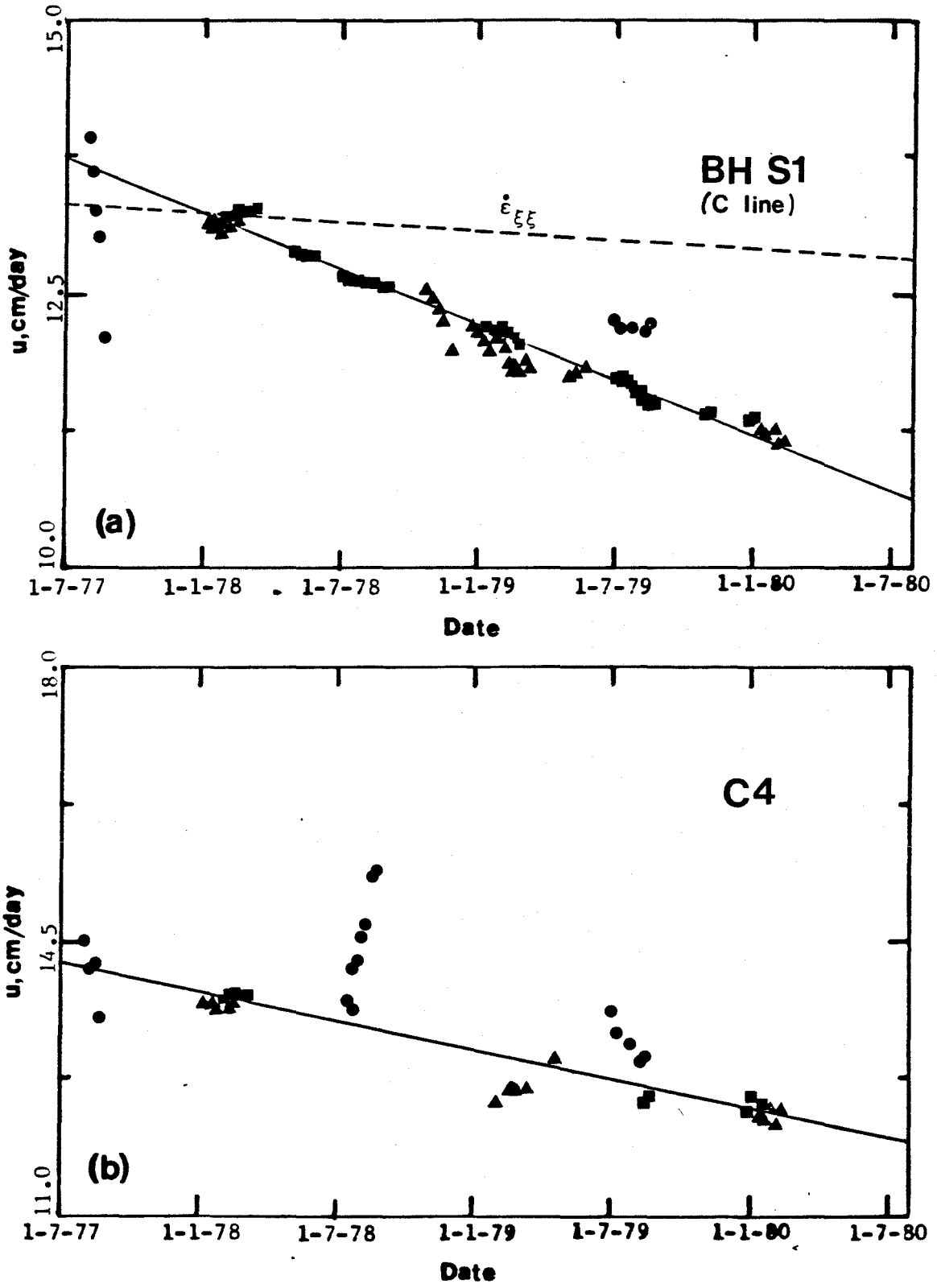
BH S1
(C line)
$\dot{\varepsilon}_{\xi\xi}$
(a)
u,cm/day
15.0
12.5
10.0
1-7-77
1-1-78
1-7-78
1-1-79
1-7-79
1-1-80
1-7-80
Date
C4
(b)
u,cm/day
18.0
14.5
11.0
1-7-77
1-1-78
1-7-78
1-1-79
1-7-79
1-1-80
1-7-80
Date

Figure 4.3

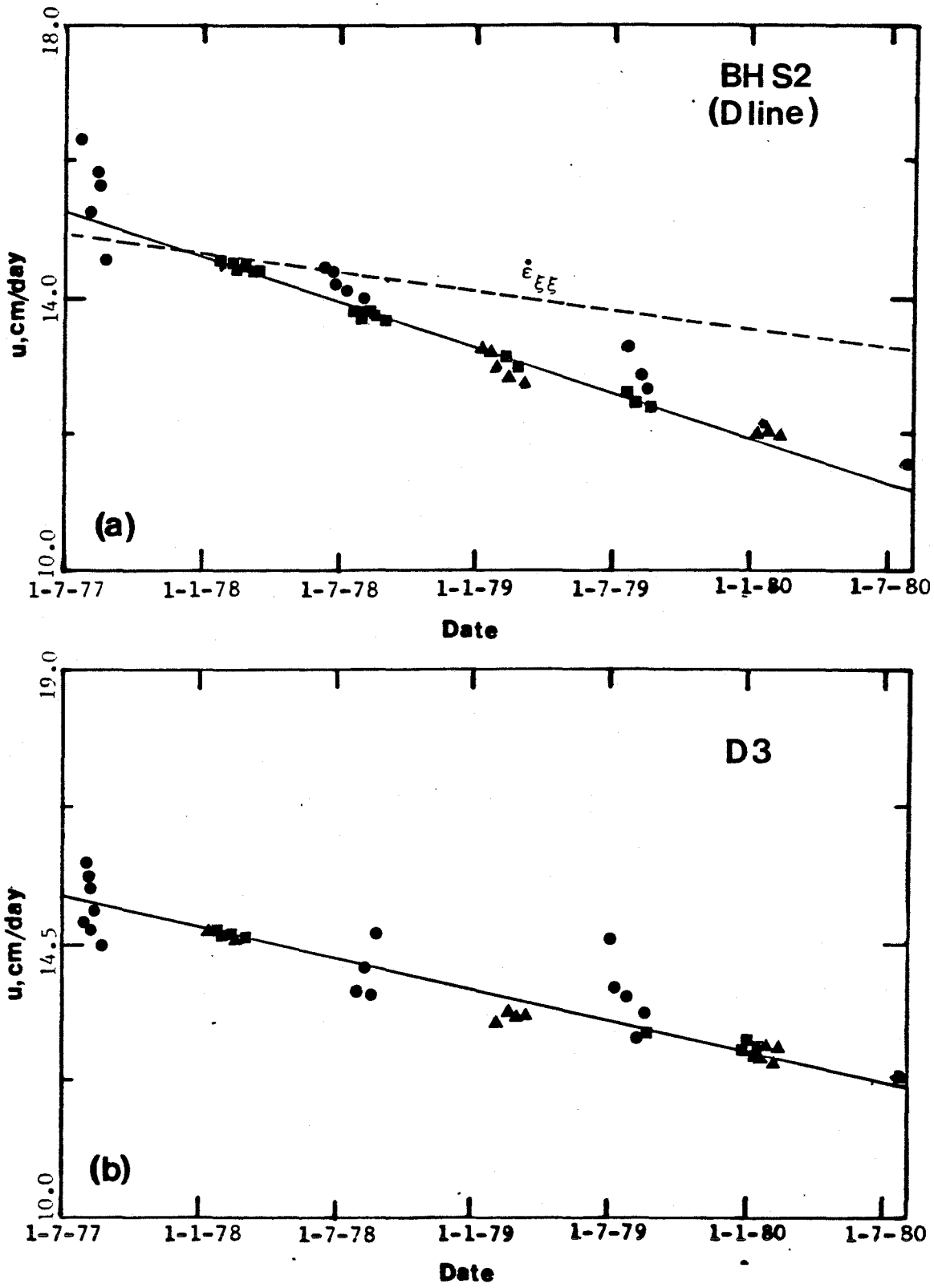
BH S2
(D line)
$\dot{\varepsilon}_{\xi\xi}$
(a)
u, cm/day
18.0
14.0
10.0
1-7-77
1-1-78
1-7-78
1-1-79
1-7-79
1-1-80
1-7-80
Date
D3
(b)
u, cm/day
19.0
14.5
10.0
1-7-77
1-1-78
1-7-78
1-1-79
1-7-79
1-1-80
1-7-80
Date

Figure 4.4

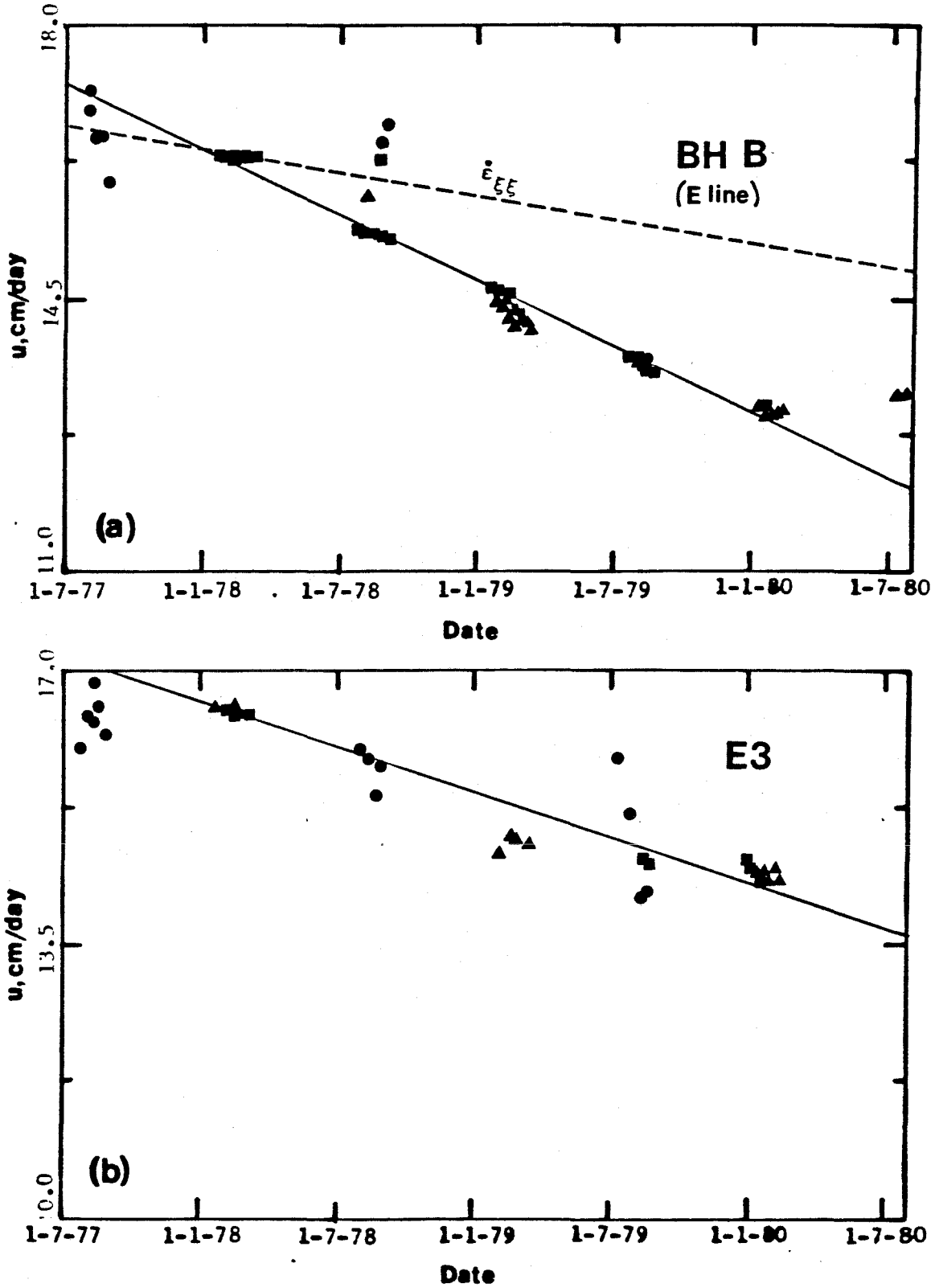
18.0
14.5
11.0
u,cm/day
BH B
(E line)
$\dot{\varepsilon}_{\xi\xi}$
(a)
1-7-77
1-1-78
1-7-78
1-1-79
1-7-79
1-1-80
1-7-80
Date
17.0
13.5
10.0
u,cm/day
E3
(b)
1-7-77
1-1-78
1-7-78
1-1-79
1-7-79
1-1-80
1-7-80
Date

Figure 4.5

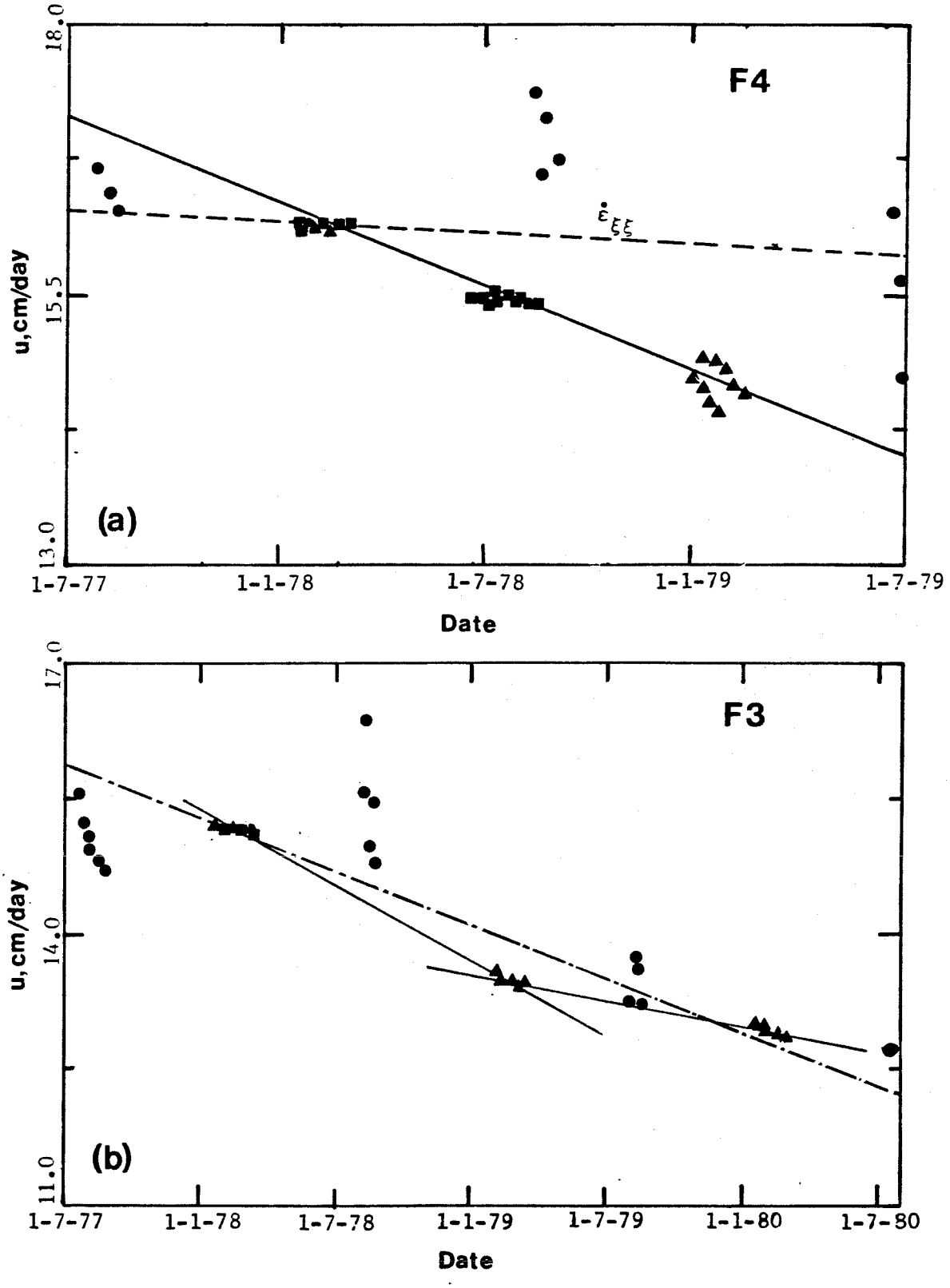
F4
$\dot{\varepsilon}_{\xi\xi}$
u,cm/day
18.0
15.5
13.0
(a)
1-7-77
1-1-78
1-7-78
1-1-79
1-7-79
Date
F3
u,cm/day
17.0
14.0
11.0
(b)
1-7-77
1-1-78
1-7-78
1-1-79
1-7-79
1-1-80
1-7-80
Date

Figure 4.6

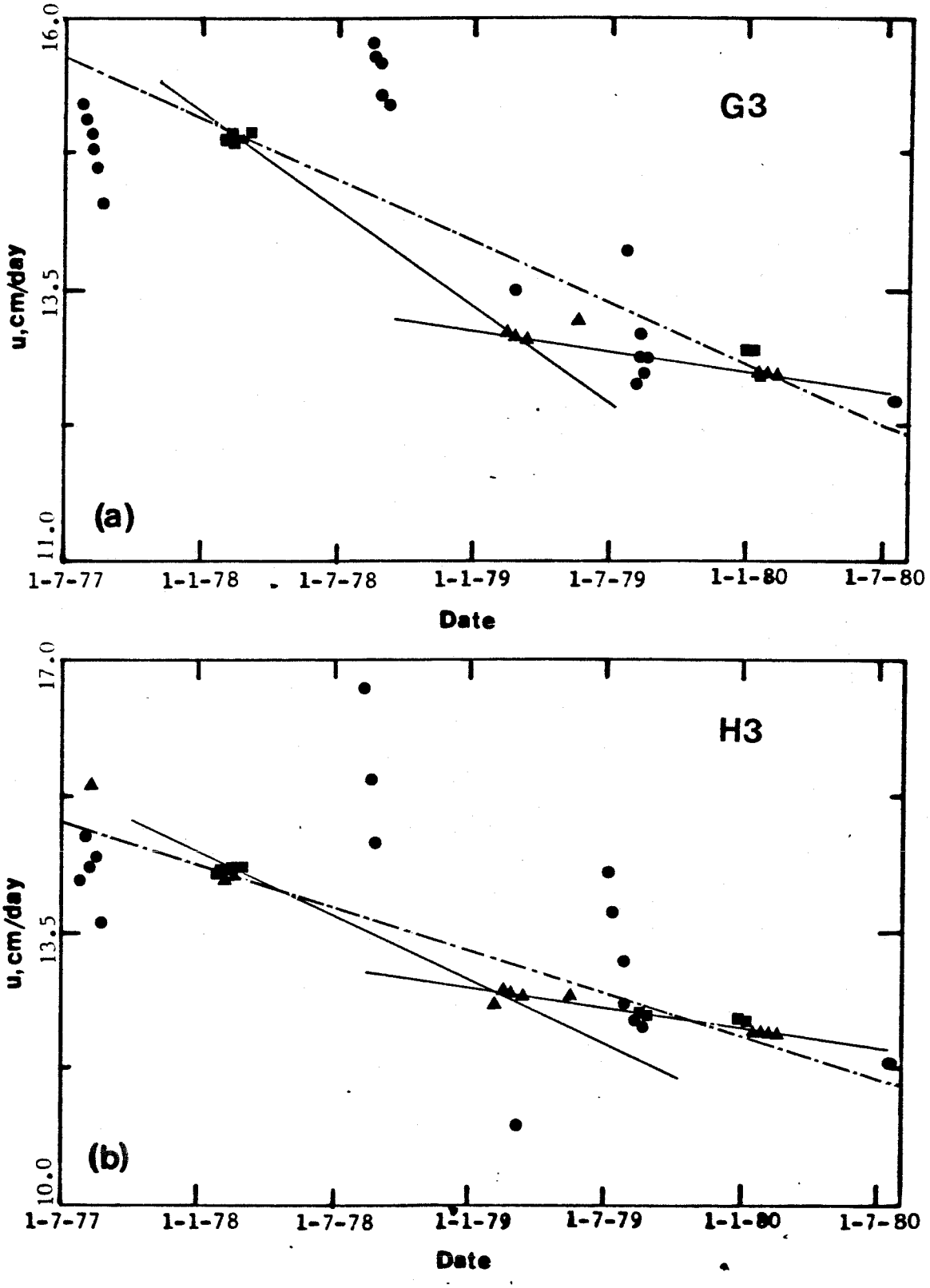
16.0
13.5
11.0
u,cm/day
G3
(a)
1-7-77
1-1-78
1-7-78
1-1-79
1-7-79
1-1-80
1-7-80
Date
17.0
13.5
10.0
u,cm/day
H3
(b)
1-7-77
1-1-78
1-7-78
1-1-79
1-7-79
1-1-80
1-7-80
Date

Figure 4.7

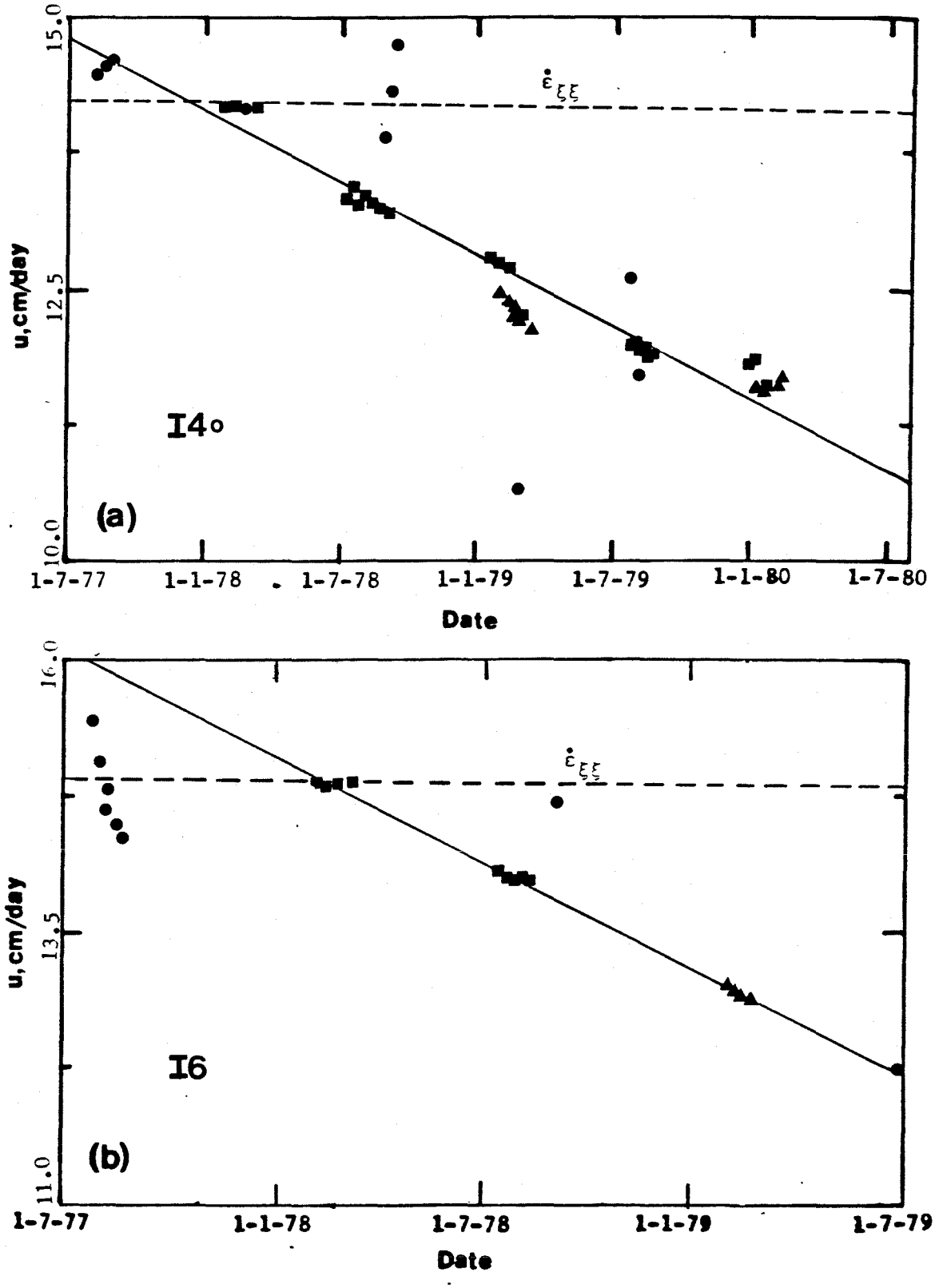
15.0
12.5
10.0
u,cm/day
$\dot{\varepsilon}_{\xi\xi}$
I4o
(a)
1-7-77
1-1-78
1-7-78
1-1-79
1-7-79
1-1-80
1-7-80
Date
16.0
13.5
11.0
u,cm/day
$\dot{\varepsilon}_{\xi\xi}$
I6
(b)
1-7-77
1-1-78
1-7-78
1-1-79
1-7-79
Date

Figure 4.8

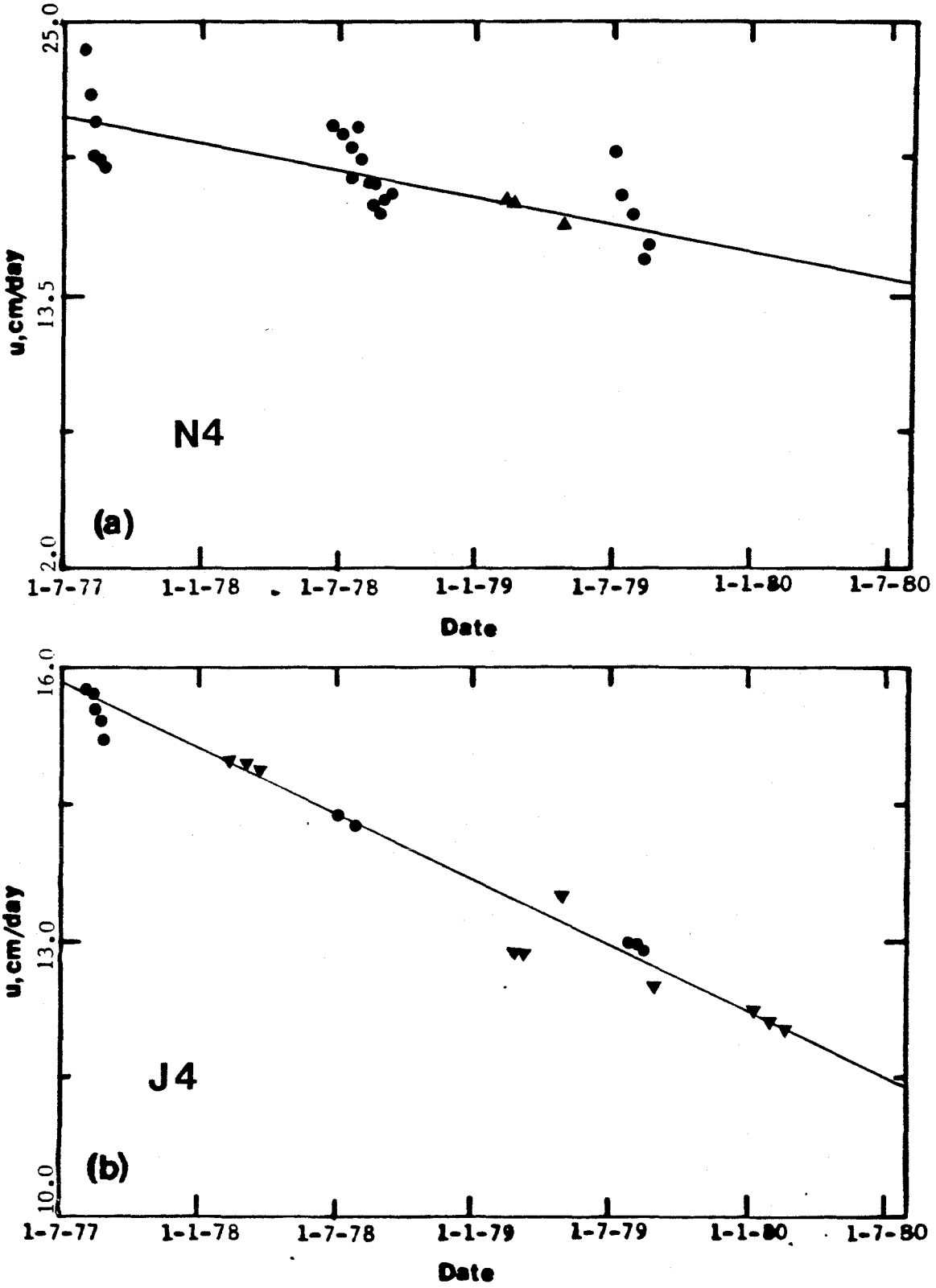
25.0
13.5
2.0
u,cm/day
N4
(a)
1-7-77
1-1-78
1-7-78
1-1-79
1-7-79
1-1-80
1-7-80
Date
16.0
13.0
10.0
u,cm/day
J4
(b)
1-7-77
1-1-78
1-7-78
1-1-79
1-7-79
1-1-80
1-7-80
Date

Figure 4.9

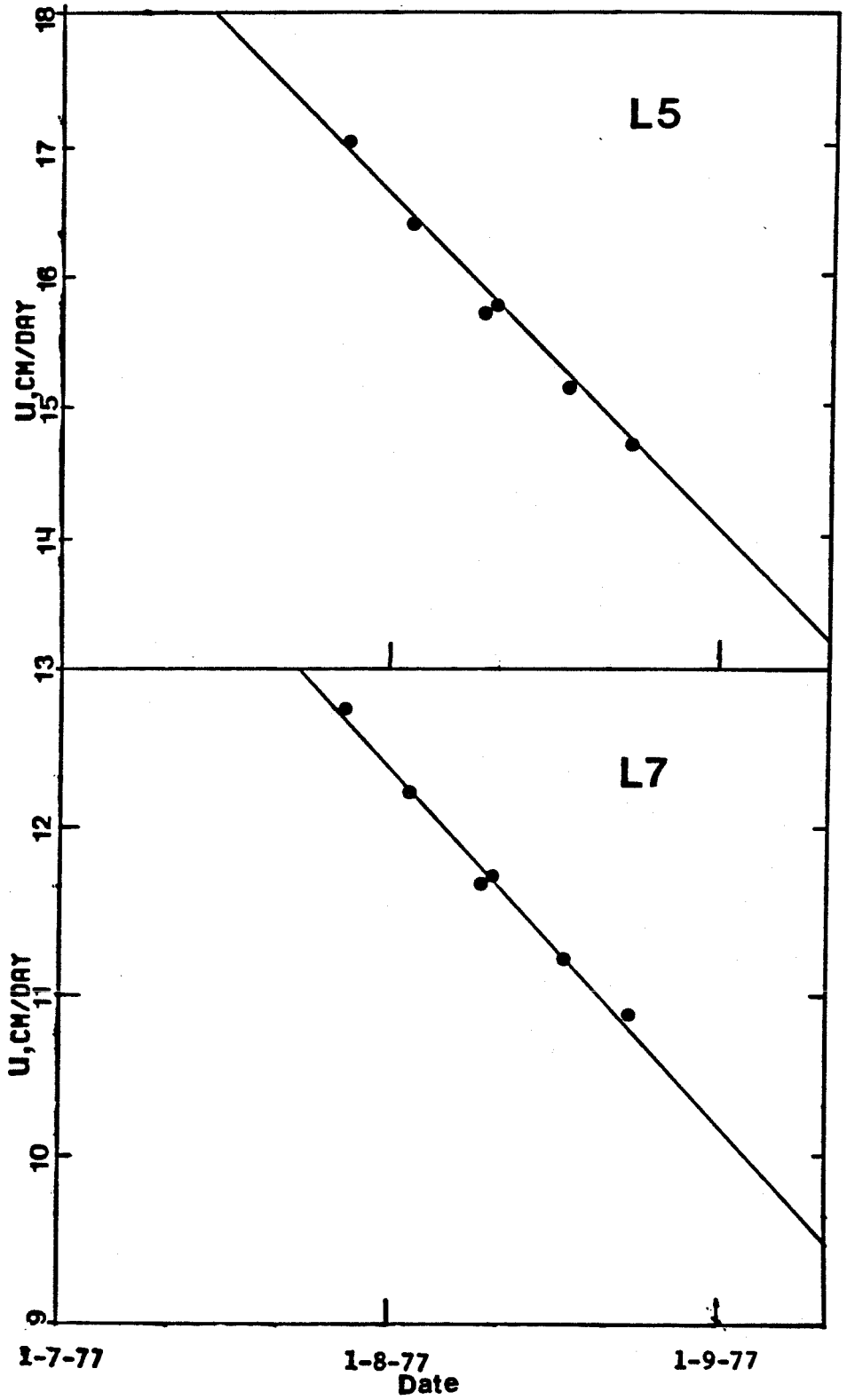
L5
L7
U,CM/DAY
U,CM/DAY
18
17
16
15
14
13
12
11
10
9
1-7-77
1-8-77
1-9-77
Date

Figure 4.10

remove the spatial variation by resetting markers upglacier at yearly intervals, and thus much of the velocity variation displayed in these figures represents temporal variation of the velocity field in the neighborhood of a each location. where ξ is the curvilinear coordinate directed along the central streamline. Certain of the markers whose velocity trends are displayed in Figures 4.3 - 4.10 traveled with the moving ice over the period 1977 - 1980. These markers were not reset to their initial positions onanannual basis, and therefore their motion must be corrected for motion in a longitudinally varying velocity field. The change in velocity due to a non-zero longitudinal strain rate, $\dot{\varepsilon}_{\xi\xi}$, is indicated on the figures corresponding to these markers by a dashed line across the figure. Here ξ is the curvilinear coordinate directed along the central streamline. The temporal variations in the flow of these 'material' markers are then the deviations from this dashed line.

The overall temporal trend shown in Figures 4.3 - 4.10 is a monotonic decrease in u_H, as is defined by values taken over time periods longer then several months (squares and triangles in diagrams). The solid lines in these figures portray this trend in annual velocities. The longitudinal variation of this deceleration is displayed in Figure 4.11. The large circular dots in this figure represent the mean trend over the period 1977-1980 while the smaller upper and lower symbols represent the deceleration during 1977-79 and 1978-80, respectively. There is a more rapid decrease in annual velocities at all points along the centerline during the interval 1977 to 1979 than from 1978 to 1980. The two solid lines of different slope in Figures 4.6a (F3), and 4.7a,b (G3 and H3) show this changing deceleration particularly well. Extrapolation of the trend in annual velocity to intervals prior to 1977-78 indicates that the maximum in velocity over lower Blue Glacier occured before 1977. It is therefore reasonable

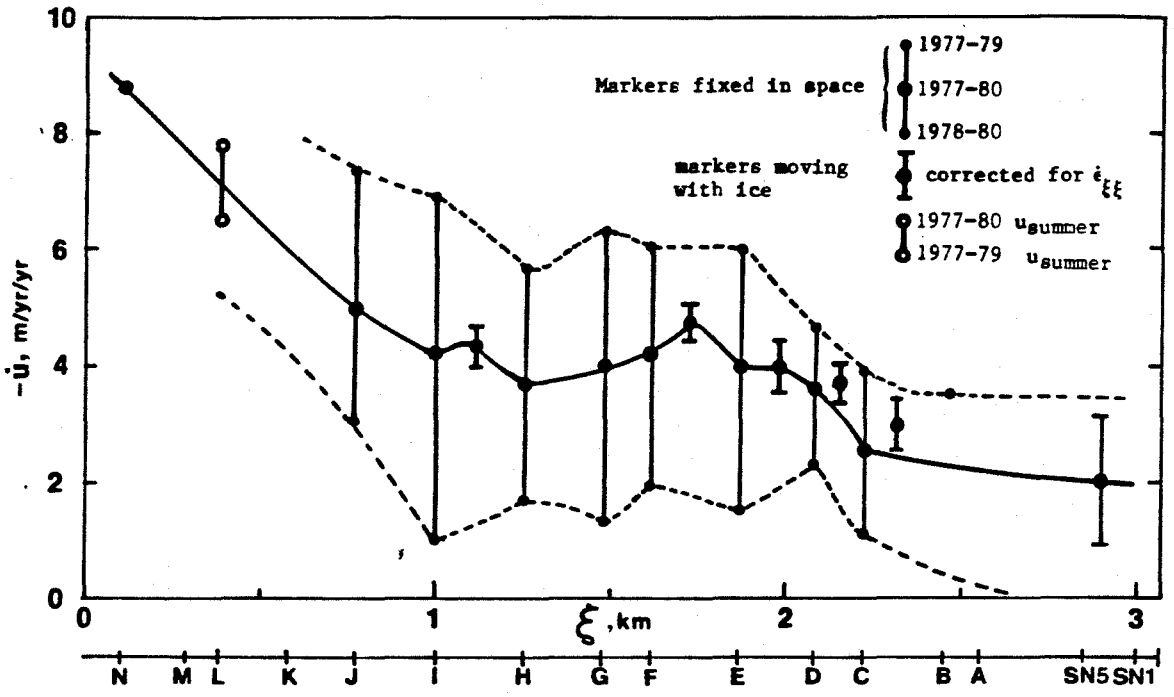

Figure 4.11

Longitudinal profile of deceleration from 1977 to 1980 as determined from decrease in annual velocity along centerline. Markers moving with the ice were corrected for longitudinal velocity gradients.

reasonable to assume that speeds in excess of those described here occurred prior to 1977.Maximum speeds were probably reached sometime in the interval 1972 to 1977 based on data from the 1960's (Harrison, pers. comm.) and borehole casing locations of Kamb (pers. comm.) in 1976. The glacier is now in a general downswing from this maximum.

The greatest deceleration occurred near the base of the icefall, where the flow speed is the greatest. The magnitude of $\dot{u}_H$ roughly follows the magnitude of the surface velocity, as is seen by comparison of Figures 4.1 and 4.11. The rate of flow at the terminus decreased over the 4-year period, while the position of the terminus still continued to advance during the period 1977 to 1980, although at a decreasing rate. This implies that the length of the glacier is not yet in equilibrium with the change in thickness (and thus climate) occurring over the last 20 years. The observed decelerations correlate with a small, spatially varying decrease in ice depth during the same time period (1977-80). This indicates that the flow velocity is dependent upon the ice thickness. A relatively uniform decrease in thickness over the lower glacier would cause a greater relative change in velocity at those locations where the surface is steep and the ice thinner. At these locations the velocity tends to be large, thus explaining the rough similarity between the magnitude of the velocity and the deceleration noted above.

4.4 Short-Term Temporal Variations and Basal Sliding

At very short periods ($\leq$ 30 days, shown as squares in Figures 4.3 - 4.10) there is significant variation in the flow velocity. Similar variation has been observed on other glaciers (for example, Hodge, 1972 and Iken, 1978) and it is believed to be a combination of measurement errors and actual variations in speed. Certain markers exhibit large, irregular flucuations on this time scale, while others show

smooth linear trends in the glacier motion. For example, L6,L7, and L9 (Figure 4.10) show a uniform decrease of about 0.6 - 0.7 %/day throughout July and August of 1977. This trend is found in all members of the L profile which are below the major icefalls (L2-L9), and represents a thinning of the firn (ΔH = 0.05%/day), motion in a compressive stress field, and variations in basal sliding. A similar decrease through the summer season is seen at J4 (Figure 4.9a) during 1977. The more random appearing short-term fluctuations observed at some markers (for example, C1 in Figure 4.3a, D3 in Fig. 4.4a, and F3 and F4 in Fig. 4.6 during the summer of 1978) are a result of errors in tilt and reset measurements, crevasses opening nearby, and small variations in actual motion. The shorter the time interval involved in the velocity average, the greater the scatter in the values (as, for example, in Figure 4.9b (N4), where a large number of very short time period (less than 2 weeks) data are included). This agrees with the results of Hodge (1972). When the same time scales are considered, there is a general increase in scatter between those markers embedded in firn and those in ice. This is a direct consequence of increased tilting of markers which are in the ice over those in firn.

Seasonal fluctuations are displayed in Figures 4.3 - 4.10 as departures from the mean trend in u_H. The shorter-term summer velocities (square symbols) during 1978 and 1979 are generally greater than the annual velocities by as much as 2-10%, as is seen in Figures 4.3b (borehole S1 at the C profile),4.5 (E3 and borehole B), and 4.7b (H3). During 1977 the summer velocities appear to be equal to or slightly less than the corresponding annual velocities, but this is not the case at all points. The increased thickness and input of meltwater in the spring contribute to increased deformational and sliding motion. Comparison of winter and summer velocities is shown in Table 4.1. The wintertime velocities (u_w) were measured during February and March of 1979 over periods ranging

Table 4.1
Seasonal Velocity Fluctuations (cm day^{-1})

	u_w	$\bar{u}_w$	u_{sp}	u_{su}^{78}	u_{su}^{79}	$\Delta(w,su)$
A2	11.8± .9	----	----	(19.8)	(12.8)	11± 6%
B3	12.2± 1.5	11.65± .10	11.98± .17	12.33± .20	12.13± .29	5%
C4	9.5± 2.5	12.43± .08	12.75± .25	14.24± .10	13.18± .11	9%
BHS1	----	11.72± .08	11.62± .10	13.91± .10	12.21± .10	10%
D4	13.3± .5	13.27± .06	13.20± .14	13.91± .08	13.29± .09	2%
E4	14.0-16.5	14.71± .07	15.58± .13	15.93± .20	15.39± .12	6%
F3	----	13.48± .06	14.14± .10	15.44± .08	13.65± .08	7%
G3	13.5± .7	13.10± .05	13.70± .12	15.10± .54	13.24± .40	8%
H3	(10.9± .9)	12.60± .08	----	(14.83)	12.98± .20	9^{+1}_{-2} %
I4	(10.6± 1.)	12.57± .06	12.90± .10	14.92± .26	11.52± .53	5%
J4	(11.6± .6)	13.41± .10	12.90± .25	15.1± .4	13.3± .1	6%
K2	12.7± 1.6	12.89± .07	13.36± .20	14.27± .33	13.3± .16	6%
L4	14.4± 1.1	14.15± .05	14.79± .16	15.78± .16	15.59± .42	10%
N4	17.5± 1.1	(17.15)	18.05± .19	18.93± .11	16.91± .07	4%
					$\overline{\Delta(u_w,u_{su})}$	= 7%

Measurement Periods:

$u_w = u$ (2/14 - 3/2/79) $\quad u_{su}^{78,79} = \bar{u}$ (~ 7 - 9/78,79)
$\bar{u}_w = \bar{u}$ (9/78 - 6/79) $\quad u_{sp} = \bar{u}$ (2 - 6/79)

$\Delta(w,su) = \Delta(\bar{u}_w,\bar{u}_{su})$ values ± 1% unless noted.
Horizontal velocities listed. Values in parentheses are approximate.

from one to three weeks. The average wintertime speed ($\bar{u}_w$) was determined from the motion of each marker over the interval September, 1978 to June,1979, and is more reliable than the mid-winter results because of the longer time interval and better surveying accuracy. Springtime velocities (u_{sp}) were determined over the interval February to June, 1979. The spring velocities are generally greater than the winter averages, which is to be expected due to the enhanced surface snow load. Summer velocities (u_{su}) were taken as the average velocity from June (or July if June data were not available) to early September in 1978 and 1979, with $\bar{u}_{su}$ the average of these two summer values, bracketing the wintertime averaging interval. (The decrease in summer velocities from 1978 to 1979 shows the deceleration described above.) In the last column of Table 4.1 is the percentage increase in velocity from winter to summer as computed from $\bar{u}_w$ and $\bar{u}_{su}$. This increase in velocity is interpreted as an increase in basal sliding speed accompanying the influx of meltwater during the ablation season. The figures in the last column of Table 4.1 indicate that sliding provides at least 2-10% of the total ice motion. Sliding has been observed by Kamb and LaChapelle (1964) in the central icefall, where it was seen to account for 90% of the motion. On the other hand, borehole deformation studies and observations by borehole photography (Shreve and Sharp, 1970; Kamb, 1970; Engelhardt and others, 1978; and Kamb and others, 1979) in the lower glacier indicate a sliding component of 10% or less, in agreement with the winter-summer velocity differences. From a combination of all these studies, it can be stated with reasonable confidence (for a glacier!) that basal sliding contributes at most ~ 10% to the overall motion of lower Blue Glacier. While this appears to be true in the global sense,there may be local regions, such as in the small icefall at the western end of the E profile, and at the terminus where the sliding component is significantly larger (as indicated by the large variations in margi-

nal sliding in these regions).

4.5 Marginal Sliding

Sliding was measured at several points along the western margin of Blue Glacier by Meier et al.(1974). Magnitudes of the marginal sliding were found to be in the range 0 to 15 meters/year, corresponding to approximately 0-30% of the centerline velocity on the related transverse profiles. The largest sliding occurred adjacent to the small icefall on the west side of the glacier between the E and F profiles, while the sliding velocity vanished at a point on the west side between the G and H profiles, adjacent to a steep moraine shieled by a bedrock knob protruding into the the glacier. For the purposes of comparison, marginal sliding at a few points along the western edge of Blue Glacier was measured in 1977 and 1978, using a procedure similar to that described by Meier,et al.(1974). The locations of the points at which the measurements were undertaken are shown in Plate 1. Table 4.2 gives the sliding velocities obtained,together with estimates of error (which was largely caused by inaccuracy in the azimuth measurement). The numbers 77 and 78 in the site specification refer to the years 1977 and 1978 respectively. Site S02-77 was located within a few meters of site S1-78.

Table 4.2
Marginal Sliding Velocity

Site/Year	Veocity(m/yr)	Azimuth	Type Location
S02-77	5.1 ± 0.8	N7E	bedrock knoll
S1-78	3.3 ± 1.1	N12E	bedrock knoll
S2-78	12.7 ± 1.2	N29E	bedrock protrusion,crevassed
S1-77	1.8 ± 1.8	N	moraine
S2-77	6.4 ± 0.5	N24W	steep bedrock,crevassed

The marginal slip rates determined in the present study are comparable with those found by M1. It does not appear that there is any substantial increase in the slip rate corresponding to an increase in the centerline velocities, but an exact comparison is not possible due to the inherent errors in the data and differences in location. Time variation in marginal slip rate seems to be indicated by the results at S02 in 1977 and 1978, which represent measurements made in similar but not exactly the same locations. Such a time variation was found by Glen and Lewis (1961).

As stated by M1 the extrapolation of these results to basal sliding is only applicable in the sense that large spatial variations in basal sliding are probable. The magnitude of the actual basal sliding cannot be inferred from this, but the independent indication of low basal sliding velocities from other measurements (see the previous section) is compatible with the generally low marginal sliding velocities observed. Such spatial variation in local basal sliding was found by Englehardt and Kamb (1978) on Blue Glacier and Raymond (1971) on Athabaska Glacier. It may be concluded that the marginal sliding varies between 0 and 10% of the centerline velocity on Blue Glacier (except in the regions of high relief, such as the small icefall, where it may approach 30% of the centerline motion).

4.6 Summary

The results of this chapter provide a detailed description of the velocity field of lower Blue Glacier, extending from the base of the ice-falls to the terminus. Patterns in the flow show that channel shape and curvature, a laterally convex or concave upper surface, and the surface slope as averaged over an appropriate length scale have significant effects on ice deformation. Chapters VII and IX will provide models of ice flow within the realistic geometry of this glacier, which, when compared with the observed flow patterns, will enable the effects of these

various factors to be isolated. Comparison of these models with the observed flow will also allow an estimation of flow law parameters. The conclusion that basal sliding accounts for at most ~ 10% of the total motion of this glacier will be invaluable to the numerical calculations of flow, as well as being extremely important in the analysis of the response to the observed change in surface configuration.

CHAPTER V

CHANGES IN ICE THICKNESS, SURFACE SLOPE, AND VELOCITY

The data described in the previous chapters and those given by Meier, et al. (1974) provide a basis from which changes in ice thickness, surface slope, and surface velocity over the 20 year period 1958-1978 can be determined. These observed changes will then allow a description of the response of the flow field of Blue Glacier to changes in geometry and an estimation of the flow law parameters and the relations which govern this response. It is the purpose of this chapter to provide a quantitative measure of the geometrical changes and of the resulting perturbation in the surface flow-field, as well as the necessary error analysis of this critical data set.

Velocity perturbations of up to 50% and thickness changes of up to 20% were observed on Blue Glacier. A consistent and meaningful measure of the changes in field quantities must be chosen,taking the relatively large magnitude of these quantities into account. This chapter begins with a simple model of flow response to a thickness and slope change, as a means of developing a framework for discussing the various observed changes in a consistent manner.

5.1 Flow Response to a Change of Thickness and Surface Slope in a Long Slab

Consider the slow creeping flow of a slab of a viscous medium down an inclined slope. The slope is inclined at an angle α to the horizontal, and the upper surface of the slab is initially assumed to be parallel to the slope. Let (x,y) be coordinates in a Cartesian system with the x axis directed downward along the slope and y normal to x, directed upward (see Figure 5.1). Assume the medium extends a very large distance in the x-direction, has a thickness H normal to the surface, and is of infinite extent out of the xy-plane. Then the flow may be assumed to take place in the xy-plane only and there will be no

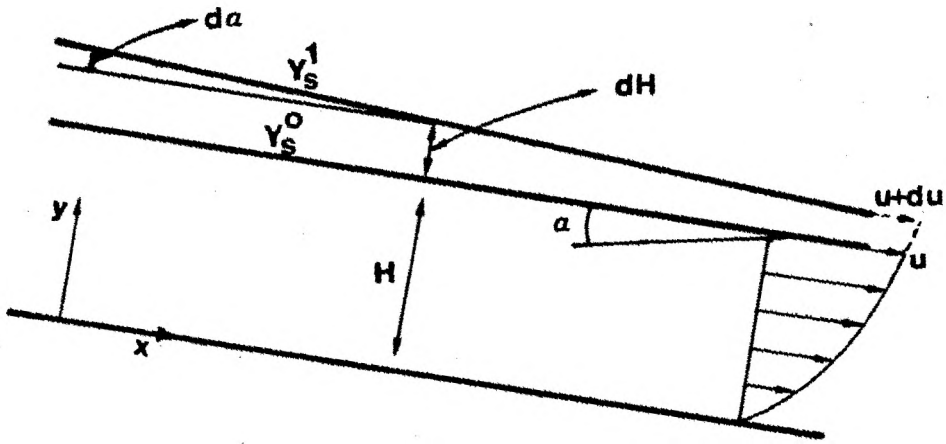

Figure 5.1 Geometry and notation for thickness change in a region of a nearly-parallel-sided slab.

gradients in the x direction. Assume the material obeys a nonlinear constitutive relation described by a power law:

$$\dot{\varepsilon}_{ij} = \frac{1}{2\eta_f} J_{II}^{(n-1)/2} \tau'_{ij} \tag{5.1}$$

where $\dot{\varepsilon}$ is the rate of deformation, τ' the deviatoric stress, J_{II} the second invariant of the deviatoric stress tensor ($J_{II} = \frac{1}{2}\tau'_{ij}\tau'_{ij}$), and n, η_f are the stress exponent and a temperature-dependent viscosity factor, respectively. For velocity components u_i the deformation-rate tensor is given by

$$\dot{\varepsilon}_{ij} = \frac{1}{2}\left(\frac{\partial u_i}{\partial x_j} + \frac{\partial u_j}{\partial x_i} \right). \tag{5.2}$$

With the boundary condition on the upper surface that the normal stress is equal to atmospheric pressure (taken to be zero)and zero shear traction and the condition on the lower surface that $\mathbf{u} = (u_B, 0, 0)$, where u_B is the prescribed sliding velocity, solution of the governing equilibrium equations yields the following relation for the surface velocity u_s (Nye,1952):

$$u_s - u_B = \frac{1}{\eta_f(n+1)} \left(\rho g \sin\alpha \right)^n H^{n+1}. \tag{5.3}$$

In this equation, ρ is the density of the ice and g the acceleration of gravity.

Suppose now that, over a small region of the slab, there is a small increase in ice thickness and a change in the surface slope, given by dH and d(sinα), respectively, and assume further that the basal sliding remains constant. Then the resulting change in surface velocity, du_s is given by

$$du_s = (n+1)u_s \frac{dH}{H} + nu_s \frac{d(\sin\alpha)}{\sin\alpha}. \tag{5.4}$$

This equation is the desired result for an infinitesimal change in thickness and surface slope. For small relative changes in these parameters the corresponding change in the surface velocity is seen to depend simply on the fractional ice-

depth change $\frac{dH}{H}$ and fractional slope change $\frac{d\alpha}{\alpha}$ and on the power law exponent n.

If there exists a finite change in the parameters over a time interval from t_o to t_1 then a possible measure of the corresponding velocity change may be given by the finite difference approximation to (5.4) at t_o

$$\frac{u_s^1 - u_s^o}{u_s^o} = (n + 1)\,\frac{H^1 - H^o}{H^o} + n\,\frac{\sin\alpha^1 - \sin\alpha^o}{\sin\alpha^o}. \tag{5.5}$$

where $u_s^1 = u_s(t_1), u_s^o = u_s(t_o)$, etc. However, the equivalent expression at t_1

$$\frac{u_s^1 - u_s^o}{u_s^1} = (n + 1)\,\frac{H^1 - H^o}{H^1} + n\,\frac{\sin\alpha^1 - \sin\alpha^o}{\sin\alpha^1}. \tag{5.6}$$

is also a measure of the relative velocity change. For large changes in either ice thickness or slope (or both) there exists an ambiguity in choosing a relation for the velocity increase, (5.5) or (5.6), and, if the results are used to determine a value of the stress exponent, widely varying values will be obtained for the same initial data set.

The proper treatment of a finite amplitude perturbation in the slab geometry is to consider an integration of infinitesimal contributions over the time period in question. Thus (assuming negligible basal sliding)

$$\int_{u_o(t_o)}^{u_s(t_1)} \frac{du_s}{u_s} = n \int_{\sin\alpha(t_o)}^{\sin\alpha(t_1)} \frac{d(\sin\alpha)}{\sin\alpha} + (n + 1) \int_{H(t_o)}^{H(t_1)} \frac{dH}{H},$$

which leads to

$$\log\left[\frac{u_s^1}{u_s^o}\right] = n \log\left[\frac{\sin\alpha^1}{\sin\alpha^o}\right] + (n + 1) \log\left[\frac{H^1}{H^o}\right]. \tag{5.7}$$

The resulting equation is applicable to changes of any magnitude in H and α. It is thus seen that the desired form of the measure of a geometrical or velocity change is that of a logarithmic difference. If, as developed later, the thickness

and surface slope determining the flow are averages over some length scale l, denoted $<\alpha>_l$ and $<H>_l$, then the logarithmic change in this mean slope and thickness enter into the expression for the velocity perturbation.

The above result has been derived for an oversimplified model of a glacier. As a first step in making a more realistic model, consider the rectilinear flow of a non-linear fluid in an inclined channel of parabolic or semicircular cross section. Analytical results discussed in Chapter IX show that it is the logarithmic difference in thickness and surface slope which are again the relevant parameters, and that the relation between geometrical changes and velocity response takes the form

$$\log\left[\frac{u_s^1}{u_s^o}\right] = \Psi\,(n+1)\log\left[\frac{<H^1>_l}{<H^o>_l}\right] + n\log\left[\frac{<\sin\alpha^1>_l}{<\sin\alpha^o>_l}\right], \qquad (5.8)$$

where Ψ is a correction factor, which is introduced because of changes in the channel geometry with changing thickness. Ψ will be termed the response factor. This factor is generally less than one, implying a deamplification of the velocity response in comparison to the infinite-slab model.

Equation (5.8) shows that if $\frac{<\alpha^1>_l}{<\alpha^o>_l}$ is effectively constant over the region studied, and if the local thickness governs the flow, then a plot of the velocity response to a change in thickness will plot as a straight line in $\left(\log\left[\frac{u_s^1}{u_s^o}\right], \log\left[\frac{H^1}{H^o}\right]\right)$ space with a slope of $\Psi(n+1)$ and a non-zero intercept of $n\log\left[\frac{<\sin\alpha^1>_L}{<\sin\alpha^o>_L}\right]$ on the abscissa. This will, of course, only hold true if the factor Ψ remains constant within the given data set, which is not the case if the channel geometry varies considerably over the reach studied or if the data set contains values obtained from points well removed from the centerline of the channel, as shown in later chapters. If, on the other hand, the surface slope

change varies significantly over the region studied, then a multivariate regression in the three dimensional space $(\log [\frac{H^1}{H^o}], \log [\frac{\sin\alpha^1}{\sin\alpha^o}], \log [\frac{u_s^1}{u_s^o}])$ will be required to define a relation of the form (5.8).

The errors in the parameters $\log [\frac{u_s^1}{u_s^o}]$, $\log [\frac{\sin\alpha^1}{\sin\alpha^o}]$, and $\log [\frac{H^1}{H^o}]$ are important in discussing the validity of any regression on the data sets. Using the relation (2.10), the standard error in the general function $f(x,y) = \log(x/y)$ is given by

$$\sigma_f = [(\frac{\sigma_x}{x})^2 + (\frac{\sigma_y}{y})^2]^{\frac{1}{2}} \qquad (5.9)$$

where σ_x, σ_y are the standard errors in the variables x, y respectively.

5.2 Comparison of 1957-59 and 1977-80 Data Sets

The remainder of this chapter is devoted to an examination of the field data with expressions (5.8) and (5.9) in mind. All data sets (α,H,u_s) from the different years are used to enable as many comparisons between the late 1950's and the more recent years as possible. However, since the 1957-59 study was limited to the lowermost section of the glacier, extending from the 1 profile down glacier to the B profile, the comparisons over the twenty year period are confined to this region.

Measurements on approximately 48 stakes can be used in comparisons between 1957-58 and 1977-78, representing the eight profiles from B to I. The markers were left in position by M1 after their survey in August, 1958, and resurveyed in August 1959, after moving approximately 100 m down-glacier from their original 1957 locations. This provided two years of velocity data, but the velocities in the second year represent averages over spatial intervals displaced about 50m downglacier from those used in the first year. On the other hand,

only a small number (8) of stakes were left in position at the close of the 1978 field study, and thus only a small number of comparisons are available between 1958-59 and 1978-79 glacier configurations. However, another set of 8 stakes were reset to approximately the same position as they occupied in the summer of 1977 (i.e. approximately 60 m upglacier from their position at the end of the 1978 survey). These markers thus allow additional comparisons of 1978-79 data with the 1957-58 data along the centerline where these stakes were located. Four of these stakes were followed until August, 1980, providing an additional set of comparisons between 1979-80 and 1958-59.

5.3 The Variation of Surface Slope

The data of the latter part of Chapter III show that the surface slope decreased from the year 1957 until 1977. The plots of surface slope across each transverse profile shown in Figure 3.8 indicate a relatively consistent difference between the 1957 values and those measured in 1977 at the same averaging scale. The results shown in Tables 3.2 and 3.3 indicate that there was a general decrease in the surface slope as measured on any of the length scales described. In addition, the longitudinal profile of thickening shown in Figure 5.2 portrays a gradual decrease in the magnitude of the thickening from the terminus region near profile B upglacier to the I profile, which represents a decrease in overall surface slope.

The slope change as determined over the short averaging scale (about one ice thickness) shows large fluctuations over the glacier surface. These spatial fluctuations appear to be random, having a distribution similar to that described in Chapter III for the variation of $<\alpha>_s$ about $<\alpha>_m$.

Table 5.1 shows the logarithmic difference between the sines of the surface slopes resulting from the medium scale averaging in 1957-58 and 1977-78.

There is a significant variation in $\Delta\alpha$ across each profile at this scale, although the variation is much less than for the shorter-scale average.[1] The steeper slopes generally appear to have changed the least over this time period, not only in fractional amount but also in the absolute magnitude of the change. At a few locations the 1977-78 slope is actually greater than the 1957-58 value, particularly at the D profile where the surface is relatively steep . Similar variations in $\Delta<\alpha>_m$ are found in the data sets for different annual comparisons. It is noteworthy that the spatial fluctuations in $\Delta\alpha$ at this medium scale are much larger than those found in the local thickness changes described in the next section. The mean slope change at this scale is

$$\log\left\{\frac{\sin<\alpha>_m^{77-78}}{\sin<\alpha>_m^{57-58}}\right\}\times 100 = -6.2$$

with a standard deviation of 7.3 over a total of 44 points. This mean change is close to the large scale value quoted below, being well within the range of error attributed to this large scale value.

The change in the overall slope ($<\sin\alpha>_L$) was determined along the centerline of the glacier. The large scale changes at profiles more centrally located in the region of study have an estimated error of 1.8 in the logarithmic ratio (due to an error of 0.08° in α).

Table 5.2 lists these large scale slope changes for the different yearly combinations. The longitudinal variation is reduced from that at shorter averaging scales. The overall slope decrease from B to I ($\Delta<\alpha>_L^{B-I}$) was about 5%.

Given the decrease of $\approx 5\%$ in the large scale surface slope, equation (5.8) predicts a negative intercept in a plot of the velocity change versus thickness perturbation if $<\alpha>_L$ is the pertinent averaging scale for the slope. For a power

1. The notation Δf where f = u, H, or $<\sin\alpha>$, will be used to indicate the logarithmic change in the variable (× 100) (i.e. $\Delta u = \log(u^1/u^0)\times 100$) in this section and in later chapters.

law exponent of 3 to 5, the planar slab model predicts a logarithmic reduction in velocity $(\log(u_1/u_o))x100$ of 15 to 25 with no change in thickness. As will be seen below, the results from Blue Glacier agree qualitatively with this expectation. A negative intercept is found, indicating the effect of an overall slope decrease superimposed upon the local thickness changes.

5.4 Temporal Variation in Ice Thickness

Through the use of the position surveys of the numerous surface markers described in Chapter II, the elevation of the surface of Blue Glacier can be evaluated at a given point in time. Comparison of this data set with that obtained by Meier, et al. (1974) will then lead to an estimate of the change in surface elevation, and therefore of a change in ice thickness (assuming a negligible bed erosion over the twenty-year period). The ice depths determined by the radio echo survey discussed in Chapter III then allow a relative thickness change to be evaluated pointwise at the spatial positions of the surface markers. The comparisons must be made at fixed spatial points even though the positions of the actual markers differ in different years.

The (x,y) coordinates of the points as surveyed on a given date in 1957,1958, or 1959 are taken as the coordinates of the fixed points at which the comparisons were made. These data were provided by M. Meier (personal comm.). The vertical coordinate of each marker was taken to be the elevation of the top of the marker pole. (Specification of the point to which the coordinates tabulated by Meier apply was not given, although the actual field data, consisting of horizontal and vertical angles presumably turned to the top of the stake, yields the tabulated coordinates in several cases, implying that these are indeed the coordinates of the top of the stake.) Additional ablation and resetting data (from Meier, personal comm.) were used to obtain an estimate of the height of the

poles on a given date. Together these data yield values of the surface elevation at particular points in space and time.

The markers in the surveys of 1977-80 were initially emplaced as precisely as possible at assigned points, using the methods described earlier. These assigned points were not the same as those of the 1957 survey; rather, they were points whose location was a projection of the 1957 coordinates up-glacier along a streamline. The distance of projection was such that the midpoint of the interval swept out by the anticipated annual motion of the stake would be expected to correspond to the midpoint of the 1957-58 interval, which was of different length. As a result, the positions of the 1977 stakes were approximately 5-15 m up-streamline of those surveyed in August, 1957. Additional differences in location arose because of errors in positioning by the alidade resection method. For the most part, however, there was an excellent agreement between the mean position in 1957-58 and 1977-78. To obtain a difference in ice thickness at this midpoint, the elevations at the initial 1957 points were compared with the elevation at those same points in 1977, and similarly, a comparison was made at the final positions in 1958 with the 1978 surface. The mean of these two elevation differences (1957-77 and 1958-78) was then taken to represent the change in elevation at the midpoint of the motion interval.(Similar calculations were made for the other years of comparison mentioned above.)

The difference in location of the markers on the glacier surface (5-15m) can cause significant differences in elevation (up to 1-2 m). Thus, each surface elevation as determined in the 1977-80 surveys was corrected to the position of the 1957-59 markers, which was taken to be the fixed point for comparison between surface elevations in 1957-59 and in 1977-80. If the horizontal vector describing the difference in 1977 and 1957 (for example) marker locations is denoted $\delta \mathbf{r}$, $\hat{\mathbf{e}}_\alpha$ a horizontal unit vector tangent to the local flow streamline (as determined by

the flow azimuth φ), and α the local surface slope in the direction of $\hat{\mathbf{e}}_\alpha$, then the corrected surface elevation at the 1957 position in 1977, Z_s^{77}, is given by

$$Z_s^{77} = Z_p - H_p - (\delta\mathbf{r} \cdot \hat{\mathbf{e}}_\alpha) \tan\alpha \,. \tag{5.10}$$

In this equation, Z_p is the elevation of the top of the stake and H_p is the height of the pole above the surface, as obtained from the measured height on the survey date corrected by an ablation term to the date of the comparison. A source of error in this procedure is the possibility of an improper local slope estimate (α), but this is small. The mean of $|\delta\mathbf{r}|$ was 9.8 m, with 90% of the markers in the 1977 data set being less than 15 m from the 1957 location, and the mean of $|\delta\mathbf{r}|$ was 6.5 m for the 1978 and 1958 sets. (The difference between $|\overline{\delta\mathbf{r}}^{77}|$ and $|\overline{\delta\mathbf{r}}^{78}|$ is a reflection of the fact that the *a priori* estimated value of the velocity increase (30-40%) was too large. This caused the 1978 markers to be closer to the 1958 positions than the 1977 were to the 1957 positions.) The mean value of the resulting correction in Z_s was approximately 0.80 m.

The corrected 1977-80 surface elevations were then differenced with the appropriate 1957-59 values to obtain the change in ice thickness at each fixed point. Thickness changes thus measured at the initial and final points of each motion interval differed by up to 2 m. It is felt that the mean thickness change, obtained by averaging the initial and final elevation differences, is the thickness change appropriate to the midpoint of the interval, at which the velocity measurement applies. The increase in elevation between 1958 and 1978 was generally larger than between 1957 and 1977, which is an indication of the relative net balances of these years.

The logarithmic difference in ice depth was calculated using the mean elevation change, $\overline{\Delta Z_s}$, and the ice thickness as measured in 1978-79 by the relation

$$\log\left[\frac{H^1}{H^o}\right] = -\log\left[1 - \frac{\overline{\Delta Z_s}}{H}\right], \tag{5.11}$$

where H refers to the measured ice thickness in 1978 and the superscripts o and 1 refer to the years 1957-59 and 1977-80, respectively.

The standard error in the quantity $\log(H^1/H^o)$ is given by

$$\sigma\left[\log\left(\frac{H^1}{H^o}\right)\right] = \frac{1}{H-\Delta Z_s}\left[\left(\frac{\overline{\Delta Z_s}}{H}\right)^2 \sigma_H^2 + \sigma^2_{\overline{\Delta Z_s}}\right]^{1/2}. \tag{5.12}$$

The error in the depth determination (σ_H) is approximately 5 meters. Suppose there is an error of 0.1 m in the 1957, 1958, and 1959 vertical coordinates and an error of 0.25 m in the surface elevations of 1977-80 (this error is larger because of the errors in the various quantities in the correction (5.10)). This leads to a standard error in the measurement of $\overline{\Delta Z_s}$ equal to 0.26 m. The resulting standard error given by (5.12) is

$$\sigma\left[\log\left(\frac{H'}{H^o}\right) \times 100\right] \approx 0.25 \quad ,$$

where a typical depth of 200 m and a change in ice depth of 15 m has been assumed.

The results of this determination of ice-depth changes are given in Table 5.3. Figure 5.2 shows the distribution of the absolute magnitude of the thickness increase as a function of the distance along the centerline, ξ_o, from the I profile down glacier to the B profile. Both the centerline and transversely averaged values are plotted. The general trend is an increase in the magnitude of the thickening as the terminus is approached. This trend gives rise to the overall decrease in surface slope, as described in the previous section. The increase in ice depth near the terminus has doubtless led to the recent advance of the terminal lobe as measured by Kamb (pers. comm.) and the author, and as described by Spicer (unpub.).

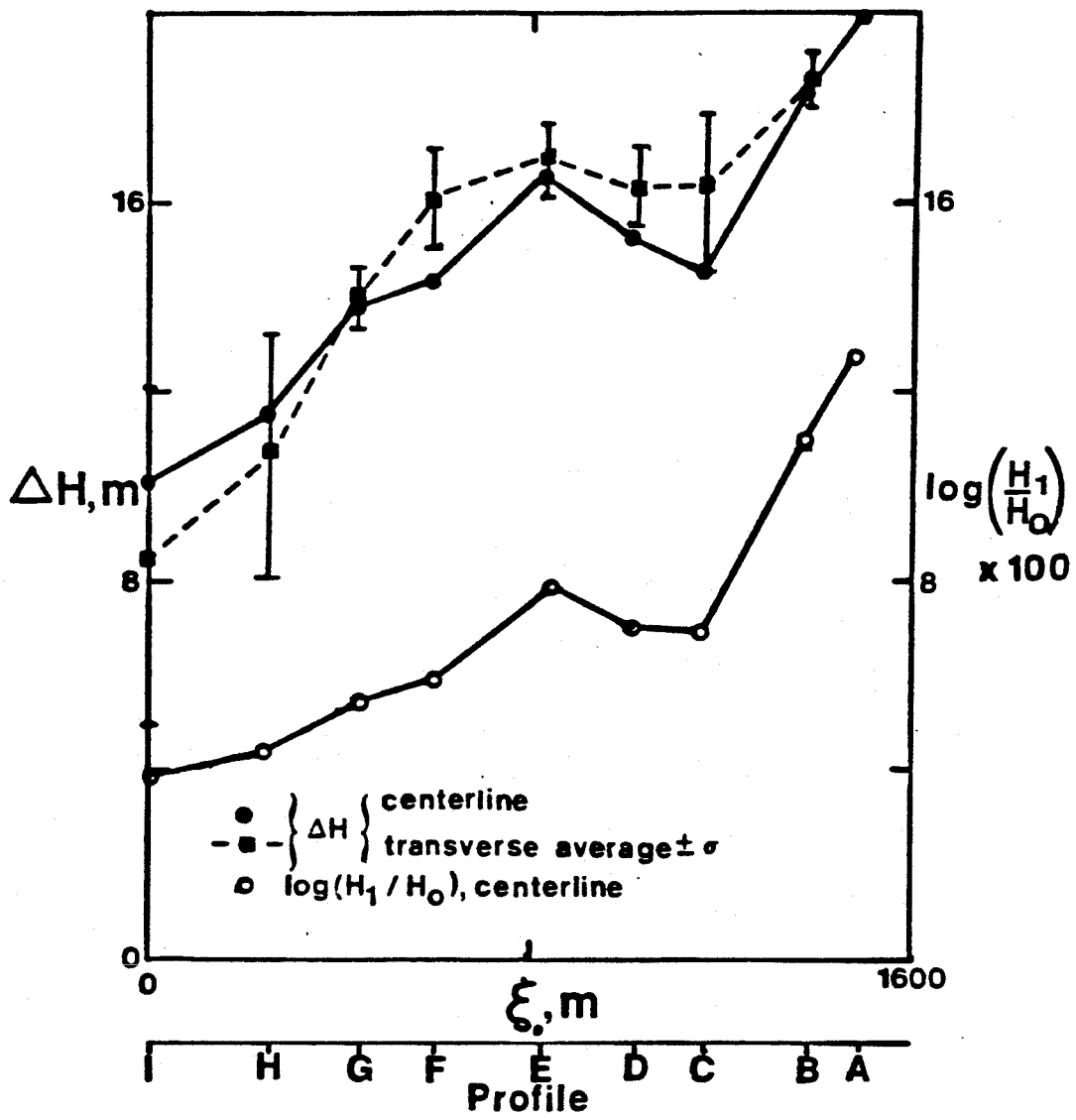

Figure 5.2 Thickness change (1957/58 to 1977/78) along the centerline of the glacier from profile I to A. Both the absolute change (ΔH, in meters) and the logarithmic increase $\{\log(H_1/H_0) \times 100\}$ are shown. The dashed line shows the transverse average of ΔH at each profile.

It is also of interest to note the relation between the centerline thickening and the transversely-averaged thickening. The tendency for the average across the profile to be slightly larger than the centerline value is directly related to the variation of the thickness change across the profiles as seen in Figure 5.3. The marginal thickness changes appear to be generally larger than these along the centerline. This effect is further enhanced when the logarithmic increase is viewed, as in the upper curves of Figure 5.3. This enhancement is due to the decreased depth in marginal locations, leading to a larger relative change. The marginal increase in the absolute magnitude of the thickening is a more puzzling feature for which no explanation is as yet evident.

If the trend toward a decrease in the magnitude of the ice-depth change up-glacier continues upward beyond the I profile at a similar rate, then the value of ΔZ_s would go to zero approximately at a point opposite Jelly Bar (TP 8). A comparison of the surface elevations obtained from the L and N profiles with unpublished data of Harrison (pers. comm.) in the early 1960's does, in fact, show a decrease in surface elevation of 2-4 m at L and 4-7 m at N between 1957 and 1977-78.

The trend for an increase in the magnitude of thickening as the terminus is approached may be a manifestation of the "whiplash" effect described by Nye (1960, 1963a) for the response of the terminal region of a glacier subjected to an overall increase in accumulation. This effect is manifested as an increase in ice thickness near the terminus which is much larger than that found at any point up-glacier, and it is the result of the longitudinal compression found in the ablation region of a glacier. If the glacier does respond to a change in net balance in a way prescribed by a linearized kinematic wave theory (Nye, 1960, 1963a,b) or by the more detailed mechanism described by Hutter (1980) and Fowler and Larson (1981), then the observed longitudinal pattern of thickening

may indicate a relatively large increase in accumulation in the cirque region above the icefalls, the resulting increase in thickness having propagated down glacier as a traveling kinematic wave.

5.5 Temporal Variation in Surface Velocity

The proximity of the midpoints of the motion intervals between annual surveys in the 1950's and those of the late 70's allows straightforward comparison of the velocities measured at the two sets of markers. The errors resulting from the small differences in location within the velocity field are essentially negligible for almost all stakes, due to the relatively small longitudinal and transverse velocity gradients in the region studied. Although the lateral gradients are generally larger than the longitudinal ones, the error in the transverse location of the markers relative to a given streamline (as determined by the 1957-58 velocity field) is usually quite small. Thus it was felt that the errors in the measurement of the surface velocities themselves overshadowed the positional errors.

Horizontal surface velocities [$u = u_h = (u_1^2 + u_2^2)^{1/2}$] as measured by M1 (listed in their Table 1) are compared with those annual horizontal velocity measurements made at corresponding points over an equivalent time period in the years 1977-80. The begining of the measurement interval was mid-August of the first year to mid-August of the following year. In some cases the azimuth of the tangent to the streamline at the midpoint was not constant from the earlier results to the later ones, but the difference was generally small. In addition, the vertical component of velocity was generally small, did not show a large temporal variation, and was subject to more error than the horizontal components. For these reasons the magnitude of the horizontal velocity, u, was compared rather than the individual components u_1, u_2, and u_3.

The error in the quantity $\log(u^1/u^0)$ varies with location and the magnitude

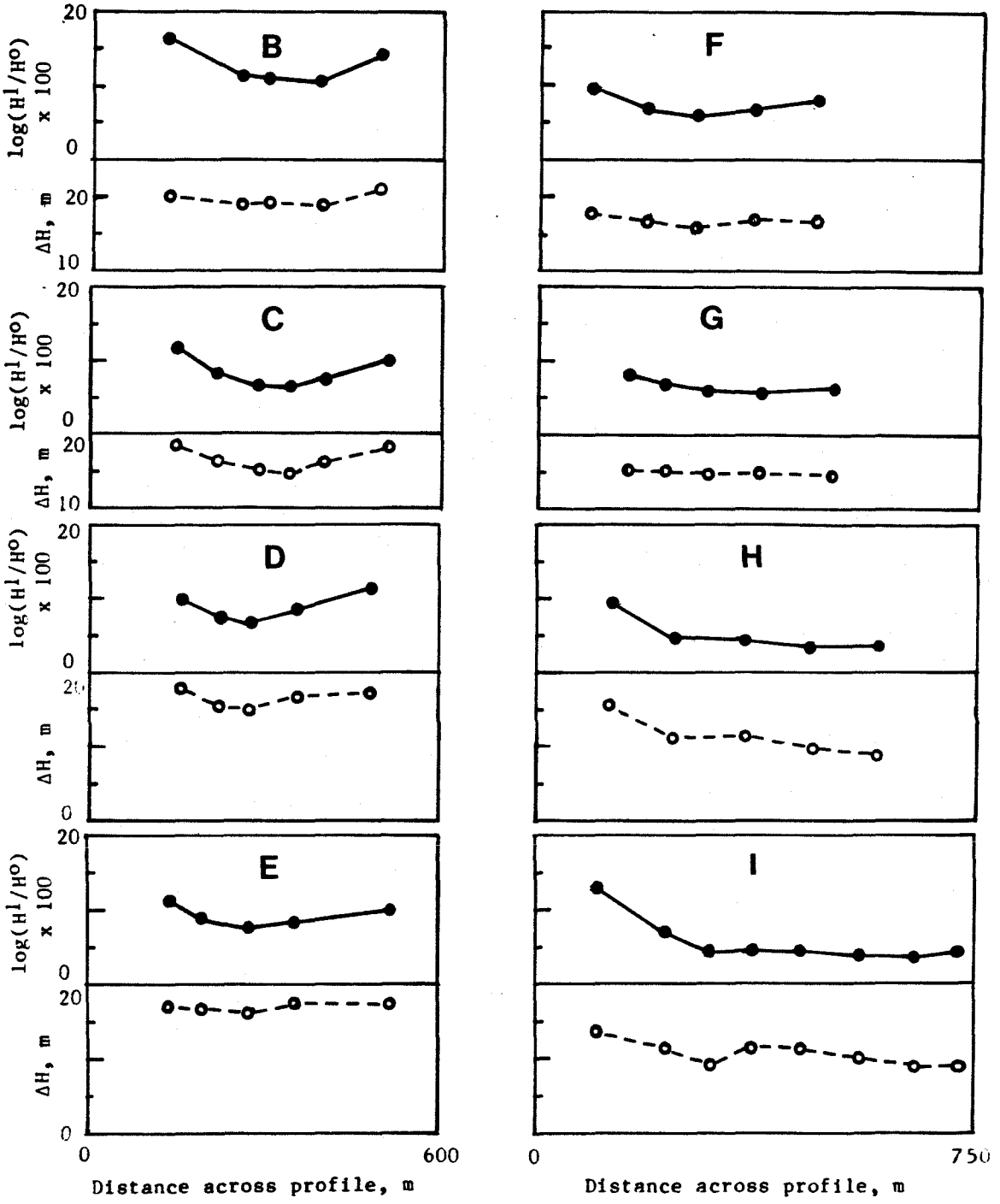

Figure 5.3 Mean thickness change and logarithmic difference in depth across transverse profiles, 1957/58 to 1977/78

of the velocity, as shown by (5.12). As an estimate of the error, the mean relative errors in the two velocity data sets may be combined. The mean relative error in the 1957-58 data is 0.88% while that in the 1977-78 set is 0.5%, giving a mean error in the logarithmic difference (× 100) of 1.0. Unless otherwise stated, this value for the error in $\log(u^1/u^0)$ will be assumed.

The results of the velocity comparison over the twenty year period are listed in Table 5.4. Figure 5.4 shows the longitudinal variation of the change in center-line velocity values and in transverse averages. The correlation with the ice-depth changes is apparent, although the break in the depth-variation trend at the D and E lines is not as strongly reflected in the velocity data, perhaps because of the effect of changes in surface slope in this steeper region. The variation of the velocity perturbation is much stronger than that of the depth change, as is expected from the relation (5.8). If the velocity trend can be continued upglacier, then a vanishing velocity change might be expected near the J profile and a reduction in velocity might occur at points above this line if the overall slope change remains in effect. Data of Harrison (unpublished) allow a semi-quantitative estimate of the velocity change in the region of the L and N profiles to be made. These data do show a decrease in the surface velocity from 1960-61 to 1977 in this region. The value of the quantity $(\log(u^1/u^0)\times 100$ lies in the range -12 to +4 for several of the L stakes and -5 to -8 across the N line. A large error (± 3) must be assigned to these values because the velocities required for the comparison are interpolated over a region of large longitudinal gradients. Even with these errors, a larger decrease in velocity might be expected in this area if both the overall slope change and the decrease in surface elevation noted in the earlier section were in effect. It may be that the large-scale surface-slope change applicable to the lower profiles does not apply in this region, which lies directly below a major (and quite steep) icefall. This

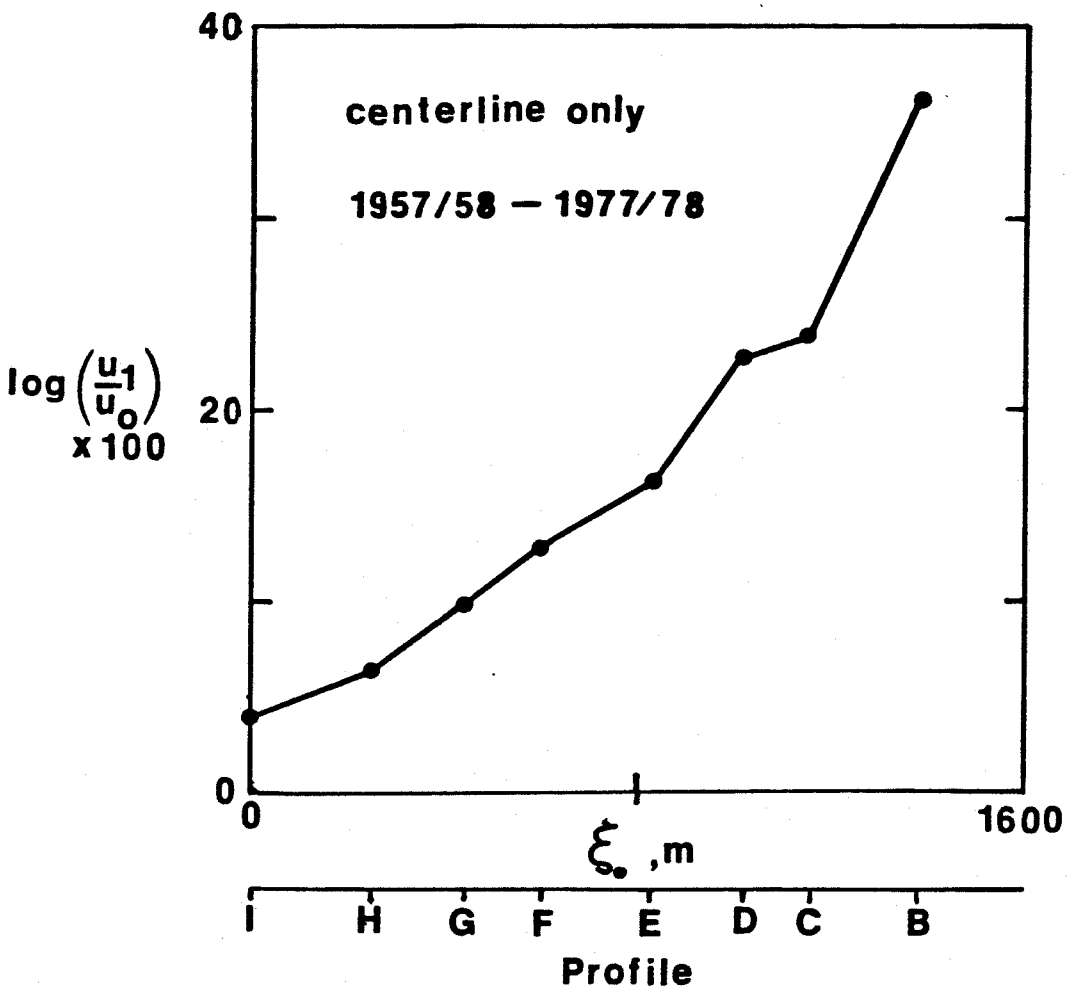

Figure 5.4 Longitudinal variation in velocity change (1957/58 to 1977/78) along centerline from profile I to B.

proximity to a zone of longitudinal compression may severely affect the slope-averaging processes, as described in the following chapter, and thus may alter the response characteristics in this area.

The lateral variation in the velocity perturbation shows trends similar to those observed in the ice-depth changes, as can be seen in Table 5.4. Larger variations were generally measured away from the centerline. Unfortunately, the twenty year comparison could not be made at points near the margins (such as C00, C8, H7, etc.) due to the lack of measurements at these points in the earlier surveys.

5.6 Comparison of Surface Velocity Changes with Thickness and Slope Variations

The relation (5.8) shows that the logarithmic velocity perturbation along the centerline of a glacier should be linearly related to logarithmic changes in thickness and an appropriately averaged slope if the channel geometry remains constant along the longitudinal axis of the glacier. Based on this linear dependence, which should remain approximately true for small downglacier changes in channel geometry, a multiple linear regression analysis of the dependence of the variance of the velocity change on the observed surface slope and ice depth changes was performed. Standard techniques were used (Seber, 1977).

Two statistical parameters may be used to measure the degree of correlation between the variables. The first is the F-statistic, which is a measure of the relative significance of an independent variable (a regressor) in explaining the variance of the dependent or response variable. The F-test for the addition of another regressor (x_j) into a model for a response variable y (as in (5.13) below) is a measure of how much the additional term improves the value of χ^2 (or, equivalently for unweighted data, the variance) for the fit of the model $y(x_i)$ to the data y_{obs}, i.e.

$$F \sim \frac{\chi^2(\text{n}-1 \text{ regressors}) - \chi^2(\text{n regressors})}{\chi^2(\text{n regressors})/N}$$

where $\chi^2 \sim \Sigma(y_{obs} - y(x_i))^2$ and N is the number of degrees of freedom. If the fit of the model to the data is improved by the addition of x_j, then χ^2 is reduced and the F-statistic is large. An F-level may be chosen such that, for a given probability (eg. P=0.01), if the F-statistic for this regressor is less than this level, then the coefficient β_j of this variable in (5.13) is probably zero (the null hypothesis). Such a value of the F-statistic may occur with a probability P in a random sample. On the other hand, if the F-statistic is higher than this level, then the null hypothesis may be rejected with some certainty, and, thus, one can be fairly confident that $\beta_j \neq 0$ and that the regressor is probably important in describing the behaviour of the response variable.

Given those variables which show a significantly high F-statistic, a multiple correlation coefficient, R, may be determined from the least squares fit of the data to a model of the form

$$y = \beta_o + \beta_1 x_1 + \beta_2 x_2 + \cdots \tag{5.13}$$

where y is the response variable, the x_i are the regressors, and the β_i are constant coefficients. The multiple correlation coefficient characterizes the fit of the data to the *entire* functional form (5.13), taking into account the simultaneous dependence of y on the x_i. The statistical distribution of R is equivalent to that of a linear correlation coefficient in one variable, if proper account is taken of the degrees of freedom. Using this distribution, the degree of significance of the estimated correlation between the velocity perturbation and the observed changes in thickness and slope (averaged over some scale) can be judged, and the null hypothesis excluded for those regressors which are significant. In addition, from the errors estimated in the regressors and the response, an estimate of the standard error in the coefficients β_i may be obtained.

The above results are true only if the regressors are independent, that is, if $\mathrm{cov}(x_i, x_j) = c\delta_{ij}$. The surface-slope change as averaged over the short to medium length scales and the local ice depth change satisfy this criterion.

Shown in Table 5.5 are the results of this regression analysis for various data sets, in which the medium-scale surface slope is the pertinent slope parameter. In all cases except the 1958-59/1979-80 data set (which has only two degrees of freedom) the F-statistic for the slope variation $\Delta\langle\alpha\rangle_m$, denoted F_α, is seen to be extremely small in comparison to that for the thickness change. In no cases is F_α greater than an F-level appropriate to a probability of 0.50 or less that such a F-statistic could have occurred in a random sample and the null hypothesis be true. It follows that the surface slope changes, as averaged over 2× the ice thickness, are *not* significant in explaining the velocity response of Blue Glacier to a change in geometry. The significance of the local slope changes in determining Δu is equally low.

Since the variation in the medium-scale slope is not significant in determining the behaviour of the velocity change, it may be dropped from the regression analysis. The remaining entries in Table 5.5 thus correspond to the single-variable linear regression of ΔH on Δu, with a linear correlation coefficient $r_{H,u}$ and F-statistic F_H.

Examination of the values of F_H in Tables 5.5 shows that changes in local ice thickness act as a highly significant regressor for the velocity perturbation. The F-statistic is extremely high in all cases, excluding the null hypothesis at a confidence level of greater than 99.9%. That is, excluding the hypothesis that ΔH at this local scale is not significant in explaining the velocity variation. ($P \leq 0.001$ for null hypothesis true.)

The large values of the correlation coefficients listed in column 5 of Table 5.5

lead to the high probabilities listed in column 6 that the fit of the data to the linear model (5.8) with the single variable ΔH is not simply by chance and that the variables are indeed linearly related . That is, the probabilities listed in Tables 5.5 are equal to $1 - P_o$, where P_o is the probability that the null hypothesis ($\beta_H \neq 0$) is the correct hypothesis for a random sample.

It is clearly seen that such a relation between velocity and thickness exists even when the data for all points across the transverse profiles are used to evaluate the regression. However, there is a higher degree of correlation within the near-centerline data sets, as is to be expected from the analytical and numerical results discussed in later chapters.

Δu against ΔH is plotted in Figures 5.5 - 5. for the different data sets, along with the best fit regression lines obtained from least-squares analysis. Error is present in both variables, $x = \Delta H$ and $y = \Delta u$, and, thus, standard linear regression analysis is not strictly applicable. Standard analysis is based on the assumption that one of the variables is free of error, (i.e. $\sigma_x=0$), and thus the appropriate minimization is that of the sum of the squares of the vertical distances to the regression line. If equal error exists in both x and y then one can imagine a minimization of the perpendicular distances to the best fit line instead. In the case of unequal but constant probable errors in x and y ($\sigma_x \neq \sigma_y$) the data may be scaled by their probable errors, thereby stretching the error ellipses into circles via a coordinate stretch. The normal distance to the line of best fit may then be minimized within this scaled topology. This idea may be further developed to include non-uniform σ_i (i.e. $\sigma_x=\sigma_x(x)$), as discussed by York (1966). For the present study the errors in ΔH and Δu may be assumed to be essentially constant throughout the data set and thus the uniform scaling procedure may be used. The slope, β_1, and intercept, β_o, of the best-fit straight line are given by

$$\beta_1 = \frac{S_{yy} - cS_{xx} + [(S_{yy} - cS_{xx})^2 + 4cS_{xy}]^{1/2}}{2S_{xy}} \qquad (8.14a)$$

$$\beta_o = \bar{Y} - \beta_1 \bar{X}\,, \qquad (8.14b)$$

where $c = \sigma_y^2/\sigma_x^2$ and S_{xx}, etc., have their usual statistical meanings (e.g. $S_{xx} = \sum_i (x_i - \bar{X})^2$, $\bar{X} = \frac{1}{N}\sum_i x_i$).

Using $\sigma_{\Delta H} = 0.25$ and $\sigma_{\Delta u} = 1.0$, the parameters of the best-fit linear model listed in Table 5.5 were obtained, along with an estimate of their errors. These parameters differ by up to 20% from those obtained by the standard analysis. (For comparison, the values $\beta_1{}^\circ$ of the slope determined by standard techniques are listed in the last column of Table 5.5.)

As expected from analytical models, the slopes resulting from the incorporation of all data points are lower than those obtained for near-centerline data only, and, as mentioned above, the correlation coefficients are lower. This reduced slope indicates a lowering of the magnitude of the effective response factor Ψ, as described in chapter IX.

The mean slope of the response curves for the centerline values in individual data sets is β_1=4.66 $\pm$ 0.41, while the intercept has a mean value of β_o=-18.5. There is no significant trend in the regression slope from year to year, although there appears to be a slight increase in the absolute magnitude of the intercept from the 1957/58 - 1977/78 data to that found in later years. An explanation of this slight increase may lie in the temporal variation in the large-scale surface slope, as indicated in Table 5.2. The change in the long-scale surface slope increases slightly in the later years.

The values of the slope and intercept are most accurately estimated for the individual annual data sets as opposed to the values listed under the heading 'all years'. The latter data set includes several data pairs (ΔH,Δu) which result from

less accurate data in the later years (1979-80), as well as including the data from different configurations of the glacier surface during the different years.

If the model of an infinite slab (5.7) is assumed, then a value of n = 3.66 is implied, along with a logarithmic decrease (x100) in overall slope of 5.05. This slope decrease is consistent with that observed over the entire region of study ($\Delta<\alpha>_L$) as listed in Table 5.2. However, more realistic models of the flow response (Chapters IX and X)will be seen to imply in a larger value of the stress exponent n and a different contribution from the surface slope term. (For example, if $\Psi \approx 0.85$ in (5.8), then $n \approx 4.5$ and $\Delta<\alpha>_L \approx 4.1$.) But it is noteworthy that the simple slab model of the flow response (5.7) can account reasonably well for the observed change with realistic values of n and a variation in an appropriately averaged surface slope consistent with the data. A value of n = 3.7 - 4.5 lies well within the "accepted" values of n, although some authors feel that n = 3 can be made compatible with most observational data (see eg. Hooke, 1981).

Much of the scatter in the data about the regression line occurs in response to factors other than the estimated errors $\sigma_{\Delta H}$ and $\sigma_{\Delta u}$. It is believed that geometrical properties relating the response parameter Ψ to the various cross-sectional profiles of the glacier lead to a position-dependent Ψ, and thus some scatter about the simple model (5.8). This will be discussed in detail in Chapters IX and X.

5.7 Summary

The results of this chapter indicate a significant linear correlation between the observed ice-thickness changes and the temporal and spatial changes in velocity over a time span of twenty years. This correlation seems to be affected by the change in overall surface slope, averaged over a long distance scale, but

slope changes averaged over shorter distance scales (1 to 3 times the ice thickness) seem to show little or no correlation with the velocity changes. This reflects the ability of a glacier to average longitudinal stresses over large distances.

Values of the stress exponent n inferred from the $\Delta H - \Delta u$ correlation on the basis of a simple flow-response model agree well with accepted values of this parameter. The analytical and numerical models described in the following chapters were developed to improve upon the simple model so as to obtain as much information as possible on the governing parameters of glacier flow from the data set described here.

Table 5.1
Slope Change, Medium Length Scale

1957-58 to 1977-78

$$\Delta\alpha = \log \frac{<\sin\alpha>_m^{77/78}}{<\sin\alpha>_m^{57/58}} \times 100 \; ; \quad <\sin\alpha>^{77/78} = \frac{1}{2}(<\sin\alpha>^{77} + <\sin\alpha>^{78}), \text{ etc.}$$

Location	$\Delta\alpha$	Mean	Location	$\Delta\alpha$	Mean
			F1	- 2.8	
B1	- 2.0		F2	- 8.3	$\bar{F}$ = - 9.0
B2	- 10.1		F3	- 6.8	
B3	- 7.5	$\bar{B}$ = - 8.8	F4	-9.1	
B4	- 9.3		F5	- 17.9	
B5	- 4.9				
			G1	- 9.5	
C1	- 3.2		G2	- 20.0	
C2	- 5.2		G3	- 11.9	$\bar{G}$ = - 16.9
C3	- 7.8	$\bar{C}$ = - 4.3	G4	-21.5	
C4	- 6.6		G5	-21.3	
C5	+ 2.2				
C6	- 5.0		H1	- 11.0	
			H2	- 19.7	$\bar{H}$ = -12.6
			H3	- 9.4	
D1	- 3.6		H4	- 9.8	
D2	+ 4.1	$\bar{D}$ = + 1.5	H5	- 13.3	
D3	+ 4.6				
D4	+ 3.3		I1	- 6.2	
D5	- 0.9		I3	- 6.7	
			I4o	0.	$\bar{I}$ = -2.5
E1	- 0.6		I5	- 3.2	
E2	+ 0.8	$\bar{E}$ = - 0.6	I6	+ 3.8	
E3	- 1.4		I7	- 1.1	
E4	-0.6		I8	-0.5	
E5	- 1.1		I4	- 3.0	

Table 5.2
Overall Slope Change

Time Period	$\Delta <\text{alpha}>_L^{B-I}$
1957/58-77/78	- 4.5
1957/58-78/79	- 6.3
1958/59-78/79	- 3.9
1958/59-79/80	(- 5.0)

$\Delta <\text{alpha}>_L^{B-I} = \log \frac{<\alpha^1>_L}{<\alpha^o>_L} \times 100$, as determined from profile I to profile B (~ 1500m)

Table 5.3
Mean Thickness Change (absolute and logarithmic)

1957/58 to 1977/78

Location	$\overline{\Delta H}$,m	$\left[\log \frac{H^1}{H^o}\right] \times 100$	Location	$\overline{\Delta H}$,m	$\left[\log \frac{H^1}{H^o}\right] \times 100$
B1	20.10	16.4	F3	15.80	6.1
B2	19.14	11.4	F4	17.00	6.9
B3	19.42	11.2	F5	16.58	8.1
B4	19.04	10.8	G1	15.12	8.5
B5	20.92	14.3	G2	15.30	7.2
C1	18.71	12.0	G3	14.70	6.1
C2	16.63	8.4	G4	14.99	5.9
C3	15.32	7.0	G5	14.86	6.3
C4	14.74	6.6	H1	15.60	7.6
C5	16.40	7.6	H2	11.30	5.0
C6	18.59	10.0	H3	11.70	4.5
D1	17.98	10.0	H4	9.92	3.6
D2	15.47	7.8	H5	8.78	3.6
D3	15.14	7.2	I1	13.48	13.0
D4	16.82	8.6	I2	11.32	7.2
D5	17.43	11.5	I3	9.14	4.3
E1	17.38	11.4	I4o	11.45	4.6
E2	17.06	9.3	I5	11.27	4.3
E3	16.62	8.2	I6	9.90	3.7
E4	18.00	8.6	I7	8.48	3.2
E5	17.66	10.2	I8	8.73	3.8
F1	17.97	9.6	I9	7.09	3.8

1957/58 to 1978/79

B3	18.43	10.6	F3	16.40	6.3
C4	14.53	6.5	G3	14.23	5.9
D3	14.58	6.9	H3	10.54	4.1
E3	15.75	7.7	I7	6.50	2.5

1958/59 to 1978/79

C3	14.70	6.7	H4	10.65	3.9
D3	13.11	6.2	I4o	11.91	4.8
E3	(16.50)	(8.1)	I6	9.51	3.6
F4	16.42	6.6	I11	11.78	4.5

1958/59 to 1979/80

C4	12.26	5.5	G3	13.35	5.6
D3	12.44	6.0	H3	9.11	3.5

Approximate Thickness Change Below Icefall, in meters, 1957 to 1977

L2	- 4.	L5	- 3.	N3	- 5.
L3	- 4.	M1	- 5.	N4	- 7.
L4	- 2.	N2	- 4.	N5	- 8.

Error in $\overline{\Delta H}$ is ± 0.20 m, in $[\log (H^1/H^o)] \times 100$ is ± 0.3 except below icefall, where $\overline{\Delta H}$ is ± 3 m. Values in parentheses are approximate.

Table 5.4
Changes in Annual Velocity (logarithmic difference × 100)

1957/58 to 1977/78

B1	37.5	F3	13.0
B2	34.7	F4	10.7
B3	36.2	F5	12.9
B4	31.5	G1	13.4
B5	30.2	G2	14.6
C1	36.5	G3	9.9
C2	25.2	G4	10.9
C3	26.5	G5	11.2
C4	23.8	H1	10.0
C5	24.0	H2	(14.6)
C6	27.2	H3	6.2
D1	(7.6)	H4	6.9
D2	23.2	H5	8.2
D3	21.3	I1	5.9
D4	24.2	I2	3.6
D5	26.9	I3	8.6
E1	(10.3)	I4o	6.7
E2	11.5	I5	4.1
E3	16.1	I6	4.7
E4	14.3	I7	5.5
E5	18.4	I8	7.8
F1	16.2	I9	12.7
F2	11.2	I4	(5.2)

1957/58 to 1977/78

B3	26.8	F3	2.4
C4	15.5	G3	-1.4
D3	11.7	H3	-3.7
E3	5.8	I7	(-8.2)

1958/59 to 1978/79

C3	7.5	H4	2.8
D3	13.0	I4o	-5.1
E3	20.6	I6	(-0.9)
F4	12.9	I11	-5.2

1958/59 to 1979/80

C4	12.5	G3	-3.2
D3	10.2	H3	-2.8

Estimated errors in $\left|\log \frac{u^1}{u^o}\right| \times 100$ are 1.5. Values in parentheses are approximate.

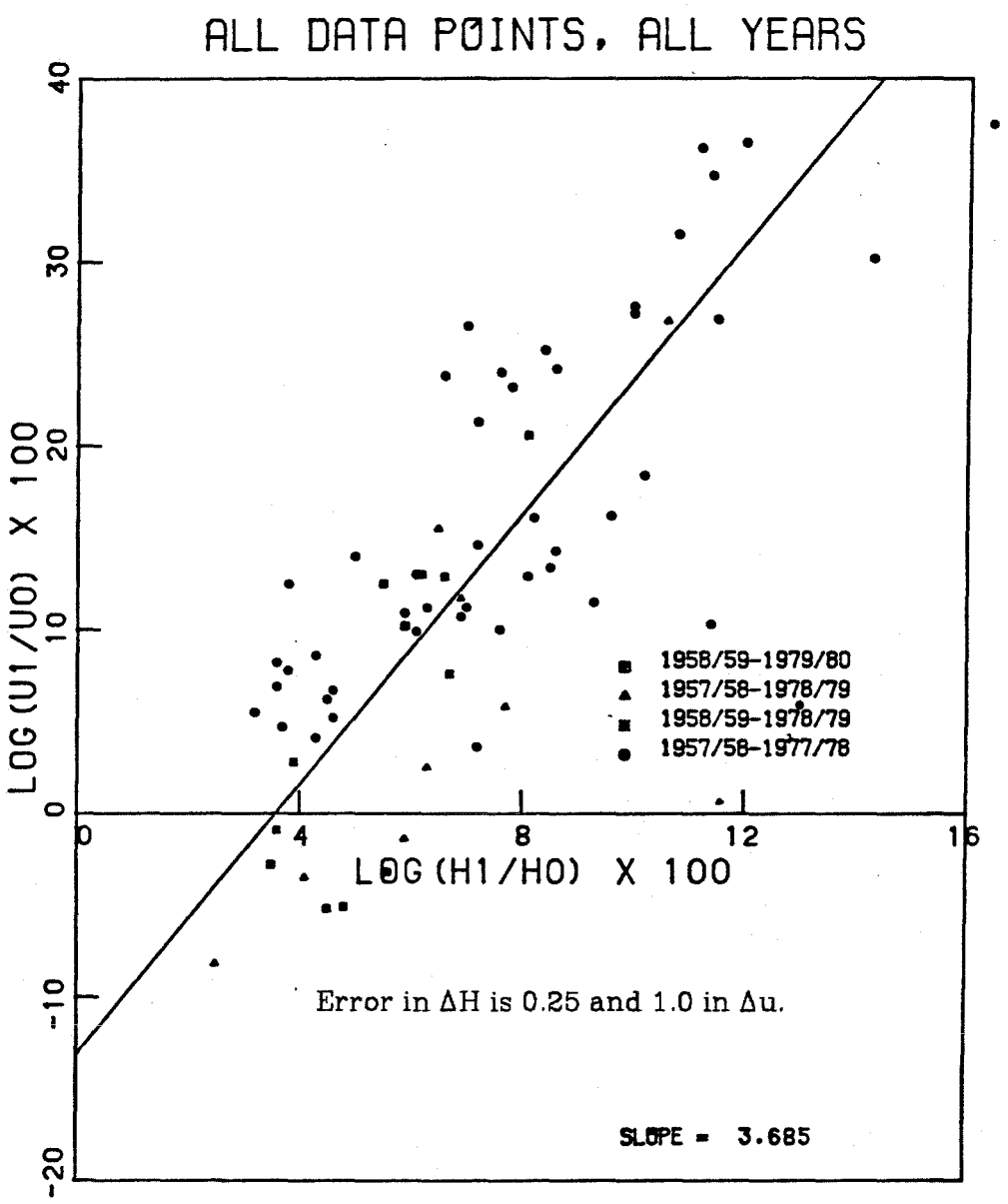

Figure 5.5 Velocity change versus thickness change for all years at all points.

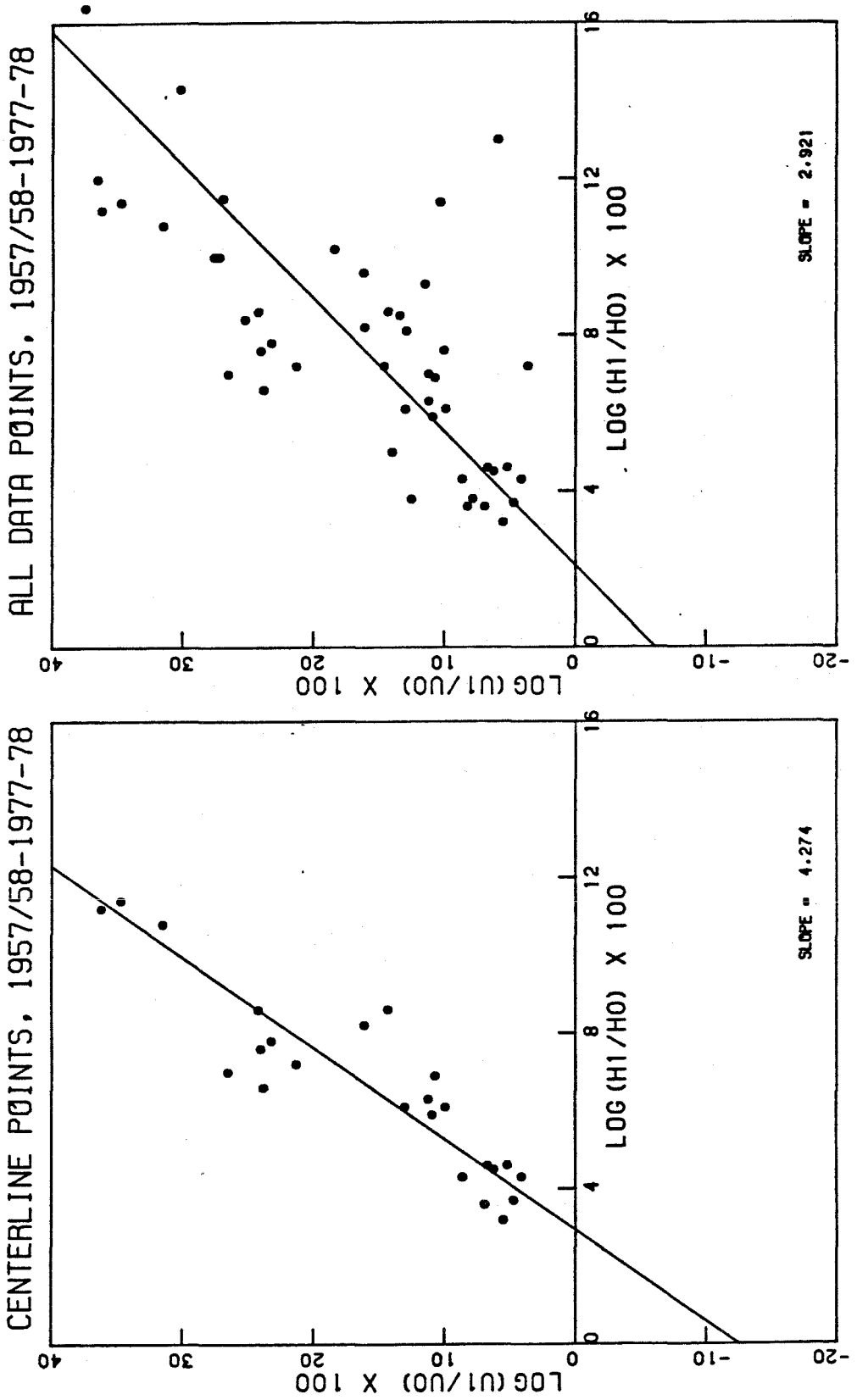

Figure 5.7 Velocity change vs. thickness change 1957/58 to 1977/78.

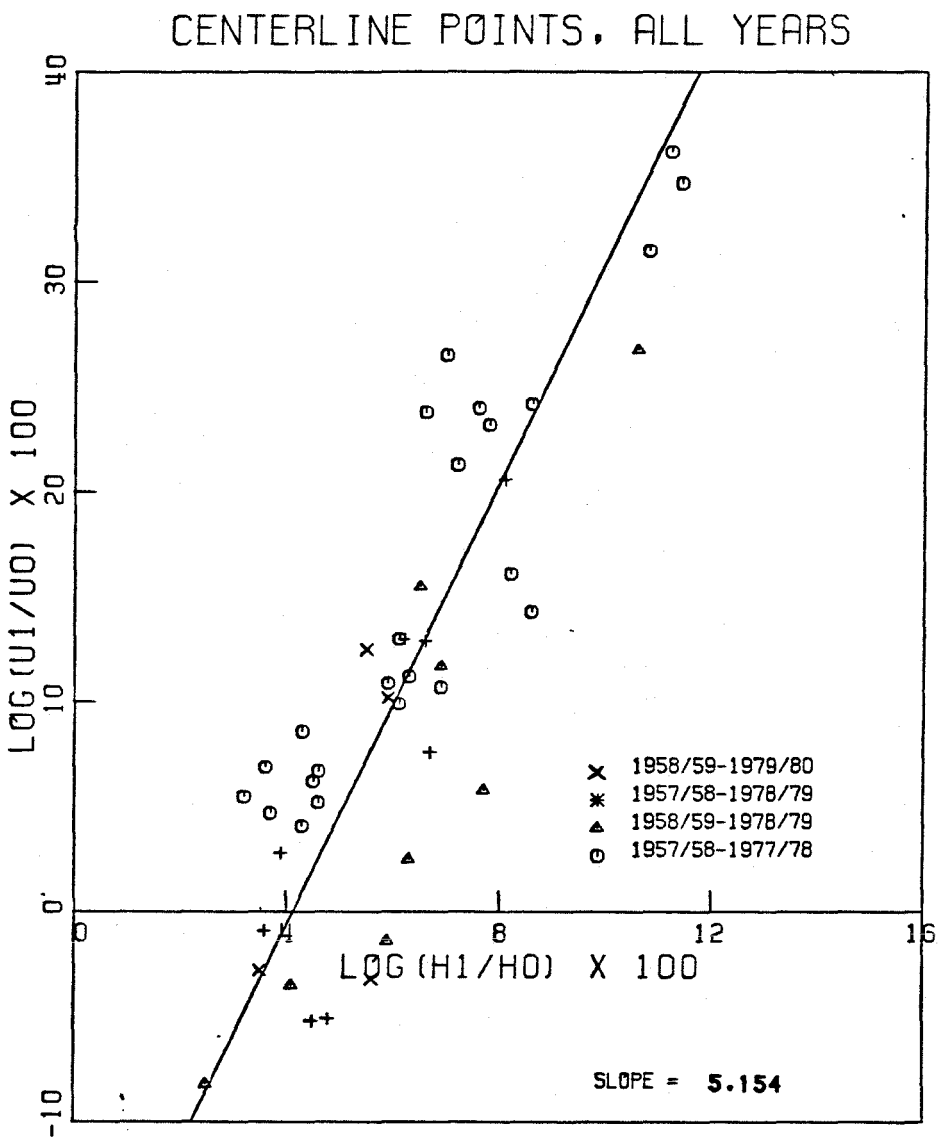

Figure 5.6 Velocity change vs. thickness change at near-centerline points for all years.

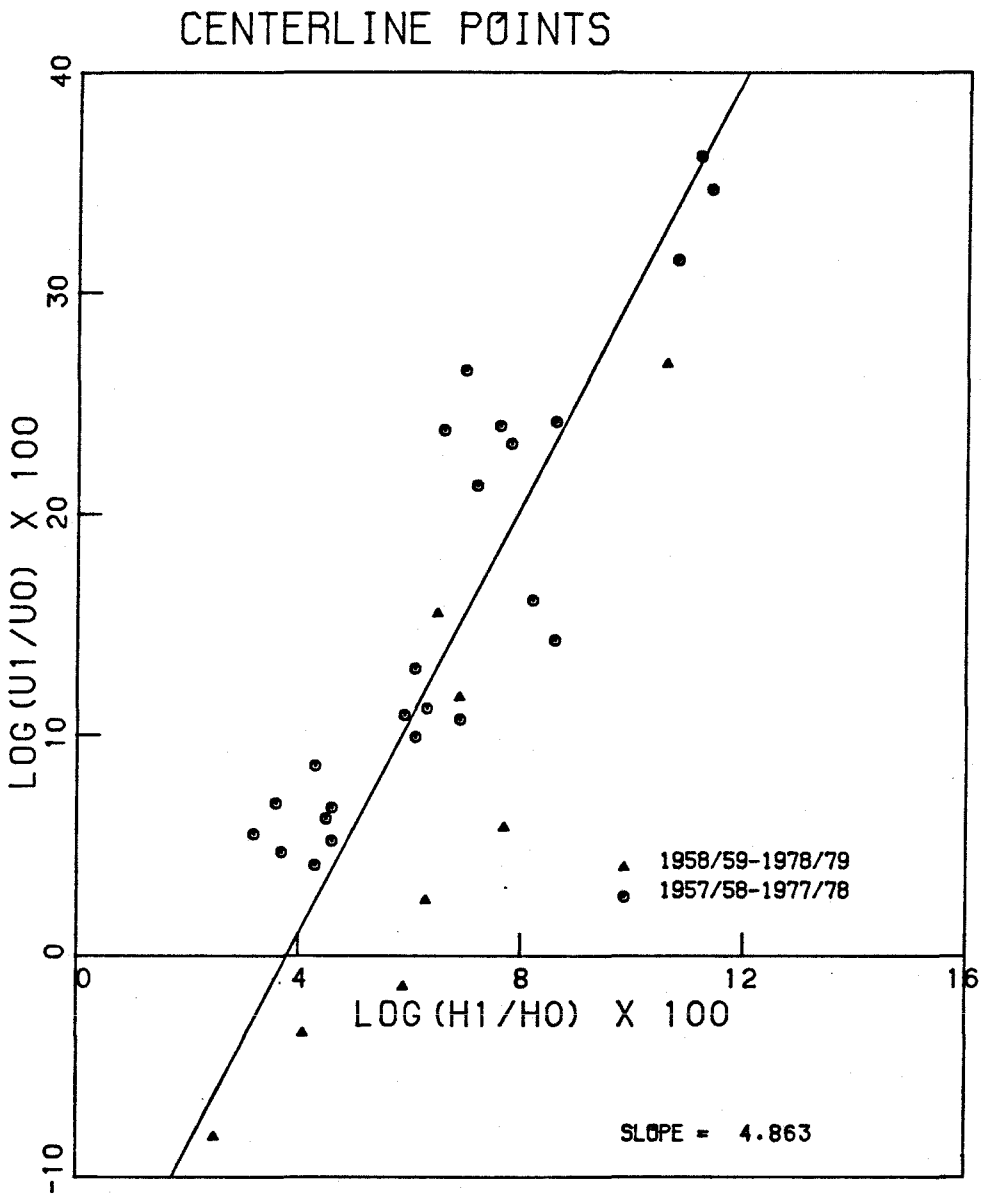

Figure 5.8 Velocity change vs. . thickness change at near-centerline points for two periods: 1957/58 to 1977/78 and 1958/59 to 1978/79.

Table 5.5
Regression Analysis of $\Delta < \alpha >_m$, ΔH, and Δu

Data Set	N	F_H	F_{α_m}	$F_{99\%}$	$r_{H,u}$	P(r)	β_o	β_H	σ_{β_H}	β_H^o
near-centerline points only										
1957/58-77/78	24	99.1	0.25	8.0	0.904	> 0.9999	-14.5	4.27	0.41	3.85
1958/59-78/79	8	17.1	0.04	11.3	0.905	0.998	-22.5	4.85	0.84	4.28
1957/58-1977/78 and 1958/59-1978/79	32	102.0	0.40	7.5	0.854	> 0.9999	-18.46	4.86	0.52	4.04
all years	44	109.5	0.52	7.3	0.856	> 0.9999	-20.87	5.15	0.42	4.26
all data points										
1957/58-1977/78	46	45.9	0.09	7.3	0.71	0.999	-6.12	2.98	0.42	2.29
all years	66	85.5	0.14	7.0	0.75	0.999	-13.2	3.68	0.39	2.85

N=number of data points, $F_{99\%}$=F-value at 99% probability level,
β_H^o=slope of regression line assuming no error in ΔH
$\sigma_{\Delta H} = 0.25$, $\sigma_{\Delta u} = 1.01$ assumed

CHAPTER VI

LONGITUDINAL AVERAGING OF SURFACE SLOPE AND ICE THICKNESS

In the previous chapter it was seen that the flow response of Blue Glacier does not show a good correlation with local slope changes, but does correlate reasonably well with local thickness variations. These results agree qualitatively with those of Meier et al.(1974), Bindschadler and others (1977), and Budd (1968,1970), who have found that the magnitude of the flow velocity appears to be determined by a long-scale average of surface slope, and not the local slope. ('Local' is used here for quantities averaged over a horizontal distance approximately equal to the ice thickness.) Although there have been several theoretical discussions of this averaging effect in terms of longitudinal stress gradients (cited below), there has been no clear means of estimating the length of this averaging scale.

In addition, two related questions remain unanswered. First, is it reasonable to assume that the averaging should be applied to the surface slope only, or should the influence of longitudinal stress gradients be reflected in a need to take into consideration longitudinal averages of both surface slope and ice thickness? There has been no definitive observational or theoretical answer to this question to date. Second, what sort of averaging of the slope and/or the depth must be employed? Previous studies have employed an unrealistic boxcar-type averaging window, where the average slope is computed over some fixed length. (Empirical results indicate that a length of 7 - 10 times the ice depth is appropriate.) But, as seen in Figure 4.1, the flow velocity does, in part, seem to follow the local surface slope: the locally steep region near profiles D and E shows an increase in velocity, whereas the long-scale surface slope does not seem to be appreciably increased over this reach. On the other hand, the

observed flow response appears to correlate reasonably well to the decrease in the overall surface slope of the glacier, as shown in Chapter V. Clearly some weighted average of the slope (and possibly thickness) over some length scale is required.

This chapter seeks to provide an answer to these questions by investigating the role of longitudinal stress gradients in determining the magnitude of perturbations in flow arising from changes in slope and thickness along the length of the glacier.

6.1 Discussion of Previous Work

Previous studies of the role of longitudinal stress gradients in glacier and ice-sheet flow (Shumsky, 1961; Robin, 1967; Budd, 1968, 1970, 1971; Collins, 1968; Nye, 1969; Hutter, 1981), have proceeded by integration of the equilibrium equations to express the basal shear stress τ_B as follows:

$$\tau_B \approx \rho g H \sin\alpha + 2G - T \tag{6.1}$$

where H is the local thickness and α the local slope, ρ the ice density, and g the acceleration of gravity. (A shape factor may be included in (6.1) if appropriate; see Chapter VIII.) The correction terms G and T arise from longitudinal gradients in the components of the deviatoric stress, and are given by

$$G = -\int_{y_B}^{y_S} \frac{\partial \tau'_{xx}(x,y)}{\partial x}\, dy \quad \text{and} \quad T = \int_{y_B}^{y_S} \int_{y_B}^{y} \frac{\partial^2 \tau'_{xy}(x,y')}{\partial x^2}\, dy'\, dy\,, \tag{6.2}$$

where y_B, y_S refer to the coordinates of the lower and upper surfaces, respectively, of the ice at longitudinal coordinate x. The x-axis is taken to be tangent to the upper surface in the direction of flow, and the y-axis normal to x in the vertical plane.

The correction terms in (6.2) involve integrals of the stress components over depth. Unfortunately, the depth variation of the deviatoric stresses is

unknown as long as the stress field within the glacier remains undetermined, and, thus, G and T may not be explicitly evaluated.

Under rather limiting assumptions the term G may be expressed in terms of the longitudinal extension ($\dot{\varepsilon}_{xx}$), as measured at the surface. From observations on the Wilkes Ice Cap, Budd (1968) finds that G is significant when averaged over distances less than about 20 times the ice depth, but on a larger scale its mean value is negligible. Theoretical analysis of Budd (1968, 1970) indicates that T is negligible when averaged over distances greater than 3-4 times the ice depth (denoted H). These results lead to the introduction of three important length scales (Paterson 1981): a large scale (> 20 H), at which the basal shear stress is given by

$$< \tau_B > = \rho g < H \sin\alpha > \quad , \tag{6.3}$$

an intermediate scale (~ 4-20 H) with

$$\bar{\tau}_B = \rho g \overline{H \sin\alpha} + 2\bar{G} \quad , \tag{6.4}$$

and a short scale at which all terms in (6.1) are important.

Following Robin (1967) and Budd (1968), the assumption is usually made that the actual basal shear stress does not vary over the length of the glacier (effectively assuming a yield stress for ice, which is an approximation only crudely valid),and that it is equal to the large scale average as given in eq. (6.3). Under this assumption, $\tau_B = < \tau_B > = \bar{\tau}_B$. Variations in the surface slope at the intermediate and shorter scales are thus supported by longitudinal stress gradients. For example, at the intermediate scale this implies $2\bar{G} = \rho g(< H \sin\alpha > - \overline{H \sin\alpha})$. Since the flow is determined mainly by the shear stress near the bed, intermediate and short scale variations in slope and thickness should not greatly affect the surface velocity if τ_B is assumed constant.

These theoretical and analytical results have severe limitations in their applicability to glaciers for several reasons. (1) The empirical results of Budd (1968) leading to expressions of the form (6.3-6.4) apply to a large ice cap, more representative of an ice sheet than a steep valley glacier, and the specific length scales are clearly not applicable to small ice masses (indeed, the total length of a valley glacier may be much less than 20 H!). (2) There is no reason to think that the basal shear stress is strictly constant beneath a glacier. (3) The integrals in eq. (6.2) cannot be evaluated with any reasonable accuracy, since the *in situ* stress field is not accurately known, and the assumptions leading to their evaluation in terms of measured strain rates may not be applicable to valley glaciers. (4) The results shown in eqs. (6.1)-(6.4) imply a longitudinal averaging of the surface slope *and* the thickness, while many observational studies assume that *local* ice depth and a longer-scale slope are the important parameters in determining glacier flow. (Budd (1968, 1970) and Bindschadler and others (1977) implicitly assume that this is the case, without justification, and thus write (6.4) as $\bar{\tau}_B = \rho g H \overline{\sin\alpha} + 2\bar{G}$, for example.)

Although the applicability of a longitudinally-averaged thickness has not been tested by previous studies, larger-scale averaged surface slopes have been examined. A slope as averaged over a longitudinal distance equal to 7-10 times the mean ice depth was found to correlate well with the observed flow of Variegated Glacier by Bindschadler and others (1977), while there was a corresponding lack of correlation at the local scale. Similarly, Meier et al. (1974) have found that a nearly constant effective slope was required on Blue Glacier to match ice fluxes determined from continuity and those calculated from the observed surface velocity and allowing internal deformation over the local thickness of ice. (Note:This constant slope value actually agrees reasonably well with the slope averaged over a distance equal to 5-7 ice thicknesses.) These empirical results

do indicate that a surface slope as averaged over a longer scale may, indeed, be more appropriate than the local slope in determining the flow of an ice mass, but again, the choice of the averaging length is not based on a physical model, and no tests have been made for other than a boxcar-type averaging window.

Recently, Hutter (1981) has developed a theoretical treatment that includes longitudinal variations in thickness and slope in expressions for the basal shear stress and surface velocity which do not involve the integrations over the unknown stress field found in (6.2). The correction terms for the spatial variation of the basal shear stress involve the curvature of the upper and lower surfaces of the ice mass and products of the surface and basal slopes, all of which can be determined by field observations. If the curvatures are small then the local slope and depth will approach their longer-scale averages, and the second order corrections will tend to zero. On the other hand, if there is a sharp curvature in either of the surfaces (upper or basal), then the slope and thickness will tend to be appreciably different than the corresponding long-scale averages. In this case, the curvature will be important, and an effective averaging scale for slope and depth will be relatively short. Therefore, it is not expected that a single length scale or weighting function will be applicable to all ice masses, rather they will depend upon the nature of the longitudinal changes in thickness and slope. The results of Hutter (1981) do not allow for an explicit expression of the weighting function or averaging length (as is developed below), but they indicate slope and thickness are intimately coupled, and thus that they must both be longitudinally averaged. The basal shear stress is found to depend on the flow law exponent, as will also be found in the results presented in the next section and in Chapters VIII and X, indicating that a detailed knowledge of the flow law parameters is required before the effects of transverse and longitudinal stress gradients can be accurately determined.

6.2 Longitudinal Averaging in an Ice Mass: Theoretical Development

The discussion in the previous section has shown that there appears to be both a theoretical and observational basis for a non-local averaging of the effects of surface slope and (possibly) ice thickness on the flow in an ice mass. The basal shear stress is smoothed by this averaging, which results from the influence of longitudinal stress gradients on the flow. In this section, explicit expressions are obtained for the length scale over which slope and thickness are effectively averaged in glacier flow and the weighting function appropriate to the longitudinal averaging process. It will be shown that the length scale is dependent upon the flow law of ice, the sliding law, and the magnitude of the longitudinal variations in slope and thickness. The averaging process applies both to the thickness and the slope, but the scale may vary up- and down-glacier.

Let us focus attention on the neighborhood of a particular point along the centerline of a valley glacier or along a flowline of a large ice sheet, which we can take to be the origin of the coordinate system (Figure 6.1). Take the x-axis directed downglacier, inclined at an arbitrary angle γ downward from the horizontal and the y-axis normal to x, directed upward.. In plane strain, the components of stress are governed by the equilibrium equations:

$$\frac{\partial \tau_{xx}}{\partial x} + \frac{\partial \tau_{xy}}{\partial y} = -\rho g_x \tag{6.5a}$$

$$\frac{\partial \tau_{xy}}{\partial x} + \frac{\partial \tau_{yy}}{\partial y} = -\rho g_y \tag{6.5b}$$

where $g_x = g \sin\gamma$ and $g_y = -g \cos\gamma$. Let the upper surface of the ice mass be given by $Y_S(x)$ and the bed be given by $Y_B(x)$. The local slope of the bed (as measured downward from the direction of the x-axis) is denoted β and the slope of the surface is denoted α. Then $H = Y_s - Y_B$ and

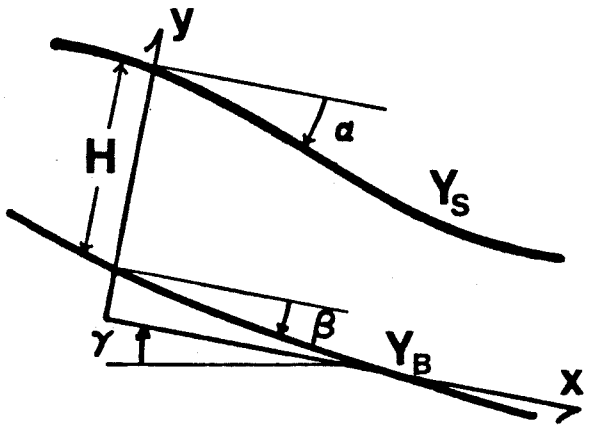

Figure 6.1 Coordinate system and definition of quantities used in this chapter.

$$\frac{dY_S}{dx} = -\tan\alpha \tag{6.6a}$$

$$\frac{dY_B}{dx} = -\tan\beta \tag{6.6b}$$

Differentiating (6.5a) with respect to y and (6.5b) with respect to x, we obtain

$$\frac{\partial^2(\tau_{xx}-\tau_{yy})}{\partial x\partial y} = \frac{\partial^2\tau_{xy}}{\partial^2 x} - \frac{\partial^2\tau_{xy}}{\partial^2 y} \tag{6.7}$$

If we integrate from Y_S to y, we find

$$\frac{\partial(\tau_{xx}-\tau_{yy})}{\partial x} = \frac{\partial\tau_{xx}}{\partial x}\Big|_{Y_S} + \frac{\partial\tau_{xy}}{\partial y}\Big|_{Y_S} - \frac{\partial\tau_{yy}}{\partial x}\Big|_{Y_S} - \frac{\partial\tau_{xy}}{\partial y} + \int_{Y_S}^{y}\frac{\partial^2\tau_{xy}}{\partial x^2}\,dy' \tag{6.8}$$

We may express the first two terms on the right hand side of (6.8) as $-\rho g\sin\gamma$ using (6.5a). The longitudinal deviatoric stress σ_{xx} is

$$\sigma_{xx} = \frac{1}{2}(\tau_{xx} - \tau_{yy})$$

and thus (6.8) can be written

$$2\frac{\partial\sigma_{xx}}{\partial x} = -\rho g\sin\gamma - \frac{\partial\tau_{yy}}{\partial x}\Big|_{Y_S} - \frac{\partial\tau_{xy}}{\partial y} + \int_{Y_S}^{Y}\frac{\partial^2\tau_{xy}}{\partial x^2}\,dy' \tag{6.9}$$

We now integrate again, this time from Y_S to Y_B. This leads to

$$2\int_{Y_S}^{Y_B}\frac{\partial\sigma_{xx}}{\partial x}dy = \rho g H\sin\gamma - \tau_{xy}|_{Y_B} + \tau_{xy}|_{Y_S} + H\frac{\partial\tau_{yy}}{\partial x}|_{Y_S} + \int_{Y_S}^{Y_B}\int_{Y_S}^{y}\frac{\partial^2\tau_{xy}}{\partial x^2}dy'dy \qquad (6.10)$$

where $H = -(Y_B - Y_S)$. The order of differentiation and integration in the left hand term may be interchanged using

$$\int_{Y_S}^{Y_B}\frac{\partial\sigma_{xx}}{\partial x}dy = \frac{\partial}{\partial x}\int_{Y_S}^{Y_B}\sigma_{xx}dy - \sigma_{xx}|_{Y_B}\frac{\partial Y_B}{\partial x} + \sigma_{xx}|_{Y_S}\frac{\partial Y_S}{\partial x}. \qquad (6.11)$$

If we define

$$\bar{\sigma}_{xx} = \frac{1}{H}\int_{Y_B}^{Y_S}\sigma_{xx}dy \quad \text{and} \quad T = \int_{Y_S}^{Y_B}\int_{Y_S}^{Y}\frac{\partial^2\tau_{xy}}{\partial x^2}dy'dy\,; \qquad (6.12)$$

then (using (6.6 a,b) and (6.11) we may write (6.10) as

$$-2\frac{\partial(H\bar{\sigma}_{xx})}{\partial x} = \rho g H\sin\gamma - \tau_{xy}|_{Y_B} + \tau_{xy}|_{Y_S} + H\frac{\partial\tau_{yy}}{\partial x}|_{Y_S}$$

$$-2\sigma_{xx}|_{Y_B}\tan\beta + 2\sigma_{xx}|_{Y_S}\tan\alpha + T$$

The normal and shear tractions along the upper surface vanish (neglecting P_{atm}). In terms of the stress components defined in our coordinate system

$$0 = \tau_{xy} + \tan 2\alpha\,\sigma_{xx} \qquad (6.14a)$$

$$0 = \sin^2\alpha\,\tau_{xx} + \cos^2\alpha\,\tau_{yy} + \sin 2\alpha\,\tau_{xy}\,, \quad \text{at } y = Y_S \qquad (6.14b)$$

At this point, it is convenient (though not essential) to assume that there is no sliding at the bed. In this case, the longitudinal strain along the bed vanishes, and thus $\sigma_{x'x'} = 0$, where the primes denote a bed-parallel coordinate system. If τ_B denotes the basal shear stress, then, in our coordinate system,

$$\tau_{xy}|_{Y_B} = \cos 2\beta\ \tau_B \qquad (6.15a)$$

$$\sigma_{xx}|_{Y_B} = \sin 2\beta\ \tau_B\,. \qquad (6.15b)$$

Using these boundary conditions, we may write (6.13) as

$$-2\frac{\partial(H\bar{\sigma}_{xx})}{\partial x} = -[\cos 2\beta + 4\sin^2\beta]\tau_B + \tan^2\alpha\,\tau_{xy}|_{Y_S} + H\frac{\partial \tau_{yy}}{\partial x}|_{Y_S} + T \tag{6.16}$$

The term $\frac{\partial \tau_{yy}}{\partial x}|_{Y_S}$ may be written (following Budd, 1970)

$$\frac{\partial \tau_{yy}}{\partial x} = \rho g \cos\gamma \tan\alpha - \tan\alpha^2 \frac{\partial \tau_{xx}}{\partial x} + \rho g \sin\gamma \tan^2\alpha \tag{6.17}$$

$$+ \frac{\partial \tau_{xx}}{\partial \xi} 2\sin\alpha \tan\alpha + \tau_{xx}\cos 2\alpha \tan\alpha \frac{\partial \alpha}{\partial x} + \tau_{xx}\sin 2\alpha \frac{\partial \alpha}{\partial x}$$

at $y = Y_S$, where ξ is the arc distance along the surface. If we introduce the curvature of the upper surface, $\kappa_S = \frac{\partial \alpha}{\partial \xi}$, then 6.16 may be written

$$\begin{aligned} -2\frac{\partial(H\bar{\sigma}_{xx})}{\partial x} = \; & \rho g H(\sin\gamma + \cos\gamma\tan\alpha) \\ & - (\cos 2\beta + 4\sin^2\beta)\tau_B + T \\ & + [\,\tau_{xy}|_{Y_S} - H\frac{\partial \tau_{xx}}{\partial x}|_{Y_S} - \rho g H \sin\gamma\,]\tan^2\alpha\,. \\ & + 2\sin\alpha\tan\alpha H\frac{\partial \tau_{xx}}{\partial \xi}|_{Y_S} \\ & + \tau_{xx}|_{Y_S} H\kappa_S[\sin 2\alpha + \cos 2\alpha\tan\alpha] \end{aligned} \tag{6.18}$$

This relation is exact for all α,β, and γ if there is no sliding at the bed. If we now make the assumption that α is small (i.e. that the surface is roughly parallel to the x-axis) then terms of order α^2 or higher may be neglected, and (6.18) becomes

$$-2\frac{\partial(H\bar{\sigma}_{xx})}{\partial x} = \rho g H(\sin\gamma + \alpha\cos\gamma) - [\cos 2\beta + 4\sin^2\beta]\tau_B + T \tag{6.19}$$

This reduces to the familiar value $\rho g H(\alpha+\gamma)$ for a nearly parallel sided slab. Correction terms arise because of non-zero longitudinal gradients in the deviatoric stresses. Under the assumption of no-slip, (6.10) agrees with that found by Collins (1968), Nye (1969) and Budd (1970).

Let u be the mean longitudinal velocity over the thickness at x = 0. In order to determine the effects of longitudinal variations in thickness and the slopes α

and β on the stress and velocity, we introduce perturbation in the field quantities about their original value:

$$\begin{aligned} H &= H_o + h & u &= u_o + u_1 \\ \alpha &= \alpha_o + \alpha_1 & \tau_B &= \tau_B^{(o)} + \tau_B^{(1)} \\ \beta &= \beta_o + \beta_1 & \bar{\sigma}'_{xx} &= \bar{\sigma}^{(o)}_{xx} + \bar{\sigma}'^{(1)}_{xx} \\ T &= T_o + T_1 \end{aligned} \tag{6.20}$$

where $h << H_o$, etc. and $u_1 < u_o$. Since basal sliding is assumed zero and the flow is therefore determined solely by internal deformation of the ice, we can write, from standard flow theory, $u \approx c(\tau_B)^n H$, where c is a flow-law dependent constant and n is the flow-law exponent. Thus

$$\begin{aligned} u &\approx c(\tau_B^o)^n \left[1 + n \frac{\tau_B^{(1)}}{\tau_B^{(o)}} \right] (H_o + h) , \\ u_1 &\approx n u_o \frac{\tau_B^{(1)}}{\tau_B^{(o)}} + u_o \frac{h}{H_o} \\ \tau_B^{(1)} &= \frac{\tau_B^{(o)}}{n u_o} [\, u_1 - c(\tau_B^{(o)})^n h \,] \end{aligned} \tag{6.21}$$

If we substitute the expansions (6.20) into (6.19), and note that the zeroth-order terms solve (6.19), we find that terms which are first-order in the perturbations satisfy

$$\begin{aligned} -2\frac{d}{dx}[\, h\bar{\sigma}^{(o)}_{xx} + H_o\bar{\sigma}^{(1)}_{xx} \,] = {} & \rho g h [\, \sin\gamma + \alpha_o \cos\gamma \,] + \rho g H_o \alpha_1 \cos\gamma \\ & - 2\sin 2\beta_o \tau_B^{(o)} \beta_1 \\ & - [\, \cos 2\beta_o + 4\sin^2\beta_o \,] \tau_B^{(1)} + T_1 \end{aligned} \tag{6.22}$$

This relation may be further simplified by using (6.21) which leads to

$$\begin{aligned} -2\frac{d}{dx}[\, h\bar{\sigma}^{(o)}_{xx} + H_o\bar{\sigma}^{(1)}_{xx} \,] = {} & -\frac{\tau_B^o}{n u_o} [\, \cos 2\beta_o + 4\sin^2\beta_o \,] u_1 \\ & + [\, \rho g (\sin\gamma + \alpha_o \cos\gamma + (\cos 2\beta_o + 4\sin^2\beta_o) \frac{c(\tau_B^{(o)})^{n+1}}{n u_o} \,] h \end{aligned}$$

$$+ [\rho g H_o \cos\gamma]\alpha_1 - [2\tau_B^o \sin 2\beta_o]\beta_1 \qquad (6.23)$$

Although the flow law of ice leads to a coupling among the various deviatoric stress components, it is approximately valid to define an effective (depth-averaged) longitudinal viscosity, η_e, along the centerline, such that

$$\bar{\sigma}'_{xx} = 2\eta_e \dot{\varepsilon}_{xx} \quad \text{and} \quad \eta_e = N|\dot{\varepsilon}_{xx}|^{\frac{1}{n}-1} \qquad (6.24)$$

where $\dot{\varepsilon}_{xx}$ is the (depth-averaged) longitudinal strain rate and N is a flow law parameter (Collins (1968), Budd (1970), Kamb (1970)). we may thus write

$$H\bar{\sigma}_{xx} = 2(H_o + h)N(\dot{\varepsilon}_{xx}^{(o)})^{1/n}\left[1 + \frac{1}{n}\frac{\dot{\varepsilon}_{xx}^{(1)}}{\dot{\varepsilon}_{xx}^{(o)}}\right]$$

$$= 2H_o N(\dot{\varepsilon}_{xx}^{(o)})^{\frac{1}{n}} + 2Nh(\dot{\varepsilon}_{xx}^{(o)})^{\frac{1}{n}} + \frac{2N}{n}H_o(\dot{\varepsilon}_{xx}^{(o)})^{\frac{1}{n}-1}\dot{\varepsilon}_{xx}^{(1)} \qquad (6.25)$$

and, therefore

$$h\bar{\sigma}_{xx}^{(o)} + H_o\bar{\sigma}_{xx}^{(1)} = 2\eta_e\frac{du_o}{dx}h + \frac{2\eta_e}{n}H_o\frac{du_1}{dx} \qquad (6.26)$$

We now substitute (6.26) into (6.23) and collect terms to obtain a differential equation in u_1:

$$4\frac{d}{dx}\left(\frac{\eta_e H_o}{n}\frac{du_1}{dx}\right) - \frac{\varphi_1\tau_B^o}{nu_o}u_1 = \varphi_2 h + \varphi_3\alpha_1 + \varphi_4\beta_1 + T_1 \qquad (6.27)$$

where

$$\varphi_1 = [\cos 2\beta_o + 4\sin^2\beta_o] \qquad (6.28a)$$

$$\varphi_2 = -[\rho g(\sin\gamma + \alpha_o\cos\gamma) + (\cos^2\beta_o + 4\sin^2\beta_o)\frac{\tau_B^o}{nH_o}$$

$$+ 4\frac{d\eta_e}{dx}\frac{du_o}{dx} + 4\eta_e\frac{d^2u_o}{dx^2}] \qquad (6.28b)$$

$$\varphi_3 = -[\rho g H_o \cos\gamma - 4\eta_e \frac{du_o}{dx}] \tag{6.28c}$$

$$\varphi_4 = [2\tau_B^o \sin 2\beta_o] \tag{6.28d}$$

We may estimate the terms φ_1 φ_4 by taking $\alpha_o \approx \beta_o$, $\gamma \approx \frac{1}{10}$, $H_o = 250m$, $\tau_B^o = \rho g \gamma_o H_o = 1.5$bars, $\frac{du_o}{dx} = .01\,yr^{-1}$ and $\eta_e = 30$ bar yr, $\frac{d\eta_e}{dx} \approx 0$, $\frac{d^2u_o}{dx^2} \approx 0$, and $T_1 = 0$. Then we find

$$\varphi_1 \approx 1$$

$$\varphi_2 \approx -[\frac{n+1}{n}\frac{\tau_B^o}{H_o}] \approx -0.0075\,\text{bar}\,m^{-1}$$

$$\varphi_3 \approx -[\frac{\tau_B^o}{\gamma_o} - 4\eta_e \frac{du_o}{dx}] \approx -[15 - 1.2] \approx -14\text{bar}$$

$$\varphi_4 \approx 0$$

and (6.27) may be approximately written as

$$\frac{u_1}{u_o} = (n+1)\frac{h}{H_o} + n\frac{\gamma_1}{\gamma_o} \tag{6.29}$$

where we have written γ_1 in place of α_1. This relation (6.29) is strangely reminiscent of equation (5.6) for the flow response of a nearly-parallel sided slab to a change in slope and thickness. If u_1,h,γ are taken to be differentials of u,H, and γ, then 6.29 may be integrated to give (5.6).

Returning now to (6.27), we assume that $\beta_1 = 0$ and that $\beta_o = 0$ (i.e. a flat bed parallel to x-axis) and, as a first approximation, we assume that $\eta_e H_o \approx$ constant (i.e. assume that $\frac{4}{n}\frac{d(\eta_e H_o)}{dx}\frac{du_1}{dx}$ can be neglected). In addition it is reasonable to take $T_1 = 0$ under the assumption of small slope and thickness variations, since this term involves the second longitudinal derivative of the shear stress. These assumptions lead us to the simplified differential equation in u_1:

$$\left[\frac{d^2}{dx^2} - \frac{1}{l^2} \right] u_1 = \frac{n}{4\eta_e H_o} [\, \varphi_2 h + \varphi_3 \alpha_1 \,] \tag{6.30}$$

or

$$\left[\frac{d^2}{dx^2} - \frac{1}{l^2} \right] u_1 = \frac{u_o}{l^2} [\, (\mu + 1) \frac{h}{H_o} + \frac{\nu \alpha_1}{\alpha_o} \,] \tag{6.31}$$

where

$$\mu + 1 = \frac{n H_o}{\tau_B^o} \varphi_2 \quad \text{and} \quad \nu = \frac{n \alpha_o}{\tau_B^o} \varphi_3$$

Written in this form (6.31) we see that μ and ν are the "effective" exponents of H and α, where $u \sim c\, \alpha^{\nu} H^{\mu+1}$. Under the simplifying assumptions stated above, $\mu \approx \nu \approx n$. In these relations

$$l = \sqrt{\frac{4\eta_e u_o}{\tau_B^o H_o}} H_o \,. \tag{6.32}$$

The solution to (6.30) may be found by constructing Green's function, $G_o(x|\xi)$, for the differential operator in (6.30), which decays at $\pm\ \infty$:

$$\left[\frac{d^2}{dx^2} + k^2 \right] G_o(x|\xi) = \delta(x - \xi) \,, \qquad k = i/l \,. \tag{6.33}$$

Using Fourier transform methods, we find the solution to (6.24) to be as

$$G_o(x|\xi) = \frac{-1}{2\pi} \int_{-\infty}^{\infty} \frac{e^{ip(x-\xi)}}{p^2 - k^2} \, dp \tag{6.34}$$

The integrand has two simple poles at $\pm$ k. By closing the contour of integration subject to the conditions at $\pm\ \infty$, and evaluating the residue at the single pole within each contour (upper and lower), we find

$$G_o(x|\xi) = -\frac{l}{2} e^{\frac{-|x-\xi|}{l}} \tag{6.35}$$

With (6.34) the solution to (6.30) can be written

$$u_1(x) = -\frac{n}{4\eta_e H_o}\frac{l}{2}\left\{\varphi_2\int_{-\infty}^{\infty} h\, e^{\frac{-|x-\xi|}{l}}\, d\xi + \varphi_3\int_{-\infty}^{\infty}\alpha_1 e^{\frac{-|x-\xi|}{l}}\, d\xi\right\} \tag{6.36}$$

The solution given by (6.35), shows several interesting features. The first is that longitudinal averages of *both* the slope *and* the thickness are important in determining the velocity within an ice mass. Secondly, the averaging process is governed by an exponential weighting function centered at the point in question. This weighting function can be approximated by a triangular window over a half-length l given by (6.31). This is in contrast to the results of previous authors (Budd, 1968, 1970; Bindschadler and others, 1977), who assume a boxcar-type averaging window for the slope, neglecting the importance of the local slope and any thickness averaging. The importance of local as well as long-scale surface slopes agrees qualitatively with observations on glaciers. The length l is dependent upon η_e and the mean basal stress, thickness, and velocity. For typical values of these parameters on Blue Glacier, l is given as in Table 6.1, along with a length scale l' obtained assuming that the overall motion is due to basal sliding of the Weertman-type ($u_o \sim c\tau_B^{o})^m$, $m \approx (n+1)/2$) rather than internal deformation, for which $l' = \sqrt{\frac{4m}{n}\frac{\eta_e u_o}{\tau_B^o H_o}}H_o$. ($H_o$ = 250 m, u_o = 50 ma^{-1}, τ_B^o = 1 – 2 bars, and $N \approx 0.9$ (from Kamb (1970)).

Table 6.1
Characteristic Length of Averaging Window

		(n = 4)		(n = 3)	
ε_{xx} yr^{-1}	η_e/yr	l/H_o	l'/H_o	l/H_o	l'/H_o
.005	48	5.1	4.0	4.1	3.3
.01	28	3.9	3.1	3.3	2.7
.05	8	2.1	1.7	1.9	1.6

The characteristic length of the averaging window (times 2) is seen to equal 6-10 H_o. Longitudinal stress gradients cause an effective averaging of α and h over this length with the appropriate exponential weighting. It is perhaps somewhat fortuitous that the width $2l$ is close to the empirical box-car length found by Bindschadler and others, (1977).

If variations in $\eta_o H_o$ is not necessarily constant, but $\beta_1 \approx$ and $T_1 \approx 0$, then (6.27) must be written

$$\frac{4\eta_e}{n} H_o \frac{d^2u_1}{dx^2} + \left[\frac{4\eta_e}{n} \frac{dH_o}{dx} + \frac{4H_o}{n} \frac{d\eta_e}{dx} \right] \frac{du_1}{dx} - \frac{\varphi_1 \tau_B^o}{n u_o} u_1 = \varphi_2 \sin\alpha_1 + \varphi_3 h \quad (6.37)$$

$\frac{dH_o}{dx}$ is $-\tan(\alpha_o - \beta_o)$ and, thus, (6.36) can be rewritten as

$$\left[\frac{d^2}{dx^2} - 2q \frac{d}{dx} + k^2 \right] u_1 = \frac{n}{4\eta_e H_o} [\, \varphi_2 \sin\alpha_1 + \varphi_3 h \,] \quad (6.38)$$

where $k = \frac{i\varphi_1^{1/2}}{l}$ is given by (6.31) and (6.28a) and $2q = \frac{\tan(\alpha_o - \beta_o)}{H_o} - \frac{1}{\eta_e} \frac{d\eta_e}{dx}$.

The appropriate Green's function is again obtained by Fourier transform methods (where the approximation must be made that q and k are either constant or so slowly varying functions of x that their variation may be ignored):

$$G(x|\xi) = \frac{-1}{2\pi} \int_{-\infty}^{\infty} \frac{e^{-ip(x-\xi)}}{p^2 - 2ipq - k^2} dp \quad (6.39)$$

There are again two simple poles in the integrand,

$$p_\pm = i\,[\, q \pm \sqrt{q^2 - k^2}\,] \,;\; p_+ \geq 2qi \,,\; p_- \leq 0i \,,\; \mathrm{Re}\,[\, p_\pm \,] = 0$$

Different solutions are obtained for $x > \xi$ (closing in the lower half-plane) and for $x < \xi$ (closing in the upper half-plane)

$$G(x|\xi) = \begin{cases} i\,\dfrac{e^{-ip_-(x-\xi)}}{(p_- - p_+)} & x > \xi \\ -i\,\dfrac{e^{+ip_+(x-\xi)}}{(p_+ - p_-)} & x < \xi \end{cases} \tag{6.40}$$

or

$$G(x|\xi) = \begin{cases} G_-(x|\xi) \equiv -\dfrac{1}{2\kappa}\, e^{-\frac{(x-\xi)}{l_-}} & x > \xi \\ G_+(x|\xi) \equiv -\dfrac{1}{2\kappa}\, e^{+\frac{(x-\xi)}{l_+}} & x < \xi \end{cases} \tag{6.41}$$

where there are now two different length scales up and down glacier:

$$l_- = [\,\kappa - q\,]^{-1} \tag{6.42a}$$

$$l_+ = [\,\kappa + q\,]^{-1} \tag{6.42b}$$

and

$$\kappa = \sqrt{q^2 + \frac{\varphi_1}{l^2}}$$

If q = 0, then (6.41) reduces to (6.34). The solution to (6.37) is

$$u_1(x) = \int_{-\infty}^{x} \frac{n}{4\eta_e H_o}(\varphi_3\alpha_1 + \varphi_2 h)\, G_-(x|\xi)\, d\xi$$

$$+ \int_{x}^{\infty} \frac{n}{4\eta_e H_o}(\varphi_3\alpha_1 + \varphi_2 h)\, G_+(x|\xi)\, d\xi \tag{6.43}$$

or, in terms of the effective exponents μ and ν defined earlier,,

$$u_1(x) = \int_{-\infty}^{x} \left[(\mu + 1)\,\frac{h}{H_o} + \frac{\nu\alpha_1}{\alpha_o} \right] G_-(x|\xi)\, d\xi$$

$$+ \int_{x}^{+\infty} \left[(\mu + 1)\,\frac{h}{H_o} + \frac{\nu\alpha_1}{\alpha_o} \right] G_+(x|\xi)\, d\xi \tag{6.44}$$

where μ,ν are defined in (6.31). Again, the slope and thickness are both averaged with an exponential weighting function, but now the weighting function

(and corresponding characteristic length scale) differ up- and down-glacier. If $\alpha_o > \beta_o$ then $l_- > l_+$, whereas, if the bed diverges from the upper surface ($\alpha_o < \beta_o$) then $l_- < l_+$. For example, if the point x is in a wedge-shaped region (such as near the terminus of a glacier) then $\alpha_o > \beta_o$. From (6.41) and (6.42) we see that the averaging window is cut short within the wedge toward the terminus (G_+ applies here) and extended up-glacier (away from the wedge shaped region), where G_- applies. The opposite relation will hold for a region where $\beta_o > \alpha_o$. (such as high in the accumulation zone or below an icefall) If l (as defined in (6.23)) $= 3H_o$, then l_- and l_+ are given as in Table 6.2 for several values of the divergence $\alpha_o - \beta_o$, and the bed slope β_o (where we take $\frac{1}{\eta_e}\frac{d\eta_e}{dx} = 0$)

Table 6.2
Characteristic Averaging Lengths, l_+ and l_-

β_o,deg	$\alpha_o - \beta_o$,deg	l_-/H_o	l_+/H_o
0	0	3	3
	1	3.08	2.92
	2	3.16	2.84
	3	3.24	2.77
	5	3.42	2.63
	10	3.90	2.31
	20	5.06	1.78
	-5	2.63	3.42
	-10	2.31	3.90
5	0	2.98	2.98
10	0	2.91	2.91
10	10	3.75	2.25

Except for small differences in surface and bed slopes, the characteristic length up-glacier is seen to differ significantly from the length down-glacier. An asymmetric averaging window may therefore be required in regions such as near the base of an icefall or near the terminus, as is shown in Figure 6.2. In such cases, the above assumptions about the constancy of k and q may not hold, and

numerical integration of the Green's function problem equivalent to (6.37) may be required, with the x-dependence of k and q given explicitly.

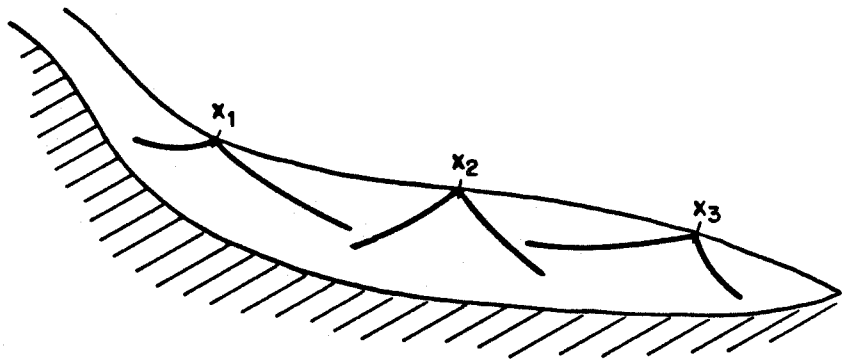

Figure 6.2 Schematic drawing of a glacier showing Green's functions G_+ and G_- for longitudinal averaging of slope and thickness, where $(x_1)dH_0/dx > 0$, $(x_2)dH_0/dx \approx 0$, $(x_3)dH_0/dx < 0$. The differences beteen windows at x_1, x_2, x_3 have been exaggerated.

The above treatment assumes that the effects of the cross-sectional channel geometry are not important in determining the stress field of the ice mass. However, the channels in which valley glaciers flow do affect the stresses. The weight of the glacier is supported by the entire perimeter of the channel. The averaging of the basal shear stress by the the channel cross-section can be roughly approximated by the inclusion of a shape factor f (Paterson,1981; and Chapter VIII of the present text), such that, when longitudinal gradients are neglected, $\tau_{xy} = f\rho gH\sin\alpha$ at the bed along the centerline. Thus, f may be included in the first term on the righthand side of (6.7) in order to approximately account for the presence of a channel. If the channel form is slowly varying along its length, then a perturbation in f about its mean value may be introduced ($f = f_o + f_1$). Following along lines similar to the above, there then results a longitudinal averaging of f_1 with the same weighting function as the

slope and thickness (that given by the Green's function (6.26) or (6.41)). Therefore, if the channel form is longitudinally varying, a weighted average of f over the length l should be included in any expressions for the stress (and flow) along the centerline. The idea of a shape factor breaks down off the centerline, and one must resort to a more complex analysis of the stress and velocity fields. However, the averaging scale determined for H and α along the centerline may hold for positions off the channel centerline, to a good approximation. (This requires that the transverse variation in slope be small. If it is not small, as may be the case within a curving channel, then an appropriately longitudinally -averaged slope may be required at each point across the channel. This is investigated in Chapter VIII.)

6.3 Application of Longitudinal Averaging to Observed Flow Response

The discussion in Chapter V dealt with local thickness and slope changes and their relation to the observed flow response. It was also noted that variations in a long-scale slope (as calculated with a boxcar-type window over the entire reach under study) showed a better correlation with velocity perturbations than did local slope changes. Local thickness changes did show a reasonable correlation with the velocity change, however. In this section, the theory developed in the previous section is applied to the observed response data, testing the effects of an exponentially -weighted average of slope and thickness variations on the change in velocity.

Between profiles B and I the slope of the bed and surface do not differ significantly, as is seen in Figure 3.7, and H_o is nearly constant. Thus, a symmetric averaging window was used. The exponential weighting function of equation (6.26) was approximated by a triangular window of unit amplitude and a half-width at the base equal to l. The length l is taken to be $3H_o$. Data required

for the averaging at the upper and lower profiles were extrapolated from the two contour maps available (with some adjustment), since the window extended well beyond the reach for which accurate data exist. Longitudinal averaging was performed along the centerline only. Thickness changes along the centerline obtained with the triangular averaging window for 1957/58 - 1977/78 data do not differ greatly from the local values (< 20%), while the longitudinally - averaged slope changes differ significantly from the local variations.

The righthand diagram in Figure 6.3 shows the logarithmic velocity change relative to the longitudinally-averaged (with the triangular window) thickness increase, $\Delta < h >_{\Delta}$ at the eight centerline points where the averaging was performed. The correlation between Δu and $\Delta < h >_{\Delta}$ is extremely good, r = .993 [P(null hypothesis) < 0.00001], with a very high F-statistic. The lefthand side of Fig. 6.3 shows the unaveraged (local) response at the same points for comparison. There is a definite decrease in the scatter about the line of best-fit when the averaged thickness is included. The slope of this line is reduced to $\beta_h = 3.60$ (the local Δh leads to a slope of $\beta_h = 4.13$) and an intercept of -9.4. From this slope a value of n=3.24 is obtained (with Ψ=0.85 in (5.8)), whereas the value of n from the local data is 3.86.

The correlation between $\Delta < \sin\alpha >_{\Delta}$ and Δu is not as pronounced as that found above for $\Delta < h >_{\Delta}$. However, there is an increase above that found for the local slope changes. With the length of the averaging window used much of the slope variation will be contained in the thickness variation (since $\frac{dH}{dx} \approx \alpha$, and, thus, the F-statistic for the inclusion of the slope changes will not be large since ΔH provides such a large decrease in the variance of Δu already). Also, the longitudinally-averaged slope changes will have larger errors associated with them than the thickness changes, especially in the regions were the data were

obtained from topographic maps (which have been found to be in error).

The variations of the data in Fig. 6.3 from the linear relation expected are a result of differences in channel geometry and slope changes at the different locations. The deviation from linearity are quite small, however, indicating that these effects are not large.

Figure 6.4 shows the centerline data shown in Fig. 6.3 as well as the response at the locations near, but not on, the centerline (one or two markers to the side of the centerline position). The longitudinally-averaged thickness change determined at centerline positions was used for these off-centerline points as well. The results again show an extremely good correlation between $\Delta < H >_{\Delta}$ and Δu ($r=0.973, F_H \approx 400$). This figure is to be compared with Fig. 5.7, which shows the local thickness changes. The longitudinal averaging of the thickness change along the centerline appears to apply at near-centerline points as well. (The local thickness changes at these points are close to the corresponding centerline values, which explains this correlation with the longitudinal averages at the centerline.) The slope of the response line in Fig. 6.4 is 3.39, which gives a value of $n=3.0$.

The results in Figures 6.3 and 6.4 show that longitudinal averages of the thickness and slope perturbations are important in determining the flow of an ice mass. The exponential weighting function derived in the previous section appears to describe the form and length scale of the averaging. Unfortunately, the length of Blue Glacier relative to its thickness and the length of the reach for which accurate data exist are not long enough to test these results further.

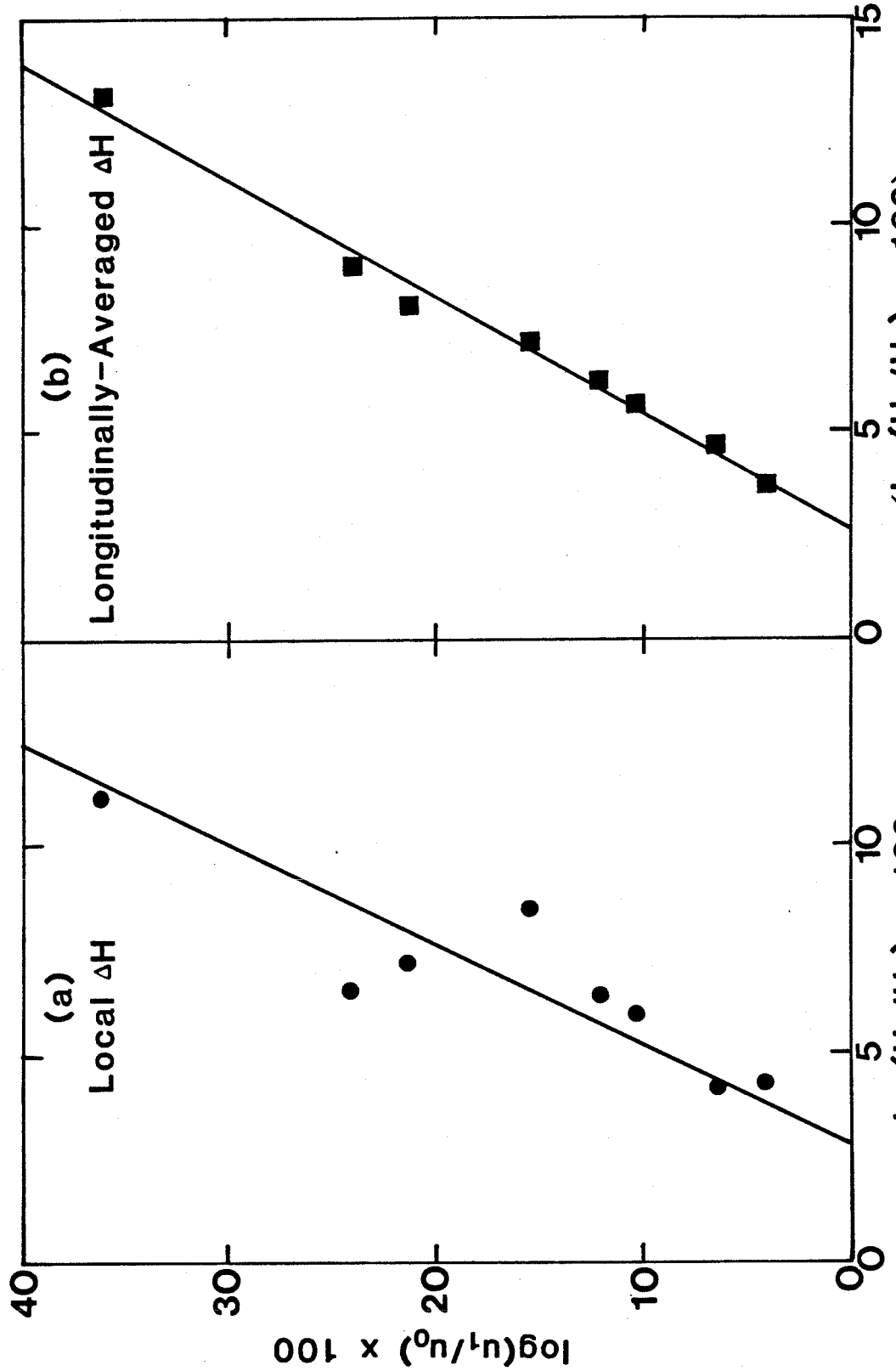

Figure 6.3 Velocity change vs. thickness change along centerline from 1957/58 to 1977/78. (a) local ΔH (b) longitudinal average of ΔH with triangular window of base = 6 x mean thickness.

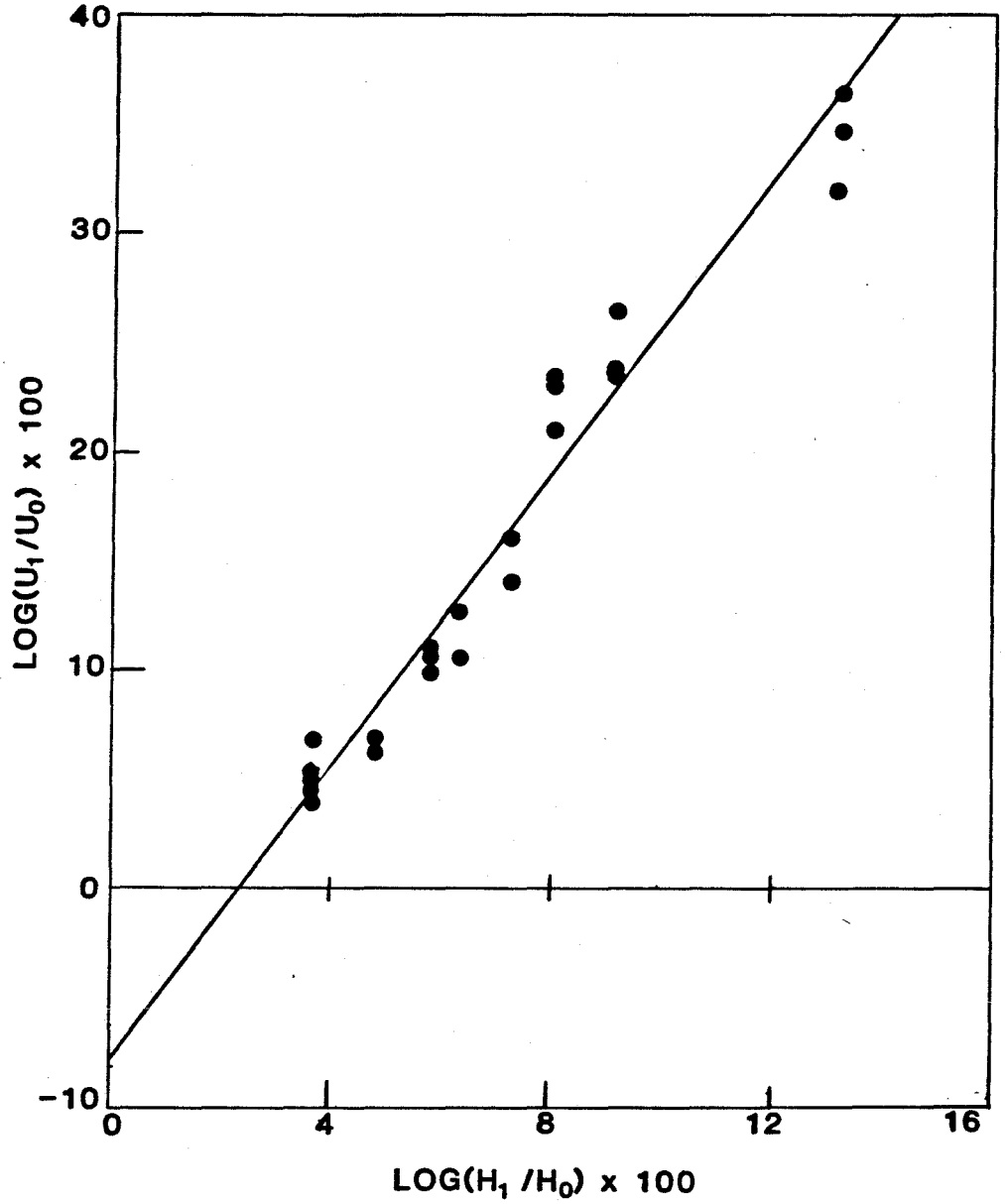

Velocity change vs. longitudinally-averaged centerline thickness change at near-centerline points, 1957/58 to 1977/78.

CHAPTER VII

FINITE ELEMENT ANALYSIS OF THE FLOW OF ICE

The steady-state stress and velocity fields of an ice mass are governed by the equilibrium equations and a non-linear constitutive relation between the rate of deformation and the stress. Several numerical techniques have been implemented to solve these coupled non-linear equations subject to mixed boundary conditions on the ice mass. Budd and Jennsen (1975) and Rassmusen and Campbell (1973) employed finite difference methods, while Hooke et al. (1979), Iken (1981), and Raymond (pers. comm.) have used two-dimensional finite-element techniques.

The finite-element method allows easy handling of very complex geometries and spatially varying material properties, and the natural incorporation of differential-type boundary conditions. The rich mathematical structure of the method and its ability to provide "optimal" accuracy in the resulting solutions make it an extremely useful tool. (These optimal properties and structure are described in Oden and Reddy, 1976.) For these reasons, the finite-element method was developed for use in this study.

This chapter gives a detailed discussion of the finite-element method (FE) and of the specific algorithm used in this study. Much of the general material in sections 7.2 through 7.9 may be found in standard texts on FE methods (Becker, et al., 1981; Hughes, pers. comm.; or Zienkiewicz, 1977), while specific results on the algorithm used here (sec. 7.5) are discussed by Hughes and Taylor (1978). However, it was felt that a complete description of the procedure is warranted here, both as a basis for the newly-developed material presented in later sections (7.10 - 7.13), and as an introduction to FE analysis for those readers

unfamiliar with this powerful method. The techniques developed here differ significantly from those used by previous authors employing finite-element methods in modeling glacier flow, and lead to an extension of FE's to more complex geometries.

In addition, section 7.11 provides a discussion of the flow law of ice used in the analytical and numerical models within this thesis.

7.1 Preliminary Discussion

Glacier ice flows as a non-Newtonian viscous fluid when the time scale of the imposed forces is large relative to its effective Maxwell time (which is on the order of 100 minutes under common stress levels). The stress-dependent viscosity leads to a non-linear constitutive relation between the rate of deformation and the deviatoric stress. The most common form of the constitutive relation is that given for power-law creep, or, as described in the glaciological literature, Glen's flow law (Glen, 1955). The dependence on the deviatoric stress implies that the ice is incompressible, i.e.

$$\operatorname{div} \mathbf{v} = 0 , \tag{7.1}$$

where $\mathbf{v}$ is the velocity. This assumption of incompressibility is valid due to the small relative magnitude of any elastic compression observed in nature, and can lead to simplification in analytical treatments. However, the incorporation of a kinematic constraint such as incompressibility into numerical treatments often leads to an increased computational complexity, an increase in the required storage and computer time, and possibly poor interpretation in the final results. The development of the penalty-function formulation for the finite-element analysis of incompressible Newtonian viscous flow (as described by Hughes, Liu, and Brooks, 1979) and the further incorporation of this formulation into studies involving non-linear fluids has led to a simple, efficient, and accurate method for

the finite-element implementation of incompressibility.

On the other hand, ice behaves elastically on short time scales, as is shown by its ability to propagate seismic waves in both shear and compression. The elastic properties of glacial ice are probably not important in determining the long-term motion of a large ice body, as the magnitude of the elastic strains is quite small. However, treatment of ice as a viscoelastic medium may be important in the discussion of some transient features of ice motion. In addition, the deletion of the requirement for incompressibility may lead to some computational simplification. Due to the availability of much of the basic computer code for FE flow analysis of a non-linear viscoelastic material and, because a thorough stability analysis has been made of an implicit algorithm for a viscoelastic solution procedure (Hughes, unpub., and Melosh and Raefsky, 1980 and Hughes and Taylor, 1978, respectively), this method was chosen for the present study.

Ice is therefore treated as a non-Newtonian viscoelastic material in which the total strain in the medium is given by a sum of the initial elastic deformation and the subsequent viscous deformation. For small displacement gradients and small rate-of-deformation gradients no distinction needs to be made between the rate-of-deformation tensor, with components

$$d_{ij} = \frac{1}{2}(v_{i,j} + v_{j,i}) , \tag{7.2}$$

where v_i are the components of the velocity field, and the time rate of change of the strain field, $\dot{\varepsilon}$, where

$$\dot{\varepsilon}_{ij} = \frac{d}{dt}\left[\frac{1}{2}(u_{i,j} + u_{j,i})\right] \quad . \tag{7.3}$$

Here u_i is the ith component of the displacement. The total strain may thus be written as

$$\varepsilon_{ij}^{tot} = \varepsilon_{ij}^{elastic} + \int_{o}^{t} d_{ij}^{v}\, dt \tag{7.4}$$

or, in terms of the time-rate of change of the strain,

$$\dot{\varepsilon}^{elastic} = \dot{\varepsilon}^{tot} - \mathbf{d}^{v} \tag{7.5}$$

where $\mathbf{d}^{v}$ is the viscous "strain rate". Let c_{ijkl} be the components of the elastic modulus tensor and σ_{ij} components of the Cauchy stress tensor. Then

$$\dot{\sigma}_{ij} = c_{ijkl}\,(\dot{\varepsilon}^{tot_{kl}} - d_{kl}^{v}) \tag{7.6}$$

where the summation convention on repeated indices is used and the superposed dot denotes time differentiation. The viscous rate of deformation is related to the stresses by the relation

$$d_{kl}^{v} = \beta_{kl}(\sigma) \tag{7.7}$$

The terms c_{ijkl} and β_{kl} will be discussed more fully below, but it should be noted that both $\mathbf{c}$ and $\boldsymbol{\beta}$ are positive-definite tensor operators. In the following sections this general viscoelastic constitutive relation (7.6 and 7.7) is used in the development of the numerical algorithm for the solution of the equilibrium equations for the stress and velocity fields within an ice mass.

Some preliminary notation will be described first. Let Ω be an open set contained in $\mathbf{R}^n$, $n \geq 2$. Denote the piecewise smooth boundary of Ω by $\partial\Omega$, and the closure of a set by an overbar (e.g. $\overline{\Omega}$). As an example, the set Ω may represent a two dimensional cross section of a glacier with boundary $\partial\Omega$ given by the bedrock channel and the glacier surface. A general point in Ω is denoted $\mathbf{x}$, with components denoted by the standard indicial notation ($\mathbf{x} = x_i \hat{e}_i$, where $\hat{e}_i$ is the i-th basis vector). Repeated indices imply summation unless underlined. Boldface quantities represent a tensor of rank 1 or higher. A comma is used to denote covariant differentiation with respect to the coordinates (e.g. in a Cartesian system, $u_{i,j} = \frac{\partial u_i}{\partial x_j}$), and t denotes time. In this chapter only, $\mathbf{u}$ will represent

the displacement field and **v** the velocity field.

Let the space of square integrable scalar functions on Ω be denoted $L_2(\Omega)$ and let $H^1(\Omega)$ denote the space of L_2 functions whose first partials are also in $L_2(\Omega)$, i.e.,

$$\|u\|_1 = \left[\int_\Omega (u^2 + u_{,i} u_{,i}) \, d\Omega \right]^{1/2} < \infty \tag{7.8}$$

where $\|u\|_1$ is termed the L-norm.

Kronecker delta is denoted δ_{ij}. The Cauchy stress tensor is considered symmetric and a prime denotes the deviatoric portion of a given tensor $(\sigma'_{ij} = \sigma_{ij} - \frac{1}{3}\sigma_{kk}\delta_{ij})$.

In order to apply the finite element method to a specific problem, the equations and boundary conditions of the problem must be cast into a weak (integral) form upon which discretization of the domain into elements and approximation of the variables may be performed. The following sections develop these various statements of the problem, leading to the coupled linearized system of equations on the discretized domain.

7.2 Strong Form of the Initial-Boundary-Value Problem

Assume the following functions are prescribed:

$$\mathbf{f} : \Omega \rightarrow \mathbf{R}^n \quad (\text{body force}) \tag{7.9}$$

$$\mathbf{g} : \partial\Omega_{\mathbf{g}} \rightarrow \mathbf{R}^n \quad (\text{prescribed displacement, e.g. basal slip}) \tag{7.10}$$

$$\mathbf{h} : \partial\Omega_{\mathbf{h}} \rightarrow \mathbf{R}^n \quad (\text{prescribed surface traction, e.g. free surface}). \tag{7.11}$$

Let **g** and **h** be defined on disjoint subsets of $\partial\Omega$ such that, for each component of **g** or **h**, the following holds:

$$\partial\Omega = \overline{\partial\Omega_{g_i} \cup \partial\Omega_{h_i}} \quad \text{and} \quad \partial\Omega_{g_i} \cap \partial\Omega_{h_i} = \phi \ . \tag{7.12}$$

Then the formal statement of the initial-boundary-value problem is: Find the vector field $\mathbf{u} = \mathbf{u}(\mathbf{x},t) : \overline{\Omega} \rightarrow \mathbf{R}^n$ and the tensor field $\boldsymbol{\sigma} = \boldsymbol{\sigma}(\mathbf{x},t) : \overline{\Omega} \rightarrow \mathbf{R}^n$, such that $\forall \mathbf{x} \in \Omega$ and $t \in [0,T]$ the following are satisfied:

$$\begin{aligned}
\nabla \cdot \boldsymbol{\sigma} + \mathbf{f} &= 0 && \mathbf{x} \in \Omega \\
u_i(\mathbf{x},t) &= g_i && \mathbf{x} \in \partial\Omega_{g_i},\ t \in [\,0,T\,] \\
\sigma_{ij}(\mathbf{x},t)\, n_j(\mathbf{x}) &= h_i && \mathbf{x} \in \partial\Omega_{h_i},\ t \in [\,0,T\,] \\
u_i(\mathbf{x},0) &= u_{oi}(\mathbf{x}) && \mathbf{x} \in \Omega \\
\sigma_{ij}(\mathbf{x},0) &= \sigma^{o}_{ij}(\mathbf{x}) && \mathbf{x} \in \Omega \\
\dot{\sigma}_{ij} &= c_{ijkl}(\dot{\varepsilon}^{tot}_{kl} - d^{v}_{kl})
\end{aligned} \tag{7.13}$$

where $\mathbf{n}$ is the outward unit normal to $\partial\Omega$, and $\mathbf{u_o}$, $\boldsymbol{\sigma}^o$ are the given initial data. This problem is well posed, and thus will admit a unique solution. (The initial and boundary data must be compatible and, at t = 0, the initial stress over the domain must equilibrate the total body force.)

The first relation in (7.13) states the conservation of linear momentum in which the inertial terms are negligible (which is easily shown to hold for slow, creeping flow of ice). The first boundary condition in (7.13) is termed the essential condition or the g-data, while the second is termed the natural boundary condition.

This strong (differential) form of the problem will be denoted (S).

7.3 Weak Formulation

Define the space of variations V_i such that

$$V_i = \{\, w_i \in H^1(\Omega) \mid w_i = 0 \ \text{ on } \ \partial\Omega_{g_i} \,\} \tag{7.14}$$

and the trial solution space S_i

$$S_i = \{ w_i \in H^1(\Omega) \mid w_i = g_i \text{ on } \partial\Omega_{g_i} \}. \tag{7.15}$$

The functions in V_i are zero on the boundary where the displacement is prescribed, while those functions in S_i are equal to the prescribed values on this portion of the boundary. The weak statement of the initial-boundary value problem may be developed by multiplying the first relation in (7.13) by an arbitrary function in V_i and integrating over the domain Ω. Integration by parts and use of the boundary conditions in (7.13) leads to the following statement of the so-called weak form of the initial-boundary value problem defined in (7.13):

Find $u_i(\mathbf{x},t) \in S_i$ such that $\forall w_i \in V_i$

$$\int_\Omega w_{(i,j)}\, \sigma_{ij}\, d\Omega = \int_\Omega w_i f_i\, d\Omega + \sum_{i=1}^{ndof} \left(\int_{\partial\Omega h_i} w_i h_i\, dS \right) \tag{7.16}$$

and

$$\dot{\sigma}_{ij} = c_{ijkl} (\dot{\varepsilon}_{kl}^{tot} - d_{kl}^{v}) \tag{7.17}$$

where $w_{(i,j)}$ denotes the symmetric part of $w_{i,j}$ and ndof is the number of degrees of freedom (i.e. number of displacement components)

The solution of the strong form is equivalent to that of the weak form, as can easily be shown (Hughes, pers. comm.). Thus, solution of the weak form (which may be done numerically, as developed below) is equivalent to solution of the boundary value problem involving the partial differential equilibrium equations (7.13). (The nature of the functions w will be described below.)

7.4 Galerkin Formulation

The weak form as stated above seeks to find a solution u in an infinite dimensional space, S. Dealing with such a space numerically is quite difficult, and thus we must seek an approximate solution in some smaller finite subspace of S. The degree of this approximation depends on the complexity of the set of functions

in which we restrict our search for the solution.

The actual problem to be solved numerically, then, is simply a finite-dimensional approximation to the weak form stated above. The functions u and w are elements of finite-dimensional trial solution and variation spaces, respectively. In what follows, we will restrict ourselves to this approximate form, which is termed the Galerkin formulation.

7.5 Matrix Formulation and Implicit Algorithm for Solution with a Non-Linear Constitutive Relation

If we introduce the concepts of the stress "vector", strain "vector", and an elastic compliance matrix into the Galerkin formulation of (7.16) and (7.17), then we may develop a time stepping implicit algorithm for the approximate solution of the system defined in equations (7.13). Taking the two dimensional case of plane strain as an illustrative example (with the required defining relations for the various stress and strain "vectors" pertinent to other cases given later), the stress "vector" $\vec{\sigma}$, strain "vector" $\vec{\varepsilon}$ and the strain operator, **L** are given as (using engineering notation)

$$\vec{\sigma} = \begin{Bmatrix} \sigma_{11} \\ \sigma_{22} \\ \sigma_{12} \end{Bmatrix}, \quad \vec{\varepsilon}(\mathbf{u}) = \begin{Bmatrix} u_{1,1} \\ u_{2,2} \\ u_{1,2} + u_{2,1} \end{Bmatrix}, \quad \mathbf{L} = \begin{Bmatrix} \frac{\partial}{\partial x} & 0 \\ 0 & \frac{\partial}{\partial y} \\ \frac{\partial}{\partial y} & \frac{\partial}{\partial x} \end{Bmatrix} \tag{7.18}$$

for a displacement field **u**. The elastic coefficient matrix, **D**, is given as

$$[D_{IJ}] = \begin{bmatrix} D_{11} & D_{12} & D_{13} \\ & D_{22} & D_{23} \\ \text{sym} & & D_{33} \end{bmatrix} = \begin{bmatrix} \lambda+2\mu & \lambda & 0 \\ & \lambda+2\mu & 0 \\ \text{sym} & & \mu \end{bmatrix} \tag{7.19}$$

where $D_{IJ} = c_{ijkl}$ with I,J chosen in the usual manner (Becker,et al.,1981) and where λ, μ are the Lamé parameters.

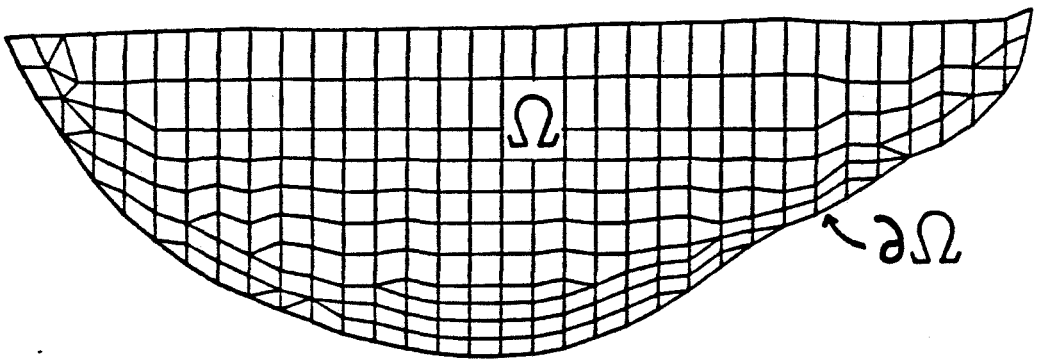

Figure 7.1 Discretization of domain Ω into non-overlapping elements. Boundary of domain is ∂Ω. Rectangular and triangular elements are shown.

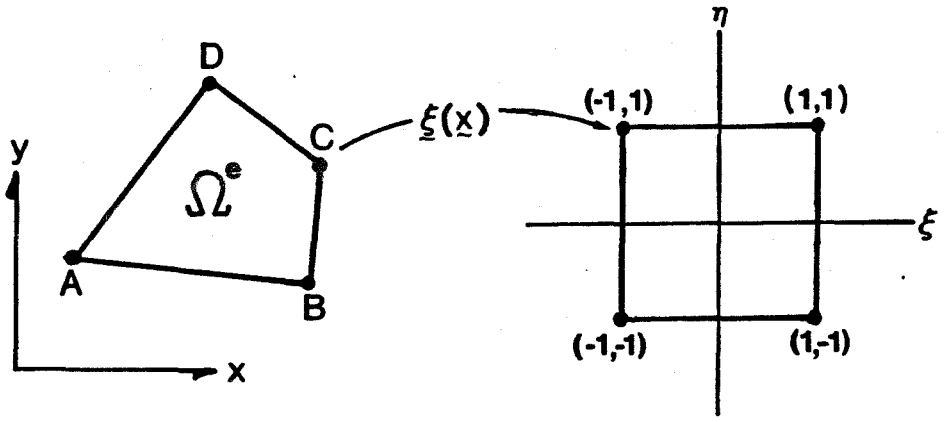

Figure 7.2 Mapping of element in Ω into master element.

The elastic stresses are given by

$$\vec{\sigma} = \mathbf{D}\vec{\varepsilon}^{\text{elast}}(\mathbf{u}) \tag{7.20}$$

If we introduce these relations into (7.16) and a finite difference approximation to (7.17) over the time interval $\Delta t_{n+1} = t_{n+1} - t_n$, we find

$$\int_\Omega (\mathbf{L}\mathbf{w})^T \vec{\sigma}_n \, d\Omega = F_n \tag{7.21}$$

where

$$F_n = \int_\Omega \mathbf{w} f_n \, d\Omega + \int_{\partial\Omega_h} \mathbf{w} h_n \, ds \quad , \quad \vec{\sigma}_n = \vec{\sigma}(t_n) \text{ ,etc.} \tag{7.22}$$

and

$$\vec{\sigma}_{n+1} - \vec{\sigma}_n = \mathbf{D}\left[\vec{\varepsilon}(u_{n+1}) - \vec{\varepsilon}(u_{n+1}) - \Delta t_{n+1} \, \beta(\vec{\sigma}_{n+\alpha}) \right] \tag{7.23}$$

where

$$\sigma_{n+\alpha} = (1 - \alpha)\sigma_n + \alpha \sigma_{n+1} \qquad \alpha \in [0,1] \tag{7.24}$$

and $\vec{\varepsilon} = \vec{\varepsilon}^{\text{tot}}$ and β is given by (7.7). For $\alpha = 0, 1/2, 1$, (7.23) and (7.24) refer to a forward, central, and backward difference approximation to (7.17), respectively.

Galerkin's method now consists of finding an approximate solution to the weak form via (7.21-7.24) within a finite dimensional subspace of S. To this end, let the domain be discretized into n_{el} non-overlapping subregions which are termed "elements" (see figure 7.1). This discretization gives rise to a set Λ of nodal points, whose dimension (n_{np}) depends on the number of elements and the number of nodes per elements, n_{en}. Let the domain of an element be denoted Ω^e and its boundary by $\partial\Omega^e$. Partition the set of nodal points into those that lie within the set of boundary points for which the displacement is prescribed and those at which u_i is unknown. If x_A denotes the position of the Ath node, then this partition takes the form

$$\Lambda = \Lambda_{g_i} \cup (\Lambda - \Lambda_{g_i}) \quad \text{and} \quad \Lambda_{g_i} = \{A \in \Lambda \mid \mathbf{x}_A \in \partial\Omega_{g_i}\} . \tag{7.25}$$

Represent the finite dimensional approximations of $\mathbf{w}$ and $\mathbf{g}$ within an element as interpolations from the values at the nodes. This interpolation is performed using a set of "shape" functions, $N_A(\mathbf{x})$, each associated with a node A:

$$w_i^h = \sum_{A \in \Lambda - \Lambda_{g_i}} \mathbf{N}_A(\mathbf{x}) w_{iA} , \tag{7.26a}$$

$$u_i = \sum_{A \in \Lambda} N_A(\mathbf{x}) u_{iA} , \tag{7.26b}$$

where w_{iA} and u_{iA} are the values of w_i and u_i at node A. Once the values of the solution u_{iA} are known at the nodes, then u_i is determined from the interpolation (6.26a). The shape functions satisfy

$$N_A(\mathbf{x}_B) = \delta_{AB} \tag{7.27}$$

In a similar manner, let

$$g_i^h = \sum_{A \in \Lambda_{g_i}} N_A(\mathbf{x}) g_{iA} , \tag{7.28}$$

where g_{iA} is the value of the prescribed boundary displacement at node A.

Substituting (7.26) and (7.27) into (7.21)-(7.24), and noting that the w_i are arbitrary elements of V_i, the following system of equations is obtained:

$$\hat{\mathbf{e}}_i^T \int_\Omega (LN_A)^T \vec{\sigma}_n d\Omega = \hat{\mathbf{e}}_i^T \int_\Omega N_A \mathbf{f}\, d\Omega + \hat{\mathbf{e}}_i^T \int_{\partial\Omega_h} N_A \mathbf{h}\, ds \tag{7.29a}$$

for every node in $\Lambda - \Lambda_g$ and each degree of freedom i (where $\hat{\mathbf{e}}$ is the unit vector in the i-th direction). The coefficients w_{iA} in the interpolation (7.26a) are constants relative to the integrations involved in (7.29a) and, thus, they cancel from the equation. In effect, then, the arbitrary functions w_i may be taken as approximate "delta" functions centered at the nodes which cast the weak form into a problem involving only the unknown solution u_i (related to the stresses). The stresses are determined by

$$\vec{\sigma}_{n+1} - \vec{\sigma}_n = \mathbf{D}\,[\,\mathbf{L}\mathbf{N}_B\mathbf{u}_{n+1} - \mathbf{L}\mathbf{N}_B\mathbf{u}_n\,] - \Delta t_{n+1}\mathbf{D}\boldsymbol{\beta}(\vec{\sigma}_{n+\alpha}) \tag{7.29b}$$

where $\mathbf{u}_n = \mathbf{u}_B$ at time t_n.

Define the strain- displacement matrix $\mathbf{B}_A$ for node A as

$$\mathbf{B}_A = \mathbf{L}\mathbf{N}_A \tag{7.30}$$

$$\left[e\,g = \begin{bmatrix} N_{A,x} & 0 \\ 0 & N_{A,y} \\ N_{A,y} & N_{A,x} \end{bmatrix} \text{for plane strain} \right]$$

and

$$\mathbf{F}_n = \int_\Omega \mathbf{N}_A \mathbf{f}\, d\Omega + \int_{\partial\Omega_h} \mathbf{N}_A \mathbf{h}\, dS \tag{7.31}$$

Let $\Delta\mathbf{u}_{n+1} = \mathbf{u}_{n+1} - \mathbf{u}_n$ and $\boldsymbol{\beta}_{n+\alpha} = \boldsymbol{\beta}(\vec{\sigma}_{n+\alpha})$. Then the final form of the approximate visco-elastic initial- boundary value problem can be written:

$$\int_\Omega \mathbf{B}_A^T \vec{\sigma}_n\, d\Omega = \mathbf{F}_n \tag{7.32a}$$

$$\vec{\sigma}_{n+1} - \vec{\sigma}_n = \mathbf{D}\mathbf{B}_A\Delta\mathbf{u}_{n+1} - \Delta t_{n+1}\mathbf{D}\boldsymbol{\beta}_{n+\alpha} \tag{7.32b}$$

An implicit algorithm for the solution of this general form is given by Hughes and Taylor (1978) for non-linear time dependent materials. In what follows, a simplified time - stepping algorithm is developed for solution of (7.32) subject to a fairly low-order non-linearity in the constitutive relation (power-law type) where results at steady state are of primary interest.

Let $t_o = 0$ and denote the Jacobian of $\boldsymbol{\beta}$ with respect to the stress components as $\boldsymbol{\beta}'\left(= \dfrac{\partial\boldsymbol{\beta}}{\partial\vec{\sigma}} \right)$. Noting that

$$\vec{\sigma}_{n+\alpha} = (1-\alpha)\vec{\sigma}_n + \alpha(\vec{\sigma}_n + \Delta\vec{\sigma}_{n+1} = \vec{\sigma}_n(1 + \alpha\frac{\Delta\vec{\sigma}_{n+1}}{\vec{\sigma}_n}) \;,\; (\vec{\sigma}_n \neq 0)\,, \tag{7.33}$$

where $\Delta\vec{\sigma}_{n+1} = \vec{\sigma}_{n+1} - \vec{\sigma}_n$, $\boldsymbol{\beta}_{n+\alpha}$ may be linearized about the value $\vec{\sigma}_n$:

$$\boldsymbol{\beta}_{n+\alpha} = \boldsymbol{\beta}_n + \alpha \boldsymbol{\beta}'(\vec{\sigma}_n)\Delta\vec{\sigma}_{n+1} \quad . \tag{7.34}$$

From (7.32b) and (7.34)

$$\Delta\vec{\sigma}_{n+1} = [\, \mathbf{D}^{-1} + \alpha\Delta t_{n+1}\boldsymbol{\beta}'_n \,]^{-1} (\mathbf{B}_A \Delta \mathbf{u}_{n+1} - \Delta t_{n+1}\boldsymbol{\beta}_n) \quad . \tag{7.35}$$

Evaluating (7.32a) at t_{n+1} and subtracting gives

$$\int_\Omega \mathbf{B}_A^T \Delta\vec{\sigma}_{n+1}\, d\Omega \; = \mathbf{F}_{n+1} - \mathbf{F}_n \tag{7.36}$$

which, using (7.35) at a node B, becomes

$$\int_\Omega \mathbf{B}_A^T [\, \mathbf{D}^{-1} + \alpha\Delta t\boldsymbol{\beta}'_n \,]^{-1} \mathbf{B}_B \Delta \mathbf{u}_{n+1} d\Omega \; =$$

$$\int_\Omega \mathbf{B}_A^T [\, \mathbf{D}^{-1} + \alpha\Delta t\boldsymbol{\beta}'_n \,]^{-1} \Delta t_{n+1}\boldsymbol{\beta}_n\, d\Omega \; + \mathbf{F}_{n+1} - \mathbf{F}_n \, . \tag{7.37}$$

This may be written

$$\mathbf{K}_{n+1}\, \Delta \mathbf{u}_{n+1} = F_{n+1} \tag{7.38}$$

where the incremental stiffness $\mathbf{K}_{n+1}$ has components $K_{n+1_{PQ}}$ defined as

$$K_{n+1_{PQ}} = \hat{\mathbf{e}}_i^T \int_\Omega \mathbf{B}_A^T [\, \mathbf{D}^{-1} + \alpha\Delta t\boldsymbol{\beta}_n' \,]^{-1} \mathbf{B}_B\, d\Omega \; \hat{\mathbf{e}}_j \tag{7.39}$$

and the components of the effective force, F_{n+1_P}, are

$$F_{n+1_P} = \hat{\mathbf{e}}_i^T \int_\Omega \mathbf{B}_A^T [\, \mathbf{D}^{-1} + \alpha\Delta t\boldsymbol{\beta}'_n \,]^{-1} \Delta t\boldsymbol{\beta}_n\, d\Omega \; + \Delta F_{n+1_P}$$

$$- \sum_{B\in\Lambda_{g_j}} \left[\sum_{j=1}^{ndof} \hat{\mathbf{e}}_i^T \int \mathbf{B}_A^T [\, D^{-1} + \alpha\Delta t\boldsymbol{\beta}\cdot n \,]^{-1} \mathbf{B}_B\, d\Omega \; \hat{\mathbf{e}}_j g_{jB} \right] \tag{7.40}$$

where the terms involving the known nodal displacements (g_{iA}) have been transferred to the lefthand side, leaving only the unknown nodal displacements (u_{iA}) on the righthand side. Also,

$$P = ID(i,A)$$
$$Q = ID(j,B)$$

The ID (location) array gives the equation number in the global system of linear equations (6.43) for a given degree of freedom k and node C,

$$ID(k,C) = \left\{ \begin{array}{cc} P & \text{if } C \in (\Lambda - \Lambda_{g_k}) \\ 0 & \text{if } C \in \Lambda_{g_k} \end{array} \right\} \tag{7.41}$$

That is, if the i-th component of displacement at node A is known, then no equation number is assigned to this value of $u_{iA}(=g_{iA})$, whereas if this component is unknown then an equation number must be assigned for the variable u_{iA}.

If there is no change in the body force or prescribed tractions between time steps then $\Delta F_{n+1} = 0$. The essential boundary condition (g-data) is directly incorporated into the solution algorithm through the final term on the right-hand side of (7.40). $\mathbf{K}_{n+1}$ is a symmetric, banded matrix if β is positive definite. The rank of K is n_{eq} x n_{eq} where

$$n_{eq} = \sum_{ndof} [\, \dim(\Lambda - \Lambda_{g_i}) \,] .$$

In creeping flow problems, Δu_{n+1} in (7.43) may be interpreted as the velocity v_{n+1} over the time internal Δt_{n+1}, i.e.

$$v_{n+1} = \frac{\Delta u_{n+1}}{\Delta t_{n+1}} \tag{7.42}$$

The main steps of the solution algorithm are summarized in Table 7.1.

The algorithm in Table 7.1 requires that the large stiffness matrix be reformed (from eq. (6.39)) and refactored for the inversion required in the solution of step III at each time step. In some situations (e.g. when the material matrix $[\mathbf{D}^{-1} + \alpha \Delta t_{n+1} \beta' \text{subn}]$ does not vary greatly between time steps), this reforming and refactoring of K need not be undertaken at each time step. This is economically desirable, since this operation is the single most time-

Table 7.1
Time-Stepping Implicit Algorithm

I. Initially, set n = 0 ($\Delta t=0$).Then $\mathbf{d}^v=0$. Compute the elastic stiffness $\mathbf{K}_o$ and force term $\boldsymbol{f}_0$. Solve for the elastic displacements $\mathbf{u}_o = \mathbf{K}_o^{-1}\mathbf{F}_o$ and then evaluate the elastic stresses $\vec{\sigma}_o = \mathbf{DBu}_o$.

II. With Δt_{n+1} given, form $\mathbf{K}_{n+1}$ and the effective force F_{n+1} where (7.51)

$$\mathbf{K}_{n+1} = \int_\Omega \mathbf{B}^T [\, \mathbf{D}^{-1} + \alpha \Delta t_{n+1} \boldsymbol{\beta}'_n \,]^{-1} \mathbf{B}\, d\Omega$$

$$F_{n+1} = \int_\Omega \mathbf{B}^T [\, \mathbf{D}^{-1} + \alpha \Delta t_{n+1} \boldsymbol{\beta}'_n \,]^{-1} \Delta t_{n+1} \mathbf{B}\boldsymbol{\beta}_n\, d\Omega + \Delta F_{n+1} - \int_\Omega \mathbf{B}^T [\, .. \,]^{-1} \mathbf{g}\, d\Omega$$

III. Solve $\mathbf{K}_{n+1}\, \Delta \mathbf{u}_{n+1} = F_{n+1}$

IV. Evaluate the stress increment

$$\Delta \vec{\sigma}_{n+1} = [\, \mathbf{D}^{-1} + \alpha \Delta t_{n+1} \boldsymbol{\beta}'_n \,]^{-1} (\mathbf{B} \Delta \mathbf{u}_{n+1} - \Delta t_{n+1} \boldsymbol{\beta}_n)$$

V. Update the displacements and stresses: $\mathbf{u}_{n+1} \leftarrow \mathbf{u}_n + \Delta \mathbf{u}_{n+1}$; $\vec{\sigma}_{n+1} \leftarrow \vec{\sigma}_n + \Delta \vec{\sigma}_{n+1}$

VI. Let $n \leftarrow n + 1$. If $\sum_{k=1}^{n} \Delta t_k < T$ go to II., otherwise stop.

---

consuming operation in the solution algorithm.

If $\alpha = 0$ then the algorithm becomes explicit, corresponding to the algorithm given by Zienkiewicz and Cormeau (1974) for solution of viscoplasticity and plasticity problems. The explicit algorithm takes the stiffness matrix to be a constant for all time steps, and this, along with the simplification in coding, makes the explicit algorithm more advantageous in some cases. However, as will be seen below, this algorithm suffers from rather severe time-step restrictions. On the other hand, the implicit algorithm ($\alpha > 0$) is numerically stable for some values of α, allowing quicker convergence to steady state. Unfortunately, in most of the models described in later chapters it was required to reform and refactor the stiffness every (or every second) time step.

7.6 Stability

The stability of the explicit ($\alpha = 0$)and implicit algorithms has been discussed by Cormeau (1974) and Hughes and Taylor (1978), respectively. The algorithms lead to a system of ordinary differential equations when the elemental numerical integration scheme (discussed below) is introduced into the system (7.32). The largest eigenvalue, λ, of this ODE system governs the size of the time step in the explicit solution procedure (Cormeau, 1974) and of the implicit scheme when $\alpha < \frac{1}{2}$. For a material governed by power-law creep at stress levels near those found in glacier flow problems this forms a rather stringent requirement on the maximum length of the time step, especially when the solution at steady state is of interest.

An amplification factor, A, may be defined as (σ designates the array of stress components at all integration points)

$$\sigma_{n+1} = A\,\sigma_n \tag{7.43}$$

Thus, if $A \leq 1$, then $|\sigma_{n+1}| \leq |\sigma_n|$ and the algorithm is stable. Hughes and Taylor (1978) find that for $\alpha > 0$

$$A_{n+1} = \frac{1 + \Delta t_{n+1}(1-\alpha)\lambda}{1 + \Delta t_{n+1}\alpha\lambda} \tag{7.44}$$

and therefore, if $\alpha \geq \frac{1}{2}$, the implicit algorithm is unconditionally stable[1]. This leads to an efficient and cost-effective scheme for solution of non-linear creeping flow problems.

7.7 Element Formulation

In any finite element scheme it is most convenient to form the arrays K_{n+1} and F_n in an element-by-element fashion. To this end, the global stiffness

1. "Unconditionally stable" means that no size restriction is placed on Δt.

and effective force may be written as the assembly of n_{el} element contributions, $\mathbf{k}^e$ and $\boldsymbol{f}^e$, respectively :

$$\mathbf{K}_n = \mathop{\mathbf{A}}_{e=1}^{n_{el}} (\mathbf{k}_n^e) \quad \text{and} \quad F_n = \mathop{\mathbf{A}}_{e=1}^{n_{el}} (\boldsymbol{f}_n^e) \tag{7.45}$$

where the assembly operator **A** effectively places each elemental contribution into a very sparse $n_{eq} \times n_{eq}$ matrix (or $n_{eq} \times 1$) with zeros everywhere except the rows and columns corresponding to the particular element contributions, and then sums the resulting n_{el} sparse arrays to form **K** and **F**.

The elemental contributions are defined in a manner similar to the global quantities. However, it is more efficient to shift to a local ordering scheme on the element nodes and local equation numbers. A general element in this study was taken to be a 4-node quadrilateral. In general there are n_{dof} degrees of freedom per node (displacement or velocity components) and thus a total of $n_{ee} = n_{en}\, n_{dof}$ elemental equations, where n_{en} is the number of nodes per element (4). There are, for example, 8 equations per 4-node element in plane strain (2 dof). Let N_a^e denote the shape function associated with node a of the eth element, and $\Omega^e, \partial\Omega^e$ the domain and boundary of this element. Then the components of the elemental stiffness and effective force (right-hand side of (7.43)) in this local ordering scheme can be written (where the time subscript, n, is dropped for clarity):

$$k_{pq}^e = \hat{e}_i^T k_{ab}^e \hat{e}_j = \hat{e}_i^T \int_{\Omega_e} (\mathbf{B}_a^e)^T \bar{\mathbf{D}} \mathbf{B}_b^e \, d\Omega \, \hat{e}_j \tag{7.46}$$

$$f_p^e = \int_{\Omega^e} N_a^e f_i \, d\Omega + \int_{\partial\Omega_{h_i}^e} N_a^e h_i \, dS - \sum_{q=1}^{n_{dof}} k_{pq}^e g_q^e + \int_{\Omega^e} (\mathbf{B}_a^e)^T \bar{\mathbf{D}} \Delta t \beta \, d\Omega \tag{7.47}$$

where

$$\bar{\mathbf{D}} = [\, D^{-1} + \alpha \Delta t \beta' \,]^{-1}$$

$$g_q^e = \begin{cases} g_j(\mathbf{x}_b^e) & \text{if } \mathbf{x}_b^e \in \partial\Omega_{g_j} \\ 0 & \text{if } \mathbf{x}_b^e \notin \partial\Omega_{g_j} \end{cases}$$

$$\partial\Omega_{h_i}^e = \partial\Omega^e \cap \partial\Omega_{h_i}$$

and

$$1 \leq p,q \leq n_{ee}$$

The elemental array numbers (p,q) are defined as $p = n_{dof}(a-1) + i$ for dof i and local node a. This leads to an 8 × 8 elemental stiffness for plane strain, where there are 2 components of displacement (dof) and 4 nodes per element (assumed here).

The choice of simple 4-node bilinear quadrilaterals (Figure 7.2) as the basic two - dimensional element in the present study perhaps requires some justification. Higher-order elements (with nodes along the sides as well as at the corners) have been used by some investigators when dealing with Newtonian-fluid dynamical problems, as well as in general elasticity. However, in an implicit iterative (or time-stepping) algorithm, such as that used here, such an element can lead to a large increase in computing cost due the large rank increase in **K**. An iterative procedure is in itself only an approximation, and therefore the relatively small increase in accuracy for a given grid discretization with higher order elements was not thought to be worth the extra computing costs. This is especially true in that, for the constitutive relation used, the stiffness needed to be reformed and refactored fairly often, which is the single most costly operation in the computational algorithm. Similarly, it was felt that the number of triangular elements required for a given accuracy within a domain precluded the use of strictly triangular elements. However, a general bilinear quadrilateral-element-based routine can easily be altered to allow the incorporation of a

number of triangular elements simply by collapsing two nodes of a rectangular region into one, and appropriately orthogonalizing the shape functions. This ability to incorporate triangular elements into the general framework allows excellent discretization of irregular domains without the introduction of high-aspect ratio elements (which are relatively inaccurate). The computational results of Hughes, Liu, and Brooks (1979) for Newtonian fluids support the ideas on versatility of the bilinear quadrilateral element.

Once the decision to use these particular elements has been made, the shape functions N_a used in many of the relations above but as yet undefined, may be explicitly determined. These functions are given in the next section.

7.8 Elemental Calculations

It is customary in finite-element calculations to work with a geometrically simple "master element" (see any general reference on FE, such as Hughes, pers. comm.; Becker et al. 1981; or Zienkiewicz, 1977). A general bilinear quadrilateral can be mapped onto a simple square master element, as is shown in Figure 7.2. The curvilinear mapping will be well-behaved if the Jacobian determinant of the transformation is greater than zero, which requires the original element to have no included angles > 180°. The definition of this mapping may be approximated by

$$\mathbf{x}(\xi) = \left(\sum_{\text{nen}} \varphi_a(\xi)\mathbf{x}_a^e \right) \tag{7.49}$$

where ξ_i are the coordinates of the master element and x_{ia}^e are the coordinates of the node in the local ordering scheme. If the interpolation functions, φ_a, are taken to be the same as the elemental shape functions, N_a, and of the same number per element, then the elements are termed *isoparametric* elements. Isoparametric elements form a smooth, complete representation over a sufficiently smooth domain with the proper continuity across element

boundaries. Elements of this type were used in the present study.

The shape functions defined on the master bilinear quadrilateral can be shown to be represented by Lagrange polynomials of order 1. Thus, for the master element shown in Figure 7.2, the elemental shape functions (and, therefore the functions defining the coordinate transformation to the master element) are[2]

$$\begin{aligned} N_1^e &= \frac{1}{4}(1-\xi)(1-\eta) & N_3^e &= \frac{1}{4}(1-\xi)(1+\eta) \\ N_2^e &= \frac{1}{4}(1+\xi)(1-\eta) & N_4^e &= \frac{1}{4}(1+\xi)(1+\eta) \end{aligned} \tag{7.55}$$

where N_a^e represents the elemental shape function at node a in the local ordering. These definitions can be seen to satisfy the orthogonality imposed by (7.32) and the smoothness criteria required for functions in $H^1(\Omega)$. For the degeneration of an element into a triangular one, N_1 and N_2 remain unchanged, while the remaining shape function becomes : $N_3 \leftarrow N_3 + N_4 = \frac{1}{2}(1+\eta)$.

7.9 Numerical Integration

Relations (7.52) and (7.53) define several terms for which accurate integration is required on an elemental scale. By transformation of these integrals to ones over a master element considerable simplification occurs, although an additional term, the Jacobian of the transformation, j, is introduced into the integrals. These integrations are performed numerically with a "sufficiently accurate" Gaussian quadrature formula (Zienkiewicz, 1977).

Numerical integration involves approximating an integral over some domain as a weighted sum of the integrand evaluated at properly chosen points within the domain. With Gaussian integration of order l the weighting factors (w_n) and the optimal integration points (x_n) are chosen so as to exactly evaluate a

2. Or, generally $N_a^e = \frac{1}{4}(1+\xi_a\xi)(1+\eta_a\eta)$, where (ξ_a, η_a) are the local nodal coordinates.

polynomial of degree l. If the number of integration points in one dimension is n_{in} then the integration is exact to order $l = 2n_{in}-1$. With the definition of the shape functions above (7.49) a 2 x 2 rule will exactly integrate the integrands found in (7.46,7.47). Therefore, in 2D, with a general integrand in (7.46) or (7.47) denoted $f(\xi)$, and setting $g(\xi) = f(\xi)j(\xi)$, the 2 x 2 integration rule leads to

$$\int_{\Omega^e} g(\xi)\,d\xi = \int_{-1}^{1}\int_{-1}^{1} g(\xi,\eta)\,d\xi\,d\eta = \sum_{n=1}^{4} g(\xi_n)\,w_n \qquad (7.50)$$

where the four integration points have coordinates

$$\xi_n = (\xi_n,\eta_n) = \left[\ (\pm\frac{1}{\sqrt{3}} \text{ and } \pm\frac{1}{\sqrt{3}}),(\pm\frac{1}{\sqrt{3}},-\pm\frac{1}{\sqrt{3}})\ \right]$$

and the weighting factors for this rule are $w_n = 1$.

7.10 Stress Smoothing

Within isoparametric elements, displacement gradients are most accurately approximated at the centroid of an element. Thus, since stresses are, in general, related to symmetric gradients of the displacement (or rate-of-deformation), the stresses are best determined at the centroid. For the purposes of data interpretation and plotting, the stresses are required at the element nodes. To obtain these nodal values from the centroidal values, the stresses are smoothly interpolated using the shape functions N. For a uniform square grid this procedure effectively determines the nodal stresses by an arithmetic average of the four neighboring centroidal values.

This smoothing procedure works reasonably well for interior nodes of the mesh. However, those nodes along the boundary require one further averaging. For non-corner boundary nodes the value σ_A obtained as the mean of the two adjacent centroidal values is combined with the value σ_B at the next nearest node toward the interior of the mesh along the element boundary

$$\sigma_A \leftarrow 2\sigma_A + \sigma_B \tag{7.51}$$

Corner node values are obtained by linear extrapolation from the three adjacent neighbors, as described by Hughes, Liu, and Brooks (1979).

7.11 Constitutive Relation for Ice

As stated above, ice is modeled as a viscoelastic fluid in order to avoid the tricky issue of the numerical modeling of an incompressible material. The elastic solution provides the initial step in the time stepping algorithm of Table 7.1, into which the body forces are incorporated so as to provide for the main stresses driving the flow down an inclined channel. A proper choice of the elastic parameters, a relatively dense finite element mesh, and double-precision numerical calculations are helpful in evaluating these initial stresses accurately.

In the constitutive relation used here, the volume strain (ε_{kk}) is elastic while the deviatoric strain is governed by non-linear incompressible viscous flow plus the elastic response. The pressure is never fully decoupled from the rest of the stress tensor and no problems are encountered in trying to maintain viscous incompressibility.

The viscous stresses of an incompressible fluid can, in general, be related to the history of deformation of the fluid. If the fluid stresses are assumed to depend only upon the instantaneous rate of deformation, $\mathbf{d}(\mathbf{x})$, at the point in question then the material is necessarily isotropic (Noll, 1955). The most general rheological law for an incompressible fluid with no memory (a Reiner-Rivlin fluid) can be written in the form

$$\sigma'_{ij} = \varphi_1(II_d, III_d)\, d_{ij} + \varphi_2(II_d, III_d)\, [\, d_{ik}\, d_{kj}\,] \tag{7.52}$$

where $\sigma'_{ij} = \sigma_{ij} - \frac{1}{3}\sigma_{kk}$ and the two functions φ_1, φ_2 are scalar functions of the two invariants of $\mathbf{d}$, II_d and III_d (I_d is identically zero) (Astarita and Marrucci,

1974). Here

$$II_d = \frac{1}{2}tr(\mathbf{d}^2) \qquad III_d = \det(\mathbf{d}) .$$

The relation (7.52) may be rewritten as an inverse relation in terms of the deviatoric stress:

$$d_{ij} = \psi_1(J_2, J_3)\sigma'_{ij} + \psi_2(J_2, J_3)\left[\sigma'_{ik}\sigma'_{kj} - \frac{2}{3}J_2\delta_{ij}\right] \tag{7.53}$$

where J_2, J_3 are the 2nd and 3rd invariants of the deviatoric stress tensor. This specific dependence on the instantaneous stress state will hold only approximately for a changing flow situation because dynamic recrystallization under the non-hydrostatic stresses present in such a flow field will lead to time-varying material properties (Kamb, 1972, Duval 1981). If the overall geometry is assumed to have remained essentially constant for a relatively long time then recrystallization will have reached a steady state and the time dependence of the material properties can be neglected.

Although the geometry of Blue Glacier changed over the period 1957-77, it is felt that the magnitude and duration of this perturbation will have been such that the geometrical changes will not cause a significant change in the material properties.

It has been shown that there exists a preferred orientation of crystals in glacial ice (Rigsby, 1958; Kamb, 1959; Duval, 1981). Single ice crystals show a very strong plastic anisotropy, both in terms of dislocation motion and in experimental deformation (Barnes, et al. 1971). With the crystal fabrics found in polycrystalline ice, it seems that glacier ice may therefore be anisotropic. This anisotropy requires a form of the general rheological relation different than that given in (7.52) or (7.53) above. However, results from various laboratory studies to date indicate that temperate polycrystalline glacial ice is only weakly

anisotropic, and thus (7.53) should remain a good approximation.

Various parameters may enter into the functions ψ in (7.52) above, such as temperature, water and debris content, impurity concentration, and bubble content. These variables will, in general lead to a spatial (in particular, depth) variation in the material properties within an ice body. Substantial literature exists on the individual effects of these various parameters; however, a consistent multi-variable relation (theoretical or empirical) is lacking. Although the temperature effects in the nearly isothermal Blue Glacier (Harrison, 1972)may be disregarded, the other quantities may lead to a spatially-variable rheological law, as yet undetermined. The effect of such a spatial variability on the flow response will be investigated in a chapter IX.

A fluid whose behaviour is governed by the general form (7.53 or 7.52) can exhibit relatively uncommon behavior through the coupling of the deviatoric stress (or rate of deformation) components. As shown by Green and Rivlin (1956), steady non-rectilinear flow down a channel of simple cross section (e.g., elliptical) is, in general, an admissible solution for the flow of such a fluid. Circulatory secondary flow can be maintained, superimposed on the down-channel motion. Although few experiments that could test this possibility for glacier flow have been carried out, it is usually assumed that terms involving $\mathbf{d}^2$ and the third invariant are identically zero. Glen (1958) has shown that a flow law of the form

$$d_{ij} = \psi (J_2)\, \sigma'_{ij} \tag{7.54}$$

is, at least approximately, valid, and can explain the results of laboratory and field studies (see also Nye, 1957; Paterson, 1977; Hooke,1981). The specific form of (7.54) called Glen's flow law in the glaciological literature, has been shown to be that of power-law creep,

$$d_{ij} = \beta_{ij}(\sigma) = \frac{1}{2\eta_f} J_2^{\frac{n-1}{2}} \sigma'_{ij} \tag{7.55}$$

where the stress exponent n is a constant and the value of the viscosity parameter η_f is dependent upon temperature, water and impurity content, grain size, etc. This specifically defines β as needed in (7.7). This flow law has a theoretical basis in dependency of the motion of dislocations and of dislocation density in ice on stress, as discussed by Weertman (1973). It should be noted, however, that a relation of the form (7.55) leads to an infinite viscosity in the limit of vanishingly small shear. In spite of this difficulty, the power-law type relation has been successful in many glaciological (and geophysical) analyses within the stress ranges incurred.

The success of the power-law creep formulation in problems of glacier flow has led to the use of this relation for the viscous deformation rate in (7.7) of the present study. Analysis of the resulting flow and response models will be seen to justify its use.

Although the glaciological community has found the power-law relation useful and successful in its studies, there seems to be little agreement as to the numerical values of the exponent n and the viscosity parameter η_f. The exponent is usually taken to be in the range 1 to 6. The natural experiment discussed in this study leads to a method of assessing the values of n and η_f applicable to Blue Glacier and possibly to many other temperate glaciers.

The constitutive relation used here for a non-linear viscoelastic material (7.6,7.7) is obtained by simply patching together the relations for a compressible elastic solid and an incompressible viscous fluid obeying a power-law-type creep relation (7.55). While the shear terms are strictly correct, the normal components will be noted to be a slight simplification of the preferred constitutive relation for a non-linear Maxwell material as obtained from first principles.

The use of the unsimplified model would require a larger amount of computer storage, longer computing times, and increased expense. Cohen (1981) has shown that, for steady-state solutions, the difference between the flow fields and stresses resulting from the exact and simplified models is negligible. (Results for postseismic rebound and stress propagation in the earth were compared with those obtained by Melosh and Raefsky, 1982, who used the simplified rheological model for plane strain.) Therefore, the results reported in this study may be assumed accurate with respect to the choice of the rheological law. (A recent comparison for a mixed in- and out-of-plane flow problem of the two approaches again shows little difference. An out-of-plane code developed by G. Lyzinga (1983,pers. comm.) with the more exact treatment of the viscoelastic transition was used for this comparison.)

7.12 Specific Formulation of Solution Algorithm Under Various Geometrical Assumptions

The general algorithm shown in Table 7.1 requires specification of the stress vector, $\vec{\sigma}$, the strain-displacement matrix, **B**, the elastic compliance matrix, **D**, the viscous rate of deformation, $\boldsymbol{\beta}(\vec{\sigma})$, and the Jacobian of $\boldsymbol{\beta}$, $\boldsymbol{\beta}'(\vec{\sigma})$. In this section explicit relations are given for these functions under various geometrical assumptions such as plane strain (or stress), out-of-plane flow (described below), and out-of-plane axisymmetry. The formalism required by the latter two geometrical situations was developed by the author for use in modelling of channel flow, while that required for plane strain was developed by A. Raefsky and H.J. Melosh (pers. comm., 1978)

7.12.1 Plane Strain

In plane strain the deformation is restricted to the $x_1 x_2$ plane. There are two degrees of freedom per node, the x_1 and x_2 displacements, and the elements are

taken to be 4-node quadrilaterals. With $(x,y) = (x_1,x_2)$ the stress vector and strain operator are given by (7.18). **B** is given by (7.30) (where $\vec{\varepsilon} = \mathbf{Bu}$), and the elastic constitutive relation for plane strain gives rise to the matrix

$$\mathbf{D} = \frac{E}{(1+\nu)(1-2\nu)}\begin{bmatrix} 1-\nu & \nu & 0 \\ \nu & 1-\nu & 0 \\ 0 & 0 & \frac{1-2\nu}{2} \end{bmatrix} \tag{7.56}$$

where E is Young's modulus and ν Poisson's ratio. For an incompressible fluid, the deviatoric stress components in plane strain are

$$\sigma'_{xx} = -\sigma'_{yy} = \frac{1}{2}(\sigma_{xx} - \sigma_{yy}), \qquad \sigma'_{xy} = \sigma_{xy} \tag{7.57}$$

$$\text{with second invariant } J_2 = \frac{1}{2}\left[\frac{1}{2}(\sigma_{xx} - \sigma_{yy})^2 + 2\sigma_{xy}^2\right] . \tag{7.58}$$

For power law flow,(7.54),(7.55), and (7.58) give

$$\boldsymbol{\beta}(\vec{\sigma}) = \frac{J_2^{\frac{n-1}{2}}}{4\eta_f}\begin{bmatrix} 1 & -1 & 0 \\ -1 & 1 & 0 \\ 0 & 0 & 4 \end{bmatrix}\begin{bmatrix} \sigma_{xx} \\ \sigma_{yy} \\ \sigma_{xy} \end{bmatrix} \tag{7.59}$$

and thus the viscoelastic constitutive relation may be written as

$$\dot{\sigma} = \mathbf{D}[\dot{\varepsilon} - \boldsymbol{\beta}(\sigma)] \qquad \text{or}$$

$$\begin{bmatrix} \dot{\sigma}_{xx} \\ \dot{\sigma}_{yy} \\ \dot{\sigma}_{xy} \end{bmatrix} = \frac{E}{(1+\nu)(1-2\nu)}\begin{bmatrix} 1-\nu & \nu & 0 \\ \nu & 1-\nu & 0 \\ 0 & 0 & \frac{1-2\nu}{2} \end{bmatrix}\left\{\begin{bmatrix} N_{a,x} & 0 \\ 0 & N_{a,y} \\ N_{a,y} & N_{a,x} \end{bmatrix}\begin{bmatrix} \Delta u_1 \\ \Delta u_2 \end{bmatrix}\right.$$

$$\left. - \frac{\sigma^{n-1}}{4\eta_f}\begin{bmatrix} 1 & -1 & 0 \\ -1 & 1 & 0 \\ 0 & 0 & 4 \end{bmatrix}\begin{bmatrix} \sigma_{xx} \\ \sigma_{yy} \\ \sigma_{xy} \end{bmatrix}\right\} \tag{7.60}$$

where Δu_1 and Δu_2 are the two components of incremental displacement within a given time step and $\sigma \equiv J_2^{1/2}$ The Jacobian $\boldsymbol{\beta}'$ is

$$\beta'(\vec{\sigma}) = \frac{\sigma^{n-1}}{4\eta_I}\begin{bmatrix} A & -A & B \\ -A & A & -B \\ B & -B & C \end{bmatrix} \tag{7.61}$$

where

$$A = \frac{1}{4}(n-1)\frac{(\sigma_{xx}-\sigma_{yy})^2}{\sigma^2} + 1$$

$$B = \frac{n-1}{\sigma^2}(\sigma_{xx}-\sigma_{yy})\sigma_{xy}$$

$$C = (n-1)(\frac{\sigma_{xy}}{\sigma}) + 1$$

Note that in the above formulation (and what follows in this chapter) engineering convention is used in the shear terms. This leads to a symmetric Jacobian β'. (By replacing E with $E/(1-\nu^2)$ and ν by $\nu/(1-\nu)$ the equations of *plane stress* are generated without further modification of the algorithm.)

The resulting elemental stiffness is an 8 × 8 matrix (4 nodes at 2 dof (velocity components)each) and the effective force term has dimension 8. Two body force components, f_x and f_y , need to be specified.

7.12.2 Out-of-Plane Flow

The flow of a fluid within a channel of uniform (or slowly varying) cross section is best modelled as the flow outward from a section of the channel taken normal to the longitudinal axis. The upper surface of this section is not generally flat, and therefore an additional component of flow may be directed transverse to the longitudinal axis within the section. A glimpse at the cross-sectional profiles found on lower Blue Glacier (Figure 3.7) shows that convex or concave upper surfaces are indeed common. The observed surface velocity profiles (Figures 4.2) show the effects of this transversely sloping surface on the flow. Thus, the development of a modelling scheme in which both flow outward from a given cross section and intra-sectional flow are admissible seems needed. To this end, an "out-of-plane" element was formulated.

Suppose there is given a finite-element grid representing a cross section of an ice stream, as in Figure 7.1. At each node there are allowed three degrees of freedom, two displacements within the plane (as in plane strain) and the third directed normal to the plane of elements along the channel. Let the x_1 (x) axis be directed horizontally across the section, x_2 (y) directed upward within the plane of the cross section, and x_3 (z) directed normal to the plane, positive down-channel. The system so described forms a right-handed Cartesian coordinate system, but the flow system is not fully three-dimensional because no out-of-plane gradients are allowed (i.e. $\frac{\partial}{\partial z} = 0$). However, there can be a component of the body force directed normal to the plane. Shear stresses may exist across the plane (as σ_{xz} and σ_{yz}) but the deviatoric out-of-plane normal stress (σ'_{zz}) must vanish, since, from the flow law (7.61) and the assumption that $\frac{\partial}{\partial z} = 0$, $\sigma'_{zz} \sim d^v_{zz} = 0$. Similarly, in the elastic case, $\varepsilon^e_{zz} = 0$ which implies that $\sigma^e_{zz} = \nu(\sigma_{xx} + \sigma_{yy})$. (Note that at this point the exact treatment of the transition from elastic to viscous assumptions on the out-of-plane longitudinal deviatoric stress is not included, as alluded to in section 7.11. However, comparison of numerical results with analytical calculations and with the numerical models performed with a code which handles this complication exactly (G.Lyzinga,pers. comm.,1983) shows that the assumptions used in the code developed here lead to accurate steady state results.)

The stress, strain, and displacement vectors, and the strain operator are given by

$$\vec{\sigma} = \begin{Bmatrix} \sigma_{xx} \\ \sigma_{yy} \\ \sigma_{xy} \\ \sigma_{xz} \\ \sigma_{yz} \end{Bmatrix}, \quad \vec{\varepsilon} = \begin{Bmatrix} \varepsilon_{xx} \\ \varepsilon_{yy} \\ \varepsilon_{xy} \\ \varepsilon_{xz} \\ \varepsilon_{yz} \end{Bmatrix}, \quad \mathbf{u} = \begin{Bmatrix} u_1 \\ u_2 \\ u_3 \end{Bmatrix}, \quad \mathbf{L} = \begin{bmatrix} \frac{\partial}{\partial x} & 0 & 0 \\ 0 & \frac{\partial}{\partial y} & 0 \\ \frac{\partial}{\partial y} & \frac{\partial}{\partial x} & 0 \\ 0 & 0 & \frac{\partial}{\partial x} \\ 0 & 0 & \frac{\partial}{\partial y} \end{bmatrix} \tag{7.62}$$

with $$\vec{\varepsilon} = \mathbf{L}\mathbf{u} \ . \tag{7.63}$$

(Again engineering notation is used, giving a symmetric Jacobian.) The strain-displacement matrix is

$$\mathbf{B} \equiv \mathbf{L}\mathbf{N} = \begin{bmatrix} N_{a,x} & 0 & 0 \\ 0 & N_{a,y} & 0 \\ N_{a,y} & N_{a,x} & 0 \\ 0 & 0 & N_{a,x} \\ 0 & 0 & N_{a,y} \end{bmatrix} \tag{7.64}$$

Inversion of the elastic relation $\varepsilon_{ij}^e = \frac{1+\nu}{E}\sigma_{ij} - \frac{\nu}{E}\delta_{ij}\sigma_{kk}$ leads to

$$\mathbf{D} = \frac{E}{(1+\nu)(1-2\nu)} \begin{bmatrix} 1-\nu & \nu & 0 & 0 & 0 \\ \nu & 1-\nu & 0 & 0 & 0 \\ 0 & 0 & \frac{1-2\nu}{2} & 0 & 0 \\ 0 & 0 & 0 & \frac{1-2\nu}{2} & 0 \\ 0 & 0 & 0 & 0 & \frac{1-2\nu}{\nu} \end{bmatrix} . \tag{7.65}$$

The non-zero viscous deviatoric stress components are

$$\sigma'_{xx} = -\sigma'_{yy} = \frac{1}{2}(\sigma_{xx} - \sigma_{yy}) \ , \quad \sigma_{xy} \ , \ \sigma_{xz} \ , \ \sigma_{yz} \tag{7.66}$$

with second invariant $$J_2 = \left\{ \frac{(\sigma_{xx} - \sigma_{yy})^2}{4} + \sigma_{xy}^2 + \sigma_{xz}^2 + \sigma_{yz}^2 \right\} \ (= \sigma^{2)}. \tag{7.67}$$

Power law flow takes the form

$$\mathbf{d}^{v} = \beta(\vec{\sigma}) = \frac{\sigma^{n-1}}{4\eta_f}\begin{bmatrix} 1 & -1 & 0 & 0 & 0 \\ -1 & 1 & 0 & 0 & 0 \\ 0 & 0 & 4 & 0 & 0 \\ 0 & 0 & 0 & 4 & 0 \\ 0 & 0 & 0 & 0 & 4 \end{bmatrix}\begin{Bmatrix} \sigma_{xx} \\ \sigma_{yy} \\ \sigma_{xy} \\ \sigma_{xz} \\ \sigma_{yz} \end{Bmatrix} \tag{7.68}$$

and thus the viscoelastic constitutive relation is given by

$$\begin{Bmatrix} \dot{\sigma}_{xx} \\ \dot{\sigma}_{yy} \\ \dot{\sigma}_{xy} \\ \dot{\sigma}_{xz} \\ \dot{\sigma}_{yz} \end{Bmatrix} = \frac{E}{(1+\nu)(1-2\nu)}\begin{bmatrix} 1-\nu & \nu & 0 & 0 & 0 \\ \nu & 1-\nu & 0 & 0 & 0 \\ 0 & 0 & \frac{1-2\nu}{2} & 0 & 0 \\ 0 & 0 & 0 & \frac{1-2\nu}{2} & 0 \\ 0 & 0 & 0 & 0 & \frac{1-2\nu}{\nu} \end{bmatrix}$$

$$\times \left\{ \begin{bmatrix} N_{a,x} & 0 & 0 \\ 0 & N_{a,y} & 0 \\ N_{a,y} & N_{a,x} & 0 \\ 0 & 0 & N_{a,x} \\ 0 & 0 & N_{a,y} \end{bmatrix}\begin{Bmatrix} \Delta u_1 \\ \Delta u_2 \\ \Delta u_3 \end{Bmatrix} - \frac{\sigma^{n-1}}{4\eta_f}\begin{bmatrix} 1 & -1 & 0 & 0 & 0 \\ -1 & 1 & 0 & 0 & 0 \\ 0 & 0 & 4 & 0 & 0 \\ 0 & 0 & 0 & 4 & 0 \\ 0 & 0 & 0 & 0 & 4 \end{bmatrix}\begin{Bmatrix} \sigma_{xx} \\ \sigma_{yy} \\ \sigma_{xy} \\ \sigma_{xz} \\ \sigma_{yz} \end{Bmatrix} \right\} . \tag{7.69}$$

where again the incremental displacements are per time step.The Jacobian of the viscous relation is

$$\beta'(\vec{\sigma}) \equiv \left[\frac{\partial \beta}{\partial \vec{\sigma}}\right] = \begin{bmatrix} \beta_{1,1} & -\beta_{1,1} & \beta_{1,3} & \beta_{1,4} & \beta_{1,5} \\ & \beta_{1,1} & -\beta_{1,3} & -\beta_{1,4} & -\beta_{1,5} \\ & & \beta_{3,3} & \beta_{3,4} & \beta_{3,5} \\ & \text{sym.} & & \beta_{4,4} & \beta_{4,5} \\ & & & & \beta_{5,5} \end{bmatrix} \tag{7.70}$$

where

$$\beta_{1,1} = \frac{\sigma^{n-1}}{4\eta_f} + \frac{n-1}{\sigma^2}\beta_1\frac{(\sigma_{xx}-\sigma_{yy})}{4}$$

$$\beta_{1,3} = \frac{n-1}{\sigma^2}\beta_1\sigma_{xy}$$

$$\beta_{1,4} = \frac{n-1}{\sigma^2}\beta_1\sigma_{xz}$$

$$\beta_{1,5} = \frac{n-1}{\sigma^2}\beta_1\sigma_{yz}$$

$$\beta_{3,3} = \frac{\sigma^{n-1}}{\eta_f} + \frac{n-1}{\sigma^2}\beta_3\sigma_{xy}$$

$$\beta_{3,4} = \frac{n-1}{\sigma^2}\beta_3\sigma_{xz}$$

$$\beta_{3,5} = \frac{n-1}{\sigma^2}\beta_3\sigma_{yz}$$

$$\beta_{4,4} = \frac{\sigma^{n-1}}{\eta_f} + \frac{n-1}{\sigma^2}\beta_4\sigma_{xz}$$

$$\beta_{4,5} = \frac{n-1}{\sigma^2}\beta_4\sigma_{yz}$$

$$\beta_{5,5} = \frac{\sigma^{n-1}}{\eta_f} + \frac{n-1}{\sigma^2}\beta_5\sigma_{yz}$$

and $\beta_i = i^{th}$ component of $\beta(\vec{\sigma}) \equiv \mathbf{d}^v$

Since there are now 3 velocity components at the 4 nodes, the elemental stiffness is 12 × 12 and the effective force has dimension 12. Three body force components must be prescribed in order to determine the five stress components and three differential displacements.

The code for this out-of-plane geometry was tested by comparison with analytical solutions for flow in an infinite slab in each direction independently, and for flow in a semicircular channel with various values of the stress exponent n. The results for a relatively coarse semicircular grid are shown in Figure 7.3a. There is excellent agreement between analytical and numerical results. Figure 7.3b shows the error in the finite element solution for the surface velocity and the velocity near the bed. The accuracy decreases as the degree of non-linearity increases and as the shear at the point in question increases. Stresses show correspondingly good agreement with the analytical results. An increase in mesh density leads to an increase in accuracy, as expected (see section 7.14).

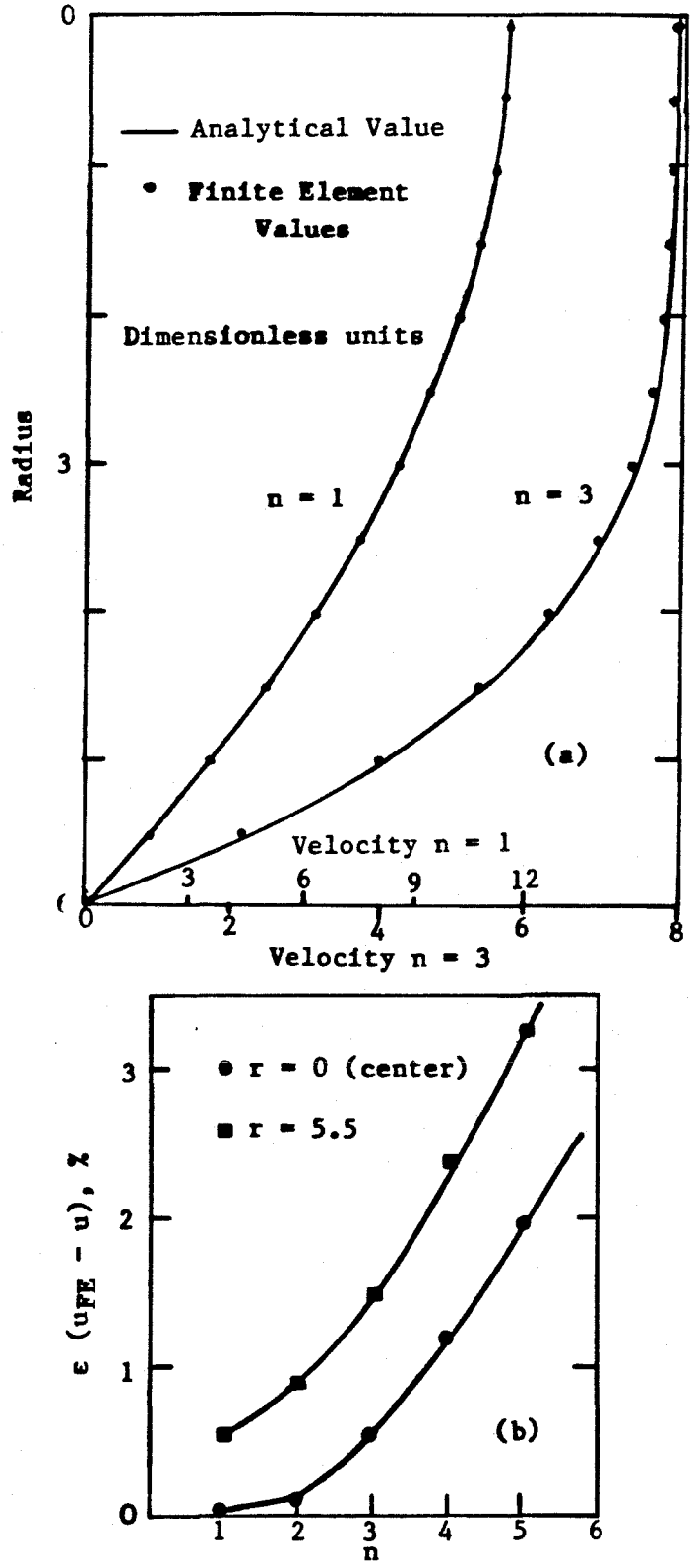

Figure 7.3 a)Comparison of analytical and FE results for flow along a semicircular channel. b)Error in FE results as a function of n, semicircular channel. R=6, n_{el}=238

This increase in density is necessary only in regions of high shear, such as near the bed of the glacier.

An analytical solution for an out-of-plane geometry in which all three velocity components are non-zero has not yet been found. Thus, a complete test of the finite element scheme in a fully coupled problem could not be performed. The above comparisons allow only a test of the uncoupled motion in any one of the three directions, prohibiting a full interaction of the different stress components through the non-linear flow law.

7.12.3 Axisymmetric Out-of-Plane Flow

Blue Glacier flows down a longitudinally curving valley. Other valley glaciers, such as Ogilvie-Gilkey Glacier in Alaska, make sharp right-angle bends. These curving channels must introduce important features into the velocity and stress fields of the ice mass, as happens in river flow.

In order to include the effects of this curving flow, an axisymmetric out-of-plane element was developed. The plane of elements was taken to represent a transverse section of the curving channel, with motion down the channel ($v_3 = v_\vartheta$) and within the plane ($v_1 = v_r$ and $v_2 = v_z$, z positive upward).Gradients in the $x_3 (= \vartheta)$ direction were taken to be zero. The flow system is, again, not fully three-dimensional because out-of-plane gradients are not allowed.

In the presence of vanishing ϑ-gradients the stress and strain vector, and the strain operator may be written as

$$\vec{\sigma} = \begin{Bmatrix} \sigma_{rr} \\ \sigma_{zz} \\ \sigma_{\vartheta\vartheta} \\ \sigma_{rz} \\ \sigma_{r\vartheta} \\ \sigma_{z\vartheta} \end{Bmatrix} \qquad \vec{\varepsilon} = \begin{Bmatrix} \varepsilon_{rr} \\ \varepsilon_{zz} \\ \varepsilon_{\vartheta\vartheta} \\ \varepsilon_{rz} \\ \varepsilon_{r\vartheta} \\ \varepsilon_{z\vartheta} \end{Bmatrix} \qquad \mathbf{L} = \begin{bmatrix} \frac{\partial}{\partial r} & 0 & 0 \\ 0 & \frac{\partial}{\partial z} & 0 \\ \frac{1}{r} & 0 & 0 \\ \frac{\partial}{\partial z} & \frac{\partial}{\partial r} & 0 \\ 0 & 0 & \frac{\partial}{\partial r} - \frac{1}{r} \\ 0 & 0 & \frac{\partial}{\partial z} \end{bmatrix} \tag{7.71}$$

The displacement vector and strain-displacement matrix are

$$\mathbf{u} = \begin{Bmatrix} u_r \\ u_z \\ u_\vartheta \end{Bmatrix} \qquad \mathbf{B} = \mathbf{L}\mathbf{N}_a = \begin{bmatrix} N_{a,r} & 0 & 0 \\ 0 & N_{a,z} & 0 \\ \frac{N_a}{r} & 0 & 0 \\ N_{a,z} & N_{a,r} & 0 \\ 0 & 0 & N_{a,r} - \frac{N_a}{r} \\ 0 & 0 & N_{a,z} \end{bmatrix} \tag{7.72}$$

and the elastic matrix is

$$\mathbf{D} = \frac{E}{(1+\nu)(1-2\nu)} \begin{bmatrix} 1-\nu & \nu & \nu & 0 & 0 & 0 \\ & 1-\nu & \nu & 0 & 0 & 0 \\ & & 1-\nu & 0 & 0 & 0 \\ & & & \frac{1-2\nu}{2} & 0 & 0 \\ & \text{sym.} & & & \frac{1-2\nu}{2} & 0 \\ & & & & & \frac{1-2\nu}{2} \end{bmatrix} \tag{7.78}$$

The deviatoric viscous stresses are $\sigma'_{ij} = \sigma_{ij} - \frac{1}{3}\sigma_{kk}\delta_{ij}$

with second invariant

$$\sigma^2 \equiv J_2 = \frac{1}{2}\,\mathrm{tr}\,[\,(\vec{\sigma}')^2\,] = \left[\frac{1}{3}(\sigma_{rr}^2 + \sigma_{zz}^2 + \sigma_{\vartheta\vartheta}^2 - \sigma_{rr}\sigma_{zz} - \sigma_{rr}\sigma_{\vartheta\vartheta} - \sigma_{zz}\sigma_{\vartheta\vartheta}\right.$$

$$+ \sigma_{rz}^2 + \sigma_{r\vartheta}^2 + \sigma_{z\vartheta}^2 \Big] . \tag{7.74}$$

Power-law flow takes the form

$$\mathbf{d}^v = \boldsymbol{\beta}(\vec{\sigma}) = \frac{\sigma^{n-1}}{6\eta_I} \begin{bmatrix} 2 & -1 & -1 & & & \\ -1 & 2 & -1 & 0 & & \\ -1 & -1 & 2 & & & \\ & & & 6 & 0 & 0 \\ & 0 & & 0 & 6 & 0 \\ & & & 0 & 0 & 6 \end{bmatrix} \tag{7.75}$$

and the viscoelastic constitutive relation is given by

$$\begin{Bmatrix} \dot{\sigma}_{rr} \\ \dot{\sigma}_{zz} \\ \dot{\sigma}_{\vartheta\vartheta} \\ \dot{\sigma}_{rz} \\ \dot{\sigma}_{r\vartheta} \\ \dot{\sigma}_{z\vartheta} \end{Bmatrix} = \frac{E}{(1+\nu)(1-2\nu)} \begin{bmatrix} 1-\nu & \nu & \nu & 0 & 0 & 0 \\ & 1-\nu & \nu & 0 & 0 & 0 \\ & & 1-\nu & 0 & 0 & 0 \\ & & & \frac{1-2\nu}{2} & 0 & 0 \\ & \text{sym.} & & & \frac{1-2\nu}{2} & 0 \\ & & & & & \frac{1-2\nu}{2} \end{bmatrix}$$

$$\times \left\{ \begin{bmatrix} N_{,r} & 0 & 0 \\ 0 & N_{,z} & 0 \\ \frac{N}{r} & 0 & 0 \\ N_{,z} & N_{,r} & 0 \\ 0 & 0 & N_{,r} - \frac{N}{r} \\ 0 & 0 & N_{,z} \end{bmatrix} \begin{Bmatrix} \Delta u_r \\ \Delta u_z \\ \Delta u_\vartheta \end{Bmatrix} - \frac{\sigma^{n-1}}{6\eta_I} \begin{bmatrix} 2 & -1 & -1 & 0 & 0 & 0 \\ & 2 & -1 & 0 & 0 & 0 \\ & & 2 & 0 & 0 & 0 \\ & & & 6 & 0 & 0 \\ & \text{sym.} & & & 6 & 0 \\ & & & & & 6 \end{bmatrix} \begin{Bmatrix} \sigma_{rr} \\ \sigma_{zz} \\ \sigma_{\vartheta\vartheta} \\ \sigma_{rz} \\ \sigma_{r\vartheta} \\ \sigma_{z\vartheta} \end{Bmatrix} \right\} \tag{7.76}$$

The Jacobian of $\boldsymbol{\beta}$ is given by (7.77)

$$\frac{\boldsymbol{\beta}'}{S} = \begin{bmatrix} (2+B\cdot R^2) & (B\cdot R\cdot Z-1) & (B\cdot R\cdot T-1) & B\cdot R\cdot RZ & B\cdot R\cdot RT & B\cdot R\cdot ZT \\ & (2+B\cdot Z^2) & (B\cdot Z\cdot T-1) & B\cdot Z\cdot RZ & B\cdot Z\cdot RT & B\cdot Z\cdot ZT \\ & & (2+B\cdot T^2) & B\cdot T\cdot RZ & B\cdot T\cdot RT & B\cdot T\cdot ZT \\ & \text{sym.} & & [6+B\cdot(RZ)^2] & B\cdot RZ\cdot RT & B\cdot RZ\cdot ZT \\ & & & & [6+B\cdot(RT)^2] & B\cdot RT\cdot ZT \\ & & & & & [6+B\cdot(ZT)^2] \end{bmatrix}$$

where $S \equiv \frac{\sigma^{n-1}}{6\eta}$ $B \equiv \frac{3(n-1)}{2\sigma^2}$ $R = \sigma'_{rr}$ $Z = \sigma'_{zz}$, $T = \sigma'_{\phi\phi}$

$$RZ = 2\sigma_{rz} \quad RT = 2\sigma_{r\phi} \quad ZT = 2\sigma_{z\phi} \ .$$

Although the elemental stiffness still has rank 12 and the effective force dimension 12 (3 dof and 4 nodes), the computations involving these forms are considerably more time consuming than those for "simple" out-of-plane flow. The integrations in (7.52) and (7.53) now involve the radius, x_1, in the element of area $d\Omega$ $(=2\pi x_1 dx_1 dx_2)$, as do some of the elements of **B**. The radius at the integration points of an element are obtained from the radii of the nodal points by shape function interpolation. The radius of curvature at the inside boundary of the plane of elements is required as part of the input data. This quantity is then added to the x_1 coordinate of each node, giving the effective radius of each point in the grid.

The specification of the body forces in the axisymmetric flow problem requires special consideration and will be dealt with in detail in Chapter VIII.

The axisymmetric algorithm was tested by comparison with analytical solutions for annular flow and flow between rotating cylinders. The development of the analytical solutions and the numerical comparison is desribed in Appendix D. Additional tests are discussed in Chapter VIII. There is again a lack of analytical results for fully coupled problems, and thus no test with this degree of complexity could be made.

7.13 Computer Code

Following the algorithm described above, with the various geometrical assumptions and the constitutive relation (7.7) and (7.61), a computer code was developed for the solution of power-law type flow problems. The basic subdivisions of the code include data input, solution of the initial elastic problem, time-

stepping solution of the viscous flow, and printing and graphical display of the results. The basic structure of the code, as well as many of the computational details and subroutines required for the solution of plane strain problems were graciously given to the author by Arthur Raefsky and T.J.R. Hughes.

7.14 Accuracy

In any finite-element solution the accuracy and rate of convergence is of interest. As described above, the explicit solution scheme ($\alpha = 0$) requires a computationally restrictive time step in order that the numerical method be stable (and thus convergent in the time-stepping). With stability in this sense confirmed, there is still the question of the accuracy and rate of convergence to the actual (exact) solution given the choice of the interpolation functions (N_A) and the density of the element mesh.

The test solutions described above and in appendix C give an estimate of the accuracy of the solution for a given grid in some simple problems for which analytical solutions are known. Suppose the descretization of Ω is refined such that there is a decrease in the maximum "diameter" of all elements. (This diameter is the so-called mesh parameter h.) Then an increase in the accuracy of the solution can be expected. If $E = u - u^h$ is a measure of the error in the approximate solution, u^h, about the true value, u, then it can be shown that the maximum error satisfies

$$\|E\|_o \leq C_1 h^{\gamma+1}, \qquad C_1 = \text{constant} \tag{7.78}$$

Here the order of convergence, $\gamma = \min(s,k)$, where s is the order of the highest derivatives of u which are elements of $L_2(\Omega)$, k is the degree of the complete polynomials contained in the shape functions, and the norm is defined in the L_2-sense on Ω. (The development of these results is described by Oden and Reddy (1976).

From (7.78) is seen that, in the FE scheme developed in this study (k=1), a decrease in mesh size by a factor of two should lead to a decrease in the error of the solution by a factor of four. Such a reduction has been demonstrated for test solutions. A refinement of the mesh in regions of high shear is all that is required for such an increase in accuracy (above a certain grid density). Choice of the appropriate descretization required for a sufficiently accurate solution is largely a matter of trial and error. In order that this increase in accuracy be obtained, it is important that elements with high aspect ratio (long and skinny) be avoided and that the nodal ordering scheme be chosen such that the bandwidth of the stiffness is minimized.

The above result (7.84) indicates that higher-order elements (k> 1) will lead to an increase in accuracy (although accompanied by a corresponding increase in cost). However, since the displacements in the weak form of the boundary value problem (7.16,17) are only required to be members of $H^1(\Omega)$, s=2. Hence, an increase in the shape functions above a quadratic may not, in general, lead to a significant increase in accuracy.

CHAPTER VIII

THEORY OF THE FLOW OF ICE IN SIMPLE CHANNELS

Before discussing the models of glacier flow within the observed geometry, it is first important to understand the features of the velocity and stress fields under geometrically simple conditions. It is the purpose of this and the following chapter to elucidate these features, beginning with very simple channels and progressively increasing the complexity as an approach to realistic geometries. This development will hopefully allow an identification of the source of the various peculiarities of observed flow fields and lead to a better understanding of the factors which govern glacier flow.

The present chapter discusses the steady flow in channels of semicircular and parabolic cross-section. Initially the upper surface of the ice mass is taken to be flat in a transverse direction. Later, convexity in the surface of the transverse profile is introduced, a feature often seen in the ablation zones of temperate glaciers. The effects of a spatial variation in the ice flow law is then considered. The last section treats the flow of ice in a longitudinally curving channel, and includes a detailed discussion of the changes induced in the stress and velocity fields by this curving channel geometry.

The calculations assume that the imposed longitudinal stress gradients are uniform over the cross section, or else negligibly small, and also that bed slip is either uniform along the ice-bedrock interface (so that it only provides an additive constant to the longitudinal velocity field) or else negligibly small. A thorough discussion of the effects of large and spatially-varying longitudinal stress-gradients must rely upon a fully three-dimensional modelling treatment. The importance of longitudinal stress gradients can be more easily be resolved

once two-dimensional effects are isolated and identified in observational data.

The assumption of small basal sliding is probably applicable to many valley glaciers. Relatively few field studies on the transverse distribution of sliding have been made. Raymond (1971) has found important variations in the component of basal sliding across a section of the Athabaska Glacier. A complete theoretical explanation of this distribution, and, indeed, of basal sliding in general, is not known at the present time. Models to date deal mainly with clean ice-bedrock interfaces and small intraglacial water pressures (Weertman, 1964, Kamb, 1970, Nye, 1970, Lliboutry, 1968 and Iken, 1981) while observational results indicate the presence of subglacial debris layers, varying water pressures, and large amounts of cavitation (Harrison and Kamb, 1973, Englehardt et al.,1978; Englehardt, 1978). Thus, although a basal sliding law (if a reliable law were available) could be easily incorporated into the numerical models, it was felt that such inclusion was not needed and not appropriate for Blue Glacier,in which the observed contribution of sliding to the actual ice motion is small (< 10%,see sec. 4.4). Prescribed non-zero velocity boundary conditions were not applied at the base of the ice mass because the distribution of the small sliding velocity was not known.

In spite of the above limitations on the models treated here, the results are helpful in explaining many features of temperate-glacier velocity and stress fields of a large number of temperate ice bodies that have not been discussed previously. Via the modular nature of the finite element code more elaborate models can be developed in the future as the need arises.

8.1 The Basic Model

Ice is taken to be a non-linear, slightly compressible viscoelastic fluid whose constitutive properties are governed by the relation given in sections 7.1 and

7.11 of the previous chapter. The viscous properties are determined by a power - law creep equation with stress exponent n and viscosity factor η_f. (The term viscosity factor and the symbol η_f used here must not be confused with the effective viscosity of a non-Newtonian fluid. The effective viscosity for a fluid obeying a power-law relation is equal to $(J_2^{(n-1)/2}/\eta_f)^{-1}$. The factor η_f is related to the factors A,B in common usage as follows:

$$\dot{\varepsilon} = AJ_2^{(n-1)/2}\tau' = \frac{J_2^{(n-1)/2}}{B^n}\tau' = \frac{J_2^{(n-1)/2}}{2\eta_f}\tau' \qquad (8.1)$$

where $\dot{\varepsilon}$ and τ' are the rate-of-deformation and deviatoric stress tensors, respectively.) The elastic properties are taken to be those observed for glacial ice. Errors in these elastic parameters do not affect the final steady state flow field. and all results given are those applying to steady state conditions. The ice mass is driven by gravity down a channel of longitudinal surface slope α. The Cartesian coordinates are those shown in Figure 8.1. When required, flow within the xy plane will be allowed in addition to the general down-channel flow in the +z direction. Stresses and velocities will be normalized by the corresponding quantities in a long, parallel-sided ice slab of thickness H, where H is the centerline depth of the given cross section (unless otherwise noted). Gravity is resolved into its down-channel (z) and y components. Although the channels discussed in this chapter are symmetric about the centerline, x=0, the results are given for the entire channel to allow comparison with the non-symmetric flow that results when curvature is introduced.

It should be noted that numerical modelling is subject to various interpolation and smoothing errors. An effort will be made to point out these possibly erroneous results (from smoothing and interpolation effects) as they appear.

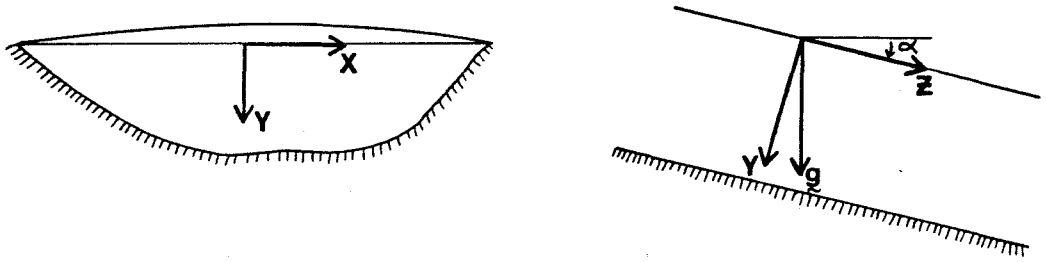

Figure 8.1 Description of coordinate system.

8.2 Stresses and Flow in Parabolic Channels with a Level Upper Surface

The flow and shear-stress distribution in a semicircular channel with a planar upper surface is easily derived analytically, and the solution has been used as a test for the numerical procedure, as mentioned in the previous chapter. The numerically calculated shear stresses within the cross section prove to vary linearly with depth, as the analytical solution requires. The proportionality factor in this linear relation is 0.500, again in agreement with theory. The commonly-used 'shape factor', f, defined as f=cross-sectional area / ("wetted" perimeter x centerline depth) = 1/2 for a semicircle, agrees with the numerically calculated proportionality factor in this case. As will be seen below, this agreement does not generally hold for parabolic channels (or for rectangles - see Nye,1965).

Most glacial valleys can be approximated by a parabola in cross section. The sides are generally sloping at the ice surface, rather than vertical as in circular or elliptical channels. The bed configuration of Blue Glacier (as shown in Chapter III) is approximately parabolic, with half-width-to-depth ratio W of 1.6

± 0.3. Flow in channels of half-width to depth ratios has been analyzed numerically, and the results are given below.

Using a finite-difference method, Nye (1965) calculated the stress and flow distribution in parabolic channels using a power-law creep exponent of 3. His results show several interesting features. The depth variation of τ_{yz} is not a linear function of depth, as is often assumed in borehole deformation studies. The often-assumed linear variation tends to overestimate the stress magnitude at depth, precisely the location where accurate stress estimates must be made. This may then lead to inaccurate estimates of the flow law parameters from such a field study. In the distribution of τ_{xz} across the surface of a channel, a maximum in the magnitude of τ_{xz} occur at points a distance in from the margins of the channel. The position of this maximum is dependent upon the value of W (and thus the steepness of the valley wall). As W increases the position of the maximum in τ_{xz} moves inward toward the center and the maximum becomes more diffuse. The distribution of τ_{xz} causes an inflection in the surface velocity profile, which moves toward the margin as W decreases. The inflection can be observed in measured velocity profiles if they have sufficient resolution near the margins. Profiles C,D,and F through J in Figure 4.2 show this inflection close to the margins.

Finite-element models of flow within parabolic channels for various values of n as well as W were calculated. Nye's (1965) results for n=3 appear to agree quite well with the FE results. The shear stresses differ by approximately 1% for all listed W, while the velocity values differ by 2 - 4%. The present values are lower than those obtained by the finite difference method.It is not known if double precision was used by Nye, as it was in the present calculations. At the error level stated by Nye, and with a similar error level expected for the finite-element (FE) calculations, the agreement between results can be regarded as a further

Table 8.1

Comparison of Surface Centerline Velocities (U_o) in Parabolic Channels as Determined by Nye (1965) and by the Finite Element Method

W	U_o (Nye,1965))	U_o (FE, this work)	ΔU_0,%
1	.0221	.0212	4.5
2	.0675	.0663	1.8
3	.104	.101	2.9
4	.131	.127	3.1

validation of the FE method used here. A comparison is given in Table 8.1. Finite-element models allow an exact zero-velocity boundary condition to be applied along the bed, while the finite-difference scheme requires interpolation within a rectangular grid, which may introduce some error in the boundary conditions. On the other hand, the FD grid of Nye was somewhat finer, giving better resolution with 121 nodes within the rectangular grid containing the half parabola while only 133 nodes were used in the full FE mesh (which are, however, all part of the actual model channel). Differences in the treatment of the material non-linearities may also lead to differences in the resulting accuracy.

Models calculated by the FE method for values of n from 1 to 5 are shown in Figures 8.2-8.8. The surface shear stress (τ_{xz}) profiles show several interesting features (Figures 8.2 and 8.3). The lower the W value the sharper the gradient in τ_{xz} is near the margin and the closer to the margin the maximum in τ_{xz} lies. The magnitude of τ_{xz}^{max} varies with W for a given n (Figure 8.4), when normalized by $\rho g H \sin\alpha$, where H is the centerline depth (the channel width (=2HW) is the same for all channels in this figure). For n=2 this change is small in the range W = 1 to 3, while for n < 2 larger values of W have significantly lower τ_{xz}^{max} and for n > 2 larger values of W have higher τ_{xz}^{max}. This is shown graphically in Figure 8.4b. For parabolic channels of different depth but the same width (that is, varying W by changing the depth), we see that shear stress along the surface of the deeper channels (smaller W) is increased. This is because the effects of the channel

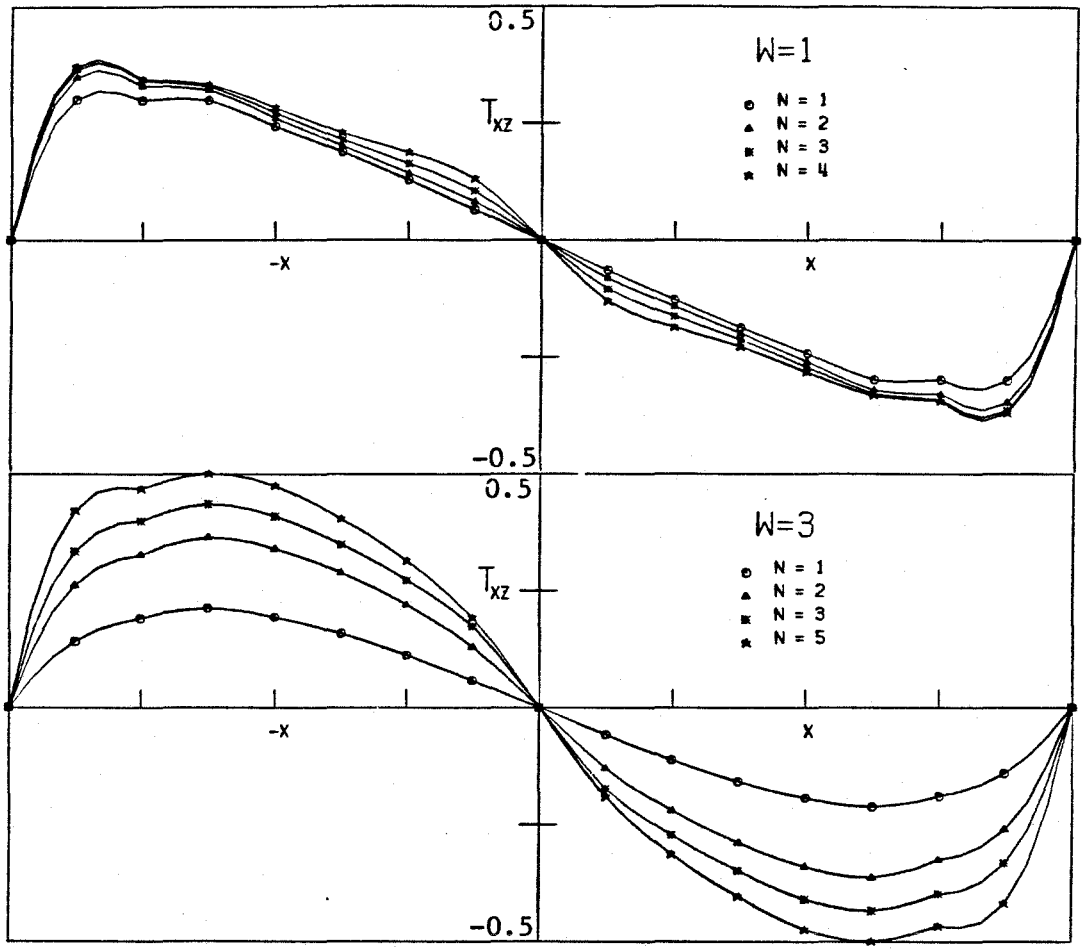

Figure 8.2 Transverse profiles of shear stress (τ_{XZ}) across surface of straight parabolic channels. Stress is normalized by $\rho g H \sin\alpha$, where H=depth at center and distance X ranges from -D to +D. D is the channel width at the surface (X = x/D).

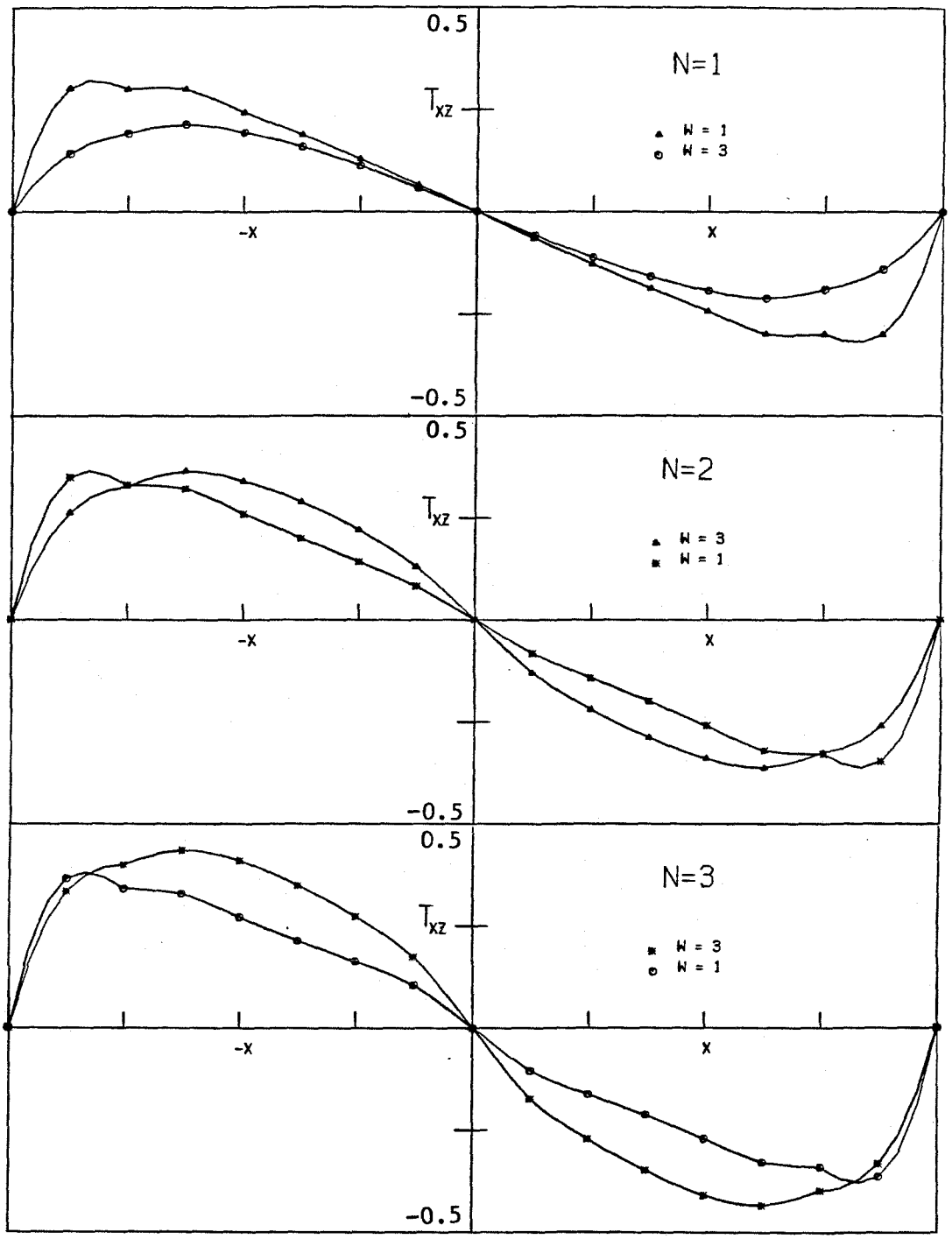

Figure 8.3 Same as Figure 8.2 except each plot for a different exponent n.

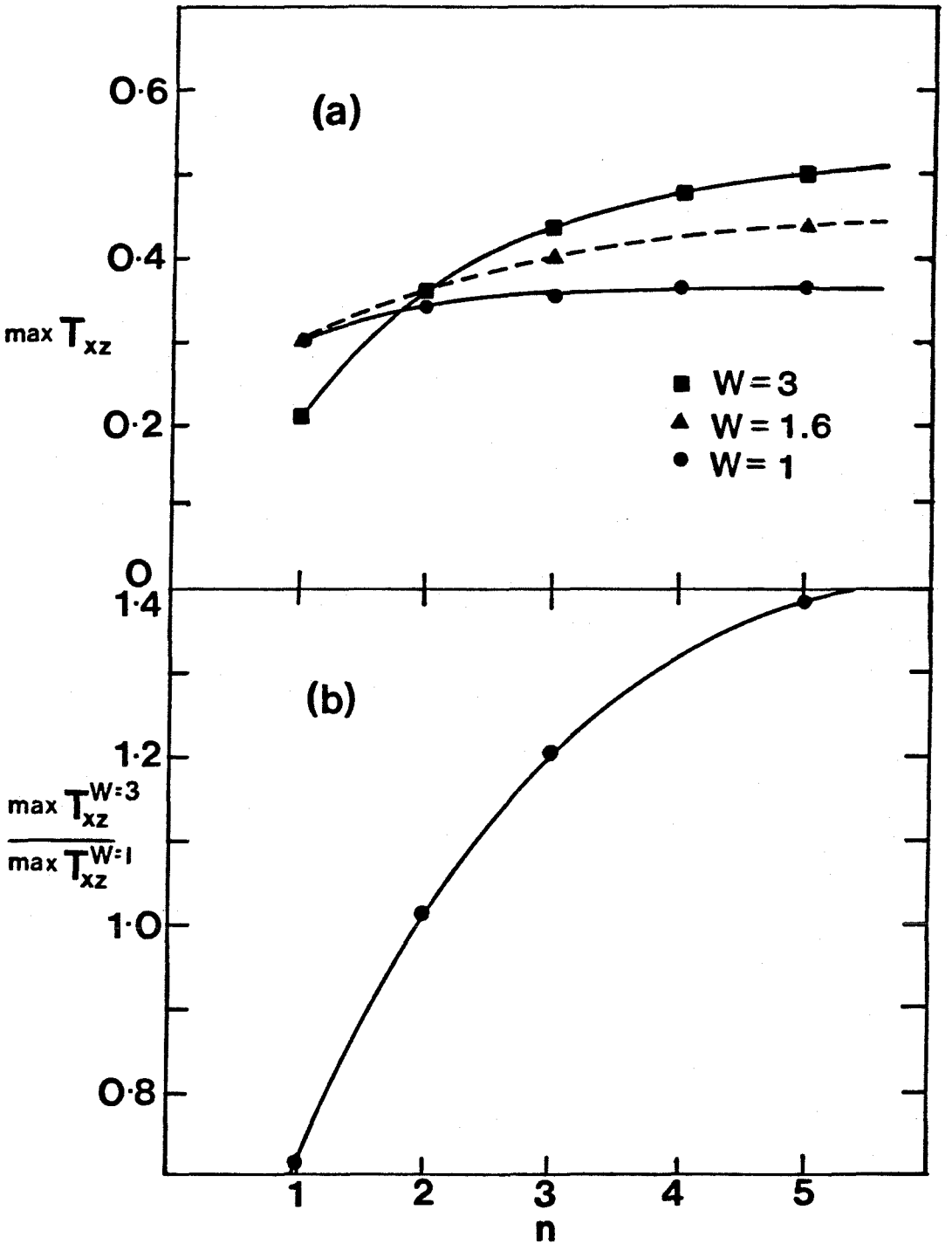

Figure 8.4 a) Maximum shear stress (normalized τ_{xz}) across surface of parabolic profiles for different W as a function of n.
b) Ratio of maximum shear stress for W=3 and maximum for W=1 parabolic channels, as a function of n.

directly beneath the points along the surface decrease with a deepening of the channel, causing the sides to support a larger shear stress. In the limiting case of W = 0 (infinitely deep, vertical walled channel) the stresses are totally supported by the walls, and they show large variations across the channel. At the other extreme, as W approaches infinity (a wide slab), there are no side walls, the bed directly beneath the surface points supports the down - glacier forces, and the transverse shear stresses vanish.

The variation of the position along the surface of the maximum shear stress also shows an interesting variation with W. As W decreases from a value of 8 to 1.6, the position of τ_{xz}^{max} moves progressively outward toward the margin in a linear fashion. For the values of W less than 1.6 which were modeled in this study (W=1,1/2,1/4), there is an abrupt shift of the position of τ_{xz}^{max} toward the margins, well off the linear progression found for the larger values of W. Although this may possibly be something arising erroneously in the numerical solution, it may also represent a real effect. The slope of the margin relative to the horizontal goes from a value less than 45° for $W \geq 1.6$ to a value greater than 45° for $W < 1.6$ (approximately). This corner angle of 45° is precisely where the analytical solution for the outward flow in a corner of a Newtonian fluid shows a singular behavior. At angles greater than 45° the velocity solution produces somewhat unphysical results. The correlation of this analytical result with the numerical results for parabolic channels is interesting, and requires further investigation. (It should also be noted that the behaviour of the velocity near the margins differs between a profile which has an inflection near the margin for $W \geq 1$ to one that tends to zero from above in a nearly-linear fashion for values of $W \leq 1.6$ (Figure 8.7))

Perhaps the most noteworthy aspect of the shear stress variations is the dependence of the stress magnitude on the value of the exponent n, as shown in

Figures 8.2 and 8.4a. The variation is more pronounced for higher W. The variation in the magnitude of τ_{xz} with n decreases as n increases, being the largest between n = 1 and 2. Similar results apply to τ_{yz} at depth, though the variation with n is less pronounced (Figure 8.5). In this figure we see that τ_{yz} is very nearly linear with depth in most parabolic channels of realistic aspect ratio. However, the magnitude of this stress component at the base of the channel may differ by as much as 15% between the values for n=1 and n=5. This leads to an effective shape factor which is a function of n.(For example, f(n=1) = 0.83 and f(n=5) = 0.72 for a channel with W=3, and f(n=1) = 0.60 and f(n=5) = 0.54 for W=1.6.) These results indicate that the method of obtaining the flow law parameters by investigating borehole deformation with depth can be quite problematical if the channel geometry is that corresponding to a large value of W. Not only can the stress variation be nonlinear with depth, but the stress itself can be implicitly dependent upon the stress exponent. The source of this dependence lies in the interaction of the no-slip boundary condition on the sloping wall and the boundary stresses. This stress dependence on flow low parameters has not been discussed before, except in the recent paper by Hutter (1981), and then only for the basal shear stress along a longitudinal profile which varies in thickness, rather than within a cross-sectional profile as described here.

It should be noted that the unsmooth nature of the stress profiles near the margins is due to the poor smoothing resolution and the order of the interpolation scheme used in fitting the drawn curve to the sharp change in stress gradient near the margin, especially for the smaller values of W.

The velocity profiles further exemplify the features of the stress field. For a given value of n the higher values of W show a more peaked and less plug-like surface velocity distribution (see Figure 8.6). Consider a fluid moving down a narrow but deep channel (low W). Along the surface a fluid element near the

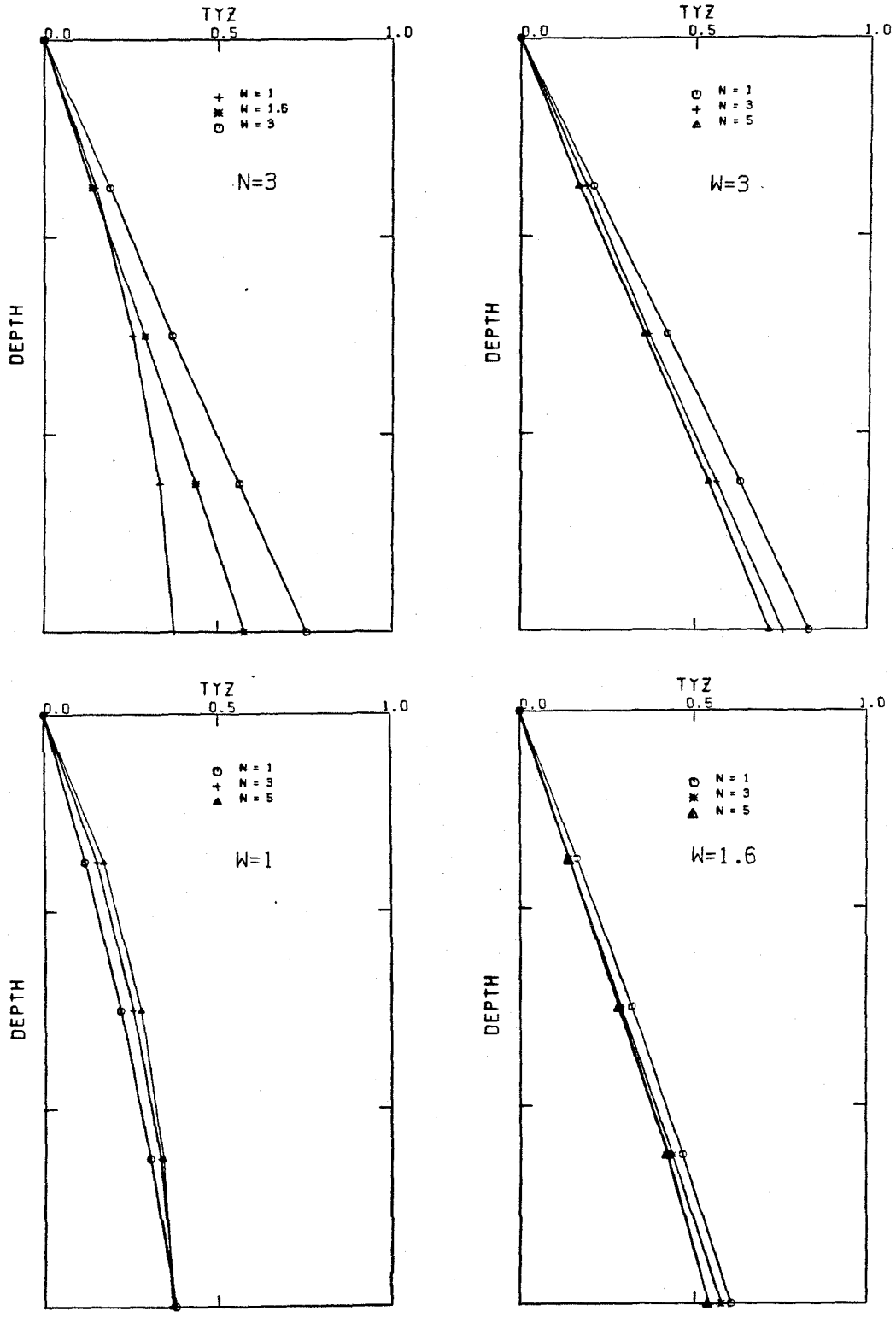

Figure 8.5 Shear stress (T_{yz}) at depth beneath channel centerline in parabolic channels of different aspect ratios W and values of n. (Stress is normalized by $\rho g H \sin\alpha$ at center.

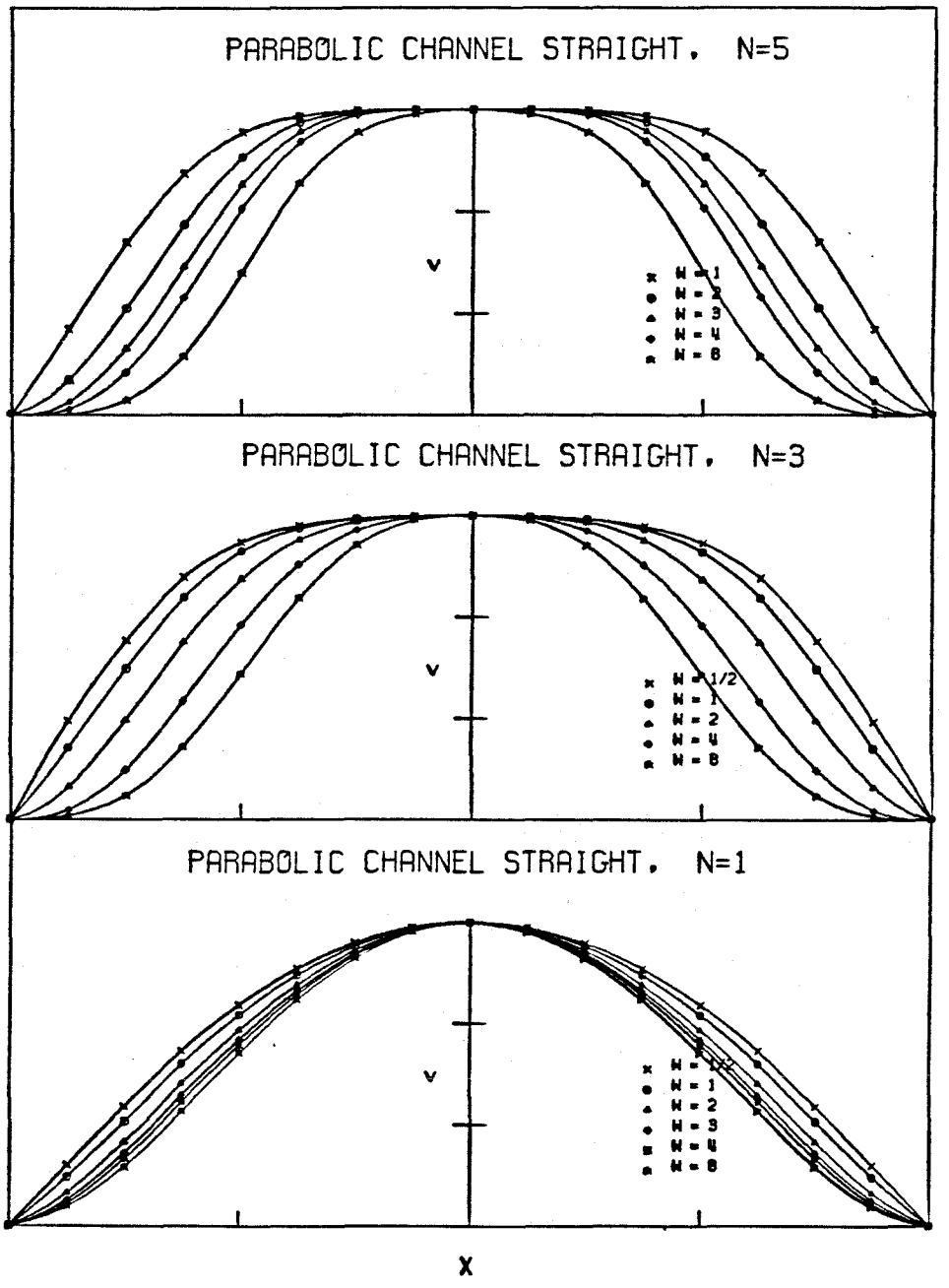

Figure 8.6 Velocity profiles for different parabolic channels and different n. Width of each channel is the same. Velocity is normalized by maximum velocity in that channel and for that n.

margin feels the drag of the wall. As the location of the element moves toward the center of the channel, the lateral distance to the wall varies linearly while the vertical distance to the bed increases much more rapidly. Thus the effect of the drag along the bed becomes dominated by the side walls, approaching a situation similar to an infinitely deep channel and approaching its characteristic plug-like flow profile. The maximum in the shear stress magnitude ($\tau^2 = \tau_{xz}^2 + \tau_{yz}^2$) along a transverse line just below the surface occurs very near the wall and thus the inflection in the velocity profile is also near the wall. Conversely, the fluid element in a wide and shallow channel (large W) senses the bed of the channel vertically below the element throughout the range of the transverse position. The point of inflection in the velocity moves away from the wall and a more peaked profile results.

As expected, for a given value of W, the higher the stress exponent the more plug-like the flow profile, as shown in Figure 8.7. The differences between n = 3.4, and 5 are relatively small, and thus one can see the difficulty in using surface velocity profiles alone to obtain flow law information.

The velocity field and shear-stress magnitude throughout a cross section are shown in Figures 8.8a,b and 8.8c,d,respectively, for W =1.6 and n = 1 and 5,As is expected, the higher values of n show higher shear-stress gradients and velocity gradients near the boundaries. For the wider channels the maximum shear-stress gradient occurs at the base near the centerline while narrower and deeper channels have the highest gradients along the side walls, as would be expected from a consideration of the portions of the boundary which have the greatest effect on the flow.

As will be seen in the following discussions, the dependence of the stress field on the power law exponent will continue to be an important feature of the

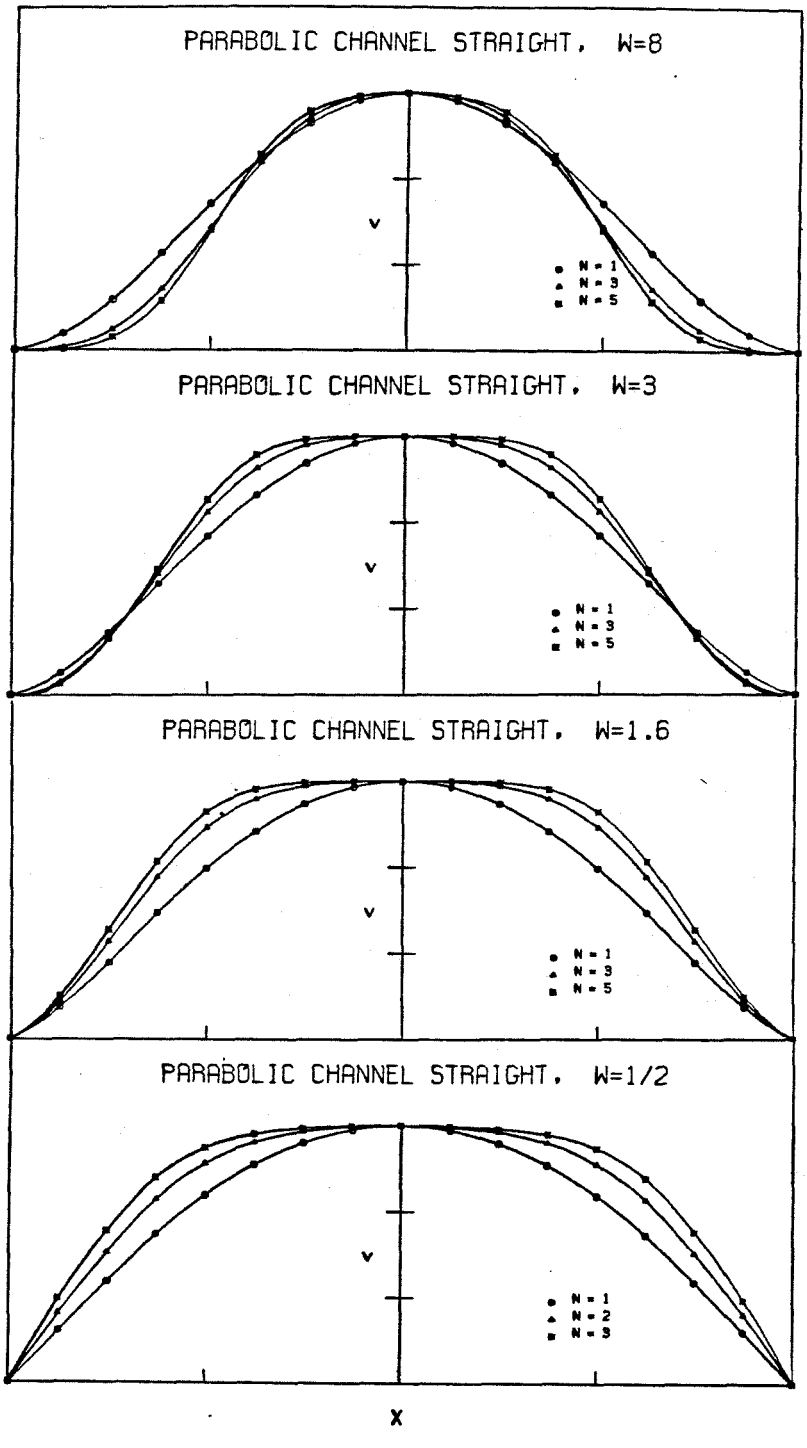

Figure 8.7 Surface velocity profiles separate plots for different W. V is normalized by maximum velocity across each particular profile.

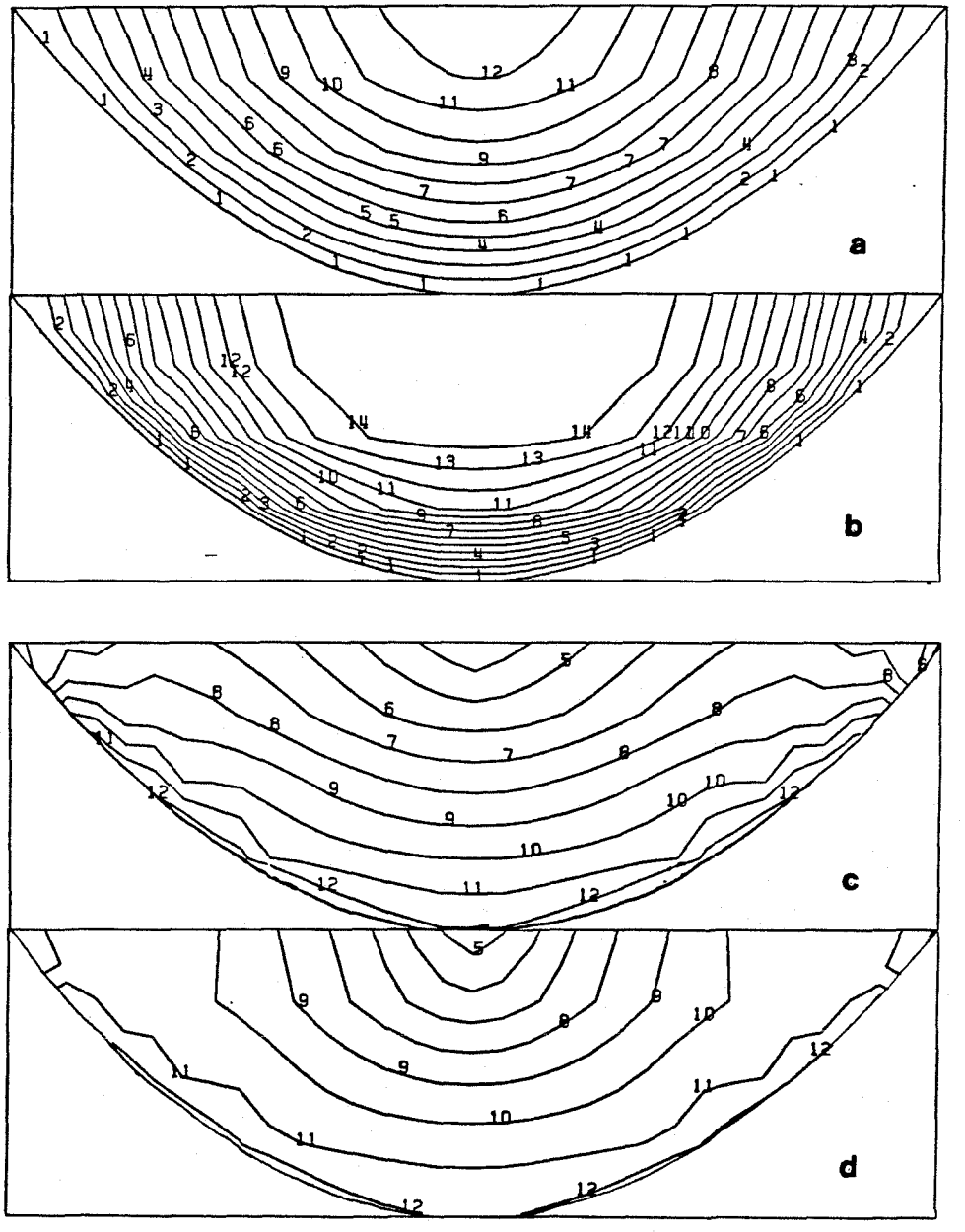

Figure 8.8 Flow and shear stress in parabolic channel (W = 1.6). (a) out-of-plane velocity, n = 1; (b) velocity, n = 5; (c) shear stress magnitude τ, n = 1; (d) τ, n = 5.

motion of a non-linear fluid (ice) within increasingly complex channels. This aspect of the flow within simple parabolic channels is the most fundamental addition made by the results of the present modelling to the results of past modelling studies. (In the analytical perturbation results of Chester (Nye, 1965) this dependence may be seen in the relations for τ_{xz} and τ_{xz} but it is not discussed in that paper.)

8.3 Flow in Simple Channels with a Convex Ice Surface

Consider now the flow within a semicircular channel in which the upper surface is convex upward in transverse profile, as might be expected within the ablation zone of a valley glacier (see Figure 8.9a). This convex upper surface will induce a flow within the plane of the cross-section. The transverse component of this flow will add vectorially with the longitudinal flow out of the cross section and cause a splaying of the surface velocity vectors. Such a splaying commonly occurs in the lower reaches of valley glaciers (see, e.g. Meier, 1962, and Sharp, 1960). Profiles B - E in Figure 4.2 show this feature on Blue Glacier. The convexity of the upper surface is derived from the effects of differential ablation in the presence of valley walls (Echelmeyer, 1972, unpub. and Paterson, 1981) and variations in longitudinal strain rates (Nielson, 1955 and Raymond, 1969).

Continuing this simple *Gedankenexperiment*, allow the transverse shear stresses generated by the non-level surface to enter into the non-linear constitutive relation for ice ($n > 1$) via the second invariant of the deviatoric stress tensor, J_2. The increase in this invariant will lead to a decrease in the effective viscosity and, therefore, an increase in the flow velocity down the channel. An estimate of this increase in velocity and the degree of splaying in the surface velocity can be obtained by introducing the additional stress $\tau_{xy} = \rho g h \sin\gamma$ where h is now the local height of the surface above the transverse horizontal baseline

and γ is the slope of the transverse upper surface. Since J_2 involves the sum of squares, the effects of this transverse flow will be small in most reasonable geometries, but they will be noticeable. However, in the extreme case of profiles D and E on Blue Glacier, as shown in Figure 4.2, the transverse flow may be almost as large as the down-channel component.

This section deals with a more quantitative discussion of transverse flow within simple cross sections, termed in-plane flow (in the plane of the elements). It should be noted that such in-plane flow is not expected for channels with level upper surfaces when the constitutive relation is that assumed for ice. However, as pointed out earlier, Green and Rivlin (1956) have shown that, for a constitutive relation involving higher-order nonlinearities (i.e., the dyadic of τ' (or d') with itself), non-rectilinear flow down a simple channel is admissible due to the interaction of shear stresses with each other.

Figure 8.9b shows the flow within the plane of a semicircular channel with a convex upper surface and no slip at the base. The maximum height of this surface above the horizontal diameter is equal to 1/12th of the channel radius (i.e., 20 m in a channel 240 m deep). The magnitude of the in-plane flow is approximately 2 orders of magnitude less than that down the channel (Table 8.2). This then introduces a small but noticeable splaying about the centerline. The magnitude of this splaying increases as the margins are approached because the importance of the additional thickness of ice relative to the thickness below a level surface increases as the ice thins near the margins. This splaying is less than that observed in nature, possibly because of a small but important component of sliding directed outward toward the margins (Raymond 1969). An in-plane circulation symmetric about the centerline is induced, with a flow downward and outward near the center, becoming upward and outward toward the margin. In nature, the flow within the ablation zone is generally emergent at all

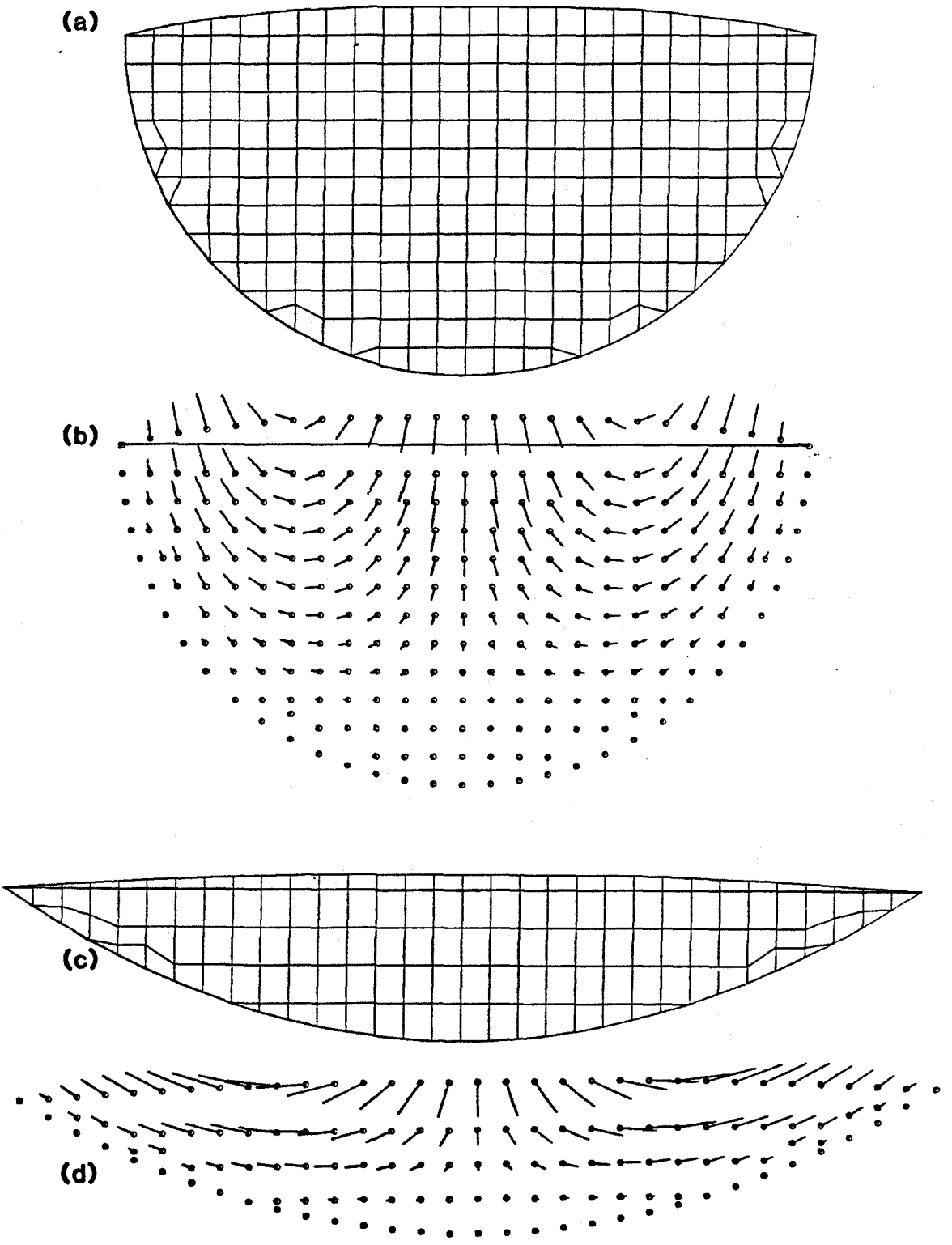

Figure 8.9 Flow in plane of channels with convex upper surface. (a) semicircular channel FE mesh, (b) flow vectors (from dot outward), (c) parabolic mesh (d) flow vectors (1 cm = 0.01 u_z(max)).

points across the surface. This discrepancy with the modeled flow may be explained if the longitudinal variation of ablation is taken into account. In order to maintain the surface profile the flow must be emergent all points, supplying the ice required to compensate melting (Nielson, 1955). In regions of strong ablation this flow will overshadow the small downward flow introduced at the center by the unlevel surface. This does not mean, however, that the circulatory motion is not important in determining the flow streamlines, and it may be important in particle tracing for isotope studies because of the spiraling induced.

Table 8.2
Velocity Components in Semicircular Channel with Convex Upper Surface

n	U_z^o	$U_z(u_x \neq 0, u_y \neq 0)$	$U_x(max)$	$U_y(max)$
3	1.00	1.0074	0.0074	0.016
5	1.00	1.0405	0.0316	0.0394

Azimuth of Surface Velocity off Centerline

n / X=	±1/6	±3/6	±5/6
3	± 0.2°	± 0.5°	± 0.3°
5	± 0.2°	± 1.2°	± 2.0°

Convexity equal to 1/12 depth, U_z^o is the surface velocity at centerline when the x,y components of velocity are fixed, $U_z(u_x \neq 0, u_y \neq 0)$ is the centerline velocity when the x,y components are allowed to be non-zero, and the azimuth is the angle off the centerline at X=x/R along y=0

The increase in longitudinal velocity within a semicircular channel with convex ice surface above that in a channel with a flat ice surface is largely due to the extra ice mass added to the upper surface. But there still remains the effect of the non-linearity of the flow law mentioned above. Figure 8.10 shows the effects of allowing non-zero in-plane flow, where the comparison is made with the thickened channel in which no in-plane flow is allowed. There is no increase for n = 1 as is expected (n - 1 = 0). The increase in longitudinal velocity becomes more prominent as the strength of the J_2 dependence increases (i.e. as n

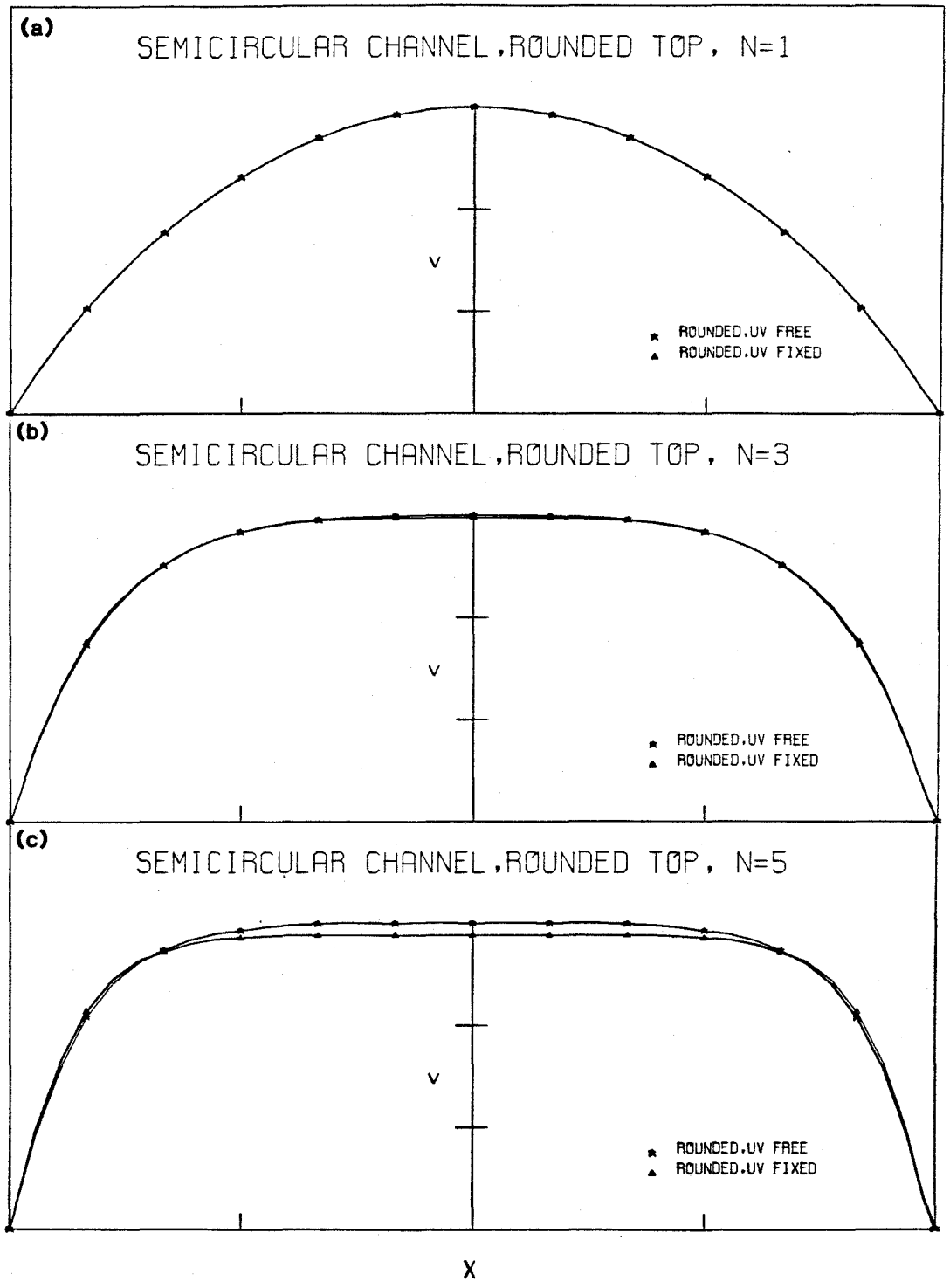

Figure 8.10 Out-of-plane flow in semicircular channel with convex top, showing increase in velocity if in-plane flow is allowed (u,v ($\equiv u_x, u_y$) free). Velocity is normalized by maximum velocity with u_x, u_y free.

becomes larger). For n = 3, the increase is barely noticeable, while for n = 5 there is a 4% increase in u_z at the centerline. Larger convexities in the ice surface would, of course, cause a larger effect in u_z.

The in-plane flow within parabolic channels of various aspect ratios (W) is shown in Figures 8.9d and 8.11b. The magnitude of the convexity at the centerline above the level surface is $\frac{1}{10}$ the depth below this level surface. The general features are similar to those found for the circular conduit. The areal distribution of in-plane flow is seen to depend on n. The dominant velocity increase is seen to arise simply in response to the thickness change, with the effects of the non-linearity in the flow law being small (Figures 8.12 and 8.13). The relative effects of the in-plane flow on the out-of-plane flow show the same variation with the stress exponent as above, but there appears to be little variation with W. The major effect is seen in the central region where the flow velocity is nearly constant.

Observational results from Athabaska Glacier (Raymond, 1969) show that, in this glacier, where basal sliding is the dominant flow mechanism, the distribution of lateral flow is quite different than that obtained above. Lateral tilting of the boreholes is concentrated at depth, rather than decaying with depth as would be expected from the above analysis. Raymond develops an approximate analytical model for this flow in which the major difference from the above model is the condition of zero shear traction of the lower and side boundaries, allowing sliding to occur. This is clearly the source of the deformational patterns which are observed on Athabaska Glacier. Although it has been assumed that sliding is negligible in the present study, even a small amount of lateral sliding (small relative to the down channel flow) could lead to a pattern of transverse flow more closely similar to that determined by Raymond, simply because the

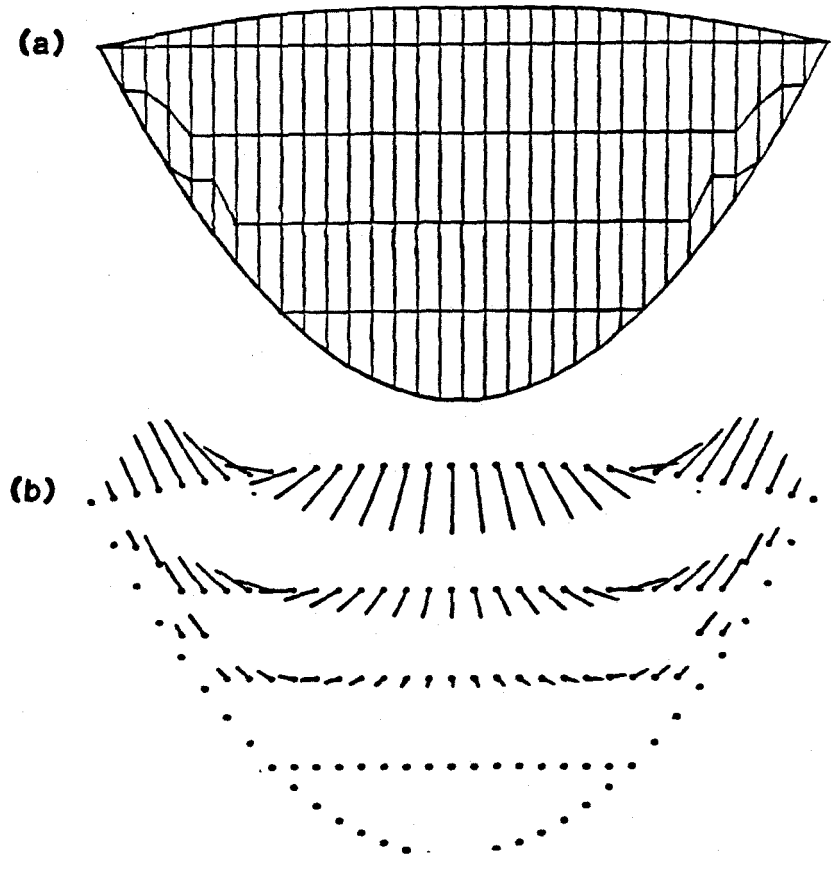

Figure 8.11 Parabolic cross section with convex top (W = 1, n = 5). (a) mesh; (b) in-plane flow 1 cm = 0.01 u_z.

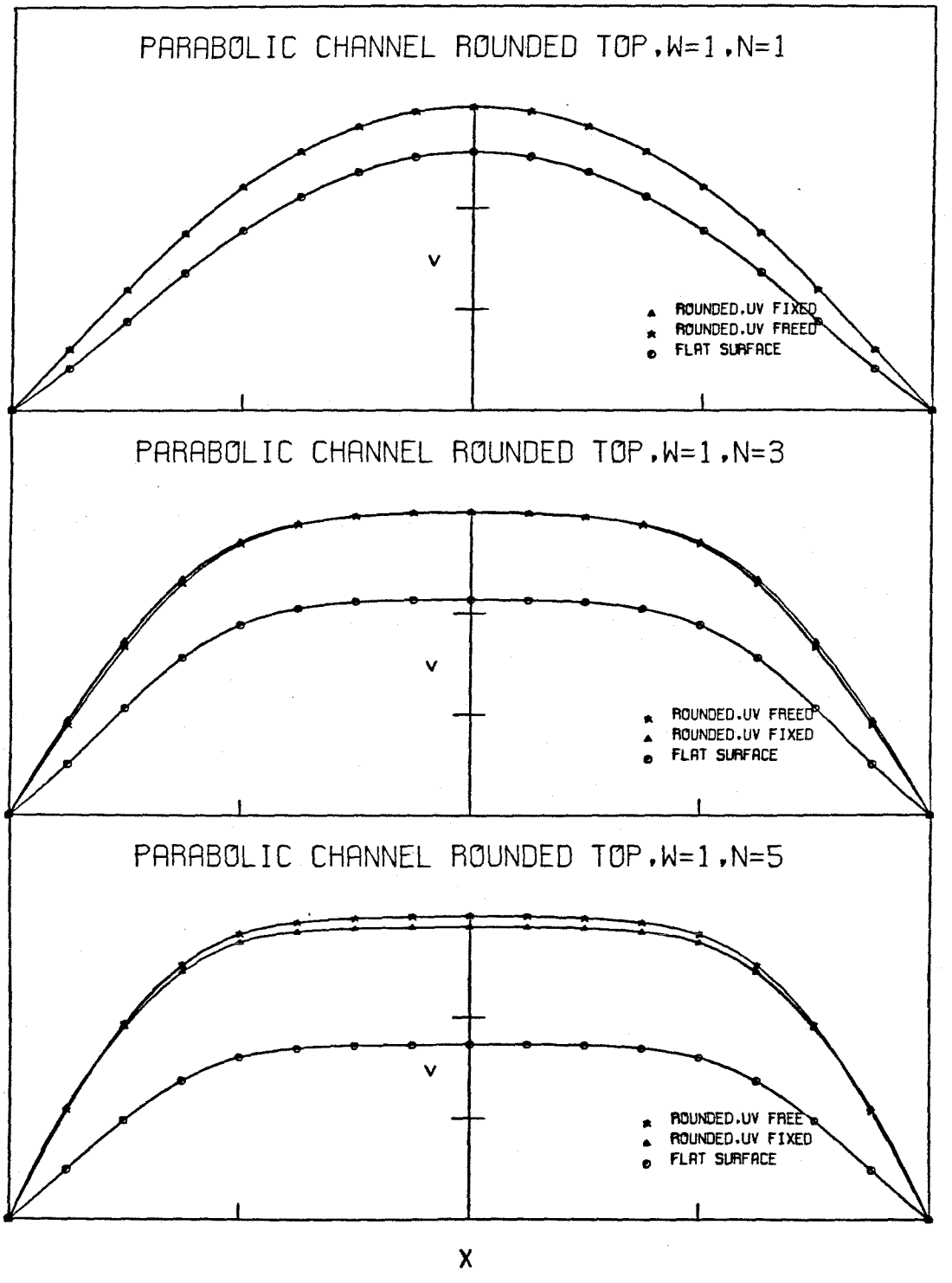

Figure 8.12 Out-of-plane flow in parabolic channel (W = 1, n=5) with convex top, with and without inplane flow allowed, and flow out of flat-topped channel.

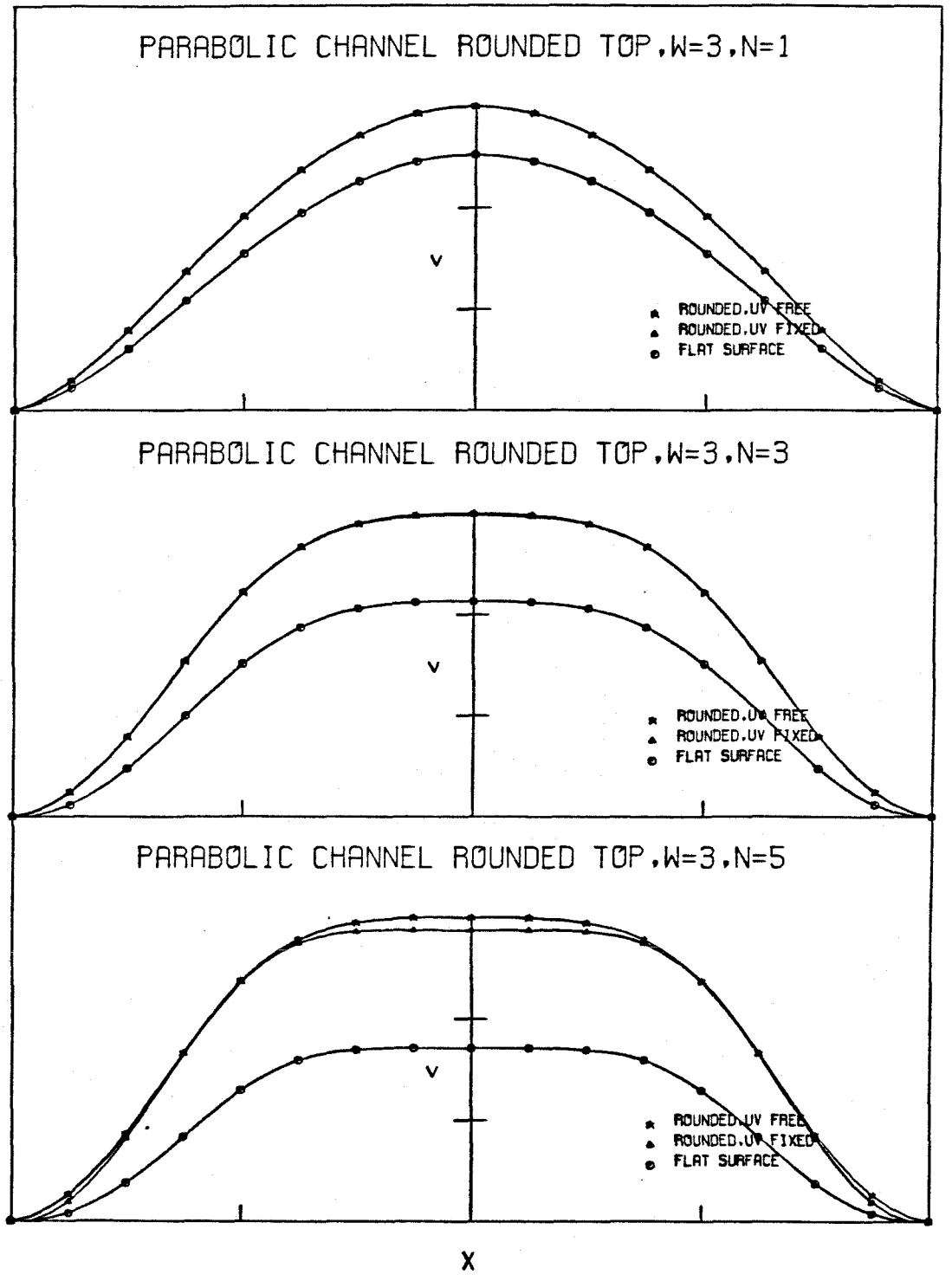

Figure 8.13 Same as Figure 8.12, except W = 3.

magnitude of the lateral motion is itself small.

In the accumulation area of a glacier, there is often a laterally concave ice surface, surface elevation being higher towards the margins (e.g. profile J on Blue Glacier). In a similar manner as above, this profile induces an inward directed component of flow whose magnitude depends upon the surface profile. The spiraling nature of the flow is in an opposite sense to that found above.

8.4 Variation of the Viscosity Factor within a Channel

In view of the evidence that the factor η_f in the flow law of ice (8.1) may vary from one element of ice to another because of a dependence on various factors (see below), the possible consequences of such a variation within the mass of a glacier need to be examined in relation to the assumption that η_f is constant. In this section the flow within a semicircular conduit in which η_f is a function of position is studied, showing its relation flow with constant η_f. Additional studies with a spatially varying η_f will be discussed when the response to a change in thickness is developed (Chapter IX).

The viscosity factor, η_f is, by definition, independent of the current stress state, but it may depend on the stress history of the ice sample.It has been found to vary with the grain size distribution, c-axis orientation, impurity content, water content, temperature, and other factors. (See, among others, Baker, 1978;Baker and Gerberich,1979; Duval, 1977, 1981; Duval and Le Gac,1980;Kamb, 1972; Glen, 1975;Goodman,Frost, and Ashby,1977; and Hooke,et al.,1972.) These parameters may depend on position and the history of deformation within an ice mass. The quantitative relationship must in general be exceedingly complex. One can, however, expect that in a general way the "softness" of glacier ice will increase toward the bedrock boundaries because of enhanced development of crystal fabrics favorable to glacier flow. On this account η_f may decrease by as

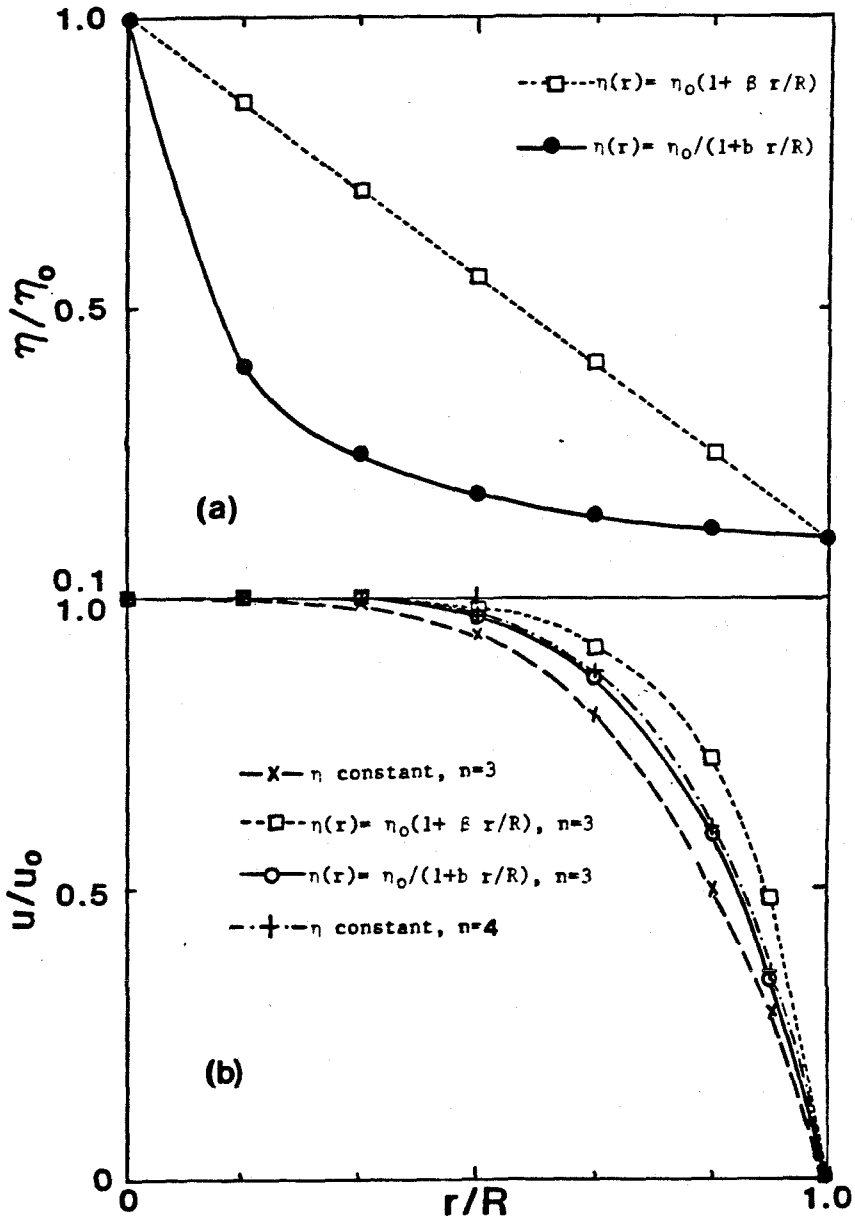

Figure 8.14 a) Variation of viscosity factor with radius in semicircular channel for two models. b) radial velocity profile in channels with different viscosity factor variations and exponent n. u_o = velocity at r = 0 for each model.

Performing the integration for the two models, with n = 3, we obtain

$$\hat{u}^A(r) = \frac{1}{3\beta R}(1-\hat{f}^3) - \frac{1}{(\beta R)^4}\left\{\frac{1}{2}(\beta R)^2[1-\hat{f}^2] - \beta R[1-\hat{f}] + \log\left[\frac{1+\beta R}{1+\beta r}\right]\right\} \quad (8.6a)$$

$$\hat{u}^B(4) = 1 + \left[\frac{n+1}{n+2}\right]bR - \hat{f}^{n+1}\left[1 + \left[\frac{n+1}{n+2}\right]br\right] \quad (8.6b)$$

while, for $\eta_f = \eta_0$ (constant), the usual relation

$$\hat{u}(r) = 1 - \hat{f}^{n+1} \quad (8.7)$$

is obtained. In the above, $\hat{f} = r / R$.

The results are shown in Figure 8.14b, where $\hat{u}_o$ is the value of $\hat{u}$ at r = 0. The rate of shear deformation shows stronger gradients at depth when $\eta_f = \eta_f(r)$ than when it is a constant, with little deformation near the surface. This is, of course, expected from the softening of the ice at depth. The magnitude of the centerline velocity in model B is increased almost a factor of ten in response to the decreased viscosity factor, which, as is seen in Figure 8.14a, is nearly constant at a value $0.2\eta_o$ at large radii. The linear variation of η_f with radius (model A) does not produce such a large increase in centerline velocity, but it does produce stronger shear strain rate gradients at depth (radius) than does the variation in model B.

The most noteworthy feature of the velocity profiles is seen by comparison with velocity profiles for η_f constant, with higher values of n. Model B agrees rather well with a constant-η_f profile for n = 4. Similarly, model A agrees with a constant-$\eta_f$profile for an even higher value of n.

By means of this simple model, it is thus seen how the velocity field of a glacier for which the ice appears to obey a single flow law with fixed n and η_f may in fact be generated by ice having spatially varying η_f and a different n. It is not sufficient to use the observed rates of deformation within a single borehole or

across the surface of the ice mass to distinguish between these two flow models. Nor may it really be necessary, if the flow behaviour of the steady-state glacier is the only thing of interest. As will be seen in the next chapter, however, the response of a glacier to a climatic change (and subsequent change in geometry) is different for the two flow models.

8.5 Flow of Ice Around a Circular Bend

8.5.1 Basic Equations Like rivers, glaciers flow down channels which may curve or bend. And, as in rivers, bends can introduce interesting and important features in the stress and velocity fields of the moving fluid. Previous discussion of these features on glaciers is limited to that of Meier, et al. (1974), in which few analytical details are given. In this section the results of an analytical and numerical study of the flow of a non-linear fluid such as ice, obeying the power-law creep relation, around a bend in a channel will be given. A qualitative comparison with observed glacial features will be made.

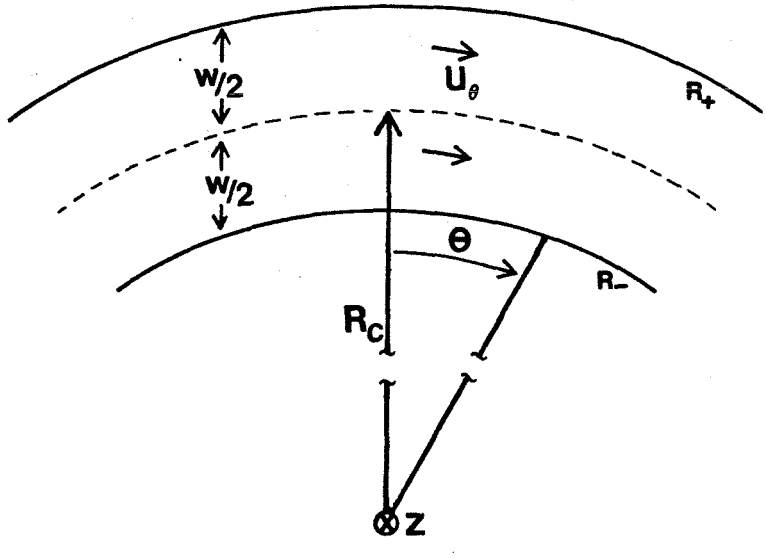

Figure 8.15 Geometry and notation for flow in deep, curving channel.

To formulate the equations governing fluid flow about a bend, consider the equations of equilibrium (conservation of momentum) in the cylindrical coordinates defined in Figure 8.15:

$$\frac{\partial \tau_{rr}}{\partial r} + \frac{1}{r}\frac{\partial \tau_{\vartheta r}}{\partial \vartheta} + \frac{\partial \tau_{zr}}{\partial z} + \frac{1}{r}(\tau_{rr} - \tau_{\vartheta\vartheta}) = -f_r \tag{8.7a}$$

$$\frac{\partial \tau_{r\vartheta}}{\partial r} + \frac{1}{r}\frac{\partial \tau_{\vartheta\vartheta}}{\partial \vartheta} + \frac{\partial \tau_{z\vartheta}}{\partial z} + \frac{2\tau_{r\vartheta}}{r} = -f_\vartheta \tag{8.7b}$$

$$\frac{\partial \tau_{rz}}{\partial r} + \frac{1}{r}\frac{\partial \tau_{\vartheta z}}{\partial \vartheta} + \frac{\partial \tau_{zz}}{\partial z} + \frac{1}{r}\tau_{rz} = -f_z \tag{8.7c}$$

and relations for the components of the rate-of-deformation tensor, $\dot{\varepsilon}$:

$$\dot{\varepsilon}_{rr} = \frac{\partial u_r}{\partial r}, \qquad \dot{\varepsilon}_{\vartheta\vartheta} = \frac{1}{r}\frac{\partial u_\vartheta}{\partial \vartheta} + \frac{u_r}{r}, \qquad \dot{\varepsilon}_{zz} = \frac{\partial u_z}{\partial z} \tag{8.8a-c}$$

$$\dot{\varepsilon}_{r\vartheta} = \frac{1}{2}\left[\frac{1}{r}\frac{\partial u_r}{\partial \vartheta} + \frac{\partial u_\vartheta}{\partial r} - \frac{u_\vartheta}{r}\right], \tag{8.8d}$$

$$\dot{\varepsilon}_{rz} = \frac{1}{2}\left[\frac{\partial u_r}{\partial z} + \frac{\partial u_z}{\partial r}\right], \tag{8.8e}$$

$$\dot{\varepsilon}_{\vartheta z} = \frac{1}{2}\left[\frac{\partial u_\vartheta}{\partial z} + \frac{1}{r}\frac{\partial u_z}{\partial \vartheta}\right]. \tag{8.8f}$$

Besides the replacement of the operator $\frac{\partial}{\partial x_2}$ by $\frac{1}{r}\frac{\partial}{\partial \vartheta}$ (because the element of arc length along $\hat{\vartheta}$ is r d ϑ), there is one major difference between each of the equations (8.7a-c)and (8.8b,d) and their rectangular counterparts. In each equation in cylindrical coordinates there is a $\frac{1}{r}$x(··) term.

These terms in (8.7a-c) arise due to the difference in areas of the constant-radius faces (at r and r+dr) of a small element of volume and to the non-parallelism of the constant-angle faces (ϑ and ϑ+dϑ). The extra terms in (8.8b,d) account for the circumferential and shear strains arising because of the differences in length of two circles differing by $u_r\Delta t$ in radius and because of the

change in the radial direction at different ϑ. The most important of these terms in determining the stresses and velocities in the out-of-plane direction (down the channel) are those in (8.7b) and (8.8d).

Considering first the rate-of-deformation equation first (8.8d), note that the curvature term tends to reduce the rate of shear when u_ϑ is positive. This will cause the location of the point(s) at which $\dot{\varepsilon}_{r\vartheta}$ vanishes to shift inward (to lower r) from the point(s) of maximum velocity ($\frac{\partial u_\vartheta}{\partial r} = 0$). From the general flow law of a Riener-Rivlin fluid (of which power-law creep is an example) it follows that the shear stress $\tau_{r\vartheta}$ will then vanish at this shifted location. Following M1, the point on the surface at which $\dot{\varepsilon}_{r\vartheta}=0$ will be termed the stress centerline. Thus, the stress centerline will not correspond to the point of maximum surface velocity for a curving channel, but it will tend uniformly to that point as $r \to \infty$. The velocity profile in a curving channel will be asymmetric about the geometrical centerline of the channel, as will the stress field.

The term $2\tau_{r\vartheta}/r$ in (8.7b) will give rise to nonlinearities in the shear stress profiles at depth and across the surface of the channel.

8.5.2 Deep, Curving Channel As a first model, consider the flow of a fluid in a deep curving channel with vertical walls and with zero shear traction at the base for which the effects of the base of the channel can be neglected. This simple but,for most glaciers, rather unrealistic model is treated because it brings out in the clearest way the effects of flow in a curving channel. The geometry of the flow is shown in Figure 8.15. The inner and outer radii of the channel are R_- and R_+, respectively. The centerline of the channel follows a path of radius of curvature R_c and the channel has a uniform width of w. Along the vertical channel walls no slip is allowed. The streamlines are assumed to follow paths of constant radius and no gradients exist around the curve ($\frac{\partial}{\partial \vartheta} = 0$) and only hydrostatic

conditions in the vertical.

Assume that the surface of the glacier is transversely level as the ice flows down a spiralling path between vertical walls. Then, since the ice must drop a fixed distance for a given angular motion $\Delta\vartheta$, the surface slope must vary inversely to radius r across the surface from R_- to R_+. If $z=Z(r,\vartheta)$ represents the ice surface, then where Z_o is the initial coordinate of the surface at ϑ_o, then

$$Z(r,\vartheta) = Z_o - r\vartheta\tan\alpha(r) \; . \tag{8.9}$$

where Z_o is the initial coordinate of the surface at ϑ_o. But the surface remains level across a line of constant ϑ. Therefore, if, at $r = R_-$, we take $\alpha = \alpha_o$, then

$$\tan\alpha(r) = \tan\alpha_o \frac{R_-}{r,} \qquad r\,\text{member}[\, R_-,R_+ \,] \; . \tag{8.10}$$

or, for small angles

$$\alpha(r) = \alpha_o \frac{R_-}{r} \qquad . \tag{8.11}$$

Note that the transverse variation in surface slope described by (8.10)is actually observed on Blue Glacier as a decrease in α form the western to the eastern margin, which was noted in Chapter III. The effect is the strongest along those profiles located at the sharpest part of the bend, from D to I, and is partly instrumental in generating the small icefall on the inside of the bend at E. From the observed variation in α, an estimate of the radius of curvature pertinent to Blue Glacier may be obtained from (8.10) (using slopes as averaged over the length of the bend, see Chapter X).

With the above assumed geometry, the following relation for the effective body force component in the ϑ direction holds :

$$f_\vartheta = \rho g \tan(\alpha_o \frac{R_-}{r}) \; ,$$

(8.12)

or, for small slopes

$$f_\theta \approx \rho g \alpha_o \frac{R_-}{r}. \tag{8.13}$$

Under the assumptions of a deep, curving channel with level free surface, $\mathbf{u} = (0, u_\theta, 0)$; u_θ will be denoted u in what follows. Following this, we find

$$\dot{\varepsilon}_{rr} = \dot{\varepsilon}_{zz} = \dot{\varepsilon}_{\theta\theta} = \dot{\varepsilon}_{rz} = \dot{\varepsilon}_{\theta z} = f_r = 0$$

and

$$\dot{\varepsilon}_{r\theta} = \frac{1}{2}\left(\frac{\partial u}{\partial r} - \frac{u}{r}\right). \tag{8.14}$$

This leads to the following equations when a power-law creep relation is employed :

$$\tau_{rr} = \tau_{\theta\theta} = \tau_{zz} \quad , \quad \tau_{rz} = \tau_{\theta z} = 0 \quad ,$$

$$\text{and} \qquad J_2^{1/2} = \tau_{r\theta}. \tag{8.15}$$

Equations (8.7),(8.13),(8.14), and (8.15) yield the following reduced boundary value problem (assuming no slip at the walls): Find u, $\tau_{r\theta}$ and τ_{zz} such that

$$\frac{\partial \tau_{r\theta}}{\partial r} + 2\,\frac{\tau_{r\theta}}{r} = -\rho g \alpha_o \frac{R_-}{r} \tag{8.16a}$$

$$\frac{\partial \tau_{zz}}{\partial z} \approx \rho g \tag{8.16b}$$

$$\frac{1}{2}\left(\frac{\partial u}{\partial r} - \frac{u}{r}\right) = \frac{\tau_{r\theta}^n}{2\eta} \qquad \text{for} \quad r \in (R_-, R_+) \tag{8.16c}$$

$$u(R_-) = 0 \tag{8.16d}$$

$$u(R_+) = 0 \tag{8.16e}$$

$$\tau_{zz}(Z) = 0 \tag{8.16f}$$

The solution will be developed in detail because several important features of the final results come to light in the solution procedure. From (8.16b) and (8.16f) we find

$$\tau_{zz} \approx \rho g(z - Z) .$$

If we denote $\tau_{r\vartheta}(R_-)$ by $F_\vartheta T_{R_-\vartheta}$ and $F_\vartheta = -\frac{1}{2}\rho g \alpha_o R_-$, then (8.16a) yields

$$\tau_{r\vartheta}(r) = F_\vartheta \left\{ 1 - \left(\frac{R_-}{r} \right)^2 + \left(\frac{R_-}{r} \right)^2 T_{R_-\vartheta} \right\} , \tag{8.17}$$

while(8.16c,d) lead to

$$u(r) = \frac{1}{\eta} r \int_{R_-}^{r} \tau_{r\vartheta}^n \frac{dr'}{r'} \qquad r \in (R_-, R_+) . \tag{8.18}$$

Since the walls are taken to be vertical the shear stress need not necessarily vanish at R_-. In order to determine $TR_-\vartheta$ (and thus fully specify $\tau_{r\vartheta}$), we must evaluate (8.18) at R_+ using (8.17) and then apply the condition of no slip (8.16e). That is,

$$0 = \int_{R_-}^{R_+} \left\{ 1 - \left(\frac{R_-}{r} \right)^2 \left(1 - T_{R_-\vartheta} \right) \right\}^n \frac{dr}{r} . \tag{8.19}$$

For different n this yields a polynomial of degree n in the unknown $T_{R_-\vartheta}$ Exact solution for n = 1 yields

$$T_{R_-\vartheta} = 1 - \frac{R_+^2}{R_c W} \log \frac{R_+}{R_-} . \tag{8.20}$$

For n = 3 and 5, $T_{R_-\vartheta}$ is the solution to the following equations:

$$n = 3 \qquad 0 = \frac{1}{6} c^3 \varphi_6^+ + \frac{3}{4} c^2 \varphi_4^+ + \frac{3}{2} c \varphi_2^+ - \log \rho_+ \equiv \psi_3(\rho_+) \tag{8.21}$$

$$n = 5 \qquad 0 = \frac{1}{10} c^5 \varphi_{10}^+ + \frac{5}{8} c^4 \varphi_8^+ + \frac{5}{3} c^3 \varphi_6^+ + \frac{5}{2} c^2 \varphi_4^+ + \frac{5}{2} c \varphi_2^+ - \log \rho_+ \equiv \psi_5(\rho_+)$$

(8.22)

where

$$\varphi_m^+ = 1 - (\rho_+)^m$$

$$\rho_+ = \frac{R_-}{R_+}$$

and $$c = (T_{R_-\theta} - 1) \ . \qquad (8.23)$$

Given a channel width and radius of curvature, these equations may be solved for $T_{R_-\theta}$. Once this is obtained, u(r) may be from

$$u(r) = \frac{1}{\eta} r (F_\theta)^n \psi_n (\rho) \ , \qquad (8.24)$$

where the ψ_n are given as in (8.21) and (8.22) with c given by (8.23) and $\rho = \frac{R_-}{r}$.

For n = 1 these relations give explicitly

$$\tau_{r\theta}(r) = F_\theta \left[1 - \frac{(R_- R_+)^2}{R_c w} \left[\log \frac{R_+}{R_-} \right] \frac{1}{r^2} \right] \qquad (8.25a)$$

and

$$\frac{u(r)}{r} = \frac{F_\theta}{\eta} \left\{ \log \frac{r}{R_-} + \frac{1}{2} \frac{(R_+ R_-)^2}{R_c w} \log \frac{R_+}{R_-} \left[\frac{1}{r^2} - \frac{1}{R_-^2} \right] \right\} , \qquad (8.25b)$$

where, again,

$$F_\theta = -\frac{1}{2} \rho g \alpha_o R_- \qquad \text{and} \qquad r \in [R_-, R_+] .$$

The solution above shows an important feature of the stress field. The magnitude of the shear stress at a fixed radius, as given by (8.25a) (or(8.17) in conjunction with the solutions to (8.21,22)) is dependent upon the stress exponent in the flow law. Thus, as was noted in the discussion of the flow down a parabolic channel, the boundary conditions of no sliding cause the stresses to depend

upon the degree of non-linearity in the constitutive relation. (A similar dependence on n would probably arise from a sliding boundary condition.)

In addition to this flow-law dependence, the stress and velocity depend upon the radius of curvature and channel width. The stress is not a linear function of radius, nor is it symmetric about the center of the channel.

As a numerical example, consider a deep channel of width w = 9 forming a bend with radius of curvature R_c = 8.5 ($R_- = 4, R_+ = 13$, in arbitrary units). If we introduce normalization of the stress by the value for straight channel flow (taking the slope in this straight channel to be that at the centerline of each particular curving channel, $\alpha_c = \alpha_o \frac{R_-}{R_c}$), then

$$T_{r\theta} = \frac{\tau_{r\theta}(r)}{\frac{1}{2} w \rho g \alpha_c} ,$$

and the following are the solutions:

Table 8.3
Stress and Flow in a Deep, Curving Channel

n	$T_{R_-\theta}$	$T_{R_+\theta}$	R_τ	R_v	U_{max}
1	1.52	-0.71	6.46	7.69	0.479
3	1.16	-0.75	5.97	8.52	0.210
5	1.04	-0.76	5.80	9.01	0.140

Here the stress centerline, R_τ is defined as the radius at which $\tau_{r\theta}$ changes sign (following M1), and R_v denotes the radius at which the maximum velocity U_{max} occurs.($U = u / [(\frac{1}{2} w \rho g \alpha_c)^n w / 2\eta]$) (For a symmetric straight channel, the stress centerline coincides with the channel centerline.) The skewed stress distribution in a curving channel ($R_\tau \neq 8.5$ here) gives rise to a non-symmetric velocity profile. Instead of occurring at the center of the channel (in this case, r=8.5), the maximum velocity occurs at a radius, R_v, which varies with n, as tabulated above.

The stress and velocity distributions for the numerical example above are shown in Figures 8.16 and 8.17.

As expected, the position of the stress centerline and velocity maximum vary with the radius of curvature, as is shown in Table 8.4 (for w = 9).

Table 8.4
Variation of R_τ and R_v with Curvature

	R_-=	4	10	100	1000	$\rightarrow \infty$
n=3	$R_\tau - R_-$	1.97	2.98	4.29	4.48	4.5
	$R_v - R_-$	4.52	5.05	5.29	(5.02)	4.5
	U_{max}	0.210	0.242	0.249	.250	.250
n = 1	$R_\tau - R_-$	2.46	3.32	4.34	4.48	4.5
	$R_v - R_-$	3.69	4.05	4.45	4.49	4.5
	U_{max}	0.479	0.494	0.499	0.500	0.500

The effects of channel curvature are strongly displayed by the results from this simple model (Tables 8.3 and 8.4). These effects are as follows:

1. The stress centerline is shifted toward the inside of the bend. The amount of this shift increases with the curvature of the channel. For a straight channel, the stress centerline is at the channel center, while for tight bends, it tends toward the inside edge.

2. For a fixed centerline curvature, the higher n the more pronounced the inward shift of the stress centerline.

3. The magnitude of $\tau_{r\theta}$ is dependent upon the channel curvature and n.

4. $\tau_{r\theta}$ (as a function of transverse coordinate r) shows an increasing departure from linearity with decrease in R_c (increasing curvature).

5. The velocity profile is no longer symmetric about the center. The asymmetry increases as R_c decreases or n increases.

6. The position of the maximum velocity shifts with changing curvature and n.

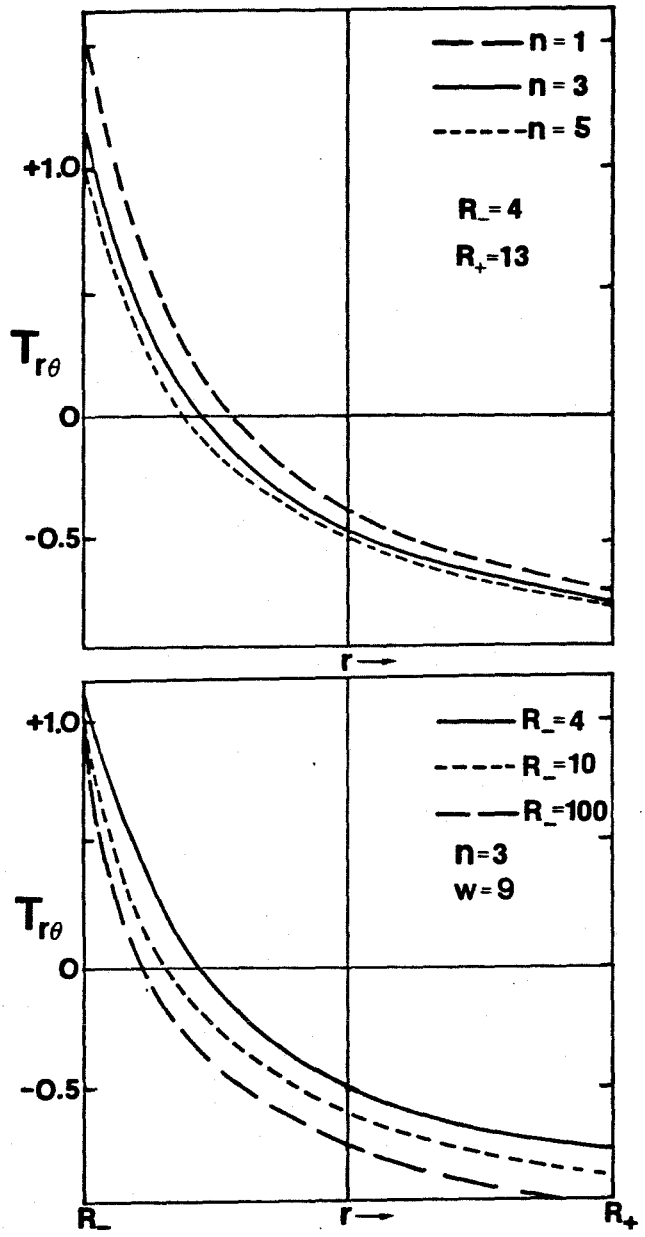

Figure 8.16 Normalized shear stress($T_{r\theta}$) across width of deep,curving channel(vertical walls). a) different n, b) different R_.

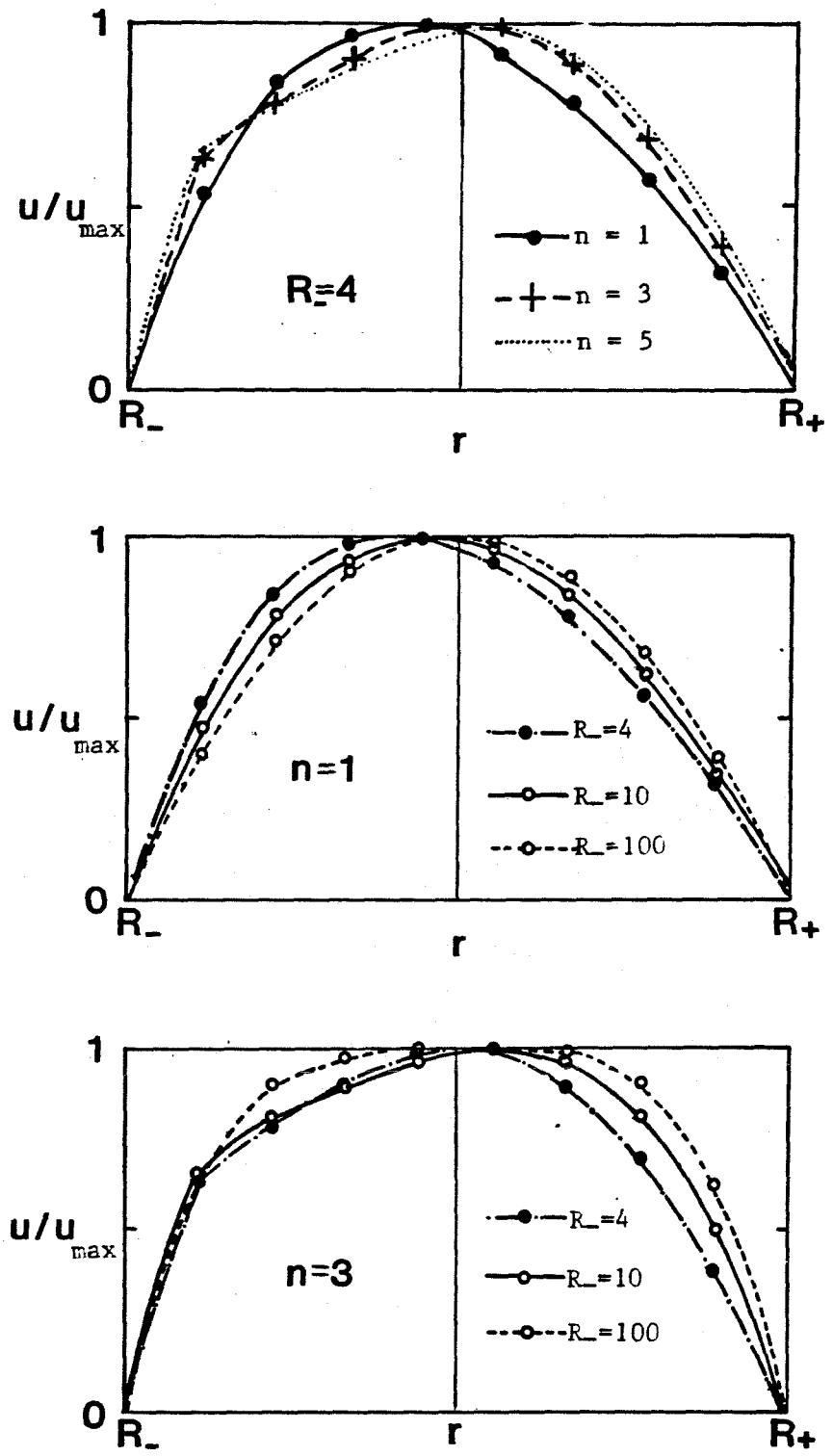

Figure 8.17 Velocity profiles across infinitely deep channel (normalized by maximum velocity across profile).
a) Different n, $R_-=4$, $R_+=13$
b) Different curvatures, n=1, width=9
c) Different curvatures, n=3, width=9
Analytical results

For fixed curvature, it moves outward toward the outside margin as n increases. ($\lim_{n\to\infty} R_v = R_+$.) For $n < \sim 3$, the maximum velocity occurs at a point inside the center, while for n=3 the maximum occurs at or outside of the center (depending on R_c), and, for $n > 3$ it is located toward the outside of the bend. An interesting feature is noted for n=3 and n=5 (and probably for any value of n greater than 3). As the curvature decreases (R_c increases) there is an apparent shift in the position of the velocity maximum away from the geometric centerline toward the outside of the bend. If this trend continues, then, as a straight channel is approached ($R_c \to \infty$), the position of maximum velocity will not be the channel centerline, as is expected from standard flow theory (Nye,1965)! (Note, however, that for R_- the velocity maximum is closer to the center than for larger curvatures. This value is somewhat approximate as the velocity solution involves the products of very large numbers and small ones, leading to some round-off error.) This dilemma may be resolved if one considers an ideal velocity profile within a curving channel. The profiles in Figure 8.17 may be approximated by high-order parabolas which are tilted by an angle β about their foci (or, even more approximately, a rectangle tilted about its center). The tilt β is inversely proportional to R_c. The point of intersection (R_v) of the parabola (or rectangle) with a horizontal line at a height $u_{max}(\beta)$ above some reference will move outward with decreasing tilt (increasing R_c) until some angle is reached at which a point inward from the previous maximum is as high as that previous point, and, then, R_v will move inward toward the centerline with any increase in R_c. The value of R_v for R_-=1000 and n=3 shows an example of this changing trend. In the case of a rectangle, there is a singular behavior as the face of the rectangle becomes as high as the rotating corner (i.e. the face becomes horizontal). If the parabola is too peaked, as for n=1,

the maximum will never move outward of the centerline.

These basic features of fluid motion around a bend are observed in nature. In particular, the crevasse pattern and the asymmetry in the velocity profiles can be observed on Blue Glacier. A detailed examination of these features will be given when the flow in realistic channels is discussed in the following sections and in Chapter X.

8.5.3 Curving Channels of Finite Depth In order to calculate the effects of channel curvature for channels of finite depth, an axisymmetric out-of-plane element was introduced into the finite element algorithm (Sec.7.12.3). The algorithm was tested by comparison with the above results and with analytical results for the flow of a non-Newtonian fluid between two rotating coaxial cylinders and down an annular conduit. (These results are given in Appendix C.) The FE scheme shows good agreement with the analytical results if a sufficiently dense mesh is used and careful attention is paid to the timestep in relation to the viscosity. As usual, the error in the solutions tends to increase as the order of nonlinearity increases.As for the straight channel, the possibility of lateral or in-plane flow is allowed in the FE scheme. This increases the complexity of the solutions in some cases, as well as the storage requirements and computing time due to the large increase in the dimension of the stress and velocity vectors and rank of the stiffness K.

8.5.4 Rectangular Channel The presence of a no-slip boundary at the bottom of a shallow rectangular channel introduces additional shear stresses into the less complex problem discussed above. These additional stresses cause a redistribution of the velocity field and cause minor changes in the features noted in section 8.5.2.

For n = 1 to 5, the shift in the position of the maximum velocity is toward the

inside of the bend, and the magnitude of the shift is generally greater than that observed for the deep channel. The thinner the channel, the more marked the shift. This may be explained by considering the strain-rate, which includes the term -u/r. With the increasing resistance at the bed, u is reduced and the rate of deformation becomes more dependent upon the channel geometry and boundary conditions. That is, u becomes more locally controlled by the basal shear stress, while the relative effects of $\tau_{r\theta}$ diminish as the depth decreases. But the local basal shear stress is determined by the slope, which is inversely related to r. Thus, there is a shift of the velocity maximum inward to where the slope is larger.

An increase in the radius of curvature causes an outward shift in R_v for a given n, similar to that observed in the previous section. The stresses follow patterns similar to those in the deep channel.

8.5.5 Semicircular Channel The symmetry in the stress and velocity within a semi-circular conduit is broken by the introduction of channel curvature, with the departures from symmetry increasing as the radius of curvature decreases. Figure 8.18 shows an example of the form of the asymmetry in the surface velocity which arises in a curving channel. (This and related figures will be discussed in detail below.)

Contours of shear stress magnitude in a straight channel form concentric cylinders about the center of the channel, increasing outward. In addition, the individual components of stress are linear with depth (τ_{yz}) and linear across the surface (τ_{xz}). The departure from these patterns for a curving channel is shown in Figure 8.19. Contours of the shear stress magnitude τ (where $\tau^2 = \tau_{r\theta}^2 + \tau_{z\theta}^2$) shown in this figure for several values of R_c (and n = 3) indicate the asymmetries introduced by curvature. A monotonic increase in skewness toward the

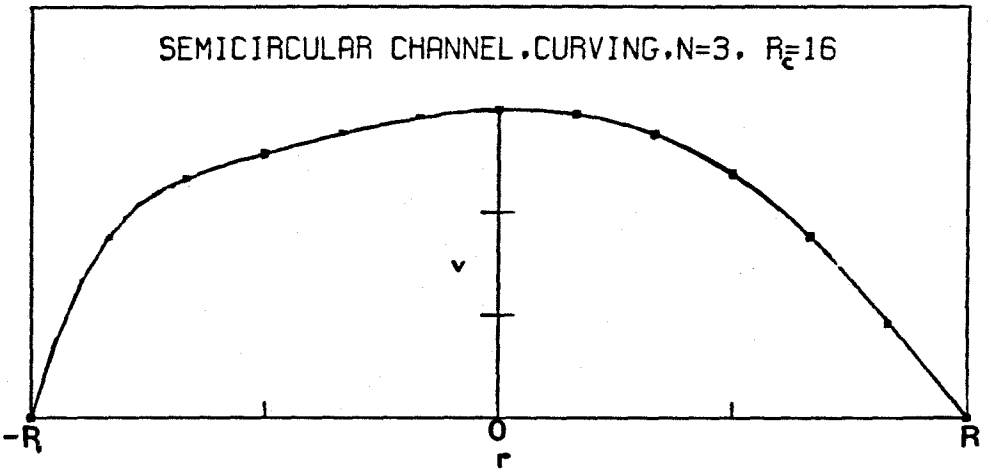

Figure 8.18 Example of surface velocity profile out of curving semicircular channel, showing asymmetry of profile about center (R = 0), R_c = 16 units (radius of channel is 6 units in all figures).

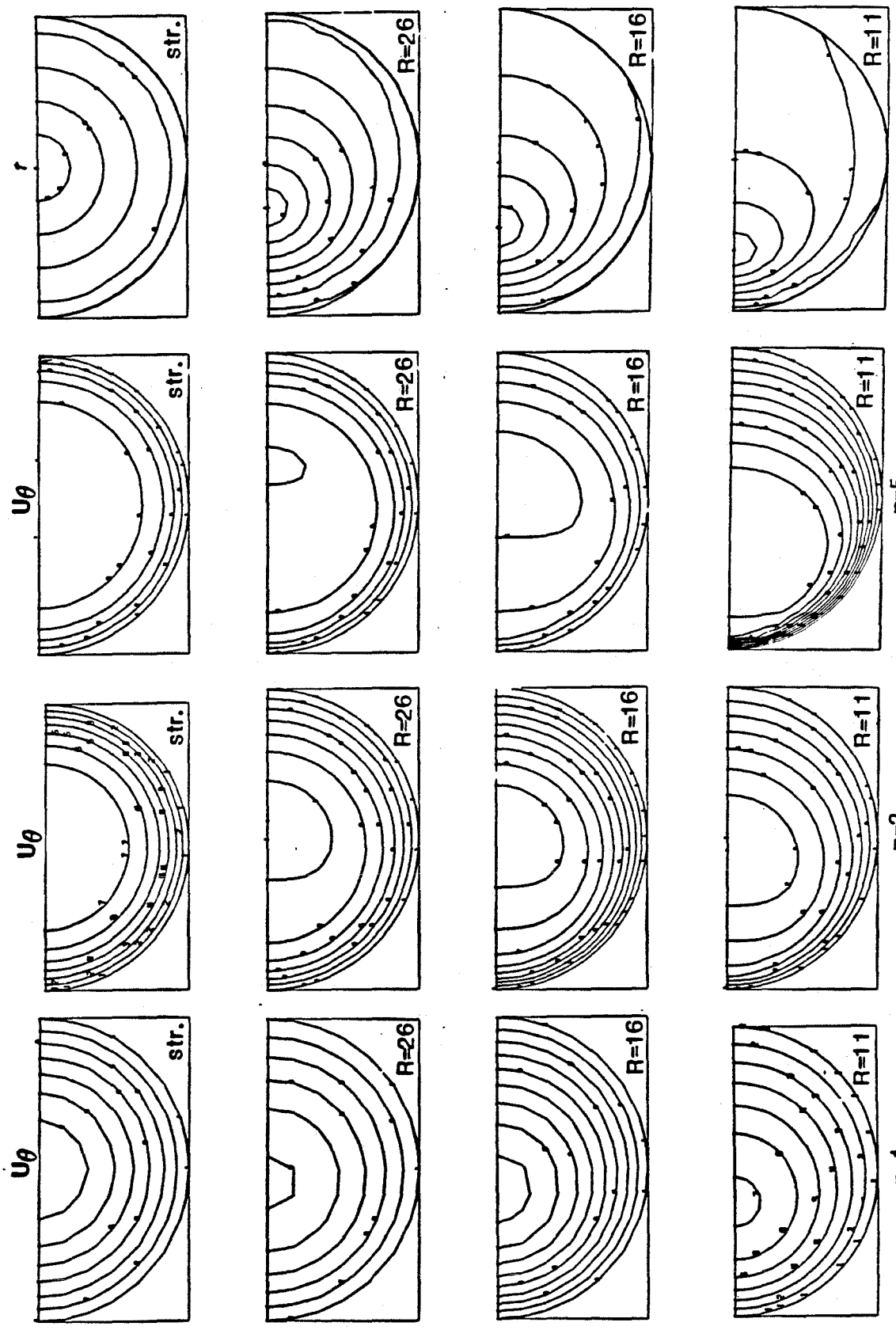

Figure 8.19 Contours of velocity u_θ and shear stress magnitude (τ) in semicircular channels of different curvatures.

inside of the bend accompanies a decrease in the radius of curvature. The highest shear occurs along the inside of the bend, as well as the sharpest gradients in τ. Down the geometrical centerline of the channel the transverse shear ($\tau_{r\theta}$) is no longer zero, and, in fact, it varies with depth. Hence τ varies nonlinearly with depth along the geometric centerline of the channel. (Figures 8.20c and 8.21d). The tighter the bend, the greater the increase in τ at the surface (due to $\tau_{r\theta} \neq 0$). The stress centerline along the surface ($\tau_{r\theta}=0$) is shifted toward the inside of the bend (Figures 8.20a,b and 8.21b), as was seen for the deep, vertically walled channel above. For a radius of curvature (as measured to the center of the channel) approximately equal to the diameter of the channel, the stress centerline is moved halfway toward the inner margin from the center.

Figure 8.20 shows the stress at depth beneath the geometric centerline and across the surface for a fixed R_c and n = 1,3 (n = 5 is very similar to n = 3). The variations with n are not large, but they are significant in that this is the first indication that shear stresses in a semicircular channel may be dependent upon the flow law parameters. (Remember that this was the case for straight parabolic conduits.) As in the very deep and rectangular channels, the higher the n, the closer R_τ is to the inside edge of the boundary.

The shear stress $\tau_{z\theta}$ is very nearly linear with depth, as in the straight semicircular channel, but it is dependent on the stress exponent n and the radius of curvature (Figure 8.22). The effective shape factor is therefore dependent on n and R_c, being somewhat different than the value of 1/2 for a straight channel. The curvature of a glacier channel may thus introduce important effects into the analysis of borehole deformation and flow of ice at depth.

The out-of-plane velocity for several different n and curvatures are shown in Figures 8.19. As with the stresses, the velocity field becomes increasingly asym-

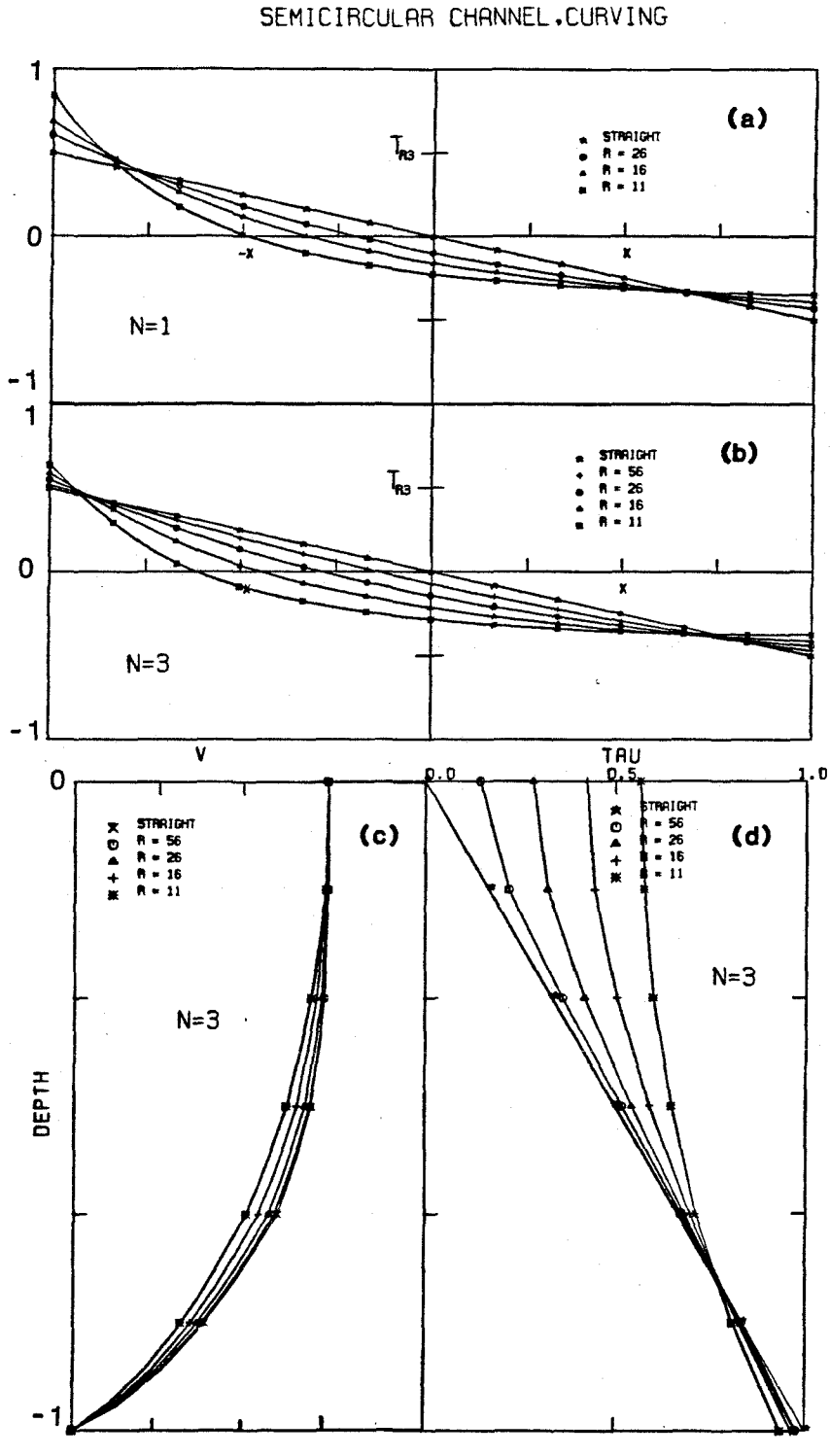

Figure 8.20 (a) Shear stressacross surface of curving semicircular channel for (a)n=1,(b)n=3 and and velocity (c) and τ (d) at depth

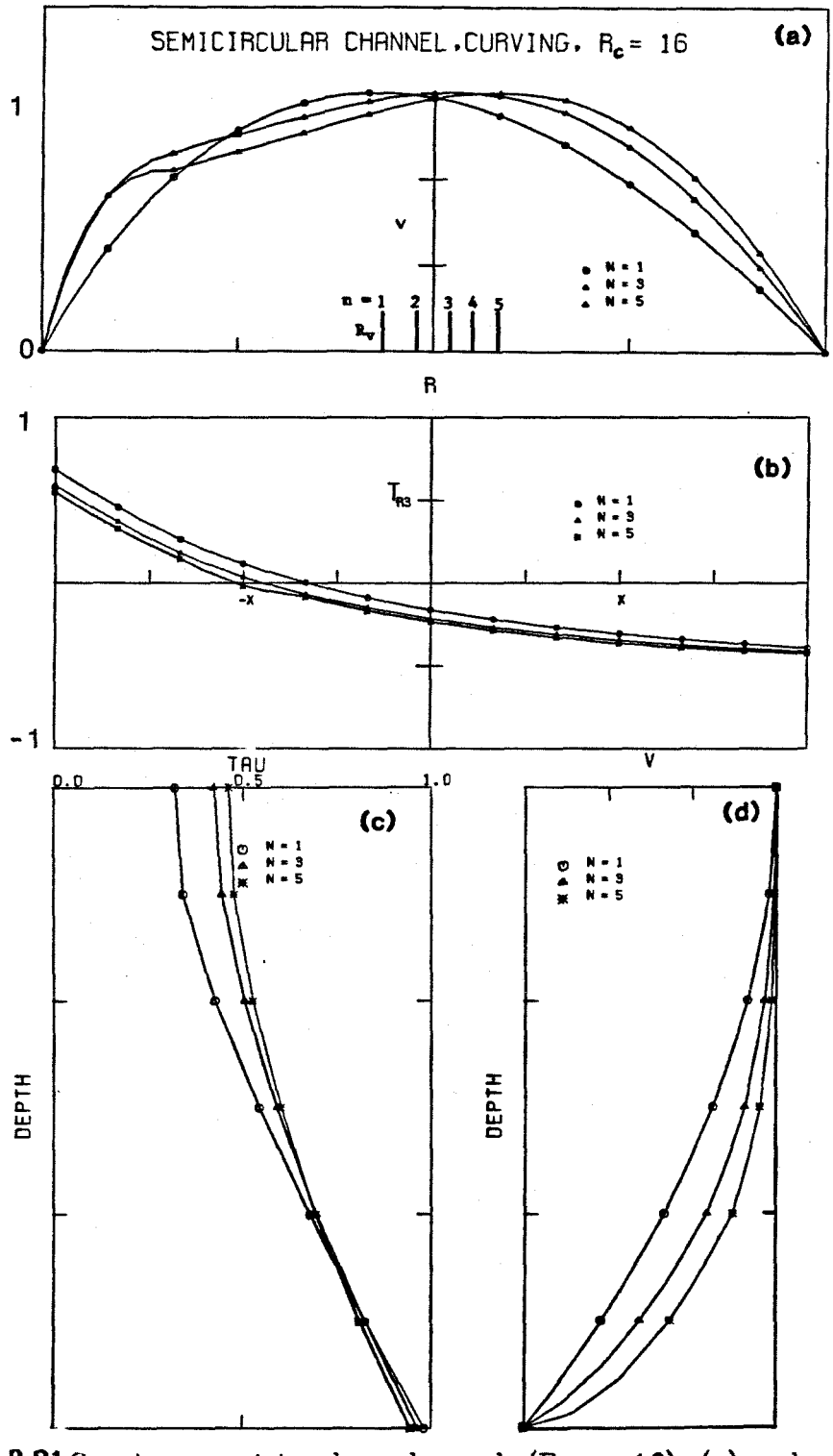

Figure 8.21 Curving semicircular channel (R_c = 16) (a) velocity profiles, different n, and position of max. velocity (R_v), (b) shear stress $\tau_{r\theta}$ across surface, (c) shear stress magnitude with depth, (d) velocity with depth.

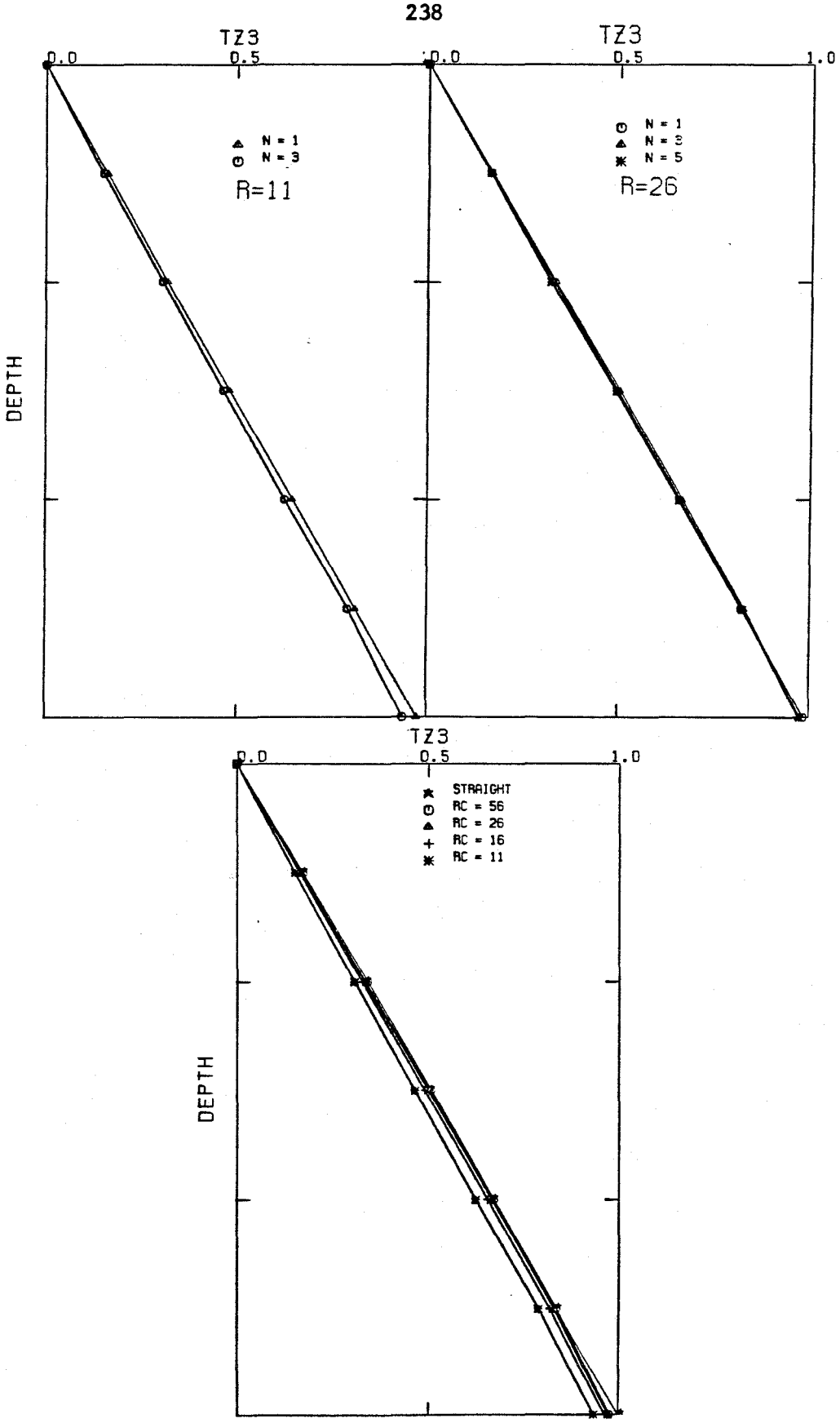

Figure 8.22 $T_{z\theta}$ at depth beneath centerline in curving semicircular channel.

metric with a decrease in R_c. (Note that in these figures the contour interval is not necessarily uniform from figure to figure.) The surface velocity profiles (Figures 8.21a and 8.23) for a given n show marked differences with a decrease in R_c. The profiles begin to develop some of the notable features of the observed velocity field on Blue Glacier, namely the displacement of u_{max} from the center of the channel and the large gradients near the inner margin (Fig. 4.2). The position of u_{max} (R_v) can lie inside or outside of the channel centerline depending on R_c and n (see inserts on Figures 8.21a and8.23). Thus, unless the effective radius of curvature for a channel is known, the stress exponent cannot be determined from a knowledge of R_v.

The magnitude of the maximum velocity in a curving semicircular channel is very nearly equal (within the error level of the FE models) to the straight channel velocity if the slope α in the straight channel is taken to be the mean slope across the curving channel $\bar{\alpha}$. ($\bar{\alpha} = \alpha_o \frac{R_-}{D} \log(\frac{R_+}{R_-})$, where D is the diameter of the channel.) For $n \lesssim 3$, this effective slope is approximately equal to the slope at the center of the channel. Thus, although the distribution of stress and velocity is changed by the introduction of curvature, the magnitude of the flow is not. This will hold for parabolic channels, as well (see next section).

The velocity profiles with depth along the centerline again show a departure from that obtained for a straight channel. These profiles display a more uniform strain-rate with depth, giving rise to a less plug-like flow pattern for a given n. However, the changes from the straight channel are less pronounced than those observed in the surface velocity profiles. This is probably due to the presence of the curvature term $-u_\theta/r$ in the definition of $\dot{\varepsilon}_{r\theta}$. Both u_θ and r vary across the surface, while only the velocity will vary along a line of fixed r, as in the depth profiles.

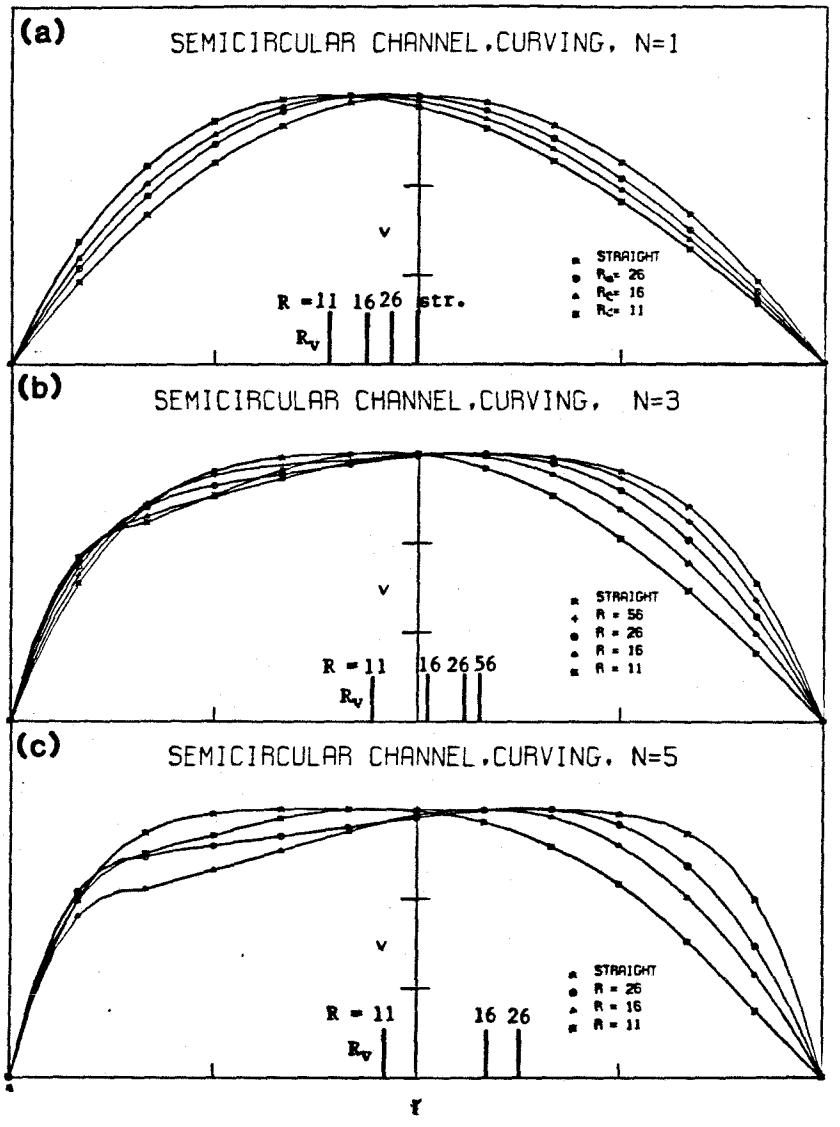

Figure 8.23 Flow out of curving semicircular channel, n = 1,3,5 for different R_c. Position of maximum velocity is shown (R_v).

For a given curvature, the surface and depth profiles of velocity show a dependence on n similar to that shown by the deep channel considered above. An example is given in Figure 8.21. . As n increases, the asymmetry of the surface profiles increases and R_v moves outward.

8.5.6 Parabolic Channels The flow of a non-Newtonian fluid, such as ice, in a straight parabolic channel has been seen to involve stresses which are non-linear in depth and in distance across the free surface. These stresses depend on the flow law parameters. Curvature should tend to introduce asymmetries into these stress patterns and therefore into the flow field. The interaction of these curvature effects with the already non-linear stresses gives another dimension to the complexity of channel flow which was not present in the parabolic channels discussed in section 8.2.

The contours of shear stress magnitude for a channel of half-width to depth ratio W = 4, shown in Figure 8.24 indicate a significant shift in the zones of high shear and of the stress centerline relative to straight channel flow. The maximum shear stress magnitude near the inside of the bend occurs at a location that moves closer to the inner margin as the bend gets sharper, while the maximum τ outboard of the centerline occurs at a point progressively further from the outer margin as R_c decreases. The maximum shear is thus displaced from the margin as in the straight parabolic channels, although by different amounts inside and outside the bend. This is further indicated in Figure 8.25b and showing the surface variation of $\tau_{r\theta}$.

The variation in the patterns of stress with R_c is similar for channels of various aspect ratio. Figure 8.26 shows τ and $\tau_{r\theta}$ for a channel of W = 1.6. The magnitude of $\tau_{r\theta}^{max}$ for different W at equal R_c follows similar trends as in its variation with W for straight channels, namely a decrease with decreasing W.

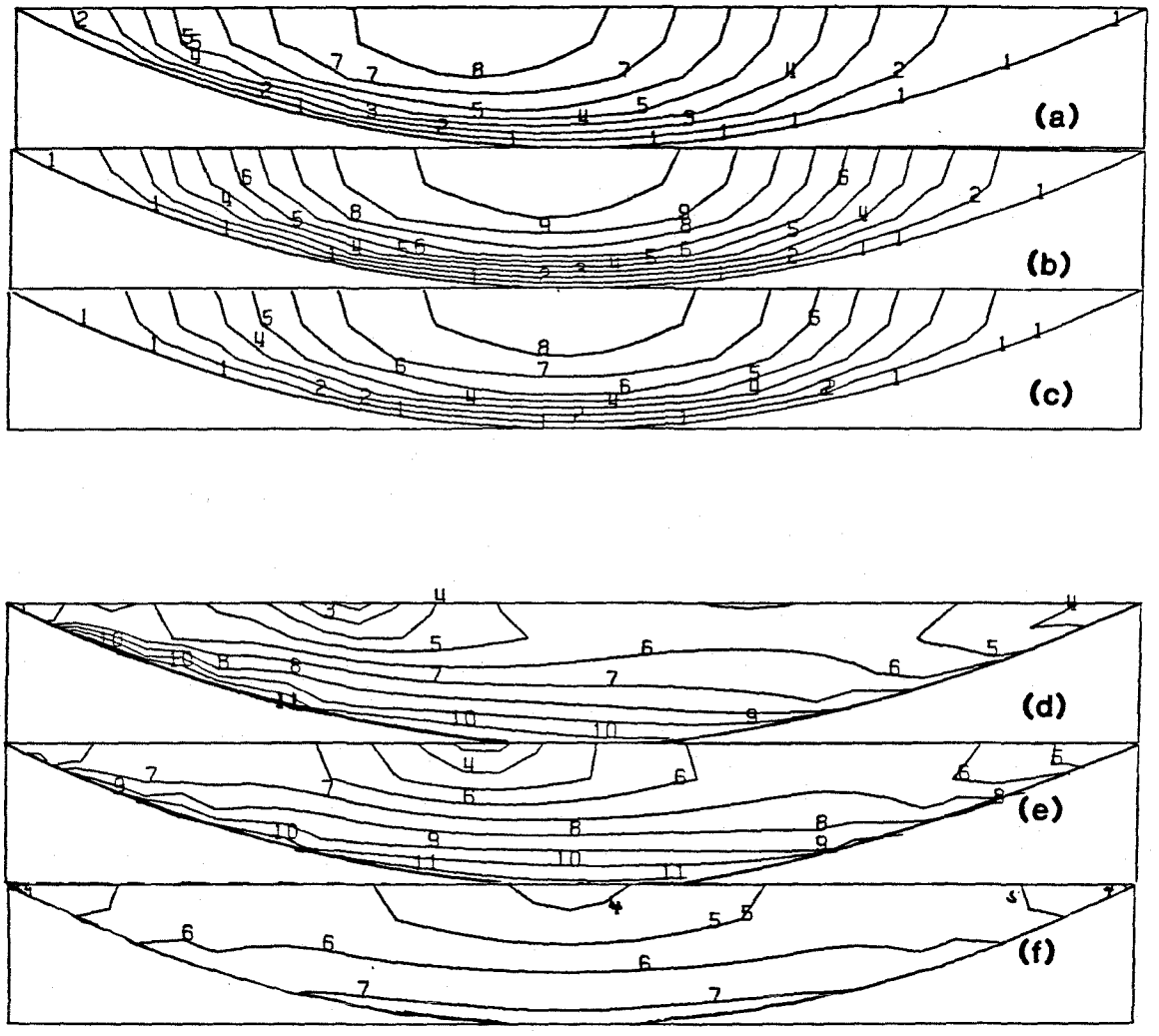

Figure 8.24 (a-c) Contours of flow in curving parabolic channels, W=4 (a) R_c = 26, (b) R_c = 64, (c) R_c = 128, (d-f) shear stress magnitude, (d) R_c = 26, (e) R_c = 64, (f)R_c=128.

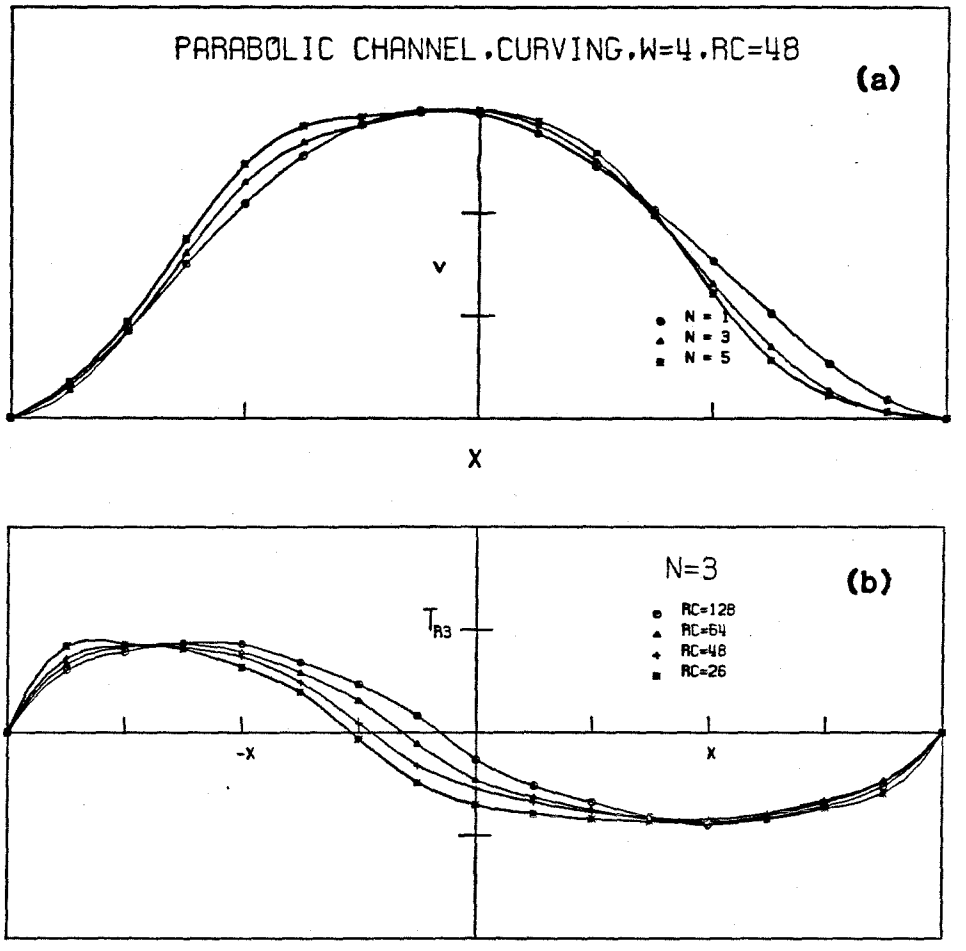

Figure 8.25 Flow (a) and surface shear stress (b) in curving parabolic (W = 4) channel. $T = T_{r\theta}$

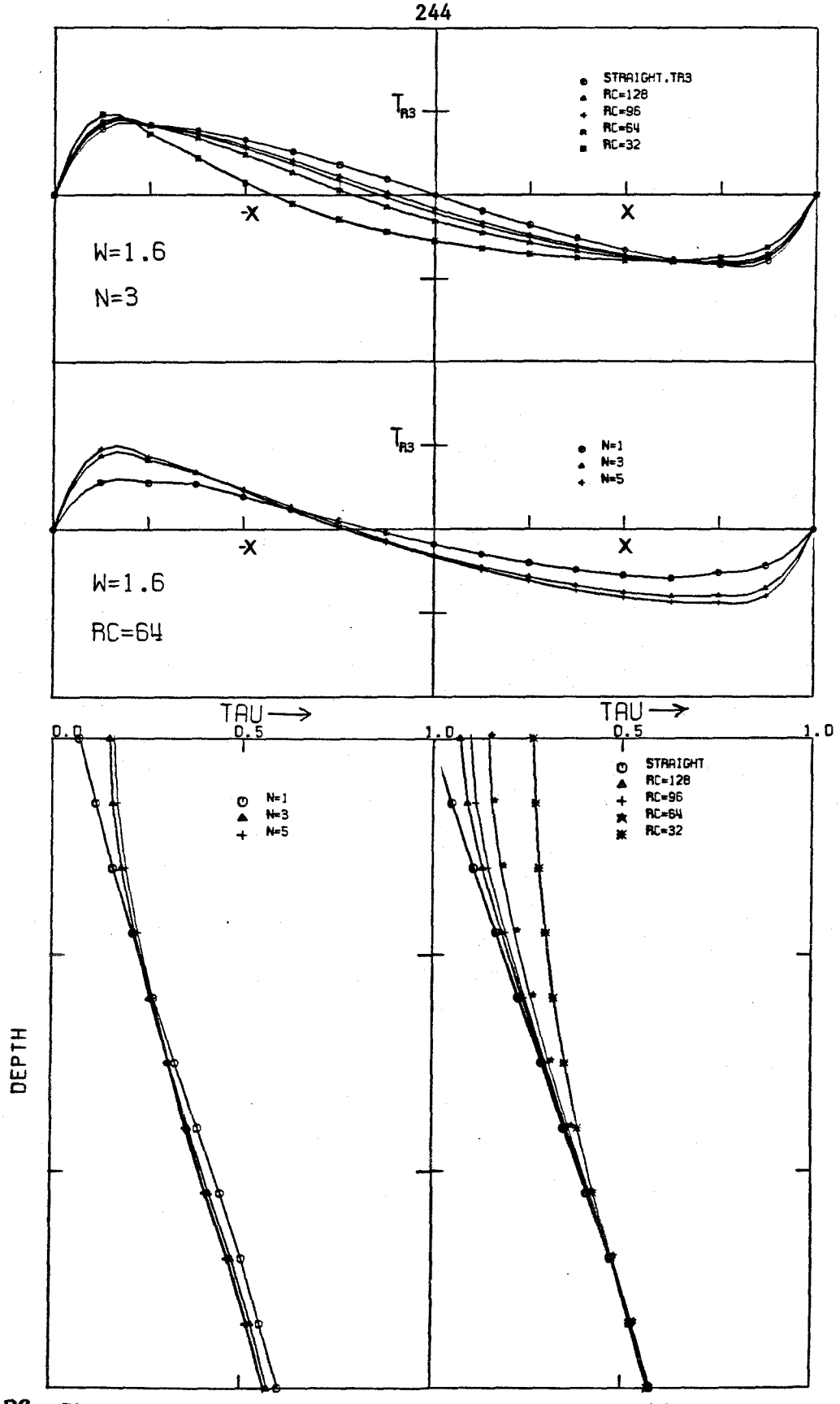

Figure 8.26 Shear stress $\tau_{r\theta}$ and shear stress magnitude (τ) curving parabolic channel, W = 1.6.

The nonlinearity of the shear stress magnitude (τ) with depth at the channel centerline is similar to that found in straight channels, being only slightly less linear with depth, as shown in Figures 8.26c,d. This depth variation is similar to that found in a curving semicircular channel. The stress component $\tau_{z\vartheta}$ is nearly linear with depth below the channel centerline for a wide range of curvatures in channels of aspect ratio greater than approximately 1.6 (Figure 8.27). The slope of this linear depth dependence (equal to the effective shape factor) is little changed from that found in a straight parabolic channel.

For a fixed radius of curvature and W there is a difference between the stress fields for different stress exponents, as is seen in Figures 8.26b,c and 8.27. The differences are greater between lower values of n than between higher values. This trend has been seen in earlier sections for both straight and curving conduits. For a realistic shape of W=1.6, this variation with n is about 5-10% from n=1 to 5.

The velocity fields corresponding to these stress fields are shown in Figures 8.25a and 8.28. The surface velocity profiles are again asymmetric with respect to the channel centerline, as was seen in the semicircular channel. The asymmetry increases with decreasing R_c, as expected. The variation with R_c is more pronounced for W = 4 than for W = 1.6, perhaps because of the enhanced effects of the shallower channel (the closer proximity of a surface element to the fixed boundary, as described in sec.8.5.3). The inflection points in the surface velocity move closer to the inner margin and further away from the outer wall as the curvature increases. Similarly, there exists a sharp gradient near the inside of the bend and a less abrupt gradient toward the outside. The variations with n (Figure 8.28a) are similar to those found for the semicircular channel, again showing a decrease in the changes between profiles with increasing n.

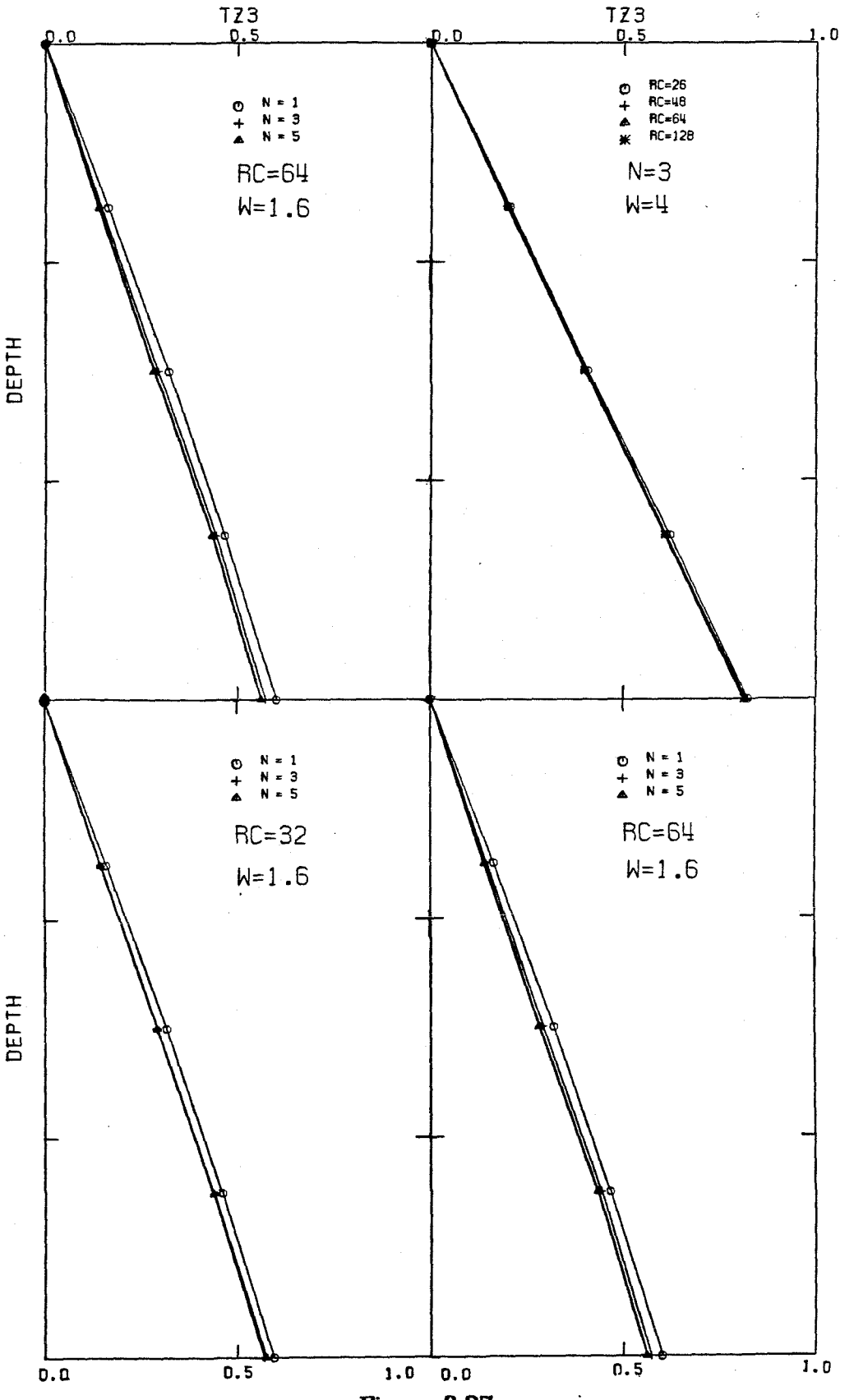

Figure 8.27

$T_{z\theta}$(=$\tau_{z\theta}$ normalized by depth and slope at center) in curving parabolic channels

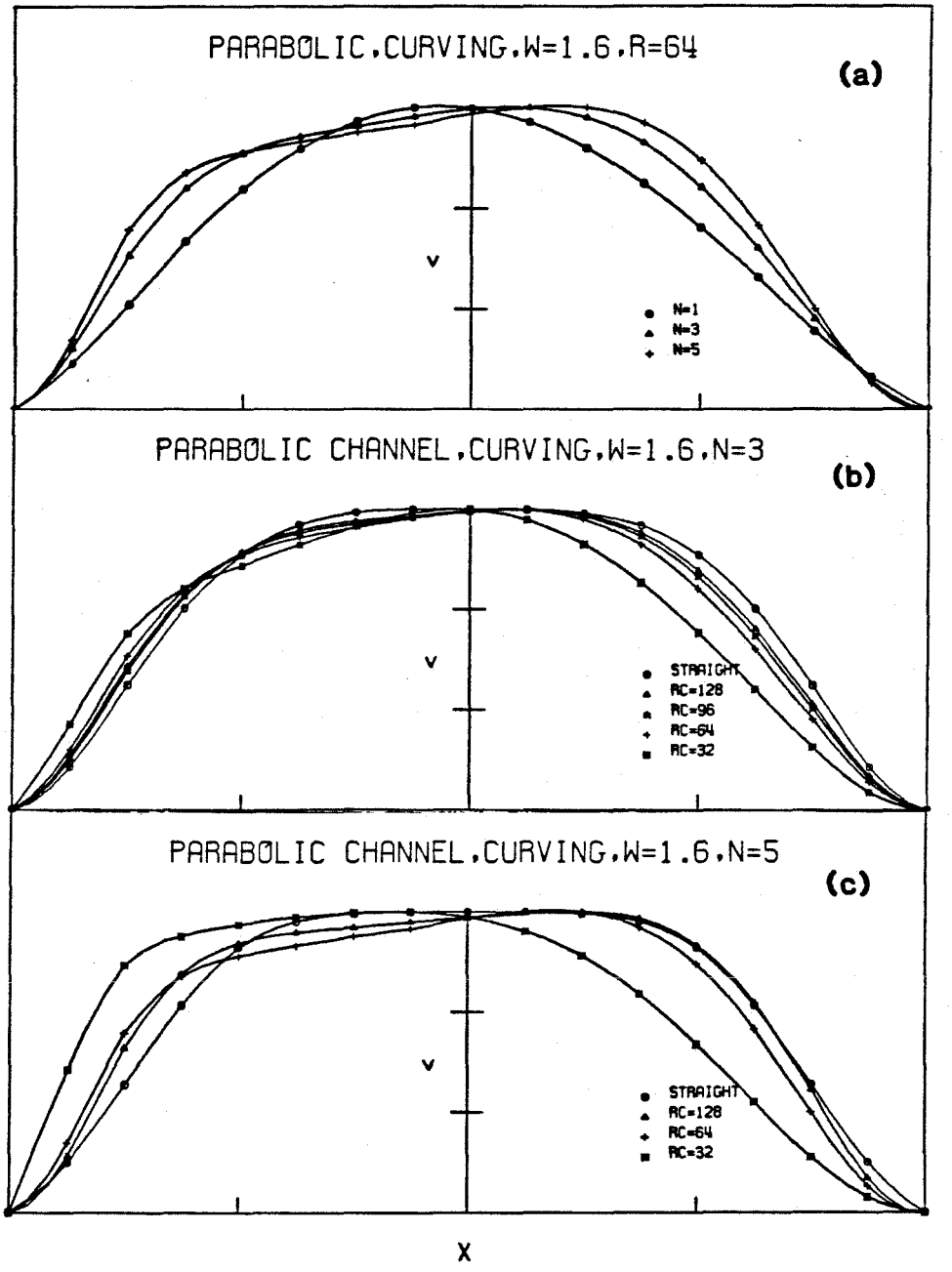

Figure 8.28 Surface velocity profiles for curving parabolic channel (W = 1.6) R_c the radius of curvature to the centerline of a channel whose width is 32 units.

The position of the stress centerline and maximum velocity along the surface are again dependent upon R_c and n (Figure 8.29). There is an additional dependence upon W, as is shown in Figures 8.29a and c. In these figures the radius of curvature and R_v,R_τ are taken relative to the channel width at the surface, D, as indicated. The stress centerline is shifted inward of the channel centerline in all cases, due to the $-u_\theta/r$ term in the definition of $\dot{\varepsilon}_{r\theta}$. For sharp bends ($R_c < D$) this shift is extremely large, being on the order of one half the distance to the inner margin from the center. The position of the maximum velocity, on the other hand, may be located either inside or outside of the centerline depending upon the exponent n and R_c. For n = 3 the larger values of W give less displacement of R_τ from the center than do the lower values for a given R_c. The location of maximum velocity is shifted toward the inside of the bend with increasing W, and, again, the results for a semicircular conduit are similar to those found for a parabolic channel of W = 1 (which is, of course, the closest a parabolic curve can approximate a semicircle). For channels approximating realistic glacier cross sections (W ~ 1-3), only for bends with R_c / D ≤ 1 is the velocity maximum shifted inward of the channel centerline for n = 3 -5, while it is always displaced toward the inside margin for n = 1.

8.6 Summary of Results

Finite element analysis was used to extend the numerical results of Nye (1965) to values of the stress exponent different from n=3 in straight channels. In all but the simplest cases (e.g. a straight semicircular conduit), the magnitude of the shear stresses were found to be dependent upon the flow law exponent n. In addition, there is a non-linear variation of the stresses with depth or distance from the walls. The maximum shear stress at the surface is located at a point in from the sloping margins, giving rise to a (possibly) crevasse-free region along the margins, as found by Nye (1965). The assumption

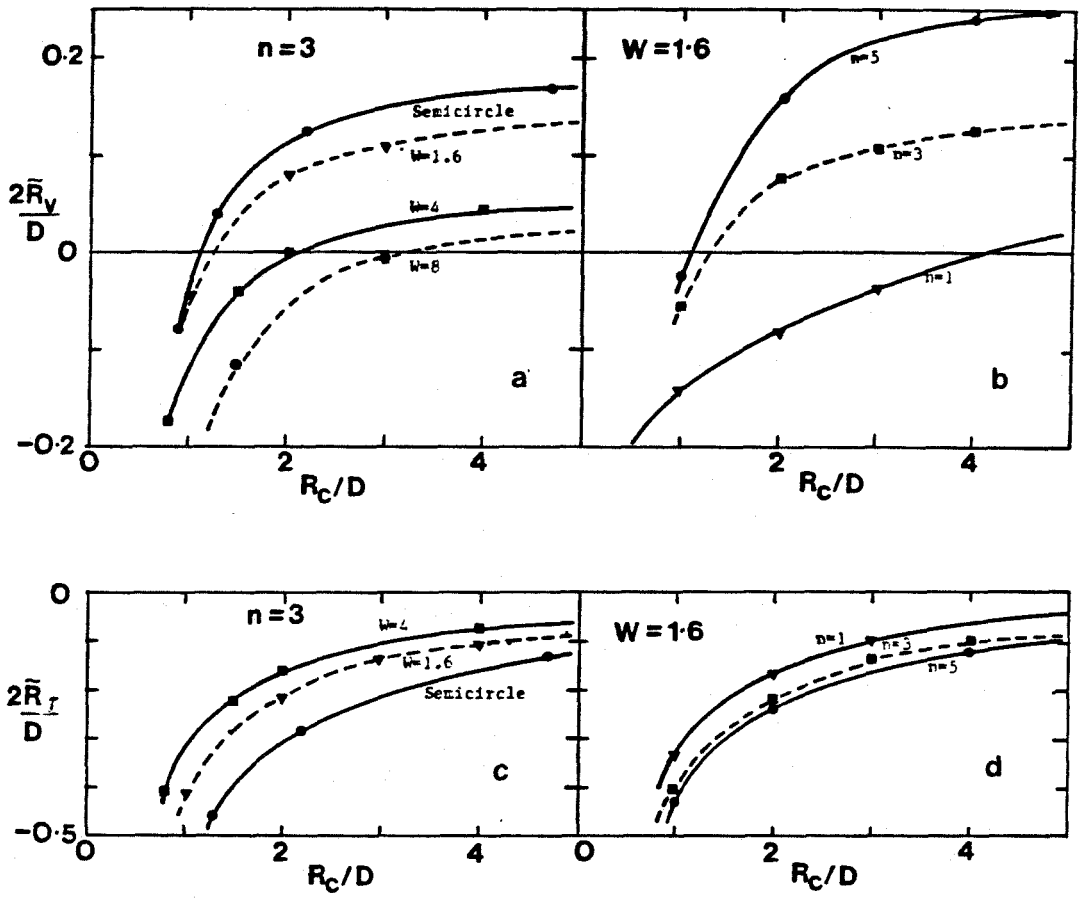

Figure 8.29 a. Position of maximum velocity $\tilde{R}_v(=R_v - R_c)$ as a function of curvature R_c for different channel types (parabolic and semicircular), D = channel width at surface (= 32 for all parabolic channels).

b. Variation of $\tilde{R}_v$ with n and R_c in parabolic channel, W = 1.6 .

c. Position of stress centerline $\tilde{R}_\tau(=R_\tau - R_c)$ in different channels and for different R_c.

d. Variation in $\tilde{R}_\tau$ with n and R_c.

of a linear depth-dependence of the shear stresses may give rise to an overestimation of the stresses at depth, thus making ice within glaciers appear stronger than it really is (a possibility discussed by Hooke,1981). However, significant nonlinearity in the dependence of the vertical shear stress (τ_{yz}) with depth was found only for deep, narrow channels ($W \sim 1$).

The possibility of a decrease in the viscosity factor η_f with depth, as suggested by Hooke (1981), was seen to mimic a larger value of the stress exponent. This may perhaps lead to some of the discrepancies between values of n found from laboratory and field data (although it appears from the results of the next chapter that this is not the case).

The capability of including in-plane flow driven by a convex (or concave) cross-sectional ice surface in the numerical models has been seen to account, in part, for the flow vector divergence (or convergence) seen in the ablation (accumulation) areas of many glaciers. In addition, the in-plane stress components contribute to the effective shear stress, causing a slight decrease in the effective viscosity, and leading to slightly higher flow rates.

Analytical and numerical models of the flow of ice around a bend show that channel curvature can introduce major complexities in the flow and stress fields present in glaciers. The surface slope is generally greater near the inside of the bend than the outside, giving a radially dependent effective body force. This increased surface slope near the inside of the bend is observed on Blue Glacier. Combined with the effects of curvature on the equilibrium distribution of stress and the rate-of-deformation tensor, this radially-dependent effective body force produces an asymmetric velocity profile and a shift in the position of maximum velocity from the channel centerline, either inward or outward depending upon the radius of curvature, stress exponent, and channel shape. The term

$-u_\theta/r$ in the definition of the transverse strain-rate $\dot{\varepsilon}_{r\theta}$ causes significant shifting of the stress centerline from the straight channel position (which is the geometric centerline), moving R_τ toward the inside margin. This introduces a nonlinearity and asymmetry into the distribution of stress across the surface. In addition, there are nonlinearities introduced into the distribution of τ with depth beneath the center of the channel by curvature (because the stress centerline does not coincide with the geometric centerline). On the other hand, the vertical component of shear stress ($\tau_{z\theta}$) remains nearly linear with depth for most reasonable channel shapes. The magnitude of the stresses are dependent upon the flow law exponent in straight parabolic channels and all curving channels.

As discussed by Meier et al. (1974), the shift in the stress centerline in a glacier flowing around a bend gives rise to a unique crevasse pattern. The strike of the crevasses is normal to the direction of the maximum principle extension. When this direction is aligned with the flow streamlines the shear stress components vanish and thus any crevasses would be purely transverse in orientation. This is the case at the stress centerline. Normally, in a glacier flowing down a straight, uniform channel, the position of the stress centerline is along the geometrical center of the channel. In a straight channel where longitudinal extension occurs as well as marginal shear, the crevasses will form transverse curves, symmetric about the channel centerline (Figure 8. 30a) as described by Nye (1952). However, if the channel is curving, the shift in the stress centerline will cause an asymmetry in the crevasse field, being much wider on the outside of the bend than on the inside (Figure 8.30b). This striking pattern is seen on the Blue Glacier (see Allen et al.,1960) and on other valley glaciers, directly manifesting the effects of channel curvature on the stress distribution.

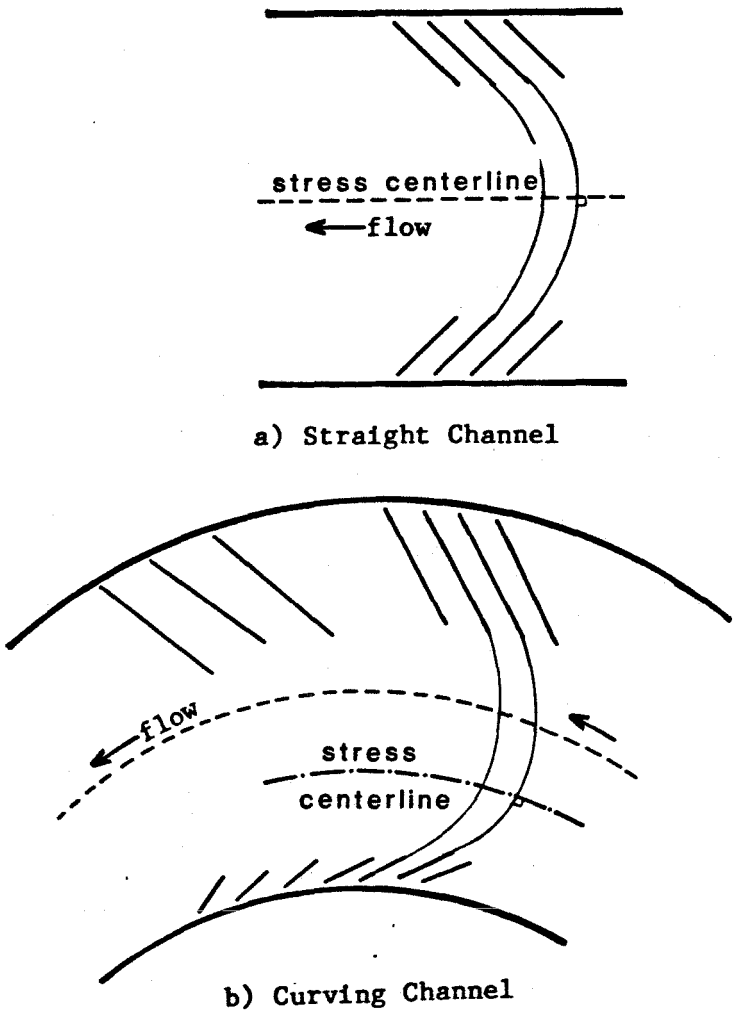

Figure 8.30 Crevasse patterns in (a) straight channel and (b) curving channel. Crevasses are perpendicular to stress centerline.

As an example of the curvature-derived features, take the cross-sectional shape of Blue Glacier to be approximated by a parabola of W = 1.6, with a mean centerline depth of 250 m and channel width of 800 m. Let the radius of curvature be 1000 m (as measured from a plan-view map at profile F). Then R_c/D = 1.25. If we take n = 4, then the stress centerline would be located 140 m inward of the channel centerline, while the velocity maximum would be located toward the outside of the bend 20 m from the centerline. This agrees remarkably well with the observations at profiles E-G (see Chapter IV and Meier et al., 1974). The velocity profiles of Chapter IV show this expected asymmetry about the centerline, although the actual cross-sectional geometry must be taken into account in order to obtain better agreement between the models and the observed flow patterns.

The effects of curvature and sloping valley walls in the nearly parabolic cross-sections of Blue Glacier determine the routes which climbers must take when traveling up the glacier. The presence of a marginal zone of low shear stress (Figures 8.2 and 8.3) makes a route up the margins of the glacier often feasible. However, the increased surface slope at the inside of the bend can cause problems, so the preferred route would be the outer (eastern) margin. In other circumstances, a climber may wish to avoid the avalanche- and rockfall-prone margins. Then, especially in zones of low longitudinal extension, the best route often lies not along the geometric centerline of the glacier, but rather along the shifted stress centerline, some 100-200 m in toward the inside of the bend from the center. These predicted routes correspond to those used by experienced climbers and mountain goats.

CHAPTER IX

RESPONSE OF A GLACIER FLOWING IN A SIMPLE CHANNEL TO CHANGES IN THICKNESS AND SLOPE

Given the variability in channel geometry along the Blue Glacier, the observational results of Chapter V show a remarkably good fit to a linear model for the response of a wide ice slab to a change in thickness and surface slope (equation (9.1),below). But how do the effects of channel geometry enter into this response and how do they alter the information obtained about the flow law of the ice from this natural experiment? As a first approximation to the answers to these questions, this chapter treats the change in the velocity field of an ice mass flowing in a simple channel (as described in the previous chapter) which has undergone a non-infinitesimal change in ice thickness and surface slope. Analytical models are developed as fully as possible and are then followed by numerical experiments to extend the results to more realistic situations. These results indicate that the simple model (9.1) requires some modification, but that the linearity of the response remains an important feature.

Only the steady-state response will be treated here, we neglect the transient features, such as those governed by the kinematic wave equation (Lighthill and Whitham, 1955, and Nye 1960, 1963a, 1963b) or those discussed by Hutter (1981) involving Burger's equation and a modified kinematic wave equation. Comparison of the observed response of Blue Glacier with the results described in this chapter and those of Chapter X suggest *a posteriori* that this assumption is well founded for the case in study.

It was shown in Chapter V, eqn.(5.7) that a finite perturbation in the appropriately averaged surface slope ($<\alpha>_l$, denoted α throughout this chapter) and ice thickness ($<H>_l$, denoted H) will cause the surface velocity, u,

of a long, wide, inclined slab of thickness H to change in the manner given by

$$\log \frac{u_1}{u_o} = (n + 1) \log \frac{H_1}{H_o} + n \log \frac{\sin\alpha_1}{\sin\alpha_o}, \qquad (9.1)$$

where, as usual, the subscripts o and 1 refer to the initial (t_o) and final (t_1) values of the various quantities. It will be shown below that the change in the longitudinal surface slope enters into the velocity change in the same manner as in this simple model for all channel shapes, while the thickness term is channel-dependent and requires modification.

9.1 Variation in Longitudinal Surface Slope

In those models which are amenable to analytic solution, the shear stress is found to vary linearly with the surface slope. Numerical results indicate that this same linear dependence holds for all channel shapes. From the nature of the flow law of ice, the n-th power of the surface slope enters into expressions for the velocity. A change in slope should therefore determine the relative change in velocity in a manner determined by the righthand term in (9.1).

As a simple example, consider the flow within an inclined semicircular channel of radius R and inclination α. The shear stress is given by $\tau_{rz} = \frac{1}{2}\rho g r \sin\alpha$, and the velocity is given by $u(r) = (\frac{1}{2}\rho g \sin\alpha)^n R^{n+1} [\,1 - (r/R)^{n+1}\,] / [(n+1)\eta_f]$. If there is a finite change in α, then the velocity change $\log(u_1/u_o)$ is given by $n \log(\sin\alpha_1 / \sin\alpha_o)$ at all radii.

The stress components cannot be given in closed form for motion in a parabolic channel. However, numerical results for parabolic channels indicate that the stresses throughout the channel depend linearly on slope, as expected. Table 9.1 shows centerline velocity changes resulting from various slope changes in different parabolic conduits. This table shows that the effect of changing the

Table 9.1
Change in Centerline Velocity with Slope Change

W	n	$\log\frac{\sin\alpha_1}{\sin\alpha_o}\times 100$	$\Delta H / H$	$\log(u_1/u_o)\times 100$	$\log(u_1/u'_o)$
1.6	1	5.0	--	5.00	--
		10.0	--	10.00	--
	3	5.0	--	14.99	--
		10.0	--	30.03	--
		5.0	-5%	31.60	14.90
	5	5.0	--	24.95	--
4	3	10.0	--	29.96	--
		5.0	-5%	33.8	14.91
	5	5.0	--	24.98	--

u'_o = velocity with $\Delta\alpha=0$ but $\Delta H \neq 0$

slope enters in as determined by (9.1), as claimed. Entirely analogous results hold at all points across the surface of a parabolic channel. Thus, the change in velocity accompanying a perturbation in slope is given by n $\log(\sin\alpha_1/\sin\alpha_o)$ at all points within the channel.

The two additional cases listed in Table 9.1 are ones for which there is a simultaneous thickness change. These results show that the two effects -- the slope change and the thickness change -- can be entirely decoupled, as predicted in (9.1). The remainder of this chapter will discuss the effects of a thickness change.

9.2 Thickness Change in a Semicircular Channel

As a first example of the response of the velocity field to a change in thickness in a simple channel, consider a straight semicircular channel. An analytical approximation to a change in thickness is obtained as follows. Take initially a semicircular channel of radius R (1 + ε), $\varepsilon << 1$. In this channel,thin the ice to a centerline depth of R. Then approximate the thinned geometry by a slightly elliptical channel, in place of the partially filled semicircular channel that it actually is. By making a perturbation analysis on the semicircle, Chester (see Nye, 1965) has obtained the velocity distribution u[r,ϑ;a,b] for flow of a non-

Newtonian fluid obeying a power-law type constitutive relation in a slightly elliptical channel of semi-major axis a = R(1+ε) and semi-minor axis b=R. (He assumes no slip on the channel). His (approximate) result, in polar coordinates r,ϑ with ϑ measured from the minor axis, is:

$$u_e[r,\vartheta,(1+\varepsilon)R,R] \approx B\{1 - X^{n+1} + \frac{1}{2}\varepsilon(n+1)[1 - X^{\gamma}\cos 2\vartheta]\}, \qquad (9.2)$$

where $X = r/R$, $B = (\frac{1}{2}k)^n R/[(n+1)\eta_f]$, $k=\rho g R \sin\alpha$, and

$$\gamma = \frac{1}{2}(n-1) + \frac{1}{2}(n^2 + 14n + 1)^{\frac{1}{2}}. \qquad (9.3)$$

The velocity u_o in a semicircular channel of radius $R(1+\varepsilon)$ is

$$u_o(X) = B(1+\varepsilon)^{n+1}[1 - X^{n+1}(1+\varepsilon)^{-(n+1)}],$$

which, to first order in ε, can be written

$$u_o(X) \approx B[1 + (n+1)\varepsilon - X^{n+1}], \quad \varepsilon << 1. \qquad (9.4)$$

Evaluating (9.2) at the ice surface ($\vartheta=\pi/2$) and taking the difference between (9.2) and (9.4) we obtain

$$\frac{\Delta u}{u_o} = \frac{u_o - u_e}{u_o} = \frac{1}{2}(n+1)\frac{(1 - X^{\gamma})}{(1 - X^{n+1} + (n+1)\varepsilon)}\frac{\Delta R}{R},$$

where $\varepsilon = \Delta R/R$. In the limit,

$$\frac{R}{u}\frac{du}{dR} = \lim_{\Delta R \to 0}\frac{R}{u_o}\frac{\Delta u}{\Delta R} = \frac{1}{2}(n+1)\left[\frac{1 - X^{\gamma}}{1 - X^{n+1}}\right]. \qquad (9.5)$$

This relation shows that the logarithmic change in surface velocity at the centerline (X=0) of a semicircular channel due to a small perturbation in the depth is one half that expected on the basis of the simple slab model (9.1). This implies that, if the channel of Blue Glacier is taken to be a semicircle, then the slope of the response curves given in Chapter V are not equal to (n+1), but rather equal $\frac{1}{2}(n+1)$ (i.e. if the slope of the Δu vs. ΔH curve is observed to be 3,

then n = 5, not 2). The factor of 1/2 is, of course, only approximate, because (9.2) is only an approximation, and because the result of thinning a semicircle is not strictly a semi-ellipse.

The reasoning that leads to (9.5) also leads to the expectation that, in general, the velocity response can be related to the thickness perturbation via a modification of (9.1) in which a *response factor* Ψ is introduced:

$$\log \frac{u_1}{u_o} = \Psi(n+1) \log(\frac{H_1}{H_o}) + n \log(\frac{\sin\alpha_1}{\sin\alpha_o}) . \qquad (9.6)$$

From (9.5)one expects that Ψ will be less than 1, and perhaps near 1/2. Evaluation of Ψ for various channel geometries is carried out in this chapter.

The reason for the reduction by the factor $\Psi < 1$ in the magnitude of the response from that expected for the simple slab is that when a semicircular channel is thinned a small amount, the transverse width decreases only slightly. While the smaller ice depth causes reduced shear stress across planes parallel to the surface (τ_{zy}), the shear stress across vertical planes (τ_{zx}) is essentially unchanged. The flow rate is thus reduced by only a partial change in the total shear stress ($\tau = \tau_{rz} = (\tau_{zx}^2 + \tau_{zy}^2)^{1/2}$) and not by a change in the total driving stress, as was the case in the slab model (for which $\tau = \tau_{xz}$).

With γ given as in (9.3), the transverse variation in the velocity change (9.5) to a change depth (which is denoted ΔH at the centerline) is as shown in Figure 9.1. If the centerline depth change is used in (9.6), then this transverse variation in Δu will introduce a variation in an effective Ψ across the channel surface.

The actual geometrical change in the initially semicircular cross-section may be accurately accommodated by using finite element (FE) models. To calculate a response factor for a given channel, the FE flow calculation is done first for the channel as given, and then, independently, for the same channel but with the ice

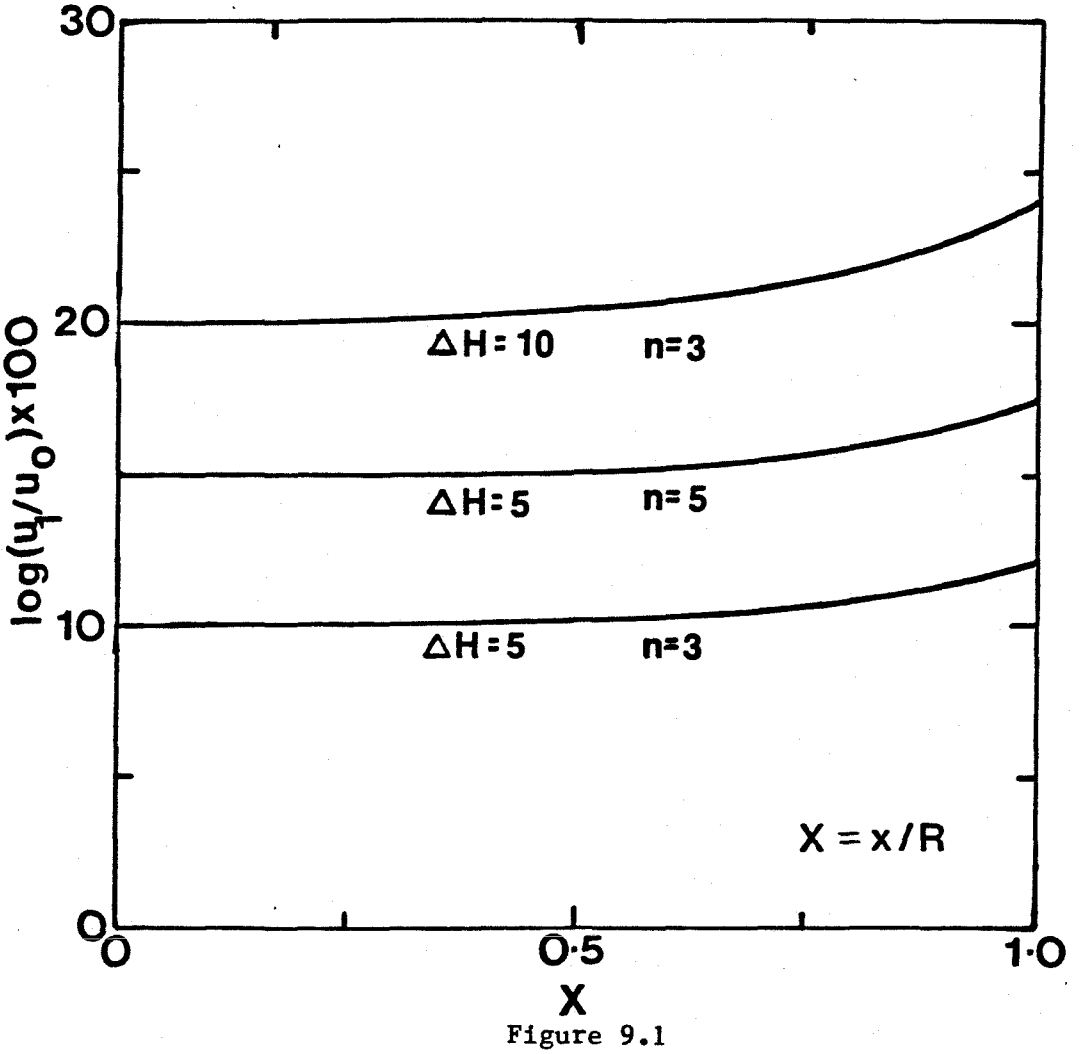

Figure 9.1

Transverse variation of velocity change in semicircular channel, for different thickness changes ΔH and exponents n: Analytical Results {$\Delta H = \log(H_1/H_0) \times 100$ = centerline depth change, R=radius, x=distance across surface of channel from center}.

thickness reduced by a prescribed amount. From the two models, logarithmic ratios of perturbed and unperturbed thickness and velocity are formed to obtain Ψ.

The change in centerline velocity of a semicircular channel for different values of the stress exponent and ΔH is shown in Figure 9.2a. There is a well-defined linear relation between the centerline thickness and velocity changes, even for large (10% or more) depth variations. Figure 9.2b shows the slopes of these response curves as a function of n. Again, there is a well-defined linearity in these results. These two figures (9.2 a,b) show that, for a semicircular conduit, linear response model of the form (9.6) applies along the centerline.

The response factor for a semicircular channel, as determined from the FE results, may be obtained from the slope of the curve in Figure 9.2b. This value is $\Psi = 0.67$, which is decidedly larger than the approximate analytical result. Hence, if the slope of the observed response curve were 3, the implied exponent would be n = 3.5, as opposed to 5 for the less accurate analytical model. It may be shown (Kamb, pers. comm.) that, if the difference in shape between the thinned semicircular channel and its approximation as a semi-ellipse is correctly accounted for, then the analytical value of Ψ is very close to the FE result. It is interesting that such an apparently small difference between the thinned semicircular channel and a semi-ellipse can cause such a large difference in Ψ.

The lateral variation in the velocity change is shown in Figures 9.3a,b. This change relative to the centerline depth change,ΔH (Figure 9.3a) is similar in form but larger in magnitude than that predicted by the analytical model (Figure 9.1). There is a distinct departure from linearity and a reduced best-fit slope when the local thickness change (the change in depth directly beneath the point

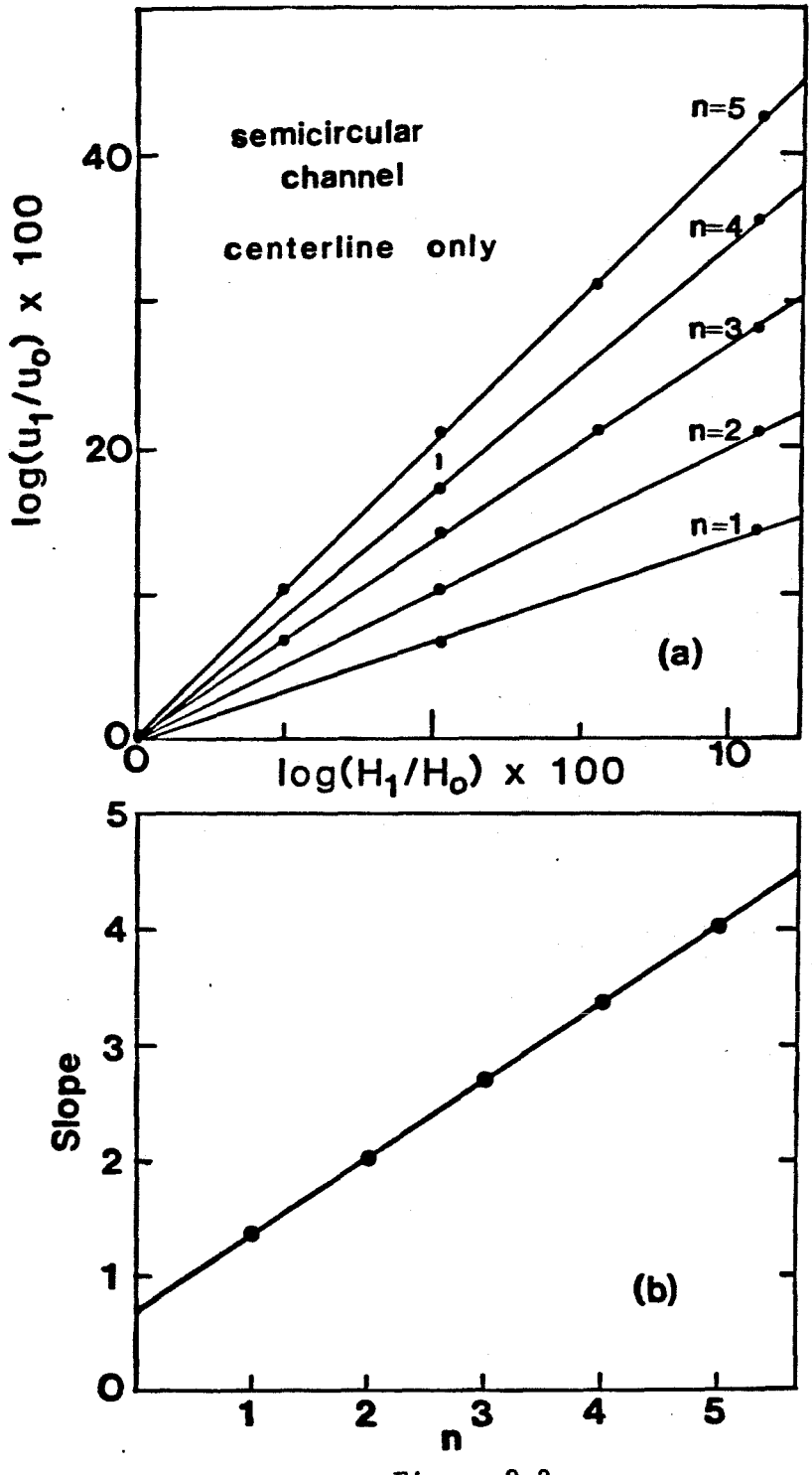

Figure 9.2

a) Velocity change in semicircular channel as a function of thickness change for different n at channel centerline. Circular dots are finite element (FE) results.

b) Slope of response curves in Figure 9.2a as a function of n.

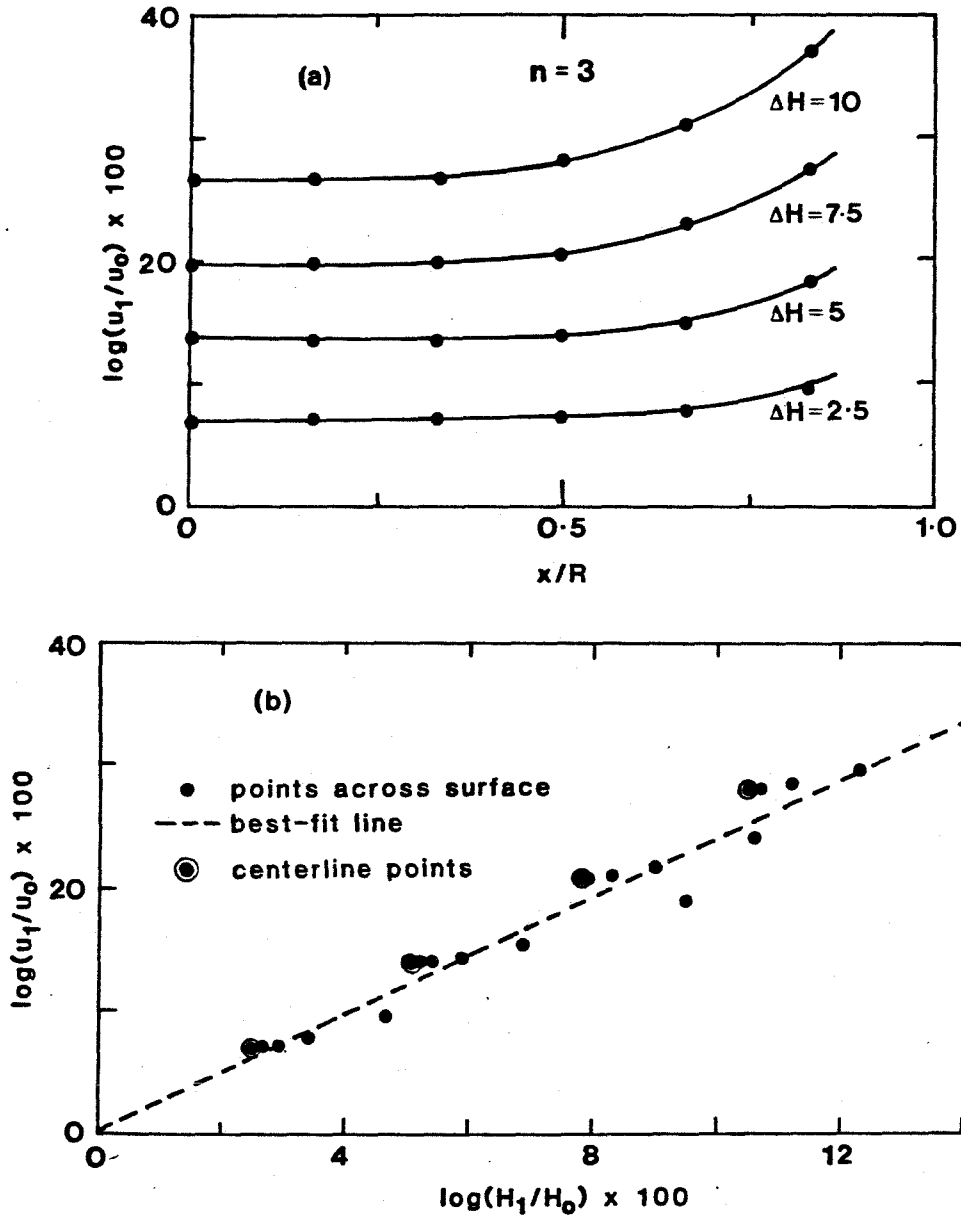

Figure 9.3 a) Transverse variation in velocity change in semicircular channel for different centerline thickness changes $\{\Delta H = \log(H_1/H_0) \times 100$ at centerline$\}$, n=3. Finite element results (compare with Figure 9.1).
b) Δu versus local ΔH at points across surface of semi-circular channel (n=3).

at which the velocity change is measured) is taken into account, as shown in Fig. 9.3b.

9.3 Calculation of Response Factor from Hydraulic Shape Factor

In order to obtain an approximate analytical representation for Δu in a parabolic channel of half-width-to-depth ratio W under a given thickness change, we require the concept of a shape factor. As described in Chapter VIII, the shape factor f is a scaling parameter introduced into an approximate relation for the average shear stress at depth beneath the centerline,

$$\tau_{yz} \approx f \rho g y \sin\alpha , \tag{9.7}$$

where y is taken directed downward from the surface along the centerline. The shape factor f represents the averaging effect of the channel cross-section in supporting the mass of the glacier. From simple static equilibrium considerations,

$$f \equiv A / PH , \tag{9.8}$$

where A is the cross sectional area, P the wetted perimeter, and H the centerline depth of the channel. The definition (9.8) is that of the hydraulic shape factor, and it may be calculated *a priori* for a given cross section. Another, more accurate though less intuitive shape factor, f, is that obtained by equating the observed or modeled centerline surface velocity with the flow rate as derived from the power-law creep relation,

$$u = f^n (\rho g \sin\alpha)^n H^{n+1} / [(n+1)\eta_f] \tag{9.9}$$

In this sense, f is taken to be the slope of the assumed linear dependence of τ_{yz} on depth y beneath the centerline. Values of f from (9.9) are given by Nye (1965) for n = 3, as previously discussed.

The two shape factors that appear in (9.8) and (9.9) are the same for a semi-circular channel (f = 1/2), but differ for parabolic channels. Although in principle we want to use (9.9) (or whatever replaces it if τ_{yz} is not linear with y) in calculating the response factor, in practice this is rarely feasible because the analytical determination of f in (9.9) represents in effect a complete solution of the non-linear flow problem. As an approximate alternative we will therefore take f from (9.8) in calculating analytically the response from (9.9).

From (9.9) we may write the derivative of u with respect to the thickness H as

$$\frac{du}{dH} = (n+1)\frac{H^{n+1}}{H}\frac{f^n(\rho g \sin\alpha)^n}{(n+1)\eta_t} + n\frac{f^n}{f}\frac{(\rho g \sin\alpha)^n}{(n+1)\eta_t}H^{n+1}\frac{\partial f}{\partial H}.$$

Thus

$$\frac{dlogu}{dlogH} = n + 1 + n\frac{dlogf}{dlogH} \qquad (9.10)$$

Relation (9.10) states that the change in velocity is directly related to the thickness change *and* to the change in the channel shape accompanying the change in thickness.

9.4 Response in Parabolic Channels

Let W be the aspect ratio of the parabolic channel (half-width to depth). If we take f = f(W) and W = W(H), (9.10) can be rewritten as

$$\frac{dlogu}{dlogH} = (n+1) + n\frac{dlogf}{dlogW}\frac{dlogW}{dlogH}$$

For a parabolic channel ($y = x^2 / b$)

$$\frac{dW}{dH} = -\frac{1}{2}\frac{W}{H},$$

and hence

$$\frac{du}{u} = \left[(n+1) - \frac{1}{2} n \frac{W}{f} \frac{df}{dW} \right] \frac{dH}{H} . \tag{9.11}$$

For finite change in centerline depth, we integrate (9.11) to give

$$\log \frac{u_1}{u_o} = (n+1) \log \frac{H_1}{H_o} - \frac{1}{2} n \int_{H(t_o)}^{H(t_1)} \frac{W}{f} \frac{df}{dW} \frac{dH}{H} , \tag{9.12}$$

or

$$\log(u_1/u_o) = \Psi \, (n+1) \log(\frac{H_1}{H_o}) \tag{9.13}$$

where

$$\Psi = 1 - \frac{n}{2(n+1)} \frac{1}{\log(H_1/H_o)} \int_{H_o}^{H_1} \frac{d(\log f)}{d(\log W)} \frac{dH}{H} . \tag{9.14}$$

Since $\frac{df}{dW} > 0$ (as seen in Table 8.1),

$$\frac{W}{f} \frac{df}{dW} > 0 ,$$

and we find that $\Psi < 1$ from (9.14).

An explicit expression of Ψ may be obtained from (9.14). For a parabola with $H = X^2/b$, where $\pm X$ is the lateral extent of the channel,

$$A = \frac{4}{3} \frac{X^3}{b} \quad \text{and} \quad P = \frac{4}{b} \int_0^X \sqrt{\frac{b^2}{4} + x^2} \, dx .$$

Let $a = \frac{2X}{b}$; then from (9.8) we find that

$$f = \frac{4}{3} \{ \sqrt{1+a^2} + \frac{1}{a} \log (a + \sqrt{1+a^2}) \}^{-1} . \tag{9.15}$$

From the definitions of W, a, and X, for a parabola,

$$\frac{df}{dW} = - \frac{1}{2} a^2 \frac{df}{da} . \tag{9.16}$$

Using (9.15) and (9.16), equation (9.14) may be written as

$$\Psi = 1 - \frac{1}{2}\,\frac{n}{n+1}\,\frac{1}{\log(H_1/H_o)}\,(I_1 - I_2)\,, \tag{9.17}$$

where

$$I_1 = \int_{H_o}^{H_1} \frac{s}{s + \frac{1}{2}\sqrt{\frac{b}{H}}\log\left(2\sqrt{\frac{H}{b}} + s\right)}\,\frac{dH}{H} \tag{9.18}$$

$$I_2 = \frac{1}{2}\int_{H_o}^{H_1} \frac{\sqrt{\frac{b}{H}}\log\left(2\sqrt{\frac{H}{b}} + s\right)}{s + \frac{1}{2}\sqrt{\frac{b}{H}}\log\left(2\sqrt{\frac{H}{b}} + s\right)}\,\frac{dH}{H}\,. \tag{9.19}$$

and $$s = \sqrt{1 + \frac{4H}{b}}$$

Although the values of Ψ given by (9.17) appear to be dependent upon the thickness change itself (through the $1/\log(H_1/H_o)$ term), the integration of (9.18) and (9.19) over the change in thickness nearly cancels any such dependence. There also exists a dependence on n. It may be that in the actual (or FE) case this n-dependence is minimized by the fact that the shape factor itself is a function of n, as was seen in the previous chapter (through the stress-exponent - dependent stresses). In any event, this dependence is not large for the range of interest (n = 3 to 5).

The calculated values of Ψ for n = 3 are shown in Figure 9.4, along with the finite-element results discussed below. These values of Ψ represent the flow effect of the change in cross-section geometry (i.e. in W) with change in thickness. The width of a parabolic channel does not vary directly with the depth, and thus W changes progressively. With increasing W the magnitude of the change ΔW increases, leading to a response more like that of a wide slab, and, thus, Ψ approaches unity for large W. For W = 1, the parabolic channel most similar in shape to a semicircular one, Ψ = 0.81 (for n=3), larger than the 0.67 found for the semicircle. This increase in Ψ arises because of the relative effects of the conduit depth and side walls in the two channels. For a channel of W = 1.6, representative of the Blue Glacier, Ψ = 0.88 from the analytical model (for n=3).

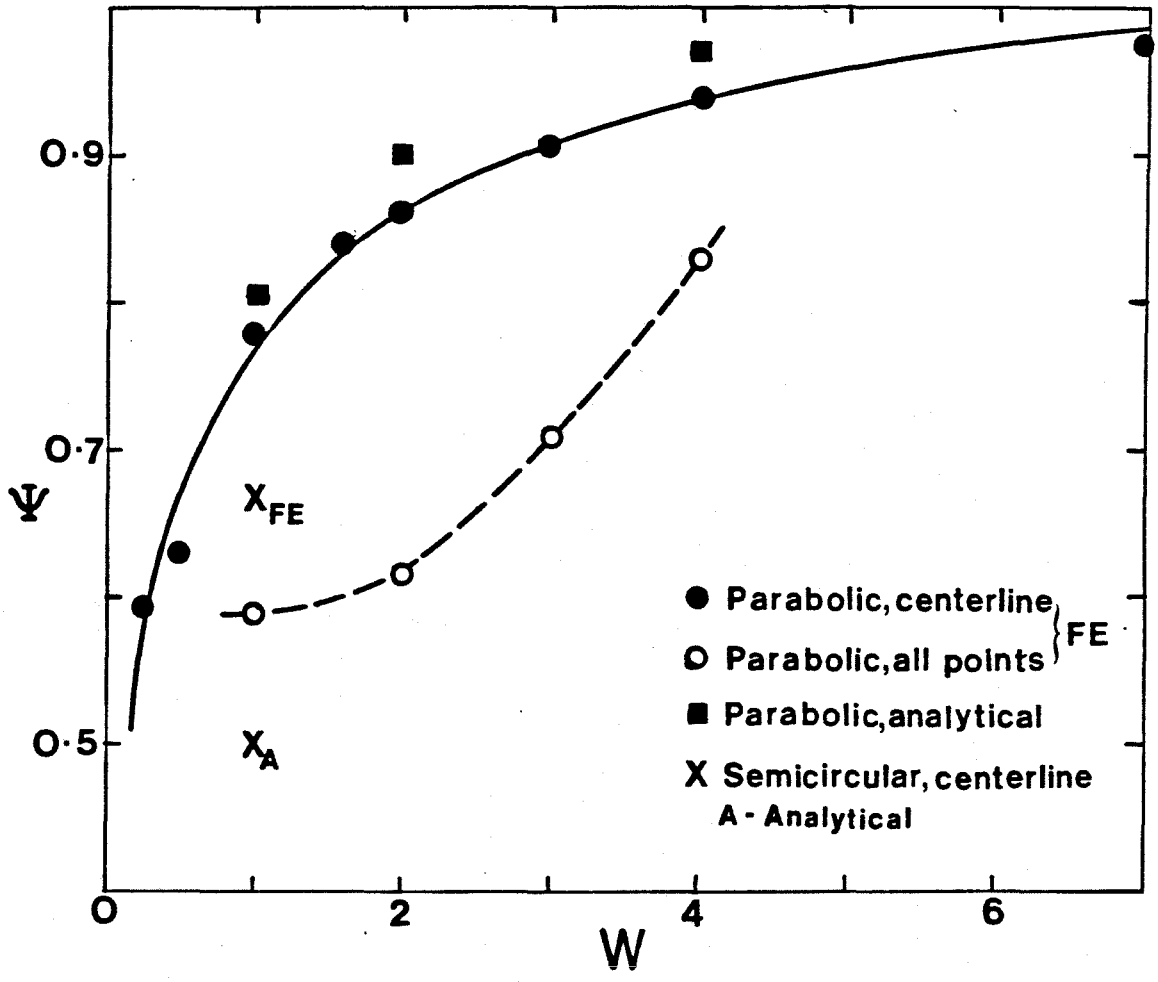

Figure 9.4

Response factor, Ψ, for different geometries, showing both analytical and finite element results. W = half width/depth of parabolic channels. Solid points refer to near centerline response only, open circles show values when response at points across channel surface is included, and x's denote value for semicircular channel.

The analytical model invokes a definition of the shape factor, (9.8), which does not fit the actual stress distribution (Nye,1965). Nor does this model allow for a nonlinear variation of shear stress with depth, as is actually seen in the FE results. The result (9.14) is, therefore, only approximate. Numerical models lead to a more accurate determination of Ψ.

In his finite-difference study of the flow of ice in simple channels, Nye (1965) has discussed the change in centerline velocity in response to a small change in thickness for n=3 (as well as approximate values for n=2 and 4). From the definition of Ψ introduced in the present study (9.6), values of Ψ can be determined from Nye's results. These results differ from those calculated below (and shown in Figure 9.4) by up to 11% (Nye's values are lower then those presented here). The reason for this discrepancy may lie in the method used by Nye in calculating the tabulated values of d(log u)/d(log H) (see Nye,1965,Table IIID). As opposed to the direct method employed in the present study of differencing the model flows in the perturbed and unperturbed channels, Nye used a graphical method which involved determining du/dW from a plot of u vs. W, which is a nonlinear curve. Small errors in this curve could lead to relatively large errors in the derivative. As described earlier, Nye's results for the flow u in parabolic In addition, Nye did not calculate the flow for any value of n other than 3, restricting accurate estimates to be made for only one value of n. As described in Chapter VIII, Nye's results for the flow velocity u in different parabolic channels with n=3 agree well with those found in the present study. Thus, it would seem that the direct approach discussed here should prove more reliable (although more costly!), since the velocities appear to be well determined. (Note:As shown by Nye (1965), $\Delta u/\Delta H$ is related to the kinematic wave speed c. It is shown that, for parabolic channels, c is less than the value calculated for a simple slab, and that, in fact, $c \sim \frac{1}{2}(n+1)u$ for values of W similar to those found in real glaciers.

The kinematic wave speed is thus even more sensitive to channel shape than is the magnitude of Δu in response to a change in thickness.)

In the present study a large number of FE models were calculated in order to define the response characteristics of flow within parabolic channels for $W \in [0,\infty)$ and for different stress exponents n. Following the procedure used with the semicircle above, flow models with various exponents n and thickness changes (along with the accompanying changes in width) were compared with flow in the unthinned channels for various values of W. The results along the centerline of representative channels are shown in Figures 9.5 a-d. There is again a well-defined linear relation between Δu and ΔH. This indicates that the response parameter is not a function of the thickness change, thus supporting the analytical results. (Any slight departure from linearity can be attributed to errors in the modelling, which are most apparent at large n and small W for which the grid was not initially designed.)

The slopes of centerline response curves (as in Figures 9.5 a-d) for various channels are plotted as a function of n in Figures 9.6 a-d. The calculated results of the FE models are shown as dots in these figures. They show, once again, a distinct linear relation between (n+1) and the slope of the response curves within a given channel, as assumed in (9.6). The additional $n/(n+1)$-dependence found in the analytical results (9.17) is not apparent in the numerical models, indicating that the nonlinear stress effects and the dependence of the stresses on n tend to cancel this additional dependence.

In Figure 9.7 the linear relations between n+1 and the slope of the response curve for many of the parabolic cross-sections modeled are shown. There is a smooth trend toward the $W \to \infty$ limiting case. Values of the response factor determined from Figure 9.7 are shown in Figure 9.4. The analytical results show

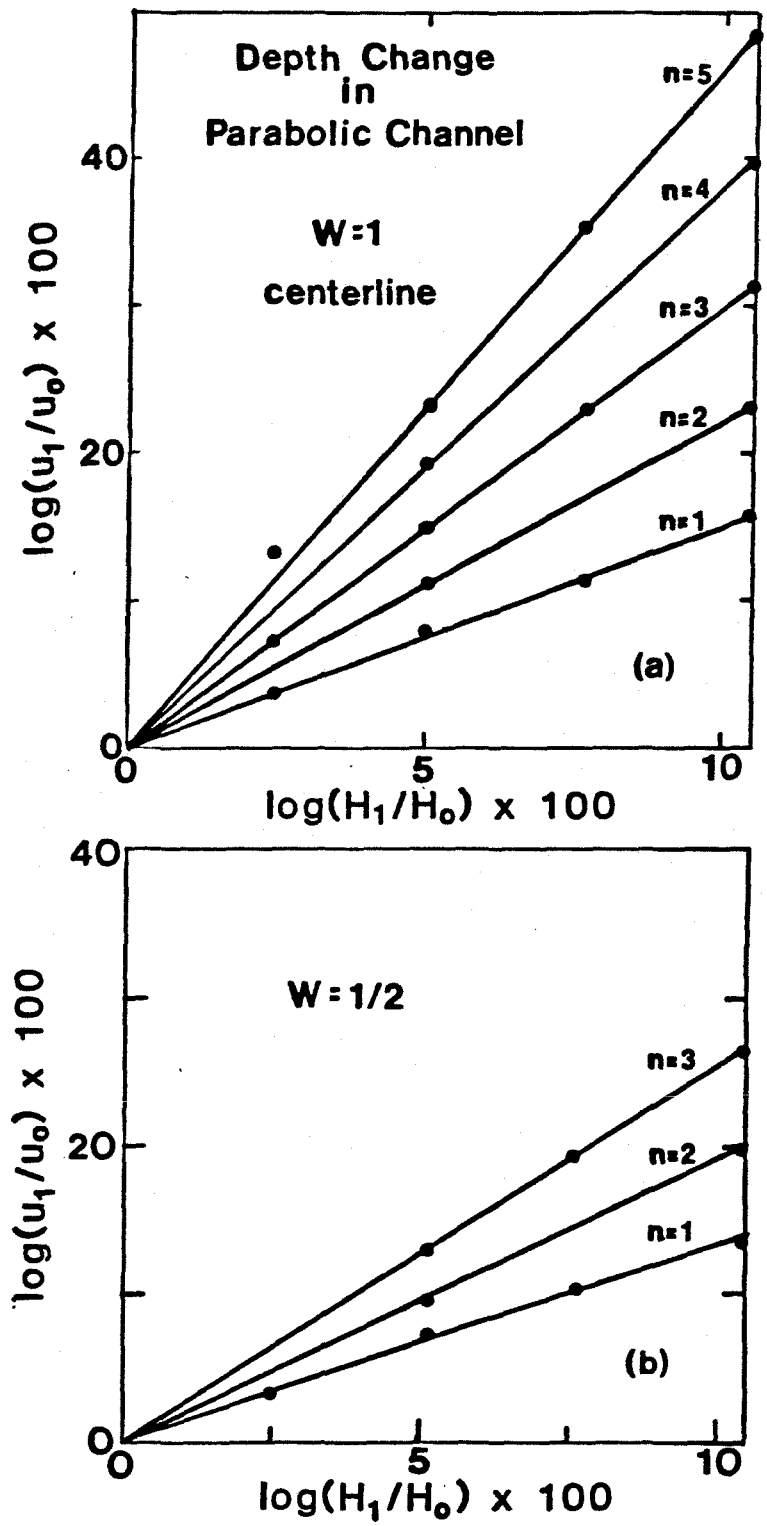

Figure 9.5 Δu versus ΔH at centerline of parabolic channels for different n. a) W = 1, b) W = 1/2, c) W = 2, d) W = 4

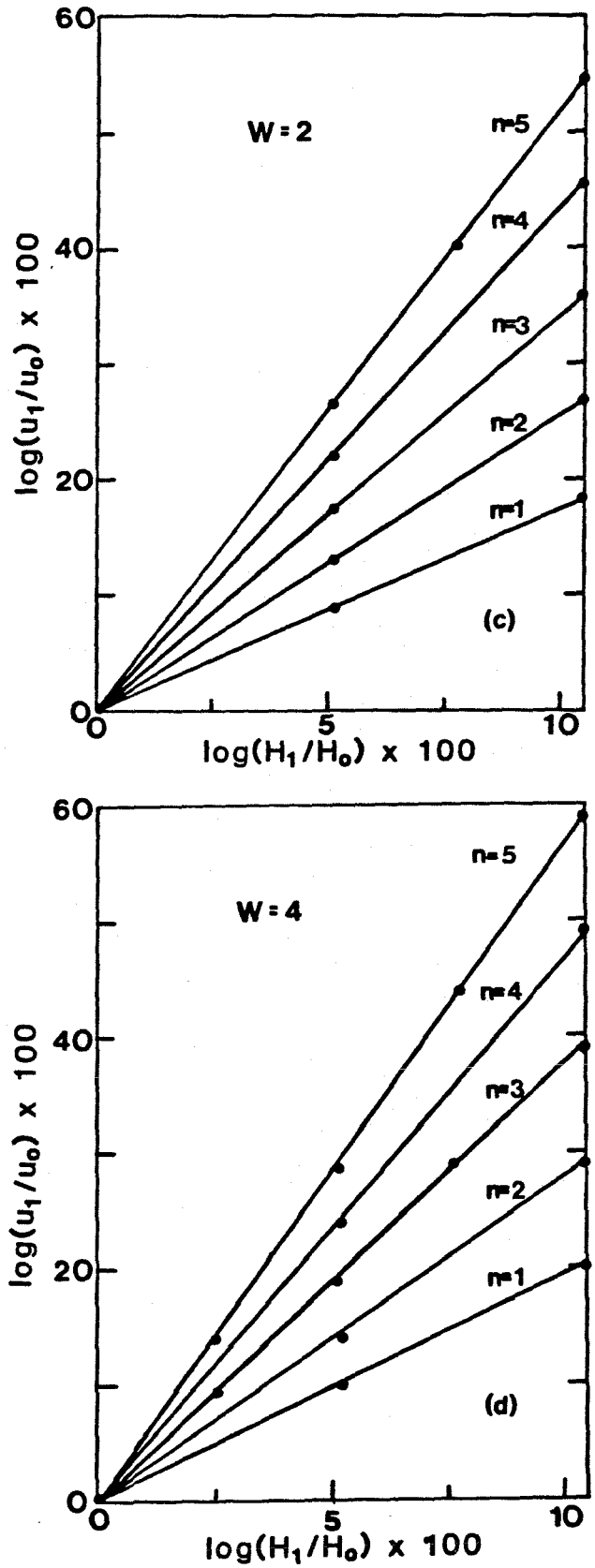

Figure 9.5 c,d

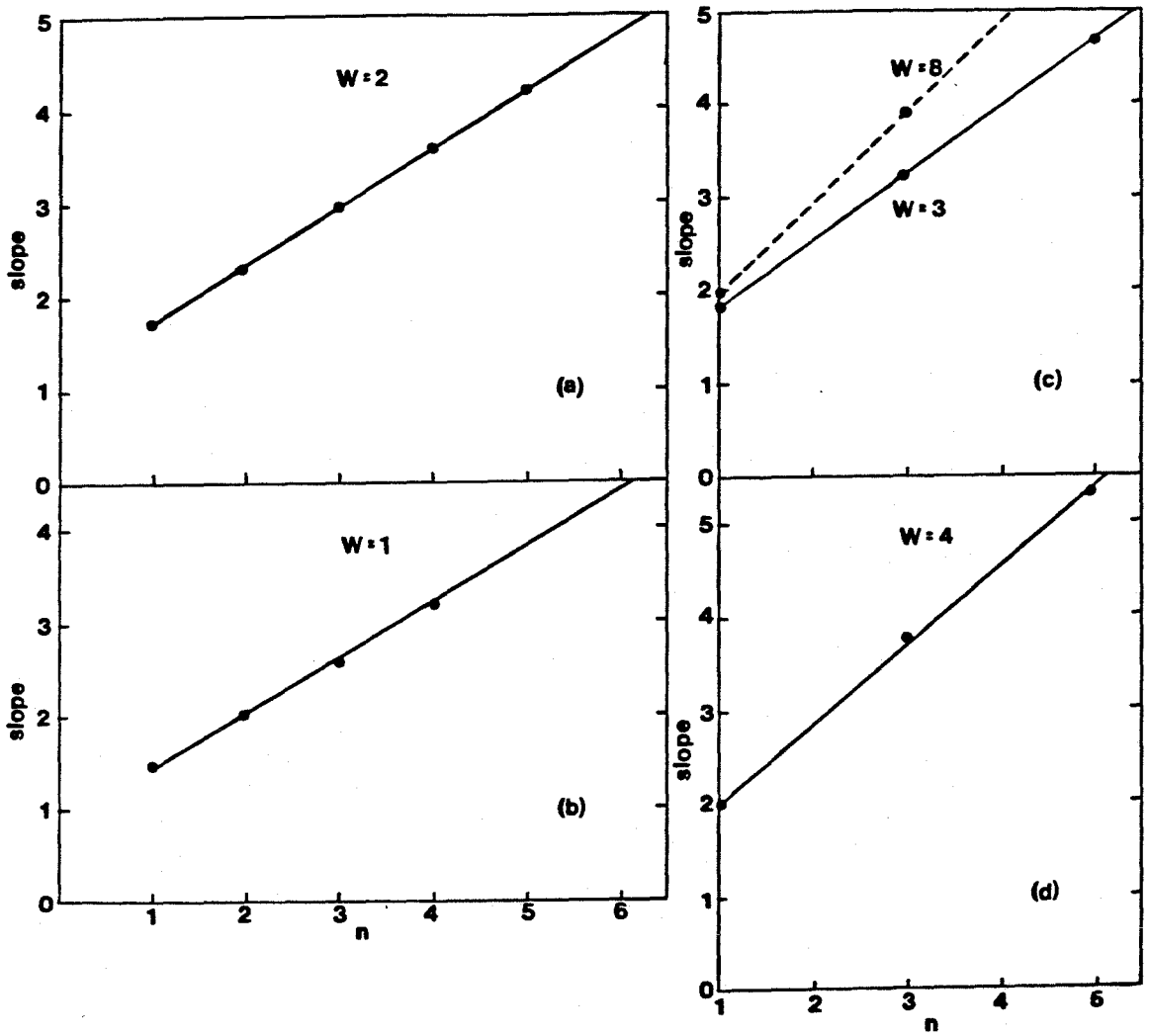

Figure 9.6 Slope of response curves in Figures 9.5a-d as a function of n (centerline values) for different parabolic channels.
a) W=2, b) W=1, c) W=3 (solid), d) W=8 (dashed), d) W=4

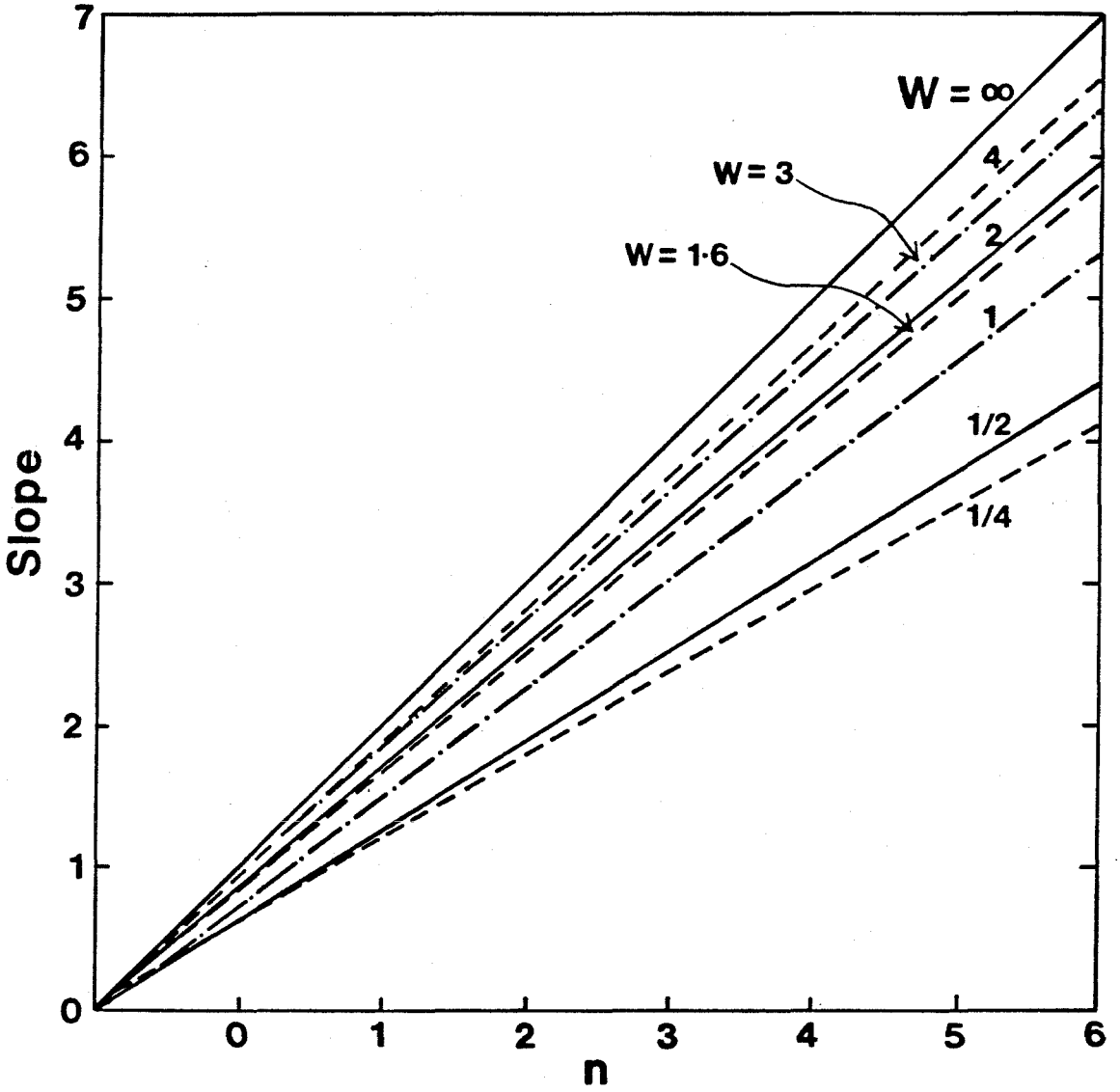

Figure 9.7 Slope of response curves for different parabolic channels as a function of n, showing progression to infinitely wide slab ($W \to \infty$), W= 1.6 corresponds to mean channel shape of Blue Glacier, (centerline values only).

surprisingly good agreement with the numerical values, considering the approximate nature of the analytical approach. This indicates that the deviation of Ψ from unity arises in response to the change in the shape of the ice cross-section with a change in thickness.

Ψ approaches unity as W tends to larger values, in agreement with the analytical results. At W = 10, Ψ is essentially unity, while for W = 1/4, $\Psi \approx 0.6$. The response factor will tend to 1/2 as W approaches zero, as is shown in the results of Nye (1965).

The Blue Glacier channel is best approximated by a W = 1.6 parabola, for which the FE calculation gives $\Psi = 0.85$. Since this differs significantly from unity, the response factor has a substantial effect on the value of the stress exponent inferred from the observational data on the response of the glacier to a perturbation in thickness. Since W ~ 1-3 for most valley glaciers, effects of similar magnitude in the velocity response for a given flow law must be taken into account in any further studies of this type.

The thickness change in the model calculations was taken to be of uniform magnitude across the surface of the cross-section. This then imposes a monotonically increasing local relative thickness change with distance from the center, since the local depth decreases outward. The question may be asked: if the local thickness change is taken into account, does the local velocity change show a similar relation to Δ H as does the centerline value?

Figures 9.8 and 9.9 show the lateral variation in Δu for parabolic channels of aspect ratios W=3 and W=1. These figures show that the departure of the response from the linear trend as defined by the centerline points increases as the responses at points at increasing distances off the centerline are included. For W=3 (Fig. 9.8) and n=5, only those values of Δu corresponding to distances

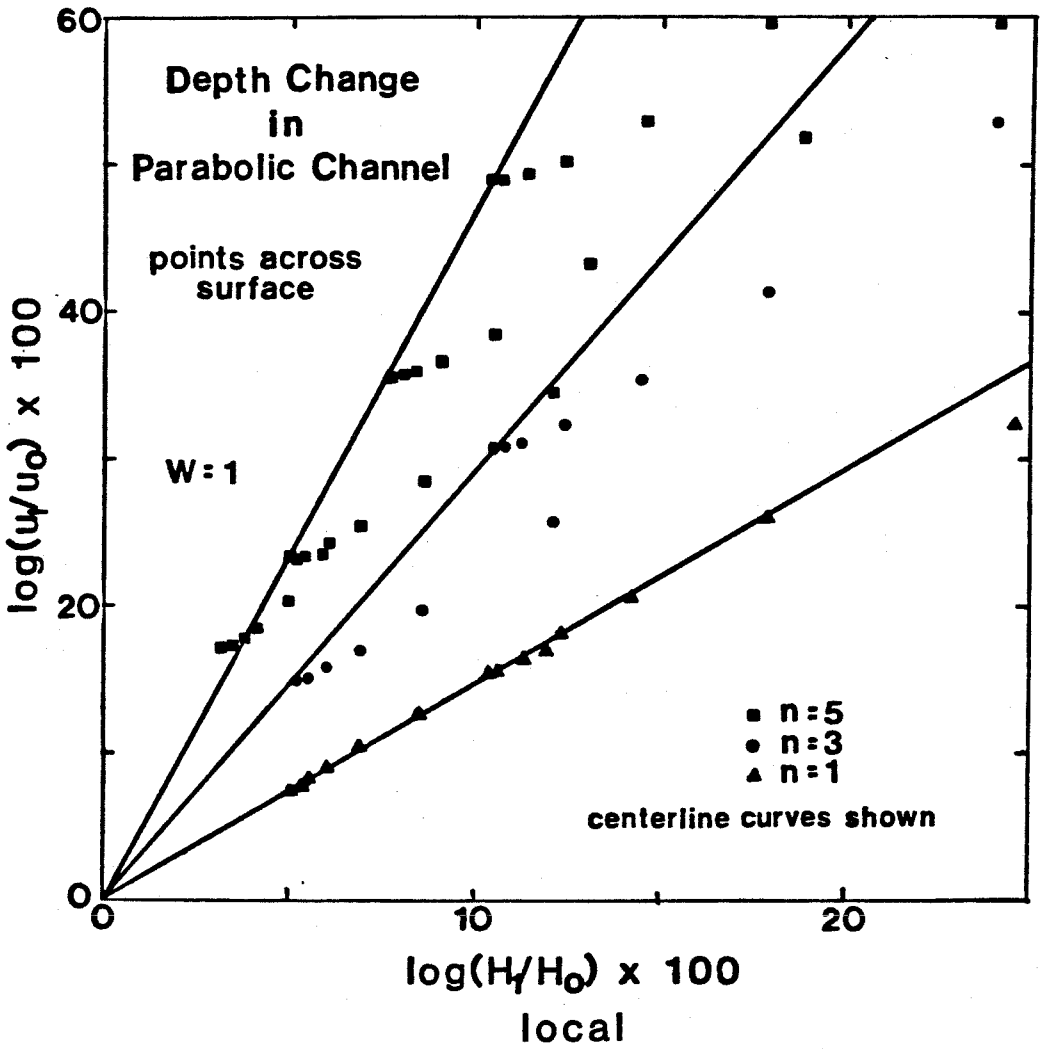

Figure 9.8 Δu versus ΔH (local) including points across the surface of the channel, for different n. W=1 solid lines represent centerline response curves.

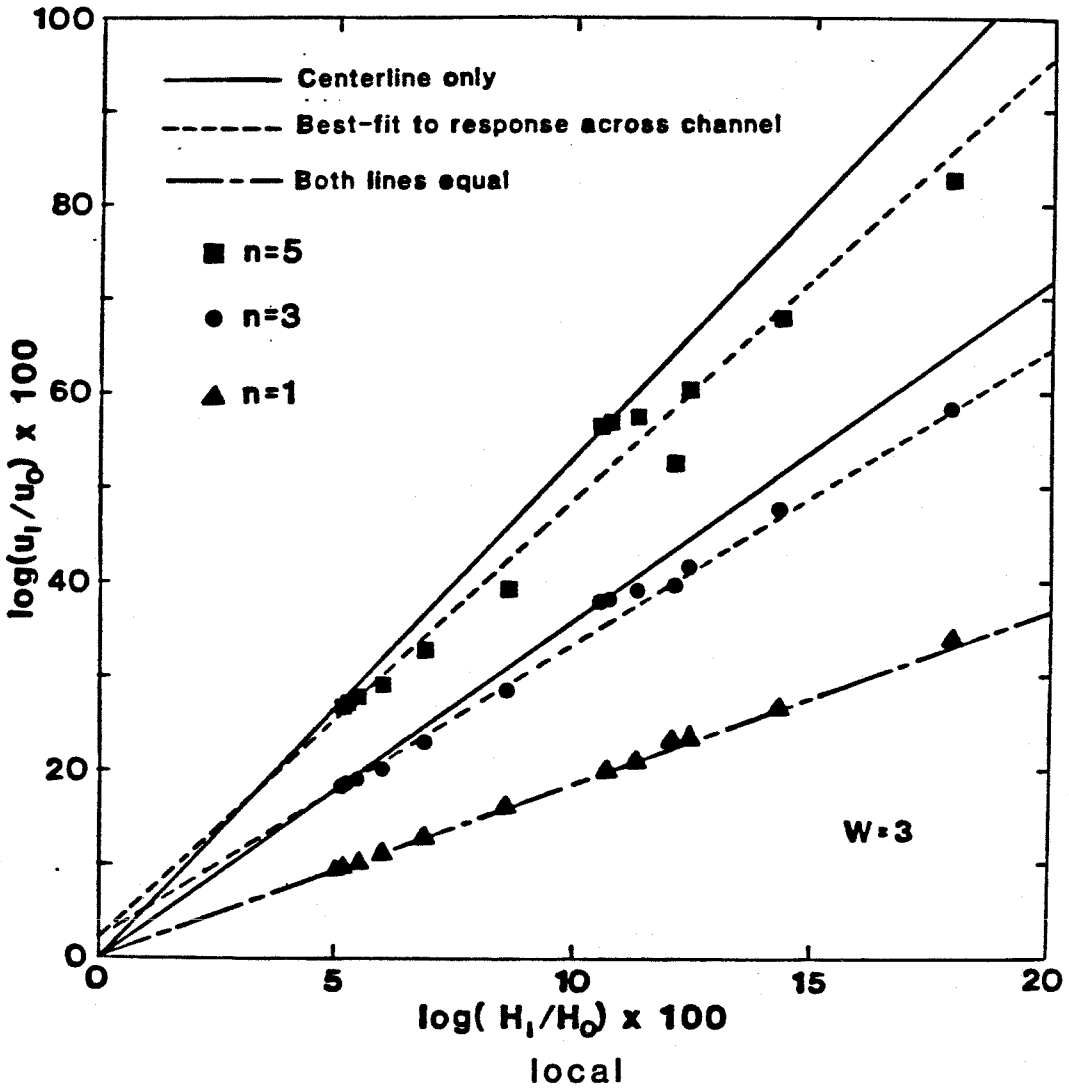

Figure 9.9

Δu versus ΔH (local) including points across the surface of channel for different n. W=3, solid lines represent centerline response, dashed lines represent best-fit to response across channel, for n=1 both lines are equal.

from the center less than one quarter the initial half-width ($X \leq 0.25$, where $X = |x| / D$, and D is the half-width of the channel at t_o) show little departure from the linear trend, while for n = 3 those points at distances $X \leq 0.375$ follow the same linear trend as the centerline values. For W = 1 (Fig. 9.9) the linearity is preserved for $X \leq 0.75$ for n = 1, $X \leq 0.19$ for n = 3, and only for $X \leq 0.12$ for n = 5. These results imply that the interval about the centerline from which data can be expected to give a reasonably linear response decreases in size with increasing exponent n and with decreasing aspect ratio W.

If a least-squares line of best fit is determined for the points within an interval of $X \leq 0.75$ in Figures 9.8 and 9.9 for the various values of n, the slope of this line decreases from that obtained for the centerline points alone (if $n > 1$). This implies that an average Ψ taken across the glacier surface is less than Ψ for the centerline. The reduction in Ψ can be as much as 25%,as illustrated in Figure 9.4.

In the observed data, there is an increase in the scatter about the linear centerline response line when off-centerline points are included (Figures 5.5-5.7). In addition, the slope of the best-fit line is reduced for the near-centerline data (Table 5.5). For W = 1.6, a transversely-averaged response parameter of 0.60 implies a value of n = 3.97, which is close to that obtained for the near centerline data 4.02.

The introduction of longitudinal curvature introduces no apparent alteration in the relation between velocity change Δu and thickness change ΔH, as is expected from the discussion in the previous chapter. (It is important in the numerical modeling of the response in a curving channel to include the change in surface slope at the inside of the bend (α_o). As the channel thins, its width is reduced by an amount ΔD and the radial dependence of the surface slope causes

α_o at the inside of the thinned channel to increase to a value $\alpha'_o = \alpha_o \dfrac{(R_c - \frac{1}{2}D)}{R_c - \frac{1}{2}(D - \Delta D)}$, where R_c is the radius of curvature and D is the initial channel width.)

9.5 Effect of a Spatially-Dependent Viscosity Factor on the Response

In the previous chapter it was shown that a radially-decreasing viscosity parameter, $\eta_f(r)$, could easily mimic the effect of an increased stress exponent in the velocity field of an ice mass flowing down a semicircular valley (Figure 8.14). Although in some instances it may be irrelevant to know, for example, whether $\eta_f=\eta_f(r)$ and n = N or whether $\eta_f=\eta_f^\circ$ and n = N' > N, it is philosophically desirable to distinguish between these two possibilities. Different stress exponents arise due to different micro-creep mechanisms, and it is important to determine which of these mechanisms act within an ice mass. A knowledge of a spatially dependent η_f would likewise give valuable information on the effects of grain size, fabric, impurity content, etc. on the deformation of the ice. But with the ambiguity evident in Figure 8.14b, how can these possibilities be distinguished?

The response of a glacier to a change in thickness can, at least partially, provide the answer to this question. For example, consider the simple model of an inclined slab presented in Chapter V. Instead of η_f being a constant, let $\eta_f=\eta_f(y)$, where the y-axis is taken positive upward from the base. In the extreme case in which the entire slab is rigid ($\eta_f \to \infty$) except for a thin basal layer of thickness L (<< L), which obeys a power-law creep relation with viscosity η_f° and exponent n, the velocity at the surface is given approximately by

$$u = \frac{1}{\eta_f^\circ}(\rho g \sin\alpha)^n L H^n$$

(9.20)

since deformation occurs only in the basal layer while the stress is determined by the entire mass of ice above. From (9.20), the change in velocity with a change in thickness of the slab is given by

$$\frac{du}{u} = n\,\frac{dH}{H} \neq (n+1)\,\frac{dH}{H} \quad . \tag{9.21}$$

This implies that the stress exponent as determined from the response to change in the slab thickness would be (n -1) if interpreted via the model with constant η_f governed by equation (9.1), not the correct value of n when η_f varies as above.

As a more realistic model, consider a slab in which η_f varies as

$$\eta_f(y) = \eta_f^{\circ}/(1-\beta y) \qquad 0<\beta H<1 \tag{9.22}$$

Then the velocity is given (from (8.6a)) by

$$u_s - u(y) = k(1-\beta H)\left[\,(H-y)^{n+1} + \left(\frac{n+1}{n+2}\right)\frac{\beta}{(1-\beta H)}(H-y)^{n+2}\right] \quad , \tag{9.23}$$

where $k=(\rho g \sin\alpha)^n/[\eta_f^{\circ}(n+1)]$. The change in the surface velocity with a small perturbation in H is (assuming no sliding)

$$H\,\frac{du_s}{dH} = (n+1)\,k H^{n+1} - k\beta\, H^{n+2} \tag{9.24}$$

A thickness dependent response factor, $\Psi = \Psi(H,n)$, may be defined from (9.6) and (9.24), as

$$\Psi = 1 - \frac{\beta H}{(n+1)(n+2-\beta H)} \tag{9.25}$$

Since β is positive for the physically realistic case of an increase in η_f with increasing distance up from the base, $\Psi \leq 1$, for all n and H. This then implies that the value of the stress exponent inferred from measured (Δu, ΔH) data and

(9.6) is higher than that inferred from the simple model of equation (9.1) if there is a variation in η_f as given by (9.22).

Although the magnitude of Ψ is dependent upon the manner in which the viscosity factor varies with depth, a second example will show that it is bounded from above by unity if there is a decrease in η_f with depth when η_f is fixed at the base.

Let η_f vary as

$$\eta_f(y) = \eta_f^{\circ}(1 + by) \qquad b \geq 0 \tag{9.26}$$

then

$$u(y) = (n+1)k\int_{H-y}^{H} \frac{\xi^n}{1 + b(H - \xi)}\, d\xi \qquad 0 \leq y \leq H \tag{9.27}$$

and

$$\frac{du_s}{dH} = (n+1)kH^n - (n+1)kb\int_0^H \frac{\xi^n}{[1 + b(H - \xi)]^2}\, d\xi\,. \tag{9.28}$$

For n = 1,

$$\frac{u_s}{(n+1)k} = \frac{1 + bH}{b^2}\log(1 + bH) - \frac{H}{b} \tag{9.29a}$$

and

$$\frac{du_s}{u_s} = \left[1 + \frac{1}{bH} - \frac{1}{\log(1 + bH)}\right]\frac{dH}{H}\,. \tag{9.29b}$$

For n = 3,

$$\frac{u_s}{(n+1)k} = \frac{1}{b^4}\left[(1+bH)^3\log(1+bH) - bH\left(1 + \frac{5}{2}bH + \frac{11}{6}b^2H^2\right)\right] \tag{9.30a}$$

and

$$\frac{du_s}{u_s} = \left\{ \frac{[1+3\log(1+bH)](1+bH)^2 - [1+5bH+\frac{11}{2}b^2H^2]}{\frac{(1+bH)^3}{bH}\log(1+bH) - [1+\frac{5}{2}bH+\frac{11}{6}b^2H^2]} \right\} \frac{dH}{H} \qquad (9.30b)$$

Values of a response factor $\Psi = \Psi(H,n)$ can be defined from the relations (9.29b) and (9.30b). It is easily seen from these expressions that $\Psi \leq 1$ for each n and b ≥ 0.

Table 9.2 shows the effective exponent n* defined by $(n^*+1)=\Psi(n+1)$ for several values of n and a viscosity variation following both models presented above.

Table 9.2
Effective Stress Exponent for Response with Depth-Dependent Viscosity

		$\eta_I=\eta_I^\circ(1+by)$	$\eta_I=\eta_I^\circ/(1+\beta y)$
	n	n*	n*
$\eta_I(H)=10\eta_I^\circ$	1	0.48	0.57
	3	2.57	2.8
	5	4.63	4.85
$\eta_I(H)=5\eta_I^\circ$	1	0.59	0.64
	3	2.68	2.80
	5	4.74	4.87

This table shows that there is a significant reduction in the value n* of the stress exponent determined from model (9.1) as compared with true value, n, when there is a variation in η_I. Similar results hold for channel forms other than parabolic. It is therefore apparent that the introduction of a variation of η_I with depth would only serve to increase the value of the true stress exponent for the ice of Blue Glacier above that inferred from the slope of the response curves in Chapter V. Indeed, the observed slope for the centerline data would lead to a stress exponent of up to n = 6 if a 10-fold viscosity parameter variation were allowed in addition to the effects of the parabolic valley form. Such a large stress exponent is well above the n = 3 proposed by some authors who promote a depth-dependent viscosity parameter (for a recent review of such work, see

Hooke, 1981). These results thus provide a means of distinguishing a flow law of the form [n = 3, $\eta_f = \eta_f(\mathbf{x})$] and one of the form [n > 3, η_f = constant]. However, if relatively large values of n are allowed, the response in a single channel geometry cannot distinguish between η_f = constant and $\eta_f = \eta_f(\mathbf{x})$ with a larger stress exponent.

To summarize the important result of this section: *the observed relation between velocity change and thickness change for Blue Glacier is not consistent with a model for which n = 3 and η_f decreases with depth, even though the unperturbed velocity distribution (from surface and borehole data) could be made consistent with n = 3 given a decrease of η_f at depth.* The response data require n> 3 regardless of whether a decrease in η_f at depth is present or not.

A comment is in order on the choice of the origin (y = 0) in (9.22) and (9.26). If the origin were taken to be located at the surface instead of at the base (and b, β chosen so as to allow a decrease in η_f with depth), then, for the first time in this study, Ψ would be greater then unity. This could allow an interpretation of the observed data with $n \approx 3$. But this choice of the origin requires fixing η_f at the surface and not at the base (as in (9.22), (9.26)). A perturbation in the ice thickness would then introduce a change in η_f throughout the ice column. With the stress related to the depth in a nearly linear way, this would, in turn, require a stress dependency of η_f. This contradicts the initial assumption that η is independent of stress (except perhaps hydrostatic) and that all of the stress dependence in the flow law is embodied in the second invariant term. This contradictory dependence of η_f on τ' would naturally reduce the equivalent stress exponent because it would offset some of the influence of $J_{II}^{(n-1)/2}$ in the flow law.

Following this reasoning, it is perhaps then worthwhile to question the suitability of allocating the dependence of the flow law on texture and fabric to varia-

tion of the η_f parameter. These features of polycrystalline ice have been seen to be dependent on the stress and deformation history through dynamic recrystallization (Kamb, 1972, Duval, 1981). A depth-dependent stress exponent may be more appropriate to the ice within a glacier than is a variation in η_f. This topic remains to be investigated.

9.6 Summary of Results and Application to Blue Glacier

The linear relation between the logartithmic change in velocity and logarithmic perturbation in slope and ice thickness found in Chapter V for the Blue Glacier indicates that a simple power-law constitutive relation is applicable to glacier ice, and that the form of this linear relation can give useful estimates of the value of the stress exponent and the longitudinal averaging scale of the surface slope. Several features of the response in geometrically simple channels can be applied to an approximate model for the Blue Glacier.

The bilinear form of equation (9.6) shows that the logarithmic slope and thickness variations may be decoupled. When the shape of the glacier valley is included in the analysis, the slope of the response curve (on ΔH) for a given n is reduced by the response factor Ψ, which expresses the flow effect of the change in the cross-sectional shape with a change in thickness. This change in shape effects the stress field within the channel, as manifested by a change in an effective shape factor, Δf. In general, $1/2 < \Psi < 1$. This means that the effective exponent n^* determined from the slope of the response curve for the simple slab model (9.1) is actually less than the true exponent in the flow law. Longitudinal curvature of the channel does not alter the response. Introduction of a physically reasonable variation in η_f with depth serves only to increase the true stress exponent implied by the data. Incorporation of the data from all points across the surface of the glacier cross-section introduces scatter from a single

linear regression and a predictable decrease in the slope of the response line. These features are seen in the observed data in Figures 5.5-5.7.

The results from the theoretical analysis of the flow response may be applied to the observed response as given in Chapters V and VI. From the slope β_H of the linear trend between ΔH and Δu in Figures 5.5-5.7 and 6.1 and a value of Ψ corresponding to the mean cross-sectional aspect ratio for the glacier valley (W = 1.6), we may obtain an estimate of the stress exponent. For near-centerline data only, $\Psi = 0.85$, while inclusion of off-centerline data requires $\Psi = 0.60$. The results for the different data sets are shown in the Table 9.3.

Table 9.3
Stress Exponent from Observed Response, Assuming a Parabolic Channel

Data Set	n
1957/58 - 1977/78, centerline	4.02 ± 0.49
" " , all points	3.97 ± 0.49
1958/59 - 1978/79, centerline	4.72 ± 0.88
all years' centerline data	5.05 ± 0.41
all years' data	5.13 ± 0.41
average	$\bar{n}$=4.58

The variation in n is due to errors in the data, variations in channel form, and the effects of a changing surface slope. As described in Chapter V, the most accurate values are those for the individual annual data sets (the first three listed in Table 9.3). The mean of these values is 4.24 ± 0.38, slightly smaller than that listed in Table 9.3, which includes the 'all years' data set, which is expected to be less reliable.

The value of $\bar{n}$ and the mean value for the more reliable data sets (the first three listed in Table 9.3) are well within the range of values found by other authors on the Blue Glacier from borehole deformation and closure studies (e.g. n = 3.3, Shreve and Sharp, 1970; n = 5.2, Kamb and Shreve, 1966, unpub.) The

results for all transverse points agree well with the corresponding centerline values, considering the relative effect of a departure from the assumed parabolic shape on the response near the centerline and at a distance from it. With n = 4.6, the predicted surface slope change affecting all profiles is $\Delta<\alpha>_L=-4.0$. This is close to the observed $\Delta<\alpha>_L=-4.5\pm 1.8$ as determined with a box-car type averaging window over a length 6-7 times the centerline ice thickness. If the specific values of n and β_o are taken for the years 1957/58 - 1977/78, then the overall slope change is $\Delta<\alpha>_L = 3.7$, again close to the observed value of -4.5 ± 1.8 for these years.

The stress exponent determined from the slope of the best-fit line resulting from the regression of the longitudinally-averaged (as in Chapter 6) ΔH on the centerline velocity perturbation (Fig. 6.1) is n = 3.24, and $\Delta<\alpha>_L$ = -2.9. These values are somewhat lower than those obtained from the local thickness changes. The reduced slope of the longitudinally averaged response curve is, in part, due to the large shift in the values of ΔH at the upper and lower profiles (B and I). The error in the longitudinally averaged ΔH at these profiles is large because no survey dataareavailable over much of the averaging window (and the window itself may change length at profile B, which is near the terminus). Thus, the value of n obtained from this reduced slope is more subject to error than that from the local ΔH values.

9.7 Mer de Glace

The data of Lliboutry and Reynaud (1981) on Mer de Glace, France, can be reinterpreted on the basis of the model described by (9.6). The observations show little or no velocity change at several locations on the glacier where there has been a substantial change in thickness. This lack of correspondence between ΔH and Δu has led these authors to discount the flow theory leading to

(9.6), and prompted them to propose the existence of specific "controlling zones" in localized areas of the glacier, which control from a distance the glacier's motion (and flow response) along its length.

Expressing the response data of Lliboutry and Reynaud (1981) in terms of logarithmic changes, we may obtain several data pairs ($\Delta H, \Delta u$). A long box-car-averaged surface-slope change may be obtained from their data over the reach of study ($\sim$ 7-8 x depth). Including this slope change in the analysis (which Lliboutry and Reynaud do not), we find that we cannot expect much velocity change at those profiles where there was a large thickening, because the slope change is quite large and offsets the effect of thickening. The large-scale logarithmic slope increase (x100) is ≈ 11, while the thickness at the profiles near the center of the reach decreased on average by $\approx$ -10 percent over the period 1935 to 1970. With $\Delta u = 0$ in (9.6) and a response factor applicable to the measured cross section ($\Psi = 0.8$), we obtain a flow law exponent of $n \sim 3 - 4$. This is a very reasonable value for n. Thus it seems that the glacier-flow theory leading to (9.6) (with longitudinal averaging of the surface slope and thickness) can explain the observations on Mer de Glace. One need not introduce a 'controlling zone' at some distance. Instead, one must properly average and include the effect of a change in surface slope. A more thorough study could be performed on the Mer de Glace data using the ideas developed in Chapter VI to develop further these conclusions.

CHAPTER X

MODELS OF FLOW AND RESPONSE FOR BLUE GLACIER CHANNEL SHAPE

The discussion in the last few chapters has been directed to the study of the flow and its response to changes in surface configuration in relatively simple geometries. Several noteworthy features have been described,with an emphasis on the causes and factors controlling them. With this as a background, we now turn to a discussion of models of flow and of flow response to observed changes in slope and thickness within the actual channel of Blue Glacier.

Two comparisons of model flow within cross-sections of Blue Glacier can be made with observational results. The first is a comparison of steady flow, as determined from numerical models for various channel curvatures, flow-law parameters, etc., with the observed surface velocity profiles as described in Chapter IV. The second is a comparison of the observed change in velocity with numerical models of the flow response under the observed thickness change within each profile. Both of these comparisons allow determination of the flow law parameters and effective surface slope governing the flow of the glacier.

The local thickness and thickness changes are known at each point within a cross-section. These parameters were used in the model calculations. The effects of longitudinal stress gradients and curvature are then describable in terms of an effective surface slope and effective curvature at each profile.

A large number of FE models were made of the flow and flow response in each channel cross section for which observational data over the period 1957 to 1977 are available, namely profiles B through I. We discuss here only those models which serve to illustrate important points, in particular, the models best fitting the observations. Each profile will be discussed in turn, followed by a summary

of the results.

10.1 Response Factors

Before beginning discussion of the flow models in each cross-section and the comparison with observations, we first describe two model results that are independent of the observed data.

The first is that, as expected, within all channels the FE calculated velocity change is related to changes in slope by the right-hand term in eqn. (9.1), namely $n \log(\sin\alpha_1 / \sin\alpha_0)$. This result is similar to that stated in section 9.1.

The second result is a value of the response factor Ψ for each cross section. The FE calculated centerline velocity changes correspond to values of Ψ shown in Table 10.1. These are averages obtained over several values of the stress exponent used in the constitutive relation for ice in the models. Differences of up to 2% were found among the Ψ values for n in the range 3 to 5. These differences arise because of the dependence of the stress field on n within these non-symmetric channels, and because of errors in the numerical models. These differences were somewhat larger than those found among the values for different n in the simple channels discussed in the previous chapter because the exponent n - dependency of the stresses is slightly larger for the actual channel shapes, which are not symmetric.

The mean value of the Ψ values listed in Table 10.1 is 0.82, which is close to the value $\Psi = 0.85$ obtained in Chapter IX for the parabolic channel most closely approximating Blue Glacier channels ($W = 1.6$). This shows that the channels are nearly parabolic in form (as they appear to be) and that minor fluctuations in the channel profiles from a parabola are, to some extent, averaged by the stress distribution within the channels.

Table10.1
Ψ for Different Cross-Sections

Profile	Ψ	Profile	Ψ
B	0.79	F	0.
C	0.84	G	0.81
D	0.88	H	0.77
E	0.89	I	0.85

10.2 Flow Models in the Individual Cross-Sections

The first figure in each subsection that follows contains the observed surface velocity profile and the finite-element mesh used to represent the cross-section, as well as various model results.

Longitudinal curvature is introduced in terms of the radius of curvature at the channel centerline (R_c), in meters. In figures showing the velocity change, the term "Large Slope Inc" represents an increase of 4% in the effective slope from 1977 to 1957 (or a slope decrease from 1957 to 1977), while "Small Slope Inc" represents an increase of 2%. Since the models in this chapter were initially calculated for the geometry as observed in 1977, we will speak of changes relative to this configuration. Thus, we will say that the glacier has thinned from the initial (1977) model to the final (1957) and that the slope has increased from initial to final (or perturbed) model, as opposed to the terminology used elsewhere in this study.

10.2.1 Profile B This profile is somewhat unusual among the profiles under study in that it is located in a reach of the glacier which is reasonably straight. We would thus expect that curvature effects are not important in determining the shape of the velocity profile. The observed velocity profile in Figure 10.1 is nearly symmetric about the centerline, with maximum at the center. However, the cross-sectional shape is not symmetric. It gives rise to the flow profiles shown in Fig. 8.1c, which have a shape that is somewhat skewed to the east

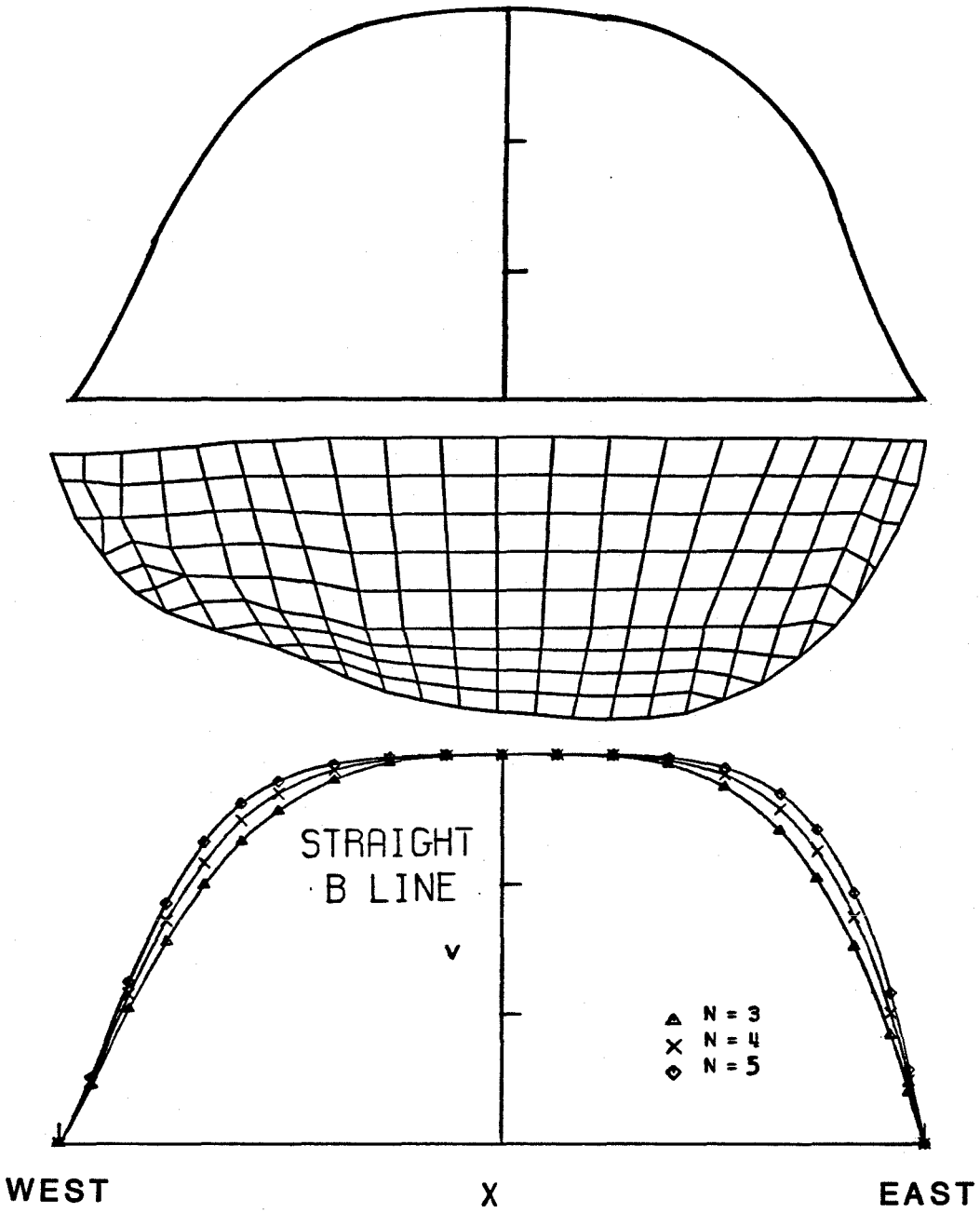

Figure 10.1 Profile B

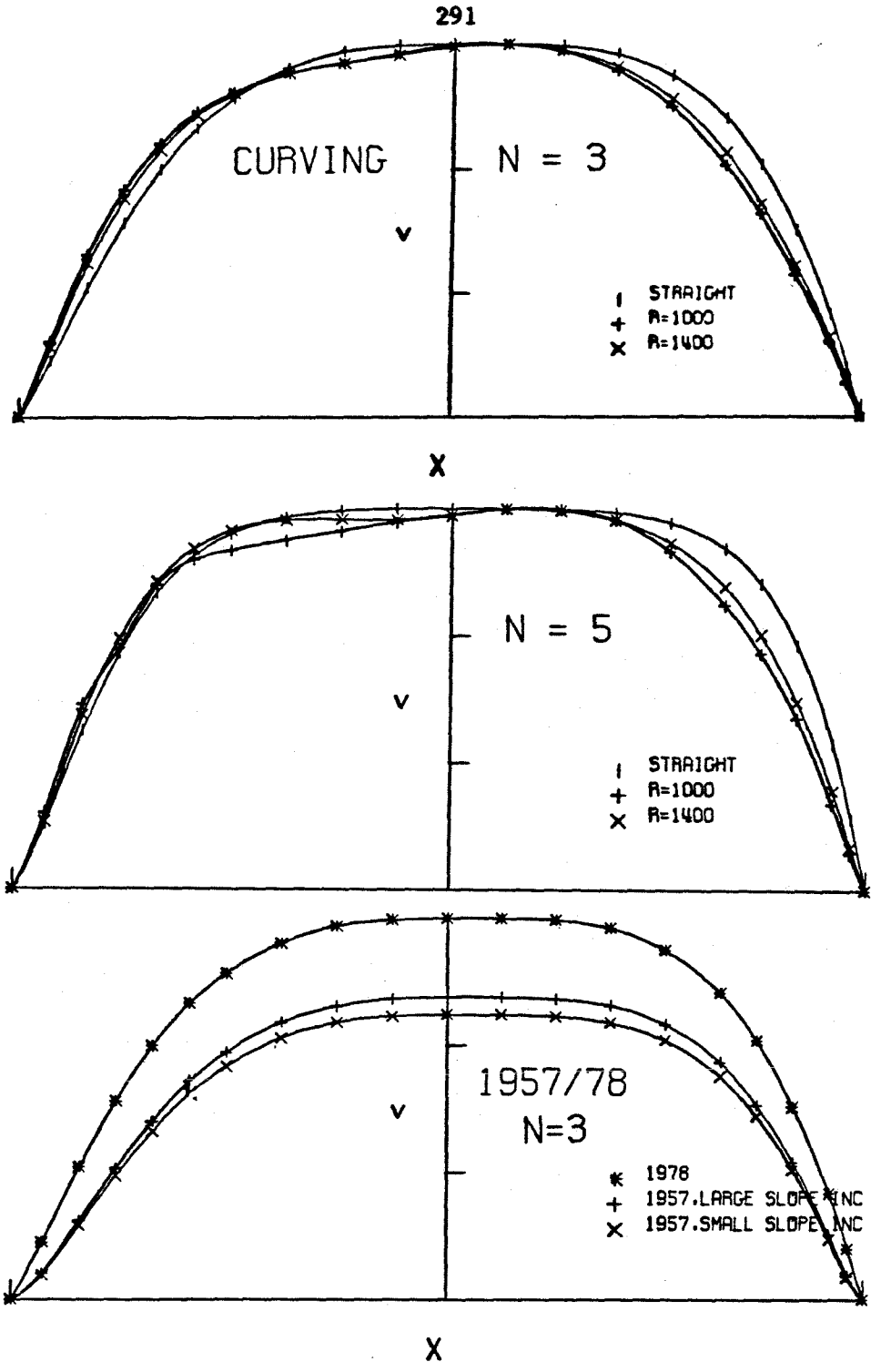

Figure 10.2 Profile B

(right), with maximum velocity over the deeper part of the channel. The introduction of some curvature, as in Figs. 10.2a,b reduces some of the effect of the asymmetric channel shape. A radius of curvature of 1600-1800 m and n=3-4 provide the best fit to u_{obs}.

The calculated flow response for this profile is shown in Fig. 10.2b,c for n = 3 and 4. The difference in magnitude and spatial variation of the velocity change is not large between n=3 and n=4, which illustrates the relative indeterminacy of the stress exponent from the data in a single channel especially when the variation in the effective slope change is considered. The modeled response for n=3 and 4 and for different effective slope changes is given in Table 10.2. With n=4 and $\Delta\alpha$ = 2.0 (from 1977 to 1957) there is a good correlation between the model and observation at all points in the B profile except B5. Δu at B5 seems anomalously low, and no model fitting the rest of B with the measured thickness change has explained its low value.

10.2.2 Profile C The channel cross-section at C is a nearly symmetric parabola with aspect ratio W=1.4, and the velocity profile is nearly symmetric about the center (Fig. 10.3). A straight channel with n=4 produces a close fit to the observed velocity. An even closer fit is obtained by the introduction of some curvature, as might be expected from the position of C along the glacier. A radius of curvature of 1200 m or less produce somewhat too large an effect (Fig. 10.4). A value of R_c= 1600 m provides the best fit.

From Table 10.2 we see that n=4 and $\Delta\alpha$=1 work well in explaining the response. Examples of the change in velocity are shown in Fig. 10.4 (with large $\Delta\alpha$).The flow within the channel for n=4 is shown in 10.3. The small undulation in the channel shape does not disturb the flow far from the margin.

Table 10.2

Observed and Modeled Velocity Increase

Location	Δu(observed)	Δu,FE(n=3)		Δu,FE(n=4)		
		Δα=2	Δα=4	Δα=2	Δα=4	
B1	37.5	35.2	29.1	39.9	32.1	
B2	34.7	29.9	24.3	34.6	26.8	
B3	36.2	29.0	23.3	33.9	26.1	
B4	31.5	29.1	23.4	34.0	26.2	
B5	30.2	31.4	25.7	36.6	28.8	
C1	36.5	18.9	12.9	22.1	14.3	
C2	25.2	16.4	10.7	19.9	12.1	
C3	26.5	15.5	9.8	19.2	11.4	
C4	23.8	15.1	9.4	18.6	10.8	
C5	24.0	15.2	9.5	18.7	10.9	
C6	27.2	18.5	12.8	22.0	14.2	
						Δα=3
D1	(7.6)	-	-	23.9	-	19.9
D2	23.2	-	-	24.6	-	20.6
D3	21.3	-	-	23.8	-	19.8
D4	24.2	-	-	23.9	-	19.9
D5	26.9	-	-	27.1	-	23.1
						Δα=6
E1	(10.3)	-	27.5	-	30.0	22.1
E2	11.5	-	21.9	-	24.5	16.5
E3	16.1	-	21.4	-	25.1	17.2
E4	14.3	-	21.2	-	24.8	16.7
E5	18.4	-	21.3	-	24.7	16.9
		n=5	(Δα=4)			Δα=3
F1	16.2	15.5		21.7	13.8	17.7
F2	11.2	10.9		16.8	8.9	12.8
F3	13.0	10.5		16.2	8.4	12.4
F4	10.7	10.3		15.8	7.9	11.7
F5	12.9	11.5		16.9	9.0	12.9
						Δα=3
G1	13.4	-	-	25.0	16.6	20.4
G2	14.6	-	-	17.4	9.4	13.5
G3	9.9	-	-	15.7	7.9	11.8
G4	11.2	-	-	16.5	7.5	11.5
H1	10	-	-	-	14.5	18.4
H2	(14.8)	-	-	-	4.1	8.0
H3	6.2	-	-	-	2.8	6.7
H4	6.9	-	-	-	2.6	6.5
H5	6.2	-	-	-	2.9	6.8
I1	5.9	-	-	18.34	10.4	
I2	3.6	-	-	12.7	4.7	
I3	6.6	-	-	10.2	2.4	
I4o	6.7	-	-	11.5	3.6	
I5	4.1	-	-	10.1	2.2	
I6	4.7	-	-	9.7	1.8	
I7	5.5	-	-	8.7	0.9	
I8	7.8	-	-	9.2	1.2	
I9	12.7	-	-	12.2	4.3	

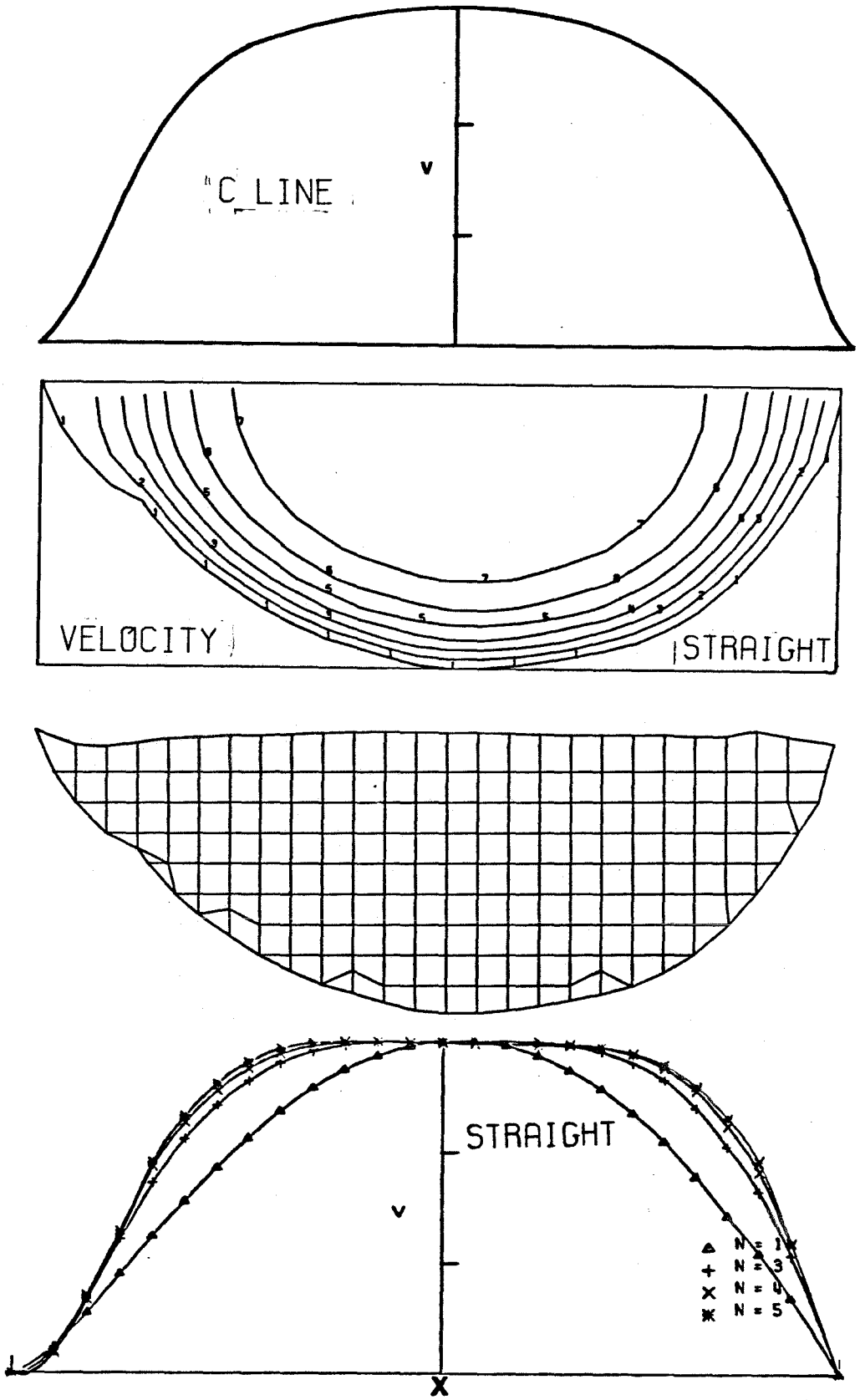

Figure 10.3 Profile C

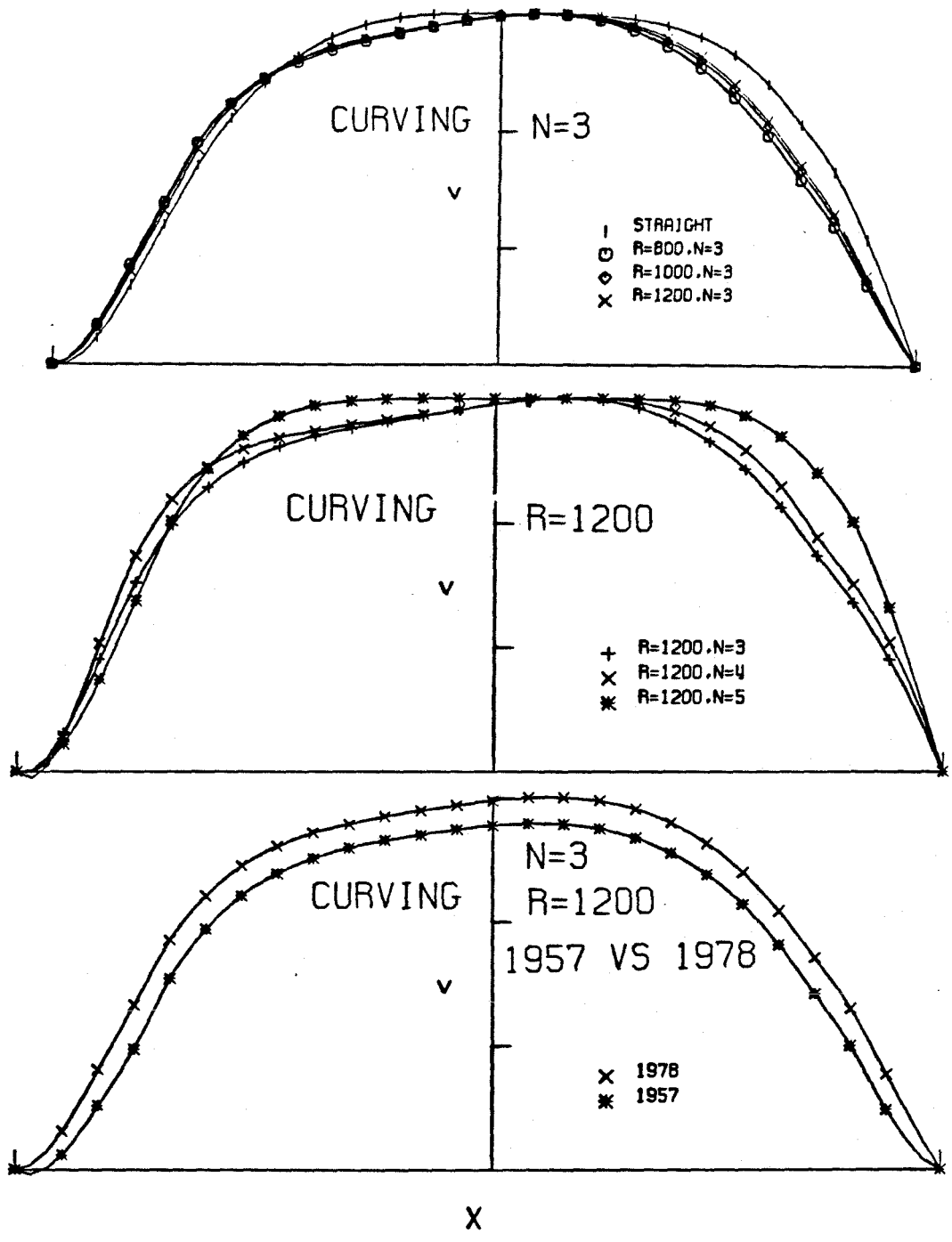

Figure 10.4 Profile C

10.2.3 Profile D The flow pattern in profile D strongly shows the effects of channel curvature, especially when the channel shape is considered (Fig. 10.5). A radius of curvature of 1000 m and n=4 fit the observed profile. The surface depression on the western (left) margin cause a component of u directed outward.

The velocity change is well modeled by a model with n=4 and $\Delta\alpha$=2.8, (Fig. 10.6), except at the point D1, where the observed change is subject to significant error. The variation in u is not large between the locations D2-D5 because they are located relatively close to the centerline.

10.2.4 Profile E The velocity profile at E (Fig. 10.7) does not show a strong asymmetry about the centerline, as would be expected for a profile at this position along the glacier, where the curvature is large. The velocity maximum is dislaced only slightly outward of center.The channel geometry suggests nothing which would alter the effects of curvature. Figures 10.7c and 10.8a,b show that the expected effects of curvature should be large. Instead, a straight channel with n=4 (or possibly 3) gives the closest fit to the observations (or, at the least, $R_c > 1800$m).

A similar anomalous result holds for the modeled velocity change. With n=4 (or 3), a large increase in effective slope ($\Delta\alpha$=6) from 19977 to 1957 is needed to fit the observations.

10.2.5 Profile F The channel cross-section along profile F is perhaps the most asymmetric of all the profiles in the reach studied. The deepest point lies approximately 100m to the west of the centerline (Figure 10.9). The observed velocity profile, on the other hand, has a maximum at nearly the same distance toward the east of center. Flow models in straight channels show a maximum west of the center (towards the deeper part of the channel). If a radius of

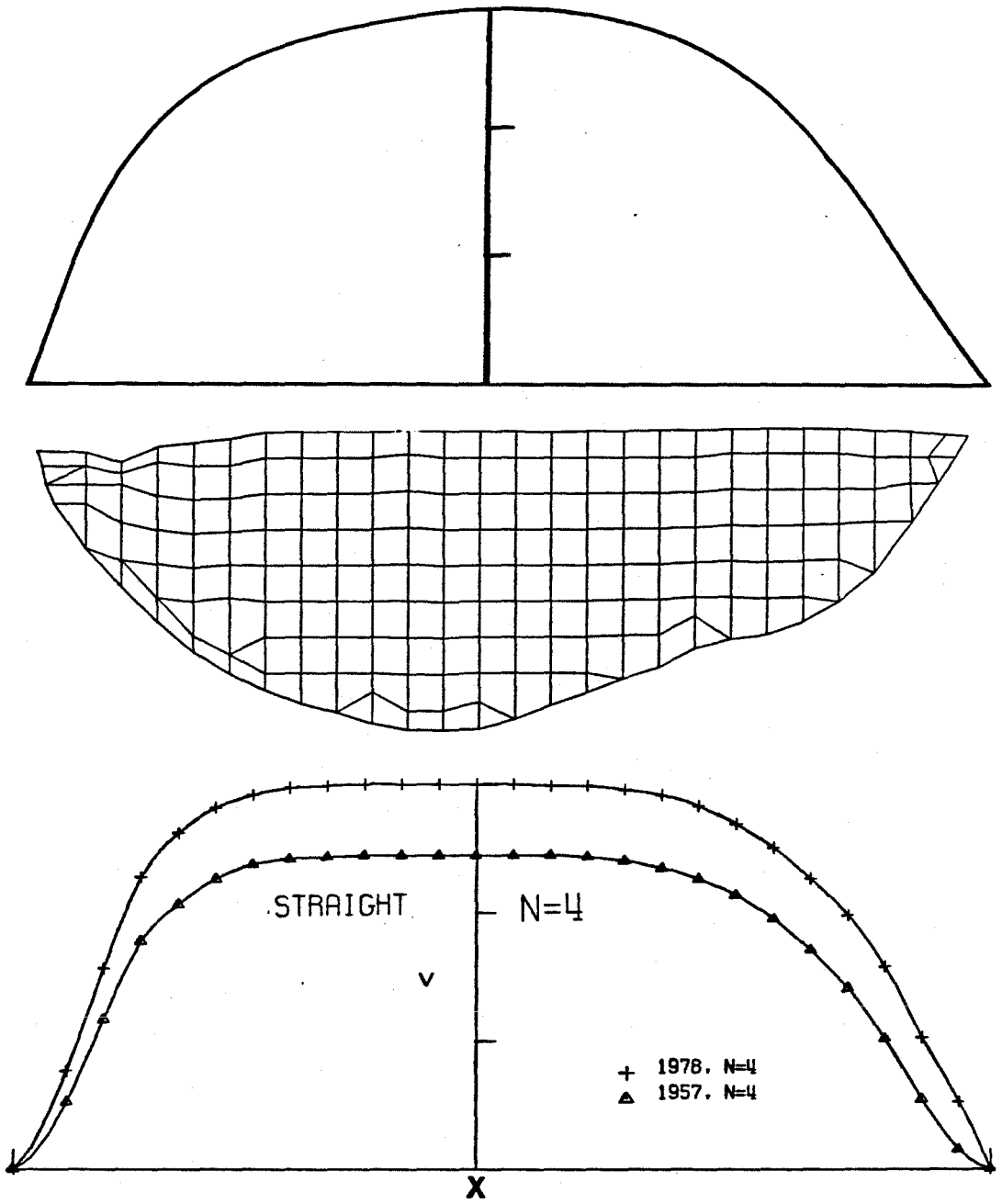

Figure 10.5 Profile D

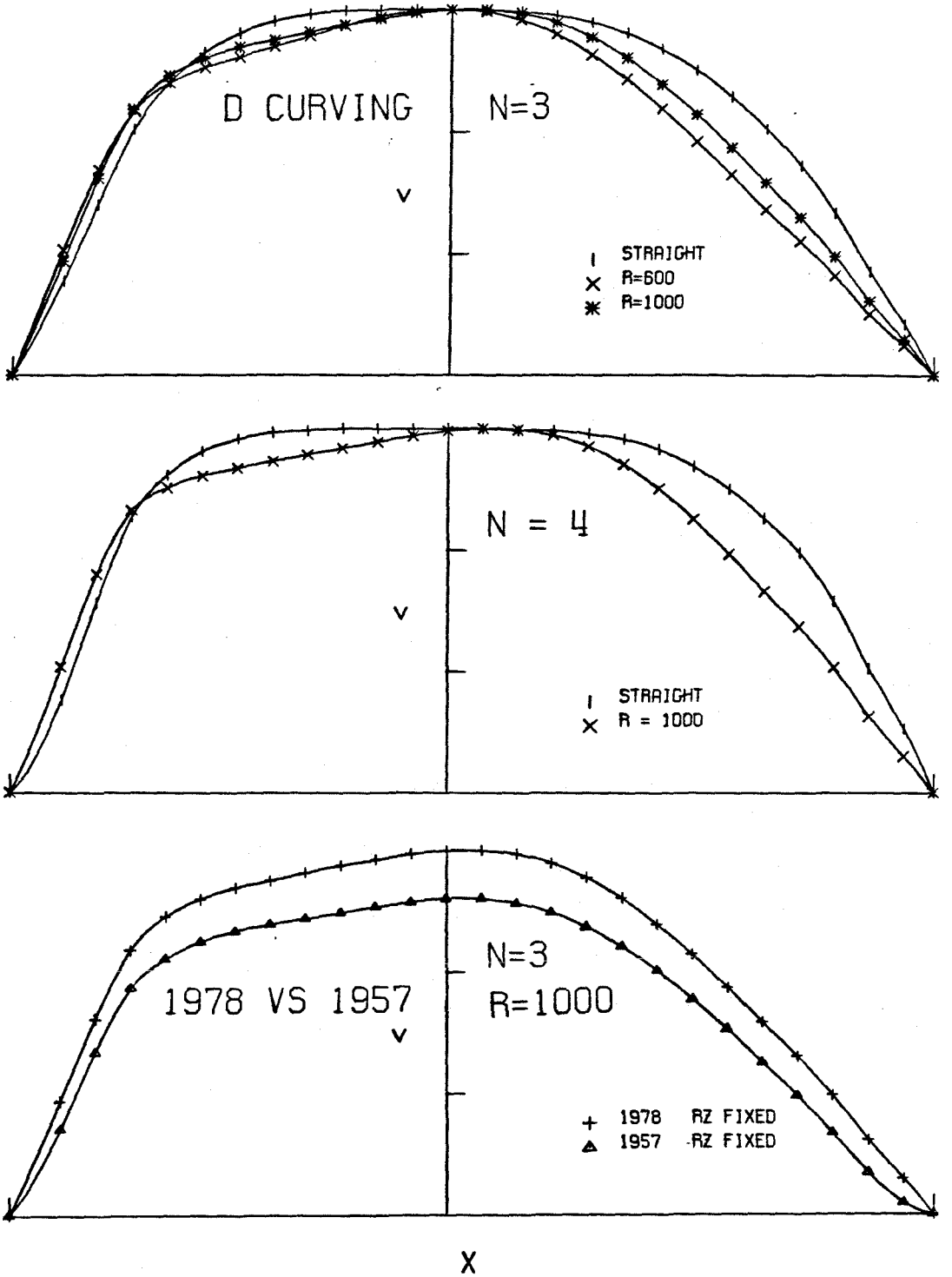

Figure 10.6 Profile D

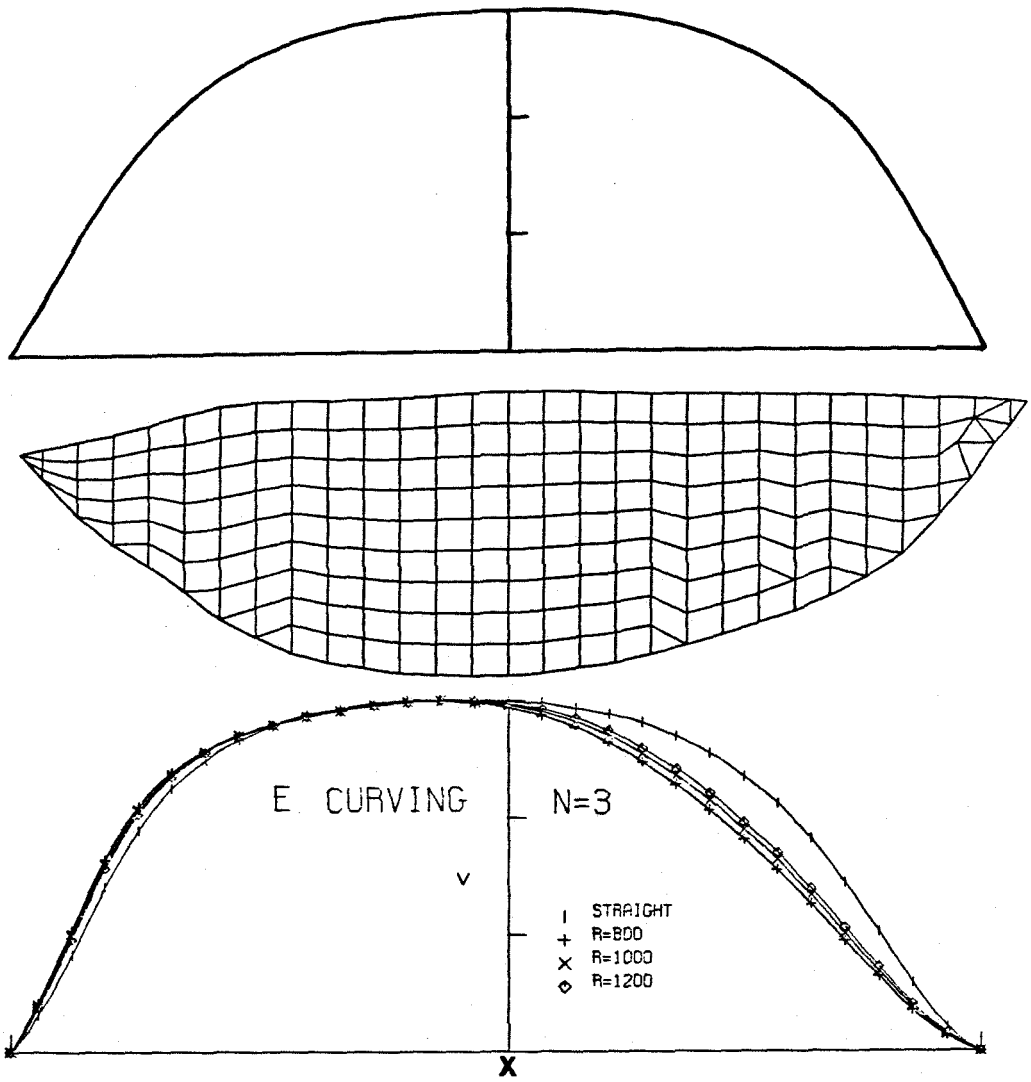

Figure 10.7 Profile E

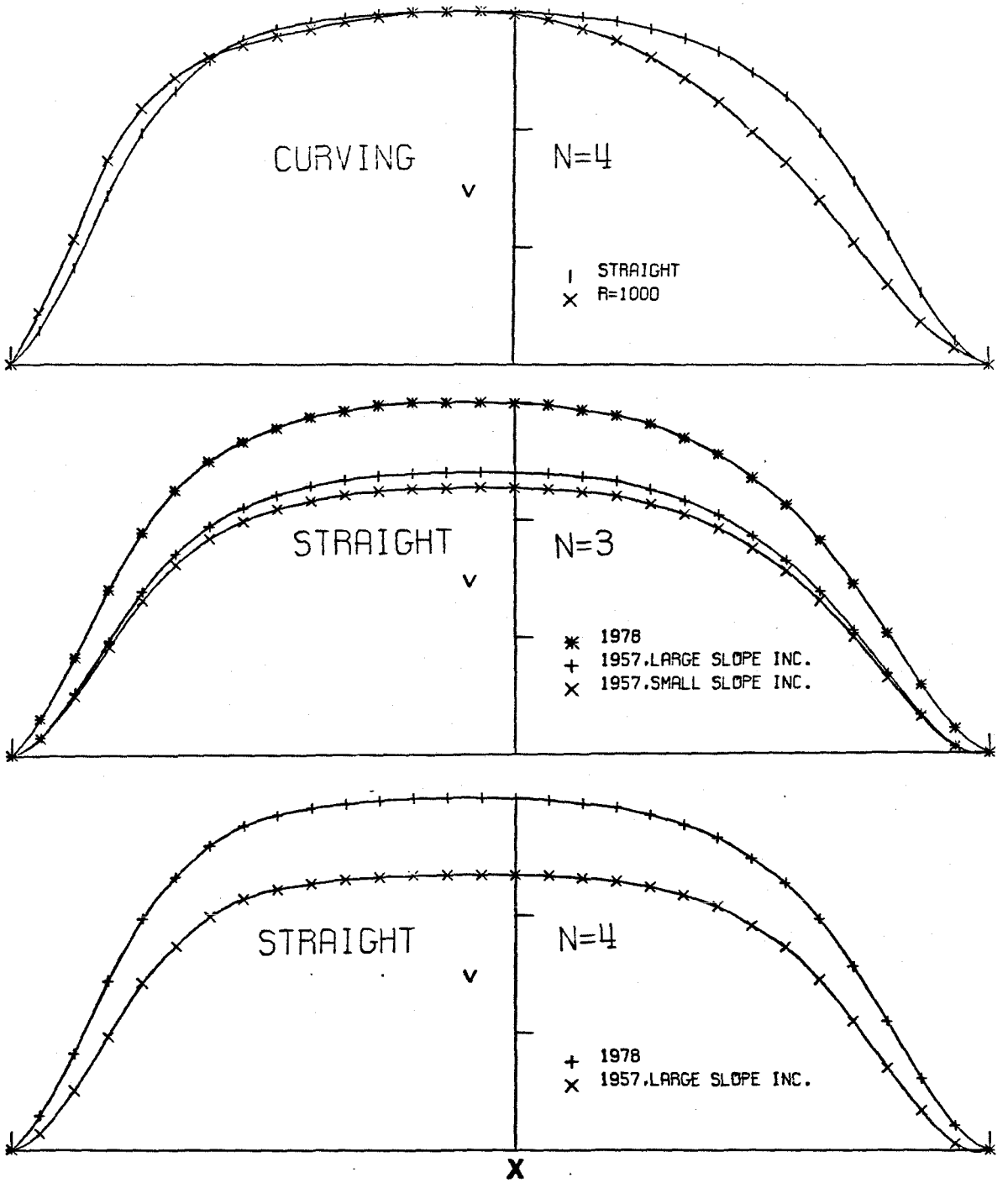

Figure 10.8 Profile E

cwrvature equal to 1000-1200m is introduced, the modelled profile better fits the data. A stress exponent of 4 to 5 gives a reasonable fit. If n=4 is used, then the model profile is in agreement with the observed data to the west of center, while it is somewhat displaced inward east of center. The opposite holds true for n=5, i.e. the model profile fits well to the east of center, but is somewhat off on the west. Thus, a mean value of n=4.5 is suggested, with R_c=1000-1200m.

Velocity changes from the model calculations agree with observations with n = 4 and $\Delta\alpha$ = 3 or with n = 5 and $\Delta\alpha$ = 4. Again, is seems that a value of n = 4.5 is indicated, with $\Delta\alpha$ = 3.5.

The flow at depth beneath the centerline is shown in Figure 10.11, and the distribution of shear stress magnitude τ in Figure 10.12. The straight-channel flow field is reasonably close to that of a symmetric parabolic channel, except near the eatern margin, where the channel shape differs significantly from a parabola. The change in the distribution of shear stress magnitude with the introduction of curvature is similar to that found for parabolic channels.

This cross section has the lowest aspect ratio of those studied (W=1.3), being relatively deep and narrow. This leads to the low value of Ψ listed in Table 10.1.

10.2.6 Profile G Channel geomtry at profile G (Fig.10.13) shows a maximum depth slightly west of the centerline and an asymmetric parabolic shape. The velocity profile has a skewed shape characteristic of flow influenced by curvature. The straight-channel model profiles shown in Fig. 10.13 thus do not agree well with the observed flow pattern. A radius of curvature equal to 1000m produces flow profiles which agree well with the observed pattern (Fig. 10.14), the curve for n=4 being the best fit.

Flow within the channel is shown in Fig. 10.14 for n = 5 and R_c = 1000m. The distribution of u (and τ) are not greatly affected by the channel asymmetry near

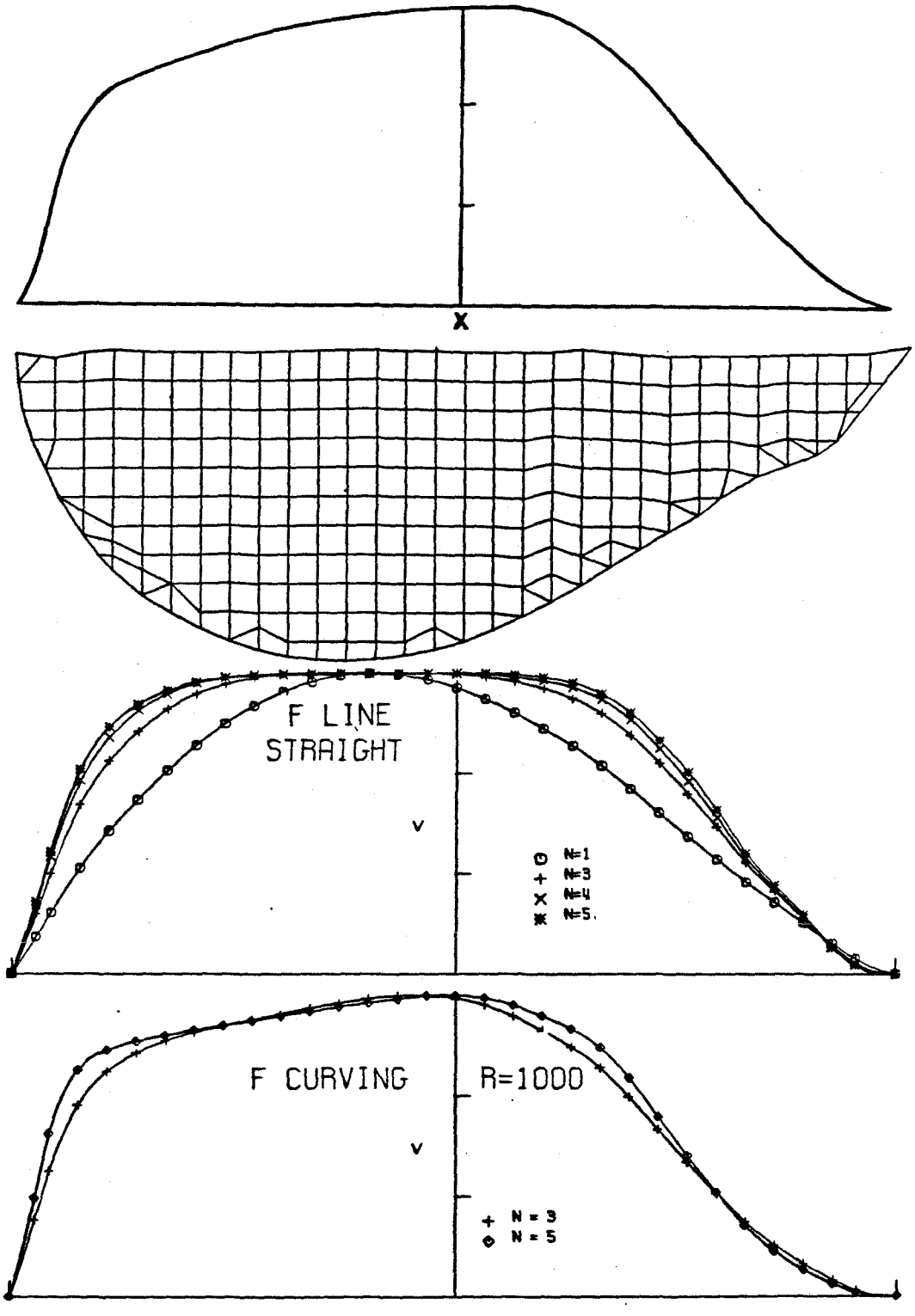

Figure 10.9 Profile F

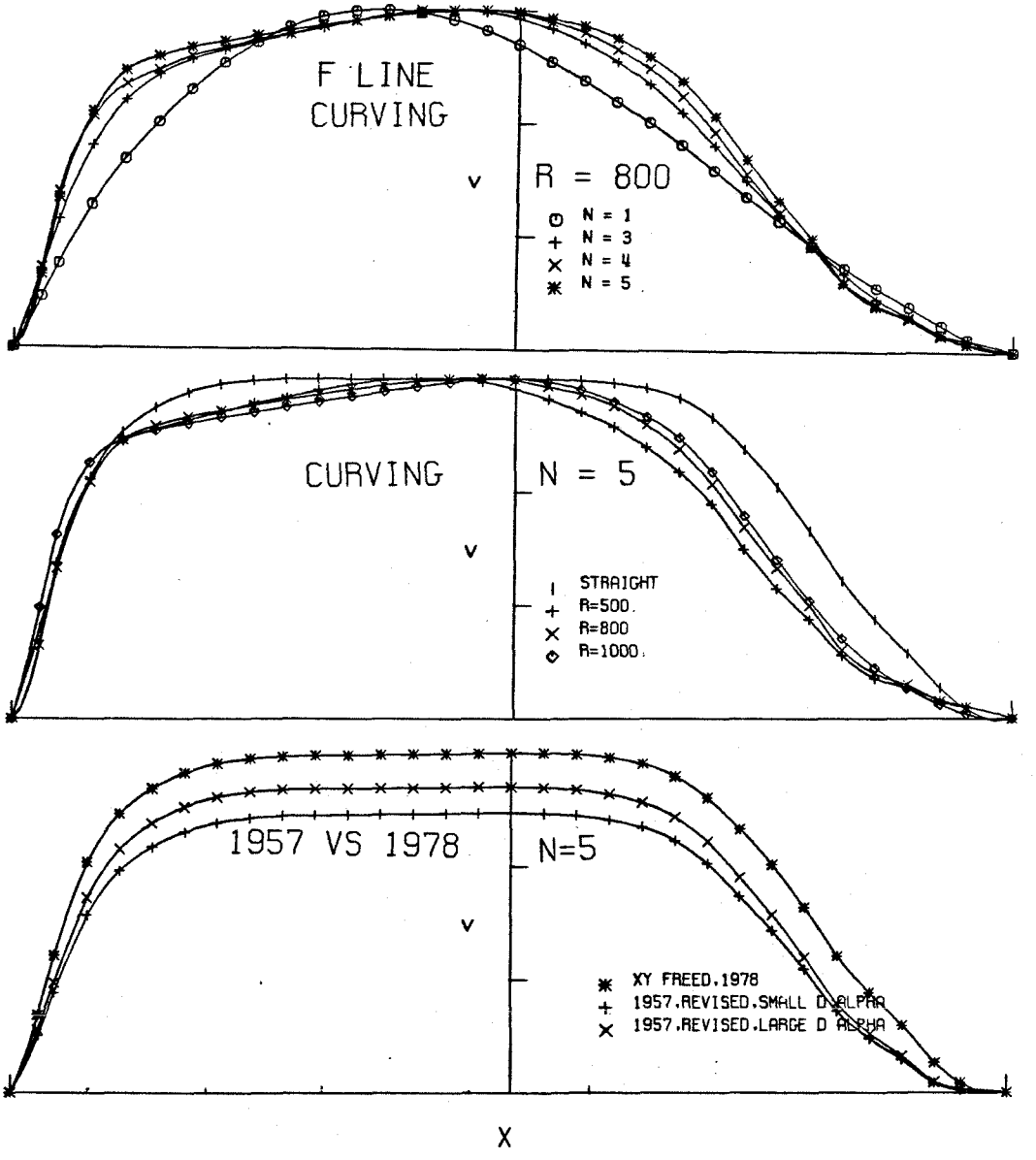

Figure 10.10 Profile F

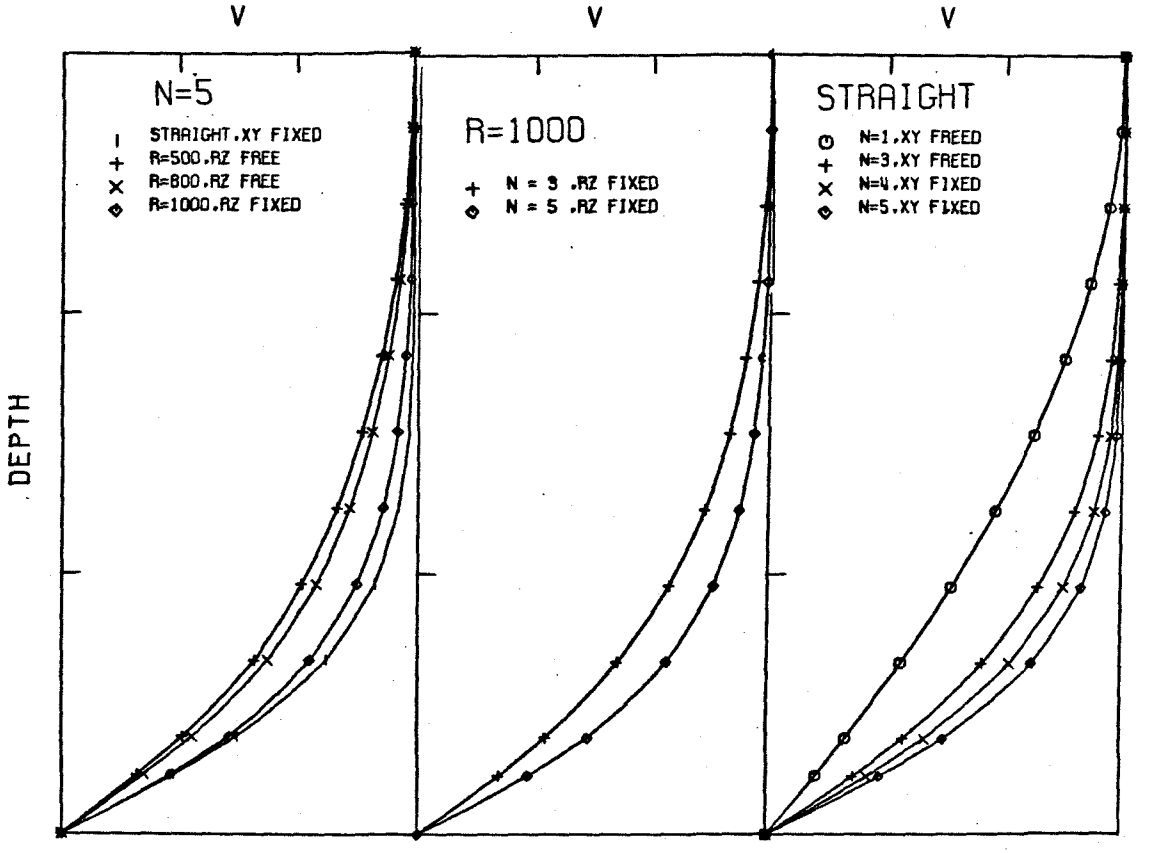

Figure 10.11 Profile F Flow at Depth

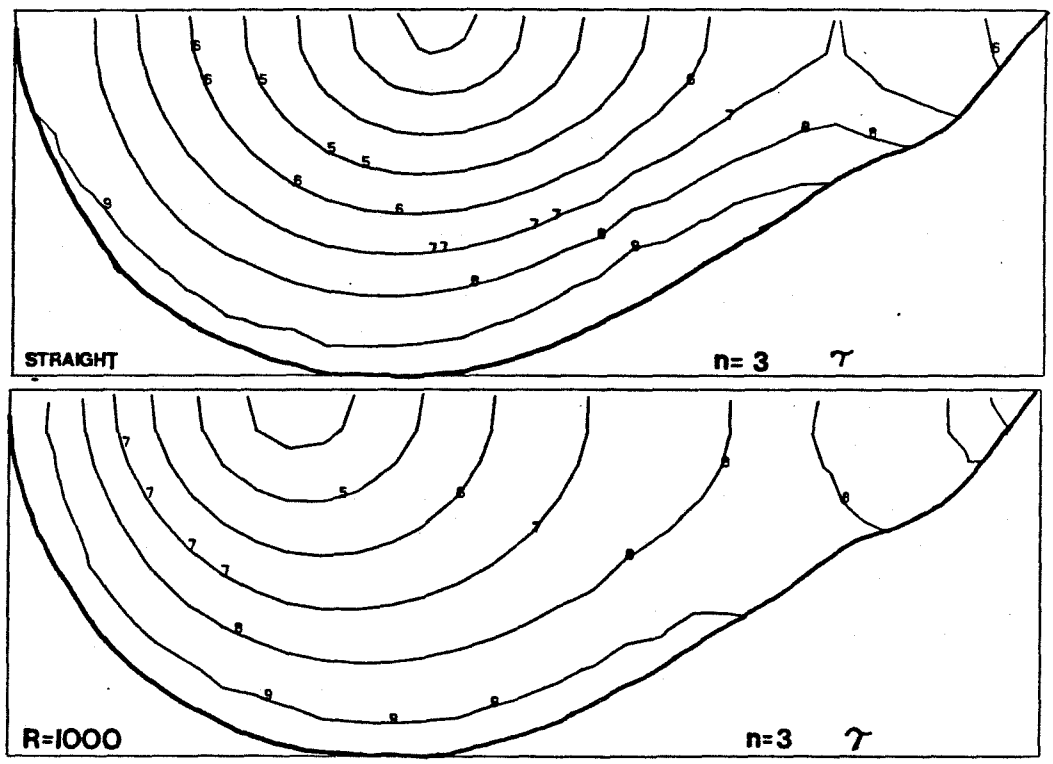

Figure 10.12 Profile F, Shear Stress

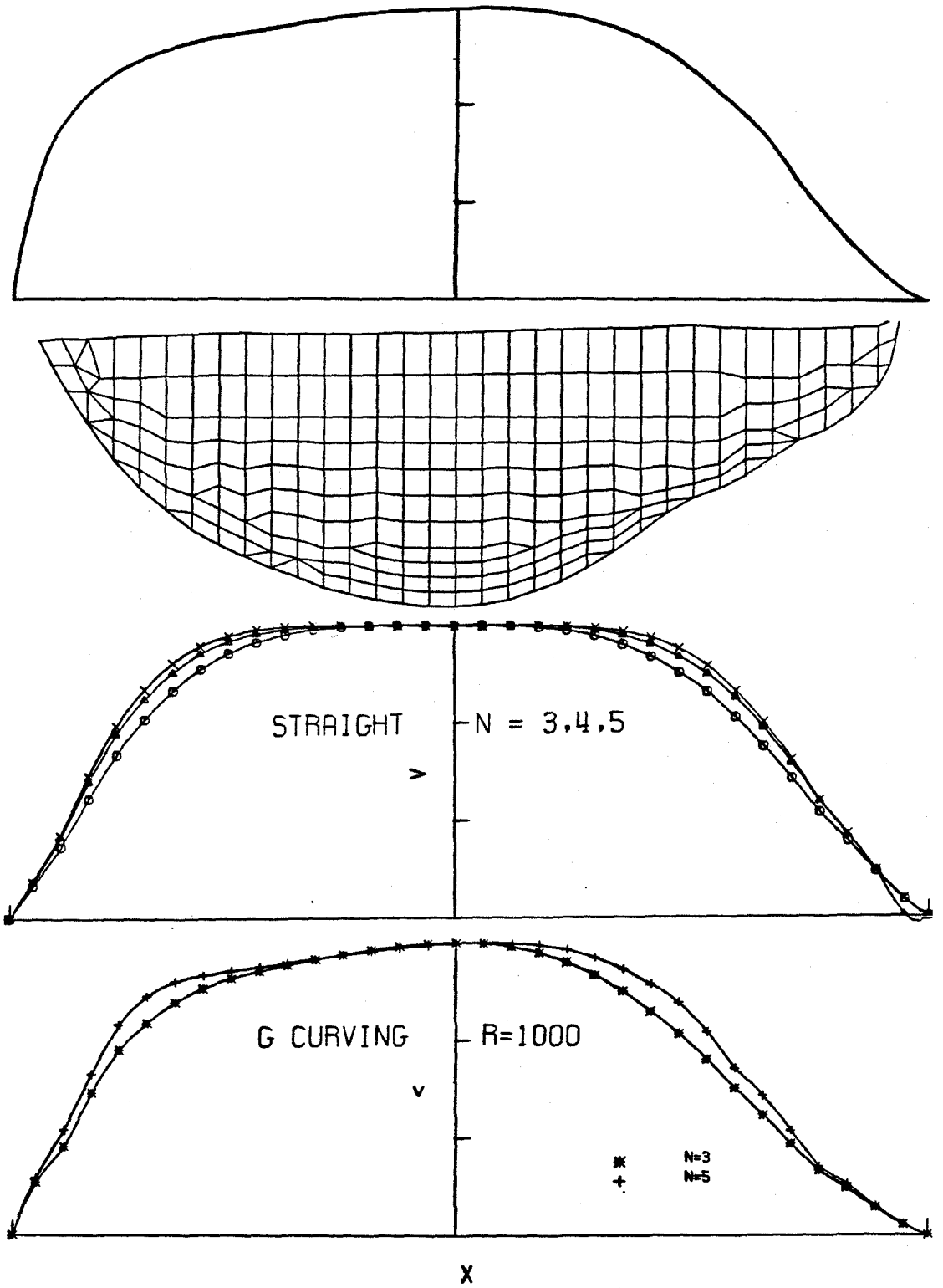

Figure 10.13 Profile G

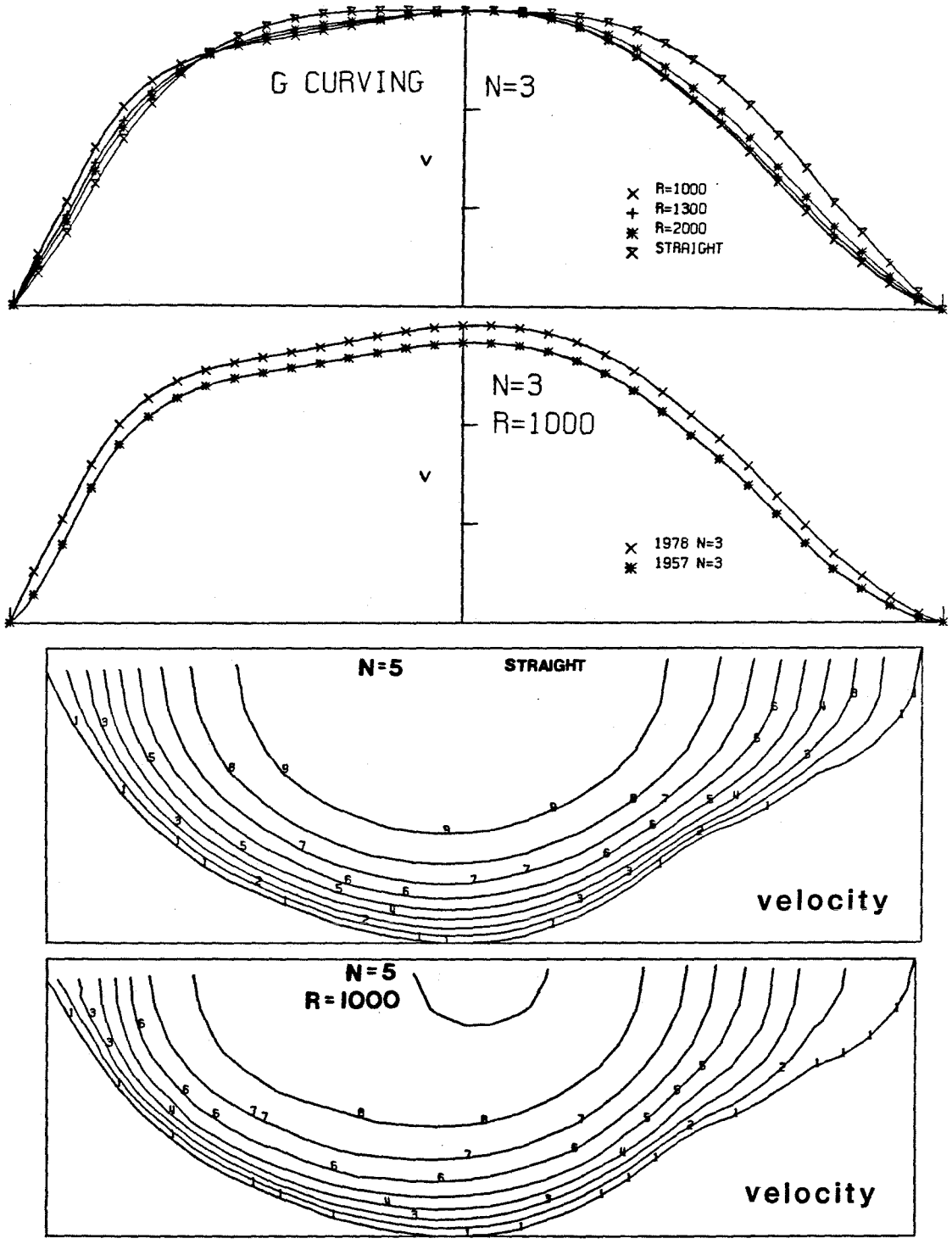

Figure 10.14 Profile G

the eastern margin.

The change in velocity is best explained by a value of n = 3.5 to 4 and $\Delta\alpha = 3$ (Table 10.2).

10.2.7 Profile H The velocity profile H is similar to that at G (Fig. 10.15). A radius of curvature equal to 1200m is required for a good correlation with the observed flow pattern. An exponent equal to 3 does not lead to a velocity profile which is steep enough near the margins,while n=4 to 5 fits nicely.

Velocity changes across profile H were relatively small, and they are best explained with n = 4 and $\Delta\alpha = 3$.

10.2.8 Profile I In addition to the effects of channel curvature, the observed velocity at profile I shows a distinct deviation from a smooth parabolic profile near both margins (Figure 10.15). The western region of the glacier is often designated the 'whaleback' because of its abrupt rise in surface level between the surface markers I4 and I1, followed by a trough closer to the margin (near IOO). The bedrock profile obtained from radio echo sounding does not show as large a bedrock feature as might be expected to explain this 'whaleback'. The model flow pattern for this cross section, with a radius of curvature equal to 1200 to 1400m and n=4,approximates the observed velocity profile reasonably well near the center of the cross section; however, as both margins are approached, the deviation between modelled flow and observed increases. The small channel irregularity to the west shown in the finite-element mesh does not significantly influence the flow within the channel (as seen in Figure 10.15), and the modelled velocity structure is different than observed. This seems to imply that the geometry of the cross section at I is not accurately represented by that shown in Fig. 10.15 near the margins. Large crevasses were present in the region near IOO to I1 when the radio echo sounding was performed, making

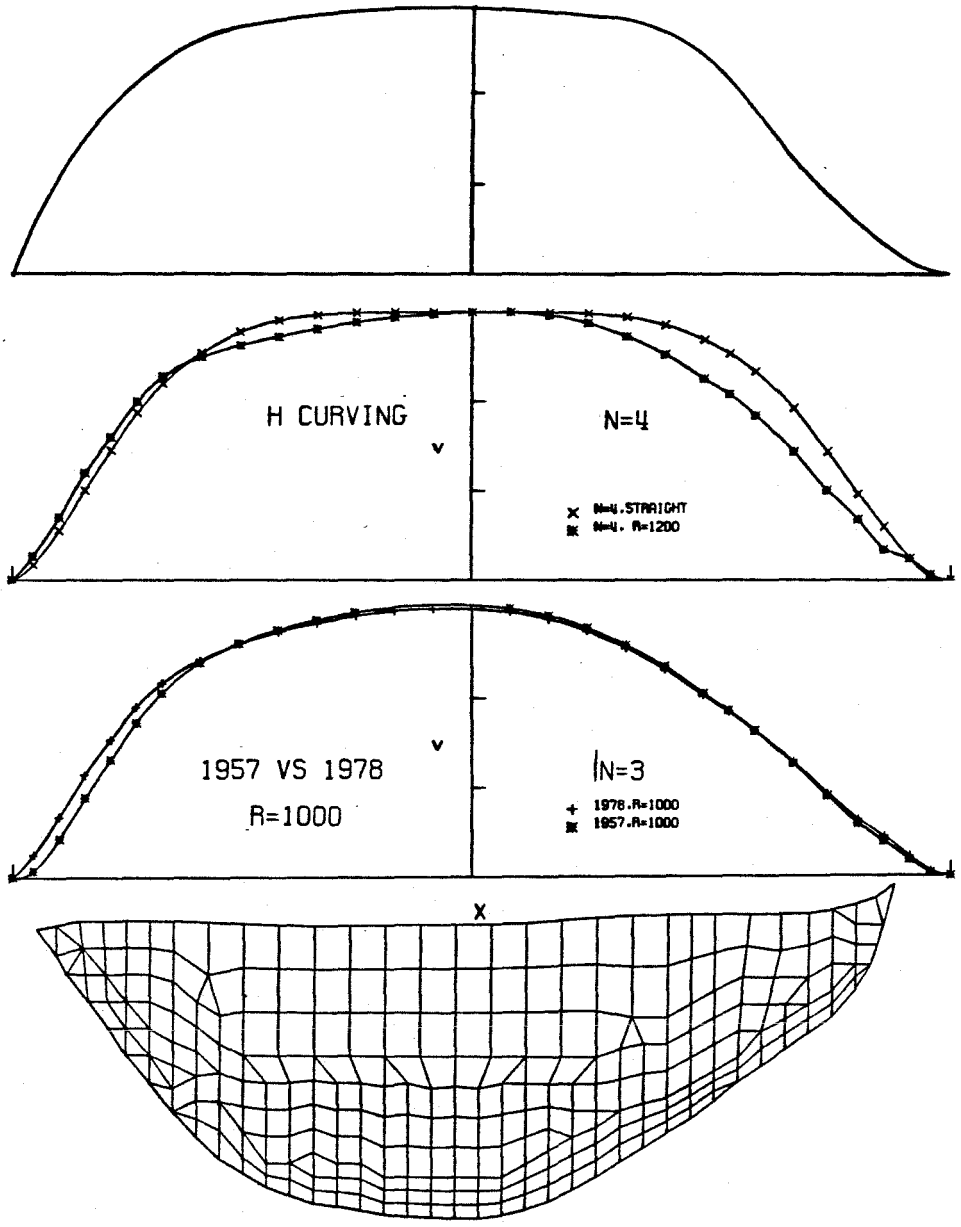

Figure 10.15 Profile H

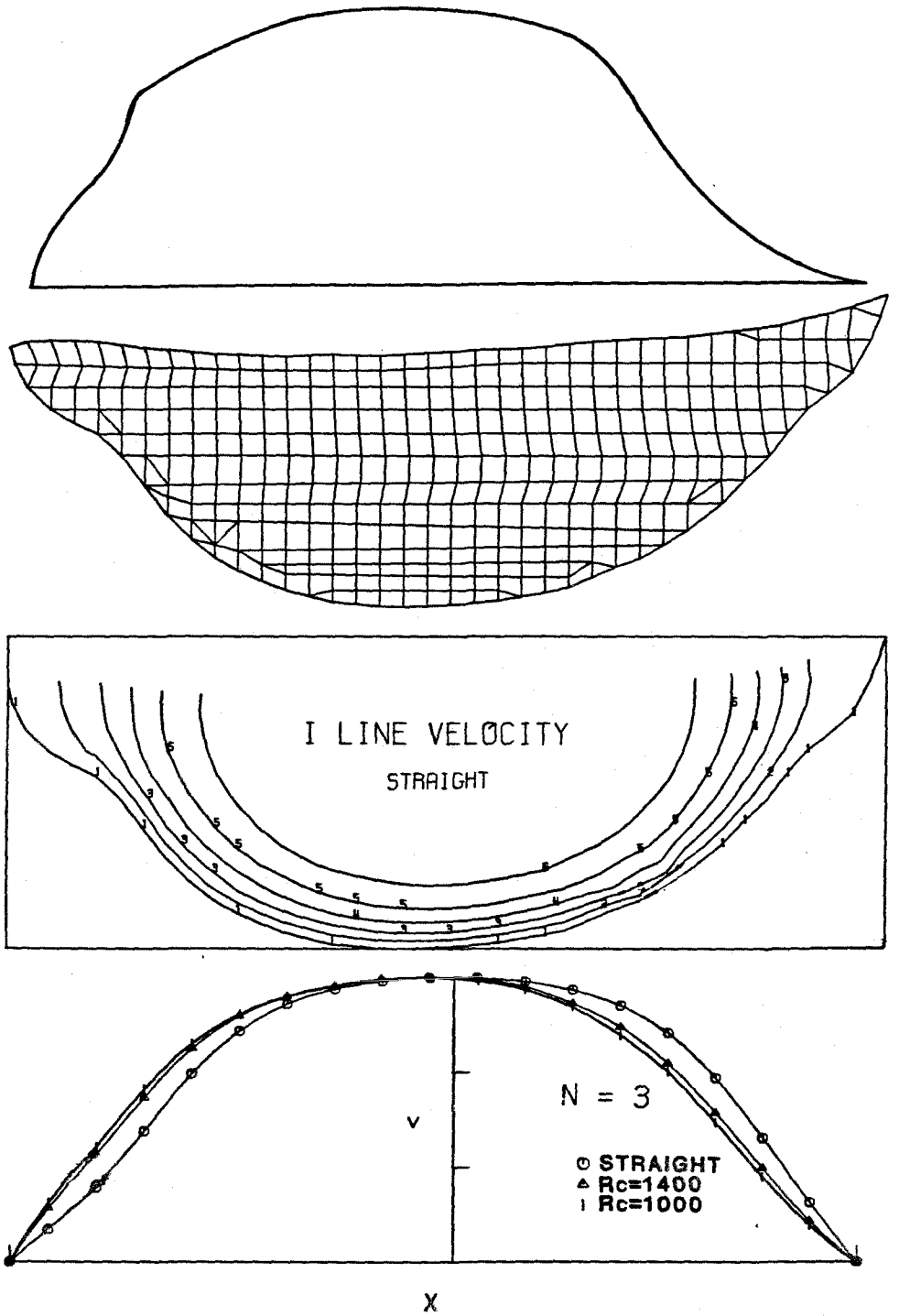

Figure 10.16 Profile I

measurements there somewhat difficult to make, and the quality of the reflections from this shallow region were not good. Thus there is a possibility that the bed is not well represented near I0. The margin of the glacier is not well defined to the east, and this poor definition probably leads to a poor cross-sectional geometry at this margin as well, the actual profile being thinner near the margin.

The change in velocity at profile I is explained by a value of n = 4 and a slope change of 3.5 (percent). (The effective radius of curvature found to fit the observed profile is slightly greater than that obtained at profiles F through H, possibly indicating a decrease in curvature, as is observed from a view of the glacier in plan view.)

10.3 Summary of Results

The results of both the comparison of the steady flow and flow response in each channel with the observations given above support a value of the stress exponent equal to 4. This agrees with that found in Chapter V and IX. The modeled change in velocity across each profile agrees with the observed response. A fairly uniform effective curvature R_c = 1000-1200 m to the center of the channel explains much of the asymmetry found in the observed velocity profiles (and the crevasse patterns), except at profiles B and E. This value of R_c agrees with the mean value of R_c as measured at each profile from a plan view map, and with the mean value as obtained from the observed slope variation across the profiles (determined from eqn. (8.9) and Figure 3.9).

The effective slope change from 1977 to 1957 varies somewhat from profile to profile (with n=4) about a mean of $\overline{\Delta\alpha} = 3.5 \pm 1$. This, again, is similar with the results of Chapters V, VI, and IX for the large-scale slope change affecting the entire reach under study.

Local discrepancies between the modeled flow and response and the observations exist within all profiles. These variations are introduced by several factors: (1) Errors in the data (Δu, Δh) exist, especially in those values enclosed in parentheses in the tables of Chapter V. (2) There will be errors in the cross-sectional geometry, particularly near the margins. Poor radio echo sounding control in these regions and inexact placement of the glacier margins along the profiles (where $u=0$) can cause large variations in the modeled flow and in the construction of the flow profiles near the margins. (3) Local variations in marginal sliding are known to exist along the glacier (sec. 4.5). Similar variations in the basal sliding velocity must exist. No slip along the ice-bedrock interface was introduced into the models, even though it does exist in places. Sliding was not introduced because its variation is not accurately known, nor can it be predicted.

The use of only integer values for the stress exponent in the models will possibly cause overall shifts in the agreement between observations and models, but it should not introduce local variations.

In addition to these local variations in the comparison between observed and modeled flow, there exists a major discrepancy at profile E. The required effective slope change along this profile is much larger than that at the other profiles and the observed flow does not appear to be influenced by the strong curvature present at E. The larger slope change is an indication that the effect of longitudinal stress gradients is larger in this region. Profile E is located at a major break in slope and there are large longitudinal strain rates in this region. These velocity gradients will give rise to a different value of the effective longitudinal viscosity, and thus the longitudinal averaging scale at E should differ from that at other profiles, as in eqn. (6.32). Relatively large sliding component exists along the western margin of profile E (in the small icefall), and it is probable

that this sliding contribution may extend well in from the margin. This high sliding rate will influence the stress distribution within the channel at E and possibly changing the effects of curvature.

The discrepancies at profile E show that large longitudinal stress gradients and possibly large contributions of basal/marginal sliding can significantly alter both the steady flow and flow response.

CHAPTER XI

CONCLUSIONS AND RECOMMENDATIONS FOR FURTHER RESEARCH

Comparison of theoretical analysis with observations of the flow response of Blue Glacier to a perturbation in slope and thickness shows that standard glacier flow theory can explain the observed flow response in detail. Within this theory, the use of a simple power-law-type constitutive relation for ice is adequate for determining that part of the motion of a glacier which is due to internal deformation.

Observed velocity changes Δu along the centerline of the glacier over the period 1957 to 1980 show a good logarithmic correlation with the measured local thickness change ΔH (ChapterV). On the other hand, variations in the local slope $\Delta\alpha$ do not correlate well with the velocity change. The slope of the best-fit line between Δu and ΔH does not go through the origin; the negative intercept indicates a negative change in velocity for zero thickness change. If data from points off the centerline is included in the regression analysis, the correlation is somewhat poorer and the slope of the regression line is reduced from the centerline-only data.

A simple model of the flow response in an ice slab shows that the logarithmic velocity change should be linearly related to logarithmic perturbations in ice thickness and surface slope (Chapter V). Analytical and numerical results indicate that this linear relationship holds for more complex (and realistic) geometries (Chapter IX). The relation between the changes in slope α, thickness H, and surface velocity u is

$$\log\left[\frac{u_1}{u_o}\right] = \Psi\,(n+1)\log\left[\frac{H_1}{H_o}\right] + n\log\left[\frac{\alpha_1}{\alpha_o}\right] \qquad (11.1)$$

where Ψ is termed the response factor. For realistic channel geometries, Ψ is in

the range 1/2 to 1. This factor represents the change in cross-sectional shape of an ice mass which accompanies a change in ice thickness within a given channel. If Ψ differs from unity, then the flow-law exponent n inferred from a study of the type presented here will differ significantly from the value obtained from the simple slab model. The value of Ψ corresponding to the mean cross-sectional profile of Blue Glacier is 0.82 $\pm$ 0.02. From the slope of the the Δu vs. ΔH line which fits the observed data, the stress exponent is found to be $n=4.0 \pm 0.4$ This value of n is well within the range of values found from borehole studies and laboratory experiments on polycrystalline ice. With the value of n=4.0, the negative intercept of the response line corresponds to an overall slope decrease, affecting the entire reach under study, of $\Delta\alpha$ =-3.5% between 1957 and 1977.

Longitudinal stress gradients caused by longitudinal variations in thickness and slope (ChapterVI) explain much of the deviation of the observed flow from the model leading to eqn.(11.1). Through a perturbation analysis of the vertically integrated equilibrium equations that describe the force balance within the glacier, we find that variations in surface slope and ice thickness about their initial (or mean) should be longitudinally averaged up and down glacier, with an exponential weighting function which has a characteristic length equal to approximately 3 to 4 times the ice thickness. The characteristic length is dependent upon the longitudinal strain rate, the flow law parameters, the amount of basal sliding. If there is a difference between the surface and bed slopes, then the characteristic length will be different for the up-glacier and down-glacier directions. This longitudinal averaging describes how an effective surface slope should be calculated from slope and thickness measurements on a glacier in order to account for the effects of longitudinal stress gradients. In combination with the local ice thickness and channel shape, this effective slope provides the necessary geometrical factors which govern glacier flow. The dependence of the

averaging process on the flow-law parameters shows that a knowledge of these parameters is required before an accurate assessment of the effects of longitudinal stress gradients can be made.

To apply these ideas to the Blue Glacier data the exponential averaging window was approximated by a triangular weighting function with base equal to approximately 6 times the thickness. The results of this averaging produced a significant increase in the correlation between the centerline thickness and slope changes and the velocity change. This shows that longitudinal averaging of slope and thickness variations in the manner developed in Chapter VI provides a useful means of including the effects of longitudinal stress gradients.

Numerical analysis of the flow of ice in channels (Chapter VIII) shows that, again, the stress distribution within a glacier is dependent upon the flow law parameters. The shear stress across horizontal planes in a glacier is approximately linear with depth beneath the centerline of most realistic channels, but its dependency upon n gives rise to a flow-law-dependent effective shape factor. This may cause the stress level to be overestimated at depth, and may possibly explain the discrepancy between flow law parameters obtained from laboratory measurements and borehole studies, as explained by Hooke (1981).

Longitudinal curvature of a glacier channel introduces important effects in the distribution of stress and velocity within the ice mass. These effects are strongly exhibited in the velocity profiles, crevasse patterns and climbing routes on Blue Glacier. An 'axisymmetric' finite-element technique (developed in Chapter VII,sec.7.12.3) and a relatively simple analytical model (sec. 8.5.2) show that the stress centerline is shifted toward the inside of the bend when curvature is introduced, the shift being greater for sharper bends. The position of the velocity maximum is also shifted from the channel centerline by channel curva-

ture, but the direction and magnitude of the shift is dependent on the stress exponent n, the channel geometry, and the radius of curvature.

Additional features in the velocity field are introduced by transverse convexity or concavity of the glacier surface. The quasi-three-dimensional out-of-plane finite element technique introduced in Chapter VII allows a full treatment of this flow problem. We find that much of the splaying of velocity vectors commonly found in the ablation zone of a glacier (or, conversely, the convergence of flow commonly found in accumulation zones) is related to the convex (or concave) upper surface, which provides an effective 'spreading' force.

Spatial variation in the viscosity factor within a glacier can lead to flow profiles at depth and across the surface which are similar to those obtained with an altered stress exponent and a constant viscosity factor. This implies that data from a single borehole deformation study cannot accurately distinguish between a suite of models describing the flow law parameters within a glacier. On the other hand, the study of the flow response to a change in geometry (such as that described herein) can possibly reduce some of this non-uniqueness by eliminating those models which require a stress exponent which is unacceptably large. (Introduction of a spatial variation in the viscosity factor in the flow law increases the value of n inferred from the flow response above that inferred if the viscosity facor is a constant.)

Comparison of the velocity distribution obtained from models of flow within the various cross sections of Blue Glacier (as obtained from the radio-echo-sounding results in Chapter III) with the observed profiles of surface velocity demonstrates that most details of the observed flow can be reasonably accounted for by the model calculations with n=4 in the flow law and no sliding at the bed or margins. The longitudinal curvature of the valley was found to be

very important in producing an accurate model of the flow.

Models of flow in the channels of Blue Glacier with the ice depth as it was in 1957 and in 1977 allow a comparison of the observed flow response with model calculations. Reasonable agreement can be obtained at all points with a flow law exponent n = 4. An effective overall slope change (decrease) of approximately 3% is inferred from the comparison. This slope change agrees well with the observed decrease in slope from 1957 to 1977 over the reach studied, and with that found from the intercept of the response curve.

In terms of the flow law of ice, all results of this study indicate that, within Blue Glacier, ice deforms as a non-linear fluid which obeys a power-law creep relation with n=4 at the stress levels involved.

Seasonal velocity variations indicate a difference between winter and summer sliding of less than 10%. The numerical flow models, in which zero basal slip was prescribed, show a good correlation with the observed flow patterns at most locations on the glacier. Combined with data from borehole deformation studies and borehole photography, these results indicate that basal sliding contributes at most 10% to the overall motion of lower Blue Glacier.

If proper account is taken of ice thickness *and* slope changes, the flow response of Mer de Glace can be explained by standard glacier-flow concepts applied via the theory developed here. It is not necessary to postulate the existence of 'controlling zones' (Lliboutry and Reynaud,1981) to explain the observed response of this glacier.

The results of the numerical models in the present study show that finite-element methods provide a versatile tool for the calculation of glacier flow within complex geometries. Material properties, effective body forces, and

boundary conditions may be easily varied to fit different needs. The development of the out-of-plane and 'axisymmetric' out-of-plane elements has made it possible to model geometrical situations more complex than the usual plane strain geometry. An important extension of the present study would be a fully three-dimensional finite-element analysis of the flow in the curving channel models would allow a complete incorporation of longitudinal stress gradients, perhaps leading to an explanation of the peculiar behavior observed at profile E, where it is believed that these stress gradient effects are important (as well as basal sliding), and where the out-of-plane formulation seems to be inadequate. Additional numerical studies should be made of the role of basal sliding in determining the stress and velocity distribution in a glacier, both within a cross-section and three-dimensionaly. A longitudinal model of the glacier along the central streamline would supplement the discussion of Chapter VI on the longitudinal averaging of slope and thickness.

The data set acquired during the course of this study (as described in Chapters II and III) provides an excellent data base for the detection of travelling waves of increased thickness and speed, which may have accompanied the change in climate that caused the observed changes in ice thickness and surface slope. The fact that the terminus is still advancing while much of the glacier is slowing down (Figures 4.3-4.11) shows that such waves may exist. The parameters required for a complete discussion of travelling waves on glaciers (as defined by Nye,1960,1963; and Hutter,1980) involve the change in velocity with thickness and slope. Explicit values of $\frac{\partial u}{\partial H}$ and $\frac{\partial u}{\partial \alpha}$ have been evaluated in this thesis, which, when combined with the data on motion and elevation of the surface markers, can perhaps lead to a better understanding of these transient features of the flow response of a glacier to changing climate.

The results of the present study will thus help establish the principles in the theory of glacier response to climatic change, which have a broad range of application.

The detailed response characteristics of the non-surging Blue Glacier will provide an important standard against which to compare and interpret the response characteristics of surging glaciers, such as Variegated Glacier, Alaska which is presently under study (Bindschadler and others,1977; Kamb,et al. 1982).

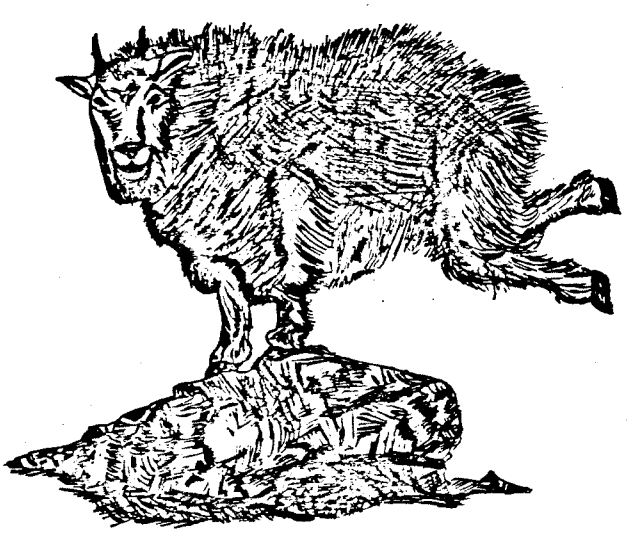

whee!

REFERENCES

Allan, A.L., J.R. Hollwey, and J.B. Maynes (1968). Practical Field Surveying and Computation. American Elsevier Pub. Co., N.Y., 689 pp.

Allen, C.R. et al.(1960)., with W.B. Kamb, M.F. Meier and R.P. Sharp. Structure of the lower Blue Glacier, Washington. *J. Geol.*, 68, 601-625.

Annan, A.P. (1973). Radio interferometry depth sounding: part I Theoretical discussion.*Geophys.*,38,557-580.

Astarita, G. and G. Marrucci (1974). Principles of Non-Newtonian Fluid Mechanics, McGraw-Hill, London, 289 pp.

Baker, R.W. (1978). The influence of ice-crystal size on creep. *J. Glaciol.*, 21, 485-497.

Baker, R.W. and W. Gerberich (1979). Effect of crystal size and dispersed solid inclusions on activation energy for the creep of ice. *J. Glaciol.*, 24, pp. 179-94.

Barnes, P., D. Tabor, and J.C.F. Walker (1971). The friction and creep of polycrystalline ice. *Proc. Roy. Soc. London, Ser. A, 324*, pp. 127-155.

Becker,E., G.Carey, and J.T.Oden(1981). Finite Elements - An Introduction. Prentice Hall, N.J. , 258 pp.

Berry, M.V. (1973). The statistical properties of echoes diffracted from rough surfaces. *Phil. Trans. R. Soc. London*, Ser. A, 273, 611-654.

Berry, M.V. (1975). Theory of radio echoes from glacier beds. *J. Glaciol.*, 15, 65-74.

Bindschadler, R. et al.(1977)., with W.D. Harrison, C.F. Raymond and R. Crosson. Geometry and dynamics of a surge-type glacier. *J. Glaciol.*, 18, 181-194.

Budd, W.F. (1968). The longitudinal velocity profile of large ice masses. *IASH*, 79, 58-75.

Budd, W.F. (1970). The longitudinal stress and strain-rate gradients in ice masses. *J. Glaciol.*, 9, No. 55, 19-27.

Budd, W.F. and D. Jenssen (1975). Numerical modelling of glacier systems. *IASH*, 104, 257-291.

Budd, W.F. and U. Radok (1971). Glaciers and other large ice masses. *Reports on Progress in Physics*, 34, 1-70.

Bull, C. and J.R. Hardy (1956). Determination of the thickness of ice of a glacier from measurements of the value of gravity. *J. Glaciol.*, 2, 755-63.

Cohen, S.C. (1981). A multilayer model of time dependent deformation following an earthquake on a strike-slip fault. NASA Technical Memorandum 82174, NASA Goddard Space Flight Center, Greenbelt, Maryland.

Collins, I.F. (1968). On the use of the equilibrium equations and flow law of ice relating surface and bad topography of glaciers and ice sheets. *J. Glaciol.*, 7, 199-204.

Corbató, C.E. 1965. Thickness and basal configuration of lower Blue Glacier, Washington, determined by gravimetry. *J. Glaciol.*,5, 637-50.

Cormeau, I.C., (1975). Numerical stability in quasi-static elasto/viscoplasticity. *Int. J. Numer. Mech. Engng.*, 9, pp. 109-127.

Duval, P. (1977). The role of water content on the creep of polycrystalline ice. *IASH-AISH Publ.*, 118, 29-33.

Duval, P. (1981). Creep and fabrics of polycrystalline ice under shear and compression. *J. Glaciol.*, 27, 129-140.

Duval, P. and H. Le Gac (1980). Does the permanent creep rate of polycrystalline ice increase with grain size? *J. Glaciol.* 25, 151-157.

Echelmeyer, K. (1971). Unpublished. Study of the radiation balance on Arikaree Glacier.

Engelhardt, H.F., (1978). Water in glaciers: Observations and theory of the behaviour of water levels in boreholes.*Ziet. Gletsch. Glacial.*, 14, 35-60.

Engelhardt, H.F., W.D. Harrison and B. Kamb (1978). Basal sliding and conditions at the glacier bed as revealed by borehole photography. *J. Glaciol.*, 20, 469-508.

Fowler, A. and D.A. Larson (1978). On the flow of polythermal glaciers: I. Model and preliminary analysis. *Proc. Roy. Soc. London* A 363, 217-242.

Glen, J.W. (1955). The creep of polycrystalline ice. *Proc. R. Soc. London*, Ser. A., 228, 519-538.

Glen, J.W. (1958). The flow law of ice. A discussion of the assumptions made in glacier theory, their experimental foundations and consequences. *IASH*, 47, 171-183.

Glen, J.W., and Lewis, W.V. (1961). Measurements of side-slip at Austerdalsbreen, 1959. *J.Glaciol.*, 3, 1109-22.

Glen, J.W. (1975). The mechanics of ice. *In T.C. Johnson (Ed.) Cold Regions Science and Engineering, Part II-C2b.* CRREL, Hanover, New Hampshire, U.S.A.

Goodman, M., H.J. Frost, M.F. Ashby(1977). The effects of dissolved impurities on creep of ice Ih and its illustration by the construction of deformation maps. *IASH-AISH Publ.*, 118, 48-77.

Green, A. and Rivlin, R. (1956). Steady flow of non-Newtonian fluids through tubes. *Quart. Appl. Math.*, 14, pp. 299-308.

Gudmanson, P. (1971). Electromagnetic probing of ice. *In Electromagnetic Probing in Geophysics*, J.R. Wait, editor, Golem Press, Boulder, Colorado. 321-348.

Harrison, C.H. (1970). Reconstruction of subglacial relief from radio echo sounding records. *Geophysics*, 35, 1099-1115.

Harrison, W.D. (1972). Temperature of a temperate glacier. *J. Glaciol.*, 11, 15-29.

Harrison, W.D. (1975). A measurement of surface-perpendicular strain-rate in a glacier. *J. Glaciol.*, 14, 31-37.

Harrison, W.D. et al. (1978) with P.McKeith and Sue Fergason. Magnetic Markers for Glacier Mass Balance and Velocity Measurements. *Univ. Alaska Geophysical Institute Publication* UAG-R-259.

Hauser, C.J. (1957). Variations of Blue, Hoh?, and white glaciers during recent centuries. *Arctic*, 10, 139-150.

Hodge, S.M. (1972). The movement and basal sliding of the Nisqually Glacier, Mt. Rainier. *University of Washington, Department of Atmospheric Sciences, Scientific Report*, 13, Seattle, Washington, U.S.A.

Hodge, S.M. (1974). Variations in the sliding of a temperate glacier. *J. Glaciol.*, 13, 349-369.

Hodge, S.M. (1971). A new version of a steam operated ice drill. *J. Glaciol.* 10, 387-393.

Hooke, R.L., B.B. Dahlin and M.T. Kauper (1972). Creep of ice containing dispersed fine sand. *J. Glaciol.*, 11, 327-336.

Hooke, R.L., C.F. Raymond, R.L. Hotchkiss and R.J. Gustafson (1979). Calculations of velocity and temperature in a polar glacier using the finite element method. *J. Glaciol.*, 24, 131-146.

Hooke, R.L. (1981). Flow law of polycrystalline Ice in Glaciers: Comparison of theoretical predictions, laboratory data, and field observations. *Rev. Geophys. Space Phys.*, 19, 664-672

Hooke, R.L., et al. (1980). Mechanical Properties of polycrystalline ice: An assessment of current knowledge and priorities for future research. *Cold Regions Sci. Technol.* 3, 263-275.

Hubley, R.C. (1956). Glaciers of the Washington Cascade and Olympic Mountains, their present activity and its relation to local climatic trends. *J. Glaciol.*, 2, 669-674.

Hughes T.J.R., and R.L. Taylor (1978). Unconditionally stable algorithms for quasi-static elasto/visco-plastic finite element analysis. *Computers & Structures*, Vol. 8, pp. 169-173.

Hughes, T.J.R., W.K. Liu, A. Brooks (1979). Finite element analysis of incompressible viscous flows by the penalty function formulaion. *J. Comp. Phys.* 30, 1-60.

Hutter, K. (1980). Time dependent surface elevation of an Ice Slope. *J. Glaciol.*, 25, 247-266.

Hutter, K. (1981). The effect of longitudinal strain on the shear stress of an ice sheet: In defence of using streched coordinates. *J. Glaciol.*, 27, 39-56.

Hutter, K. et al. (1981). First order stresses and deformation in glaciers and ice sheets. *J. Glac*, 27, 227-270.

Iken, A. (1978). Variations of surface velocities of some alpine glaciers measured at intervals of a few hours. Comparison with arctic glaciers. *Z. Gletscherkd. Glazialgeol.*, 13, 23-35.

Iken, A. (1981). Effect of subglacial water pressure on sliding of a glacier in an idealized numerical model. *J. Glaciol.*, 27, 407-422.

Jackson, J.P. (1975). Classical Electrodynamics. 2nd Edition, Wiley, N.Y., 848 pp.

Jones, S.J. and J.W. Glen (1969). Effect of dissolved impurities on the mechanical properties of ice crystals. *Philos. Mag.* 19, 13-24.

Jones, S.J. and J.-G. Brunet (1978). Deformation of ice single crystals close to the melting point. *J. Glaciol.*, 21, 445-454.

Kamb, B. (1959). Ice petrofabric observations from Blue Glacier, Was. in relation to theory and experiment. *JGR*, 64, pp. 1891-1909.

Kamb, B. (1970). Sliding motion of glaciers: theory and observation. *Rev. Geophys. Space Phys.*, 8, 673-728.

Kamb, B. (1972). Experimental recrystallization of ice under stress. *Geophys. Monogr. Am. Geophys. Union*, 18, 211-241.

Kamb, B. and E.R. LaChapelle (1964). Direct observation of the mechanism of glacier sliding over bedrock. *J. Glaciol.*, 5, 159-172.

Kamb, B. and R.L. Shreve (1963). Texture and fabric of ice at depth in a temperate glacier. *Trans. Am. Geophys. Union*, 44, 103. (Abstract)

Kamb, B., H.F. Engelhardt and W.D. Harrison (1979). The ice-rock interface and basal sliding process as revealed by direct observation in bore holes and tunnels. *J. Glaciol.*, 23, 416-419. (Abstract)

Kamb, B., et al. (1982). Initiation of a glacier surge, and abort. *AGU Annual Meeting (S.F., CA).* (Abstract only.)

LaChapelle, E.R. (1959). Annual mass and energy exchange on the Blue Glacier. *J. Geophys. Res.*, 64, 443-49.

LaChapelle, E.R. (1965). Mass budget of Blue Glacier, Wash. *J. Glaciol.* 5, 609-623.

Lighthill, M.J. and G.B. Whitham (1955). On kinematic waves. *Proc. R. Soc. London*, Ser. A, 229, 281-345.

Lliboutry, L. (1968). General theory of subglacial cavitation and sliding of temperate glaciers. *J. Glaciol.*, 7, 21-58.

Lliboutry, L. (1961). Measurement of firn deformation by a magnetic prospecting method. *J. Glaciol.* 3, 879-881.

Lliboutry, L. and L. Reynaud (1981). "Global Dynamics" of a temperate valley glacier, Mer de Glace, and past velocities from Forbe's bands. *J. Glaciol.* 27, 207-227.

Mathews, W.H. (1977). Relocation of buried markers. *J. Glaciol.* 18, 150-151.

Meier, M.F. (1960). Mode of flow of Saskatchewan Glacier, Alberta, Canada. *U.S. Geol. Surv. Prof. Paper*, #351.

Meier, M.F., B. Kamb, C.R. Allen and R.P. Sharp (1974). Flow of Blue Glacier, Olympic Mountains, Washington, U.S.A. *J. Glaciol.*, 13, 187-212.

Melosh, H.J., and A. Raefsky (1980). The dynamic origin of subduction zone topography. *Geophys. J. R. Astron. Soc.*, 60, pp. 333-354.

Nielsen, L.E. (1955). Regimen and flow of ice in equilibrium glaciers. *Bull. Geolog. Soc. America*, 66, 1-8.

Nye, J.F. (1952). The mechanics of glacier flow. *J. Glaciol.*, 2, 82-93.

Nye, J.F. (1953). The flow law of ice from measurements in glacier tunnels, laboratory experiments and the Jungfraufirn borehole experiment. *Proc. R. Soc. London*, Ser. A, 219, 477-489.

Nye, J.F. (1957). The distribution of stress and velocity in glaciers and ice-sheets. *Proc. R. Soc. London*, Ser. A, 239, 113-133.

Nye, J.F. (1960). The response of glaciers and ice-sheets to seasonal and climatic changes. *Proc. R. Soc. London*, Ser. A, 256, 559-584.

Nye, J.F. (1963a). On the theory of the advance and retreat of glaciers. *Geophys. J. R. Astron. Soc.*, 7, 431-456.

Nye, J.F. (1963b). The response of a glacier to changes in the rate of nourishment and wastage. *Proc. R. Soc. London*, Ser. A, 275, 87-112.

Nye, J.F. (1965). The flow of a glacier in a channel of rectangular, elliptic or parabolic cross-section. *J. Glaciol.*, 5, 661-690.

Nye, J.F. (1969). The effect of longitudinal stress on the shear stress at the base of an ice sheet. *J. Glaciol.*, 8, 207-213.

Noll, W. (1955). Reiner-Rivlin fluids. *J. Ratl. Mech. Anal.* 4, pp. 204-222.

Oden,J.T.,and Reddy,J.N.(1976). An Introduction to the Mathematical Theory of the Finite Element Method. Wiley,N.Y.

Paterson, W.S.B. (1964). Variations in velocity of Athabaska Glacier with time. *J. Glaciol.*, 3, 277-285.

Paterson, W.S.B. (1977). Secondary and tertiary creep of glacier ice as measured

by borehole closure rates. *Rev. Geophys. Space Phys.*, 15, 47-55.

Paterson, W.S.B. (1981). Physics of Glaciers. 2nd Edition, Pergamon Press, Oxford, 380 pp.

Rasmussen, L. and W. Campbell (1973). Comparison of three contemporary flow laws in a three-dimensional time-dependent glacier model. *J. Glaciol.*, 12, pp. 361-373.

Raymond, C.F. (1969). Flow in a transverse section of Athabaska Glacier, Canada. Ph.D. Thesis, California Institute of Tehnology.

Raymond, C.F. (1971). Flow in a transverse section of Athabaska Glacier, Alberta, Canada. *J. Glaciol.*, 10, 55-84.

Raymond, C.F. (1973). Inversion of flow measurements for stress and rheological parameters in a valley glacier. *J. Glaciol.*, 12, 19-44.

Rigsby, G.P. (1958). Effect of hydrostatic pressure on velocity of shear deformation of single crystals of ice. *J. Glaciol.*, 3, 273-278.

Robin, G. et al. (1969). Interpretation of radio echo sounding in polar ice sheets. *Philos. Trans. Roy. Soc.*, 265, 437-505.

Robin, G. de Q. (1975). Velocity of radio waves in ice by means of a bore-hole interferometric technique. *J. Glaciol.*, 15, 151-159.

Robin, G. de Q. (1975). Radio-echo sounding: Glaciological interpretations and applications. *J. Glaciol.* 15, 44-64.

Russell-Head, D.S. and W.F. Budd (1979). Ice sheet flow properties from combined borehole shear and ice core studies. *J. Glaciol.*, 24, 117-130.

Seber, G. (1977). Linear Regression Analysis. Wiley, N.Y.

Sharp, R.P. (1960). Glaciers. University of Oregon Press, Eugene, Oregon, U.S.A.

Shchigolev, B.M. (1965). Mathematical Analysis of Observations. American Elsevier, N.Y. 350 pp.

Shreve, R.L. and R.P. Sharp (1970). Internal deformation and thermal anomalies in lower Blue Glacier, Mount Olympus, Washington, U.S.A. *J. Glaciol.*, 9, 65-86.

Shumskiy, P.A. (1975). Mechanisms and causes of glacier variations. *IAHS* ,104, 318-332.

Smith, B.M.E. and S. Evans (1972). Radio Echo Sounding: Absorption and scattering by water inclusions and ice lenses. *J. Glaciol.* VII, 133-146.

Spicer, R. (1983, unpublished). Terminus variations of Blue Glacier. (Master's Thesis, Univ. Wash., Seattle.)

Strangway, D.W. et al. (1974). Radio frequency interferometry - a new technique for studying glaciers. *J. Glaciol.* 13, 123-132.

Sverrison, M. et al. (1980). Radio-echo equipment for depth sounding of temperate glaciers. *J. Glaciol.* Vol. 25, 477-486.

Tsang, L. et al. (1974). Numerical evaluation of EM fields due to dipole antennas in the presence of statified media. *JGR*, 79, 2077-2080.

Walford, M.E.R., P.C. Holdorf and R.G. Oakberg (1977). Phase-sensitive radio-echo sounding at the Devon Island ice cap, Canada. *J. Glaciol.*, 18, 217-229.

Walford. M.E.R. and M.F. Varper (1981). The detailed study of glacier beds using radio-echo techniques. *Geophys. J. Roy. Soc.*, 67, 487-514.

Watts, R.D. and A.W. England (1975). Radio-echo sounding of temperate glaciers: ice properties and sounder design criteria. *J. Glaciol.*, 15, 459-461.

Watts, R.D. and A.W. England (1976). Radio-echo sounding of temperate glaciers: ice properties and sounder design criteria. *J. Glaciol.*, 17, 39-48.

Watts, R. and D.L. Wright (1981). Systems for measuring thickness of temperate and polar ice from the ground or from the air. *J. Glaciol.* 27, 459-469.

Weertman, J. (1964). The theory of glacier sliding. *J. Glaciol.*, 5, 287-303.

Weertman, J. (1973). Creep of ice. In E. Whalley, S.J. Jones and L.W. Gold (Eds.), *Physics and Chemistry of Ice.* Royal Society of Canada, Ottawa, Canada., 320-337.

York, D. (1966). Least-squares fitting of a straight line. *Canad. J. Physics* 44, 1079-1086.

Zienkiewicz, O.C., and I.C. Cormeau (1974). Visco-plasticity and creep in elastic solids - a unified numerical solution approach. *Int. J. Numer. Meth. Engng.*, 8, pp. 821-845.

Zienkiewicz, O.C. (1977). The Finite Element Method. McGraw Hill, London, England. 3rd edition.

APPENDICES

APPENDIX A

FOUR-DIMENSIONAL LEAST-SQUARES MAGNET SEARCH

The following development of the 4-d least squares analysis for magnet location follows the 3-d procedure of Harrison et al. (1978).

Let **B** be the measured magnetic field, $\mathbf{B}^e$ be the earth's field, V the magnetic potential such that $\mathbf{B} = -\nabla V$, (x,y) the horizontal coordinates of the magnet, with y directed to magnetic north and x eastward, z the vertical coordinate (positive upward) of the center of the magnet, and let the superscripts e and m refer to properties of the earth's and magnet's fields, respectively. Then, for a vertical dipole magnet of moment M (Jackson,1972)

$$V^e = -B^e (y\sin\varphi - z\cos\varphi) \tag{A.1a}$$

$$V^m = \frac{M z}{r^3} \tag{A.1b}$$

where $r = (x^2+y^2+z^2)^{1/2}$. Since the NMR magnetometer measures the total field $B = [(\nabla V)^T \cdot \nabla V]^{1/2}$, the magnitude of the magnetic field of a vertical magnet located at (x,y,z) is given by

$$B = [(B^e)^2 + 2MB^e f + M^2 g]^{1/2} , \tag{A.2}$$

where

$$f = f (x,y,z,\varphi) = (3yz\sin\varphi + (x^2 + y^2 - 2z^2) \cos\varphi) / r^5 ,$$

$$g = g (x,y,z) = (x^2 + y^2 + 4z^2) / r^8 .$$

At (x,y) = (0,0) and at high magnetic latitudes, equation (A.2) reduces approximately to (2.20).

Equation (A.2) is the field at (x,y,z) of a magnet located at the origin. If the origin is translated to the center of the surface array then (A.2) yields an

equation of the field due to a magnet whose coordinates relative to this new origin and moment can be represented by the four-vector $\hat{\mathbf{x}} = (\hat{x}_1, \hat{x}_2, \hat{x}_3, \hat{M})$. The least squares method seeks to minimize the residuals between calculated and observed measurements at the nine array points with respect to the four unknowns $\hat{\mathbf{x}}$, i.e.

$$\delta \left(\sum_{n=1}^{9} (B_n^{calc} - B_n^{obs})^2 \right) = 0 \tag{A.3}$$

where B_n^{calc} is obtained from (A.2) after translation of the coordinates. This procedure leads to four nonlinear equations

$$\sum_n \left(B_n^{calc} - B_n^{obs} \right) \frac{\partial B^{calc}}{\partial \hat{x}_i} = 0, \quad i = 1,...4 \tag{A.4}$$

These equations are linearized about an initial guess, $\hat{\mathbf{x}}^o$,

$$B_n^{calc} \approx B_n^{calc}(\hat{\mathbf{x}}^o) + \sum_{j=1}^{4} \frac{\partial B^{calc}}{\partial \hat{x}_j} \Big|_{\hat{\mathbf{x}}^o} (\hat{x}_j - \hat{x}_j^o) . \tag{A.5}$$

Equation (A.4) then yields

$$\mathbf{A}\hat{\mathbf{x}} = \mathbf{b} \tag{A.6}$$

where the 4 x 4 matrix A has the components

$$A_{ij} = \sum_{n=1}^{9} \frac{\partial B_n^{calc}}{\partial \hat{x}_i} \Big|_{\hat{\mathbf{x}}^o} \frac{\partial B_n^{calc}}{\partial x_j} \Big|_{\hat{\mathbf{x}}^o} \tag{A.7}$$

and the 4 - vector **b** has components

$$b_j = \sum_{n=1}^{9} \left\{ B_n^{obs} - B_n^{calc}(\hat{\mathbf{x}}^o) + \sum_{j=1}^{4} \frac{\partial B_n^{calc}}{\partial \hat{x}_j} \Big|_{\hat{\mathbf{x}}^o} \hat{x}_j^o \right\} \frac{\partial B_n^{calc}}{\partial \hat{x}_j} \Big|_{\hat{\mathbf{x}}^o} . \tag{A.8}$$

Starting with an initial guess $\hat{\mathbf{x}}^0 = (0,0,-z^o,M^o)$, where z^o equals to the original estimate as derived from (2.20) and M^o equals the value measured prior to the field season, 3-6 iterations usually lead to an adequate minimization of relation (A.3).

APPENDIX B

ANNUAL VELOCITY DATA, 1977-1980

The tables in this appendix give the components of annual surface velocity determined from 1977 to 1980. Velocity components are given in cm/day as mean rates over a one year interval from mid-August to mid-August (if possible). The symbols used in the tables are defined as follows:

u = horizontal velocity, $u^2 = u_x^2 + u_y^2$

w = vertical velocity

φ = azimuth of horizontal velocity vector, measured clockwise from North

ϑ = plunge of velocity vector, taken to be positive if vector plunges downward in the direction of flow

σ_u = standard error in horizontal velocity

σ_w = standard error in vertical velocity

* indicates those markers which were reset to their initial position at the end of each field season, thus yielding annual velocities at a fixed point in space.

** summer velocities only

Tables B.1 through B.3 list the annual velocities measured from 1977 to 1978, 1978 to 1979, and 1979 to 1980, respectively.

Table B.1

Surface Velocity, 1977-78 (cm/day)

Location	u	ϑ	w	φ	σ_u	σ_w
A2**	15.44	-51.8	-1.93	7.2	0.29	0.10
A3**	12.39	-49.5	-1.14	5.3	0.30	0.09
B1	11.20	-54.5	-0.46	2.3	0.10	0.05
B2	12.65	-53.7	-0.14	0.6	0.18	0.03
B3	12.85	-48.5	0.25	-1.1	0.47	0.07
B4	12.29	-49.6	0.29	-1.4	0.13	0.03
B5	9.61	-46.3	0.67	-4.0	0.12	0.03
C00	2.16	-54.6	0.40	-10.6	0.07	0.04
C1	12.22	-50.0	-0.15	0.7	0.05	0.02
C2	12.77	-49.1	-0.22	1.0	0.05	0.03
C3	13.16	-48.9	-0.25	1.1	0.05	0.03
C4	13.67	-47.1	-0.25	1.0	0.05	0.03
C5	13.60	-45.4	-0.45	1.9	0.05	0.03
C6	12,50	-44.2	-0.50	2.3	0.05	0.03
C7	9.14	-41.9	-0.48	3.0	0.06	0.03
C8	5.15	-38.7	1.32	-14.4	0.07	0.05
BHS1	13.15	-49.6	-0.11	0.5	0.05	0.03
BSM1	13.69	-49.8	-0/07	0.3	0.05	0.03
D0	12.04	-47.8	-1.09	5.2	0.08	0.05
D1	12.90	-46.8	-1.30	5.7	0.05	0.03
D2	13.87	-42.8	-1.23	5.1	0.05	0.02
D3	14.56	-42.2	-1.32	5.2	0.05	0.02
D4	15.03	-42.3	-1.24	4.7	0.05	0.02
D5	13.54	-41.6	-0.39	1.7	0.05	0.02
D6	7.75	-38.4	0.57	-4.2	0.05	0.03
D7**	3.08	-38.9	0.10	1.9	0.65	0.10
BHS2	14.45	-43.3	-1.61	6.3	0.05	0.02
BHM2	14.63	-43.6	-0.90	3.5	0.05	0.03
E0	9.86	-45.2	-5.57	29.5	0.16	0.12
E1	13.44	-33.0	-3.70	15.4	0.08	0.04
E2	15.79	-30.7	-2.46	8.7	0.06	0.03
E3	16.51	-28.3	-1.83	6.3	0.06	0.03
E4	17.12	-26.8	-1.26	4.2	0.06	0.03
E5	16.22	-24.7	-1.54	5.4	0.06	0.03
E6**	12.22	-13.9	-1.22	5.7	0.20	0.04
BHB	16.28	-31.8	-2.16	7.7	0.06	0.03
F0**	9.60	-10.5	-----	---	0.33	----
F1	11.46	-10.2	-1.31	6.5	0.12	0.04
F2	13.55	-10.0	-1.28	5.4	0.08	0.03
F3	15.18	-9.8	-1.29	4.8	0.06	0.03
F4	16.10	-11.0	-1.06	3.8	0.06	0.02
F5	16.05	-11.6	-0.76	2.7	0.06	0.02
F6	13.86	-11.8	0.01	-0.0	0.06	0.02
F7	6.42	-5.6	-0.03	-0.3	0.07	0.03
BHA2**	16.04	-8.7	-1.48	5.3	0.29	0.08

Location	u	ϑ	w	φ	σ_u	σ_w
G0	8.21	-3.0	-1.86	12.8	0.15	0.04
G1	12.16	-1.0	-0.88	4.1	0.08	0.03
G2	14.42	0.2	-0.58	2.3	0.07	0.02
G3	14.87	-0.5	-0.65	2.5	0.06	0.02
G4	15.71	-0.9	-0.45	1.7	0.05	0.02
G5	15.53	-0.8	-0.20	0.7	0.05	0.02
G6	12.79	0.5	-0.25	1.1	0.05	0.03
G7	5.40	5.9	0.10	-1.1	0.05	0.03
H0	3.40	1.7	0.29	-4.8	0.08	0.04
H1	9.51	8.1	0.12	-0.9	0.08	0.04
H2	13.74	7.0	-0.28	1.2	0.06	0.03
H3	14.28	9.2	-0.39	1.6	0.06	0.03
H4	14.61	9.3	-0.47	1.8	0.05	0.03
H5	14.28	9.6	-0.54	2.2	0.05	0.03
H6	12.41	10.4	-0.79	3.7	0.05	0.03
H7	6.74	8.2	-0.52	4.4	0.05	0.03
I00**	3.81	22.0	-0.79	11.7	0.31	0.09
I0	6.09	22.7	-0.95	8.9	0.04	0.02
I1	10.32	21.7	-1.47	8.1	0.04	0.02
I2	11.61	21.8	-1.44	7.1	0.03	0.01
I3	12.77	18.8	-1.47	6.6	0.03	0.01
I4	14.39	21.8	-1.52	6.0	0.03	0.01
I5	14.82	20.4	-1.58	6.1	0.03	0.01
I6	14.87	18.3	-1.73	6.6	0.04	0.01
I7	14.67	17.2	-1.49	5.8	0.04	0.02
I8	13.48	16.4	-1.29	5.5	0.04	0.02
I9	9.48	12.2	-0.99	5.9	0.05	0.02
I10	14.46	15.9	-0.94	3.7	0.04	0.02
I11	14.64	16.4	-1.39	5.4	0.04	0.02
I12	14.82	21.4	-1.71	6.6	0.03	0.01
I13**	3.70	12.7	-1.13	17.0	0.43	0.10
I4o	14.18	17.7	-1.13	4.6	0.03	0.01
J1	5.50	39.6	-0.85	8.8	0.07	0.03
J2	11.48	46.0	-1.40	6.9	0.04	0.02
J3	13.68	42.4	-2.07	8.6	0.04	0.01
J4	15.00	36.0	-2.08	7.9	0.04	0.01
J5	15.35	31.3	-2.19	8.1	0.04	0.01
J6	15.28	27.6	-1.77	6.6	0.04	0.01
J7	14.61	25.1	-1.35	5.3	0.04	0.01
J8	13.17	21.5	-1.01	4.4	0.05	0.02
J9	9.49	16.1	-1.19	7.1	0.05	0.01
J10**	5.50	-3.2	-2.64	25.7	0.12	0.08
K1	13.03	53.2	-1.71	7.5	0.04	0.02
K2	12.30	48.4	-1.19	5.5	0.06	0.02
K3**	15.84	49.6	-2.56	9.2	0.08	0.06
K4	14.64	46.1	-1.83	7.1	0.05	0.02
K5	14.07	37.3	-0.08	0.3	0.06	0.04
L1**	7.78	77.6	-1.50	10.9	0.28	0.15
L2	12.33	62.1	-1.74	8.0	0.03	0.03
L3	15.60	65.7	-2.00	7.3	0.02	0.03
L4	13.79	68.5	-1.50	6.2	0.03	0.04
L5**	17.40	66.4	-2.78	9.1	0.09	0.08

Location	u	ϑ	w	φ	σ_u	σ_w
L6**	16.60	64.4	-3.03	10.3	0.09	0.08
L7**	15.76	65.0	-3.38	12.1	0.08	0.08
L8**	13.92	57.0	-4.47	17.8	0.08	0.07
L9**	11.73	51.2	-4.68	21.8	0.07	0.09
L10	8.49	18.0	0.74	-5.0	0.04	0.03
L11**	13.90	11.1	-2.76	11.24	0.09	0.08
L12**	12.93	9.2	-2.50	10.9	0.09	0.07
M1	13.51	57.1	-1.85	7.8	0.04	0.02
N2**	15.72	68.0	-4.71	16.7	0.17	0.08
N3	19.00	68.8	-4.73	14.0	0.04	0.02
N4	19.94	67.4	-4.14	11.7	0.04	0.02
N5**	21.03	71.5	-8.66	22.4	0.13	0.08

Table B.2
Surface Velocity, 1978-79 (cm/day)

Location	u	ϑ	w	φ	σ_u	σ_w
B3*	11.65	-51.2	0.33	-1.6	0.08	0.04
C4*	11.60	-46.1	-0.30	1.4	0.05	0.02
BHS1	12.03	-51.2	0.01	0.0	0.04	0.01
BHM1	12.21	-49.8	0.21	-1.0	0.05	0.01
D3*	13.28	-42.2	-1.36	5.8	0.04	0.02
BHS2	12.99	-44.8	-0.90	4.0	0.04	0.02
BHM1	12.81	-44.9	-1.44	6.4	0.04	0.03
E3*	14.81	-29.5	-1.83	7.0	0.06	0.03
BHB	14.52	-37.2	-2.27	8.9	0.04	0.02
F3*	13.49	-10.0	-1.32	5.6	0.06	0.02
F4	14.80	-13.4	-1.09	4.2	0.05	0.02
G3*	13.05	0.4	-0.69	3.0	0.07	0.03
H3*	12.73	9.4	-0.38	1.7	0.05	0.02
H4	13.41	7.6	-0.30	1.3	0.04	0.01
H7	5.81	6.4	-0.86	8.4	0.06	0.04
I4*	12.42	21.9	-1.21	5.6	0.05	0.03
I6	13.00	16.5	-1.21	5.3	0.05	0.02
I7*	12.69	16.9	-1.19	5.4	0.05	0.02
I11	13.00	14.3	-0.91	4.0	0.04	0.01
I4o	12.48	14.4	-0.83	3.8	0.04	0.01
J4*	12.92	36.2	-1.78	7.8	0.06	0.01
J6	13.22	27.3	-1.64	7.0	0.06	0.02
J8*	12.10	19.9	-1.50	7.1	0.06	0.03
J9	8.65	17.5	-1.13	7.4	0.06	0.02
K2*	12.96	49.5	-2.66	11.6	0.05	0.02
L2	10.60	58.8	-3.24	16.9	0.04	0.01
L4*	14.46	61.8	-2.62	10.3	0.04	0.02
L12**	10.13	17.9	-2.59	14.5	0.29	0.12
N2	14.03	69.7	-4.25	16.9	0.08	0.05
N4*	16.91	73.6	-5.17	17.0	0.08	0.07
Q1**	11.42	16.6	-8.41	37.0	0.34	0.12
Q2**	14.40	9.4	-6.27	23.5	0.38	0.12

Q3**	14.20	10.2	-4.49	17.5	0.41	0.15
Q4**	12.52	12.0	-3.55	15.5	0.82	0.51

Table B.3
Surface Velocity, 1979-80 (cm/day)

Location	u	v	w	φ	σ_u	σ_w
C4*	12.22	-47.1	-0.59	2.8	0.06	0.03
BHS1	11.28	-52.3	0.05	-0.3	0.05	0.02
BHM1	11.47	-50.6	0.34	-1.7	0.05	0.02
D3*	12.61	-43.8	-1.15	5.2	0.05	0.02
BHS2	12.10	-46.4	-0.53	2.5	0.05	0.02
BHM2	12.06	-46.26	-0.38	1.8	0.06	0.03
E3	14.44	-31.9	-1.89	7.5	0.08	0.04
BHB	13.10	-40.8	-2.04	8.8	0.05	0.02
F3*	13.05	-15.8	-1.60	7.0	0.04	0.01
G3*	12.73	-2.2	-1.00	4.5	0.04	0.01
H3	12.19	7.1	-0.38	1.8	0.04	0.02
I4*	12.16	17.3	-1.40	6.6	0.04	0.02
I4o	11.59	11.9	-0.87	4.3	0.06	0.03
J2**	12.07	35.3	-2.10	9.8	0.29	0.13
J4*	12.18	27.7	-1.93	9.0	0.04	0.01
K3**	12.38	4106	-2.02	9.3	0.37	0.15
L4**	13.77	62.6	-2.90	11.9	0.26	0.11
N2**	16.06	73.5	-8.34	27.4	0.26	0.13
N4**	14.90	71.2	-3.91	14.7	0.22	0.14
N5**	17.97	71.8	-8.71	25.9	0.31	0.18

APPENDIX C

FLOW OF A NON-NEWTONIAN FLUID IN AXIALLY SYMMETRIC GEOMETRY

C.1 Gravity Flow Down a Long Annular Pipe

Consider a long annular conduit of inner radius R_1 and outer radius R_2 which is inclined at an angle of α to the horizontal. Let the z axis be directed down the center of the inner cylinder and $(\hat{r},\hat{\vartheta})$ be defined in the plane normal to this in the usual sense. Let the conduit be filled completely with a fluid of density ρ obeying a power-law creep relation. Assuming only axial flow ($\mathbf{u} = (0,0,u_z)$) and neglecting entrance and exit phenomena. ($\frac{\partial}{\partial z} = \frac{\partial}{\partial \vartheta} = 0$), the problem of the flow down the annular pipe reduces to the solution of

$$\partial \frac{\tau_{rz}}{\partial r} + \frac{1}{r}\tau_{rz} = -f_z \qquad (C.1)$$

$$\dot{\varepsilon}_{rz} = \frac{1}{2}\frac{\partial u_z}{\partial r} = \frac{\tau_{rz}^n}{2\eta_f} \quad , \qquad r \in (R_1, R_2) \qquad (C.2)$$

with $f_z = \rho g \sin\alpha$, subject to the condition of no slip at the walls:

$$u(R_1) = u(R_2) = 0 \, . \qquad (C.3)$$

Equation (C.1) may be integrated to give

$$\tau_{rz}(r) = \frac{f_z}{2}\left(\frac{R_1^2}{r} - r \right) + \frac{R_1}{r}\tau_{R_1 z} \qquad (C.4)$$

where the stress at the boundary R_1, $\tau_{R_1 z}$, remains undetermined.

The velocity is obtained from (C.2)

$$u_z(r) = \frac{1}{\eta_f}\left(\frac{f_z}{2}\right)^n \int_{R_1}^{r} \left(\frac{c}{r'} - r' \right)^n dr' \qquad (C.5)$$

where $c = R_1^2 \left(1 + \frac{2\tau_{R_1 z}}{R_1 f_z} \right)$. Applying the second of (C.3) gives $\tau_{R_1 z}$ and, thus, τ_{rz}

and $u_z(r)$. For different n:

n = 1:

$$u(R_2) = 0 \rightarrow c = \frac{R_2^2 - R_1^2}{2\ln(R_2/R_1)}.$$

This determines $\tau_{R_1 z}$ and, therefore,

$$\tau_{rz}(r) = \frac{f_z}{2}\left\{\frac{1}{2r}\left[\frac{R_2^2 - R_1^2}{\ln(R_2/R_1)}\right] - r\right\}, \qquad (C.6)$$

and

$$u_z(r) = \frac{1}{2\eta_f}\frac{f_z}{2}\left\{\frac{R_2^2 - R_1^2}{\ln(R_2/R_1)}\ln\frac{r}{R_1} + (R_1^2 - r^2)\right\} \qquad \forall r \in [R_1, R_2] \qquad (C.7)$$

With $R_1 = 10$ and $R_2 = 19$ this yields

$$\frac{\tau_{rz}}{(\frac{1}{2}f_z)} = \left[\frac{203.3}{r} - r\right] . \qquad (C.8)$$

n = 3:

$$u_z(R_2) = 0 = \frac{c^3}{R_1^2}\left[1 - (\frac{R_1}{R_2})^2\right] + 6c^2\ln(\frac{R_1}{R_2}) + 3c(R_2^2 - R_1^2) + \frac{1}{12}(R_1^4 - R_2^4) . \qquad (C.9)$$

Solution of the cubic (C.9) gives $\tau_{R_1 z}$. For $R_1 = 10, R_2 = 19$, c = 197.9 and

$$\frac{\tau_{rz}(r)}{(\frac{1}{2}f_z)} = \left[\frac{197.9}{r} - r\right] . \qquad (C.10)$$

$u_z(r)/[(\frac{1}{2}f_z)^3/2\eta_f]$ is given by (C.9) with R_2 replaced by r.

n = 5:

$$\frac{u_z(r)}{[(\frac{1}{2}f_z)^5/2\eta_f]} = \frac{c^5}{2}(\frac{1}{R_1^4} - \frac{1}{r^4}) + 5c^4(\frac{1}{r^2} - \frac{1}{R_1^2}) + 20c^3\ln(\frac{r}{R_1})$$

$$-10c^2(r^2-R_1^2)+\frac{5}{2}c(r^4-R_1^4)-\frac{1}{3}(r^6-R_1^6) \qquad (C.11)$$

where c = 195.7 for $(R_1, R_2) = (10,19)$, and

$$\frac{\tau_{rz}}{(\frac{1}{2}f_z)} = \left[\frac{195.7}{r} - r\right] . \qquad (C.12)$$

The relations (C.8), (C.10) and (C.12) show that even in this simple geometry, the stresses are dependent on the flow law exponent, although the coupling is small. The stress and flow out of the annulus are shown in Figure C.1 for different n, along with finite elements results. The velocity profiles are seen to be only slightly asymmetric for the geometry prescribed, $(R_1, R_2) = (10,19)$. For this large R_1 the shear stress in nearly linear. The asymmetry in u_z and non-linear shear stress would be more marked for smaller radii of curvature. The finite element results agree quite well for all values of n tested.

C.2 Flow Between Two Rotating Coaxial Cylinders

Let R_1 and R_2 $(0 < R_1 < R_2)$ be the radii of two coaxial cylinders of which the outer one is rotating at a rate Ω. (The case where both R_1 and R_2 are rotating is similarly treated.) Assume there are no body forces acting on the system and that the cross section is taken far from the ends of the cylinders. Then there will exist no variation of the stresses or **u** in the ϑ or z directions, which are defined in the usual sense. Then, for a power-law type fluid with viscosity factor η_f, the following is a well-posed problem for the solution of the stresses and flow between the rotating cylinders $(\mathbf{u} = (0, u_\vartheta, 0))$:

$$\frac{\partial \tau_{r\vartheta}}{\partial r} + \frac{2}{r}\tau_{r\vartheta} = 0 \qquad (C.13)$$

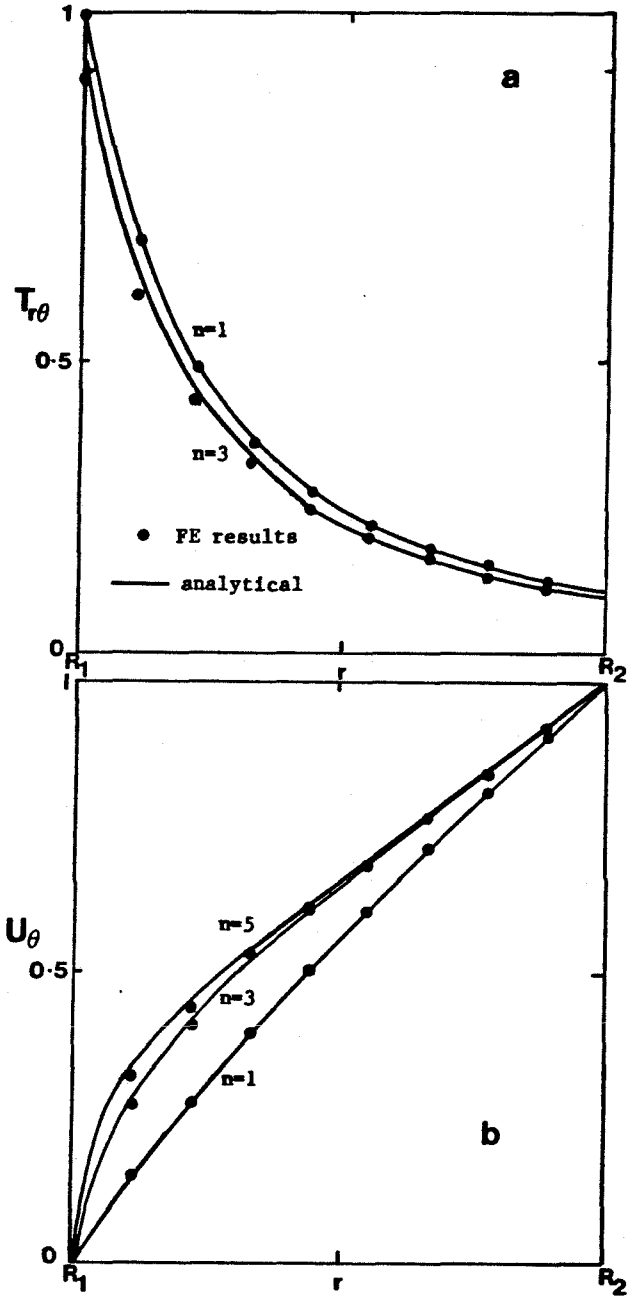

Figure C.1 (a) Velocity profile across annular conduit (R_1=10, R_2=16), showing analytical results (solid curves) and FE results (circular dots) for different n. (b) Shear stress across annular conduit, with analytical (solid curves) and FE results (dots). Shear stress has been normalized by $\frac{1}{2}f_z$.

$$\dot{\varepsilon}_{r\vartheta} = \frac{1}{2}\left(\frac{\partial u_\vartheta}{\partial r} - \frac{u_\vartheta}{r}\right) = \frac{1}{2\eta_f}\tau_{r\vartheta}^n \quad , \qquad r \in (R_1, R_2) \tag{C.14}$$

and

$$u_\vartheta(R_1) = 0 \qquad u_\vartheta(R_2) = \Omega\, R_2 \tag{C.15}$$

Then $\tau_{r\vartheta} = c r^{-2}$, where $c = R_1^2 \tau_{r\vartheta}(R_1)$

and

$$\frac{u_\vartheta(r)}{r} = \frac{c^n}{\eta_f}\int_{R_1}^{r} \frac{1}{\rho^{2n+1}}\, d\rho \, .$$

Evaluating the latter at $r = R_2$ gives the constant c, using (C.15). This then gives the solutions

$$\tau_{r\vartheta}(r) = (2n\,\Omega\,\eta_f)^{\frac{1}{n}} \frac{(R_1 R_2)^2}{(R_2^{2n} - R_1^{2n})^{\frac{1}{n}}} \frac{1}{r^2} \tag{C.16}$$

$$\text{and} \qquad u_\vartheta(r) = \Omega\, R_2 \left(\frac{R_2}{r}\right)^{2n-1} \left[\frac{r^{2n} - R_1^{2n}}{R_2^{2n} - R_1^{2n}}\right]. \tag{C.17}$$

Equation (C.16) shows that, for a specified non-zero boundary velocity, the viscosity factor, η_f, enters into the evaluation of the stress. Additionally, $\tau_{r\vartheta}$ is dependent upon the stress exponent. Figures C.2a,b show $\tau_{r\vartheta}$ and u_ϑ for $R_1 = 4, R_2 = 13$, and $\Omega\, R_2 = 0.1$. The finite element results for the same problem are also shown. The FE results again agree quite well with the analytical values for all values of n.

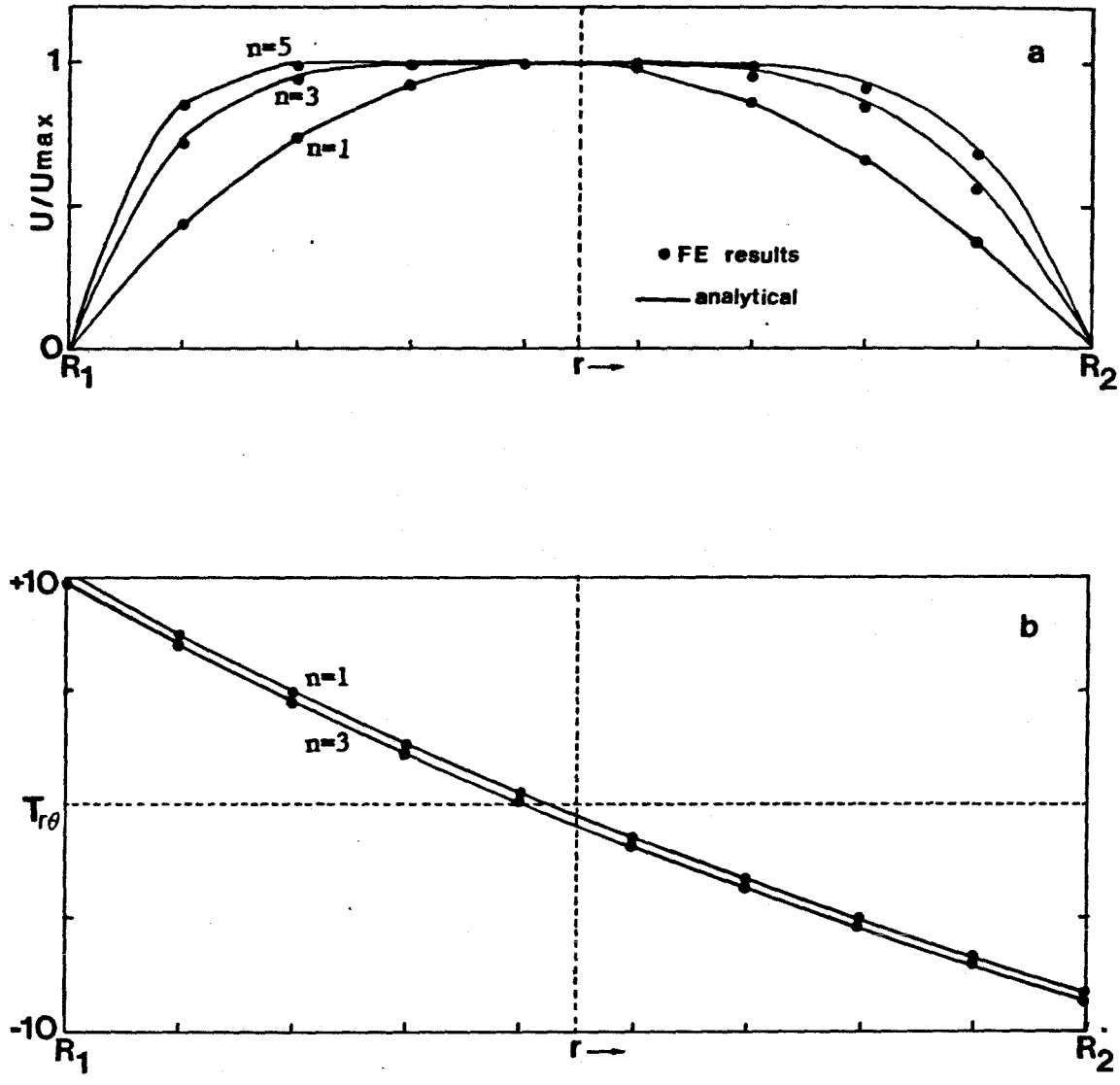

Figure C.2 Shear stress and velocity between rotating cylinders, showing FE results (circular dots) and analytical rsults (curves) for different n. $u(R_1) = 0$, $u(R_2) = \Omega R_2$ (a) $T_{r\theta} (= \tau_{r\theta}/(2n\Omega\eta)^{1/n}$, (b) $U = u_\theta/\Omega R_2$.